High-Throughput Exploration of Defect Passivation Strategies for Kesterite Photovoltaics

Andrew D. Collord

A dissertation

submitted in partial fulfillment of the

requirements for the degree of

Doctor of Philosophy

University of Washington

2015

Reading Committee:

Hugh Hillhouse, Chair

John Berg

Scott Dunham

Daniel Gamlin

Program Authorized to Offer Degree:

Chemical Engineering

University of Washington

Abstract

High-Throughput Exploration of Defect Passivation Strategies for Kesterite Photovoltaics

Andrew D. Collord

Chair of the Supervisory Committee:
Professor Hugh W. Hillhouse
Department of Chemical Engineering

The need for low-cost, sustainable energy generation has driven materials research towards the development of thin film solar cells based on earth-abundant materials. One of the leading candidates is $Cu_2ZnSn(S,Se)_4$, (CZTSSe), a material which bears many resemblances to its parent compound $Cu(In,Ga)Se_2$, but is comprised entirely of earth-abundant primary metals (metals mined for directly). CZTSSe devices have reached 12.6% efficiency,[1] but will need to improve further to be competitive to current technologies and reach grid parity. Compared to the theoretical limits, the world record CZTSSe device collects about 81% of the available current but only produces 58% of the maximum voltage. The low open-circuit voltage is believed to result from a large quantity of intrinsic defects,[2, 3] a problem faced by almost all solar cell materials. To rapidly advance the efficiency and understanding of defects in CZTSSe, we have

developed a high-throughput screening process based on a combinatorial spray deposition system and a confocal photoluminescence mapping instrument calibrated to determine the absolute photon flux. By fitting the absolute intensity photoluminescence (AIPL) spectra, we are able to extract quantitative metrics about the quantity of charged defects and determine the quasi-Fermi level splitting (the maximum possible Voc at a given illumination intensity) without making completed devices. This process allows us to test thousands of samples in the time it formerly took to test one, and reduces error due to additional processing steps. By combining over 40,000 AIPL spectra, I have been able to map out how the optoelectronic properties depend on the relative quantities of Cu, Zn, and Sn. Further, I have investigated the impact of over 25 different extrinsic species in varying concentrations, including the effect of germanium alloying to produce the larger band gap material $Cu_2Zn(Sn,Ge)(S,Se)_4$, and an in-depth study of group-I dopants. This work has contributed to the understanding of lithium as an effective dopant for CZTSSe and greatly improved the communities understanding of both intrinsic and extrinsic defects, enabling efficiencies from our lab as high as 11.8%. Additionally through Germanium alloying we have demonstrated an 11% CZTGSSe solar cell with the lowest reported voltage deficit of any kesterite device.

TABLE OF CONTENTS

LIST OF FIGURES

LIST OF TABLES

ACKNOWLEDGEMENTS

I would like to thank my supervisor, Prof. Hugh Hillhouse, for supporting my work. His motivation, energy, and enthusiasm are unparalleled. He has continually pushed me to refine my work and has helped to show me the many facets of academic research.

I want to thank my co-workers Robert McCarthy, Steve Gaik, Cori Bucherl, Chris Wolcott, John Katahara, Hao Xin, Ian Braly, Wes Williamson, Warren Pinkard, Alex Uhl, and Jac Clark. I'm glad to be able to call them friends, and it has been a pleasure working with each and every one of them. Their support, both personal and professional, helped make this work possible. In particular, I would like to thank John Katahara for numerous discussions about photoluminescence, for always keeping the Horiba running as smoothly as possible, and helping to foster a sense of comradery within the group; and Dr. Steve Gaik, whose hands-on knowledge, willingness to teach, and hours of labor spent on the spray coater enabled the completion of this work.

I would like to acknowledge all my friends within the ChemE department and on the intramural soccer teams. Between the hours of lab work they took the time win 3 championships and have a great time while doing so.

I want to thank my family. My Mom for always loving and supporting me, and encouraging me through hard times. My Dad for teaching me the hands on skills needed for life, and helping to inspire me to be an engineer. My brothers for their sense of humor and for going first.

Finally, I want to especially acknowledge the love and support of my wife Rachael Collord. Her constant support and encouragement helped me to keep going all these years. She has helped me always keep the big picture in mind and maintain a (relatively) healthy balance in life. She has been there through all the success and frustration, and I wouldn't be where I am today without her.

DEDICATION

To my wife and family, thank you.

PROLOGUE

The work included in this document covers the 5 years of research that I conducted at the University of Washington in Seattle. Here I will briefly outline the structure of this document and highlight the publications that have resulted. In Chapter 1, I discuss fundamental concepts of semiconductors and how they can be used for solar energy conversion. Chapter 2 is an unpublished review paper which includes an analysis of the cost and abundance of the constituent elements, a comprehensive review of materials properties, and design rules for developing high efficiency kesterite devices. In Chapter 3, I discuss defect passivation strategies that have been used to produce high efficiency $Cu(In,Ga)Se_2$ and CdTe solar cells. I also introduce a combinatorial screening process that I helped to design and build. This process allowed me to rapidly apply the defect passivation strategies learned from CIGS and CdTe to kesterite materials, as demonstrated in Chapters 6, 7, and 8. However prior to being able to conduct these experiments, one big hurdle that I faced was finding ways to consistently produce nanocrystal inks with controlled off-stoichiometric compositions. This is the subject of Chapter 4. In Chapter 5, I investigated how the properties of the nanocrystal inks (particle size, compositional heterogeneity, etc) impact the performance of the resulting solar cells. The results of this study highlight that there are many non-trivial aspects to using nanocrystals for solar cells. This ultimately pushed me towards focusing on molecular ink-based routes for the combinatorial experiments, which are the subject of Chapters 6-8. Finally, in Chapter 9 I propose some future work which I believe is necessary for further improving kesterite materials. In total, this work has resulted in 5 peer-reviewed publications (4 first-author) and 2 unpublished works as listed below

[1] A.D. Collord and H.W. Hillhouse. “Stoichiometry Control and the Formation Pathway of Cu-Zn-Sn-S and Cu-Zn-Ge-S Nanocrystals for Sulfoselenide Thin Film Solar Cells”. *Chemistry of Materials*, 2015, 27, 1855-1862.

[2] A.D. Collord and H.W. Hillhouse. The effect of nanocrystal reaction time on $Cu_2ZnSn(S,Se)_4$ solar cells from nanocrystal inks. *Solar Energy Materials and Solar Cells* 2015**,** *141*, 383-390.

[3] A.D. Collord, H. Xin, & H.W. Hillhouse. “Combinatorial Exploration of the Effects of Intrinsic and Extrinsic Defects in $Cu_2ZnSn(S,Se)_4$”, *IEEE Journal of Photovoltaics*, 2015, 5, 288-298.

[4] A.D. Collord and H.W. Hillhouse. “Germanium Alloyed Kesterite Solar Cells with Low Voltage Deficits” (submitted)

[5] A.D. Collord, A. Uhl, and H.W. Hillhouse. “Combinatorial Screening of Extrinsic Elements in Solution Processed $Cu_2ZnSn(S,Se)_4$” (in preparation)

[6] H. Xin, S.M. Vorpahl, A.D. Collord, et al. “Li-Doping Effects the Nanoscale Electrical Properties in $Cu_2ZnSn(S,Se)_4$ and Increases Photovoltaic Efficiency”. *Physical Chemistry Chemical Physics*, 2015.

[7] A. D. Collord, J. K. Katahara, C. N. Bucherl, H. Xin, D. S. Pruzan and H. W. Hillhouse, “Kesterite Solar Cells: State-of-the-art, Perspective, and Grand Challenges for Copper Zinc Tin Sulfide (CZTS) and Selenide (CZTSe) Materials and Devices”. Invited to Energy and Environmental Science. *2012. Unpublished. Available by request*

Chapter 1.
CONVERTING LIGHT INTO ELECTRICITY

A key result from quantum mechanics is that electrons have orbitals with very specific allowable energies, and when atoms are brought into close proximity (such as in a solid material) these orbitals overlap to form bands. These bands of allowed electron states are separated in energy from one another and between them lay energies that an electron within the solid cannot possess. The Fermi level is a concept used to indicate the probability that states at a given energy will be occupied. It is defined as the energy at which there is a 50% chance the state will occupied by an electron. If the Fermi level lies within a band of allowable states, the material is a metal. If the Fermi level lies between bands of allowable states, the materials can be either a semiconductor or an insulator, depending on the energy difference between the bands.

For both semiconductors and insulators, the highest band that is completely filled with electrons is referred to as the valence band (VB). The next highest energy band is referred to as the conduction band (CB), and the energy difference between the valence band maximum (VBM) and the conduction band minimum (CBM) is known as the band gap. Insulators have a large band gap (E_g > 3.5 eV) and as a result their electrical conductivity is very low. Semiconductors have a small band gap (0.25 > Eg > 3.5 eV) such that that ambient thermal or optical excitation is sufficient to generate free carriers, and thus just as their name would imply, they have moderate conductivities, unless doped to increase the conductivity.

1.1.1 *The Energy Conversion Limit*

Semiconductors are the basis of solar photovoltaic energy generation, and it is the solar spectrum reaching the earth's surface which dictates which band gaps are ideal for energy generation. The AM1.5GT standard spectrum is most often used to describe the solar spectrum reaching the earth's surface. In actuality it is the solar spectrum at northern latitudes, assuming the panel is tilted towards the equator. This spectrum is used because it is typical the geographies where most solar panels are currently researched and deployed. Of course, there is far greater energy potential in the equatorial regions, but political and social boundaries as well as economic

disparities limit the deployment in these regions. Figure 1.1 shows the maximum theoretical efficiency of a solar cell as a function of the band gap, calculated using the AM1.5GT spectrum. This calculation assumes a perfect semiconductor with step function absorptivity, no reflectivity losses, and a perfect back reflector.

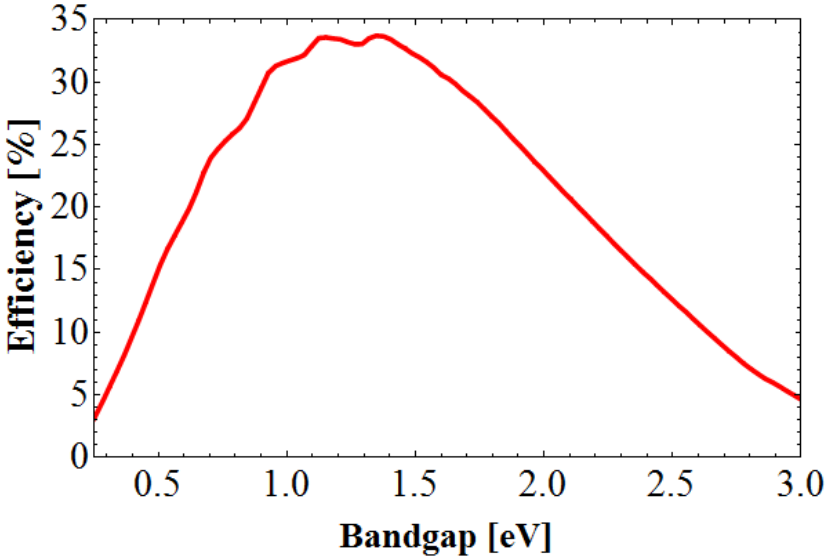

Figure 1.1 The maximum power conversion efficiency for a single junction solar cell as a function of bandgap. The AM1.5GT spectrum was used for the calculation.

1.1.2 *Charge Carrier Extraction*

The absorption of sunlight to create an electron-hole pair is the first step in photovoltaic energy generation, but a single semiconductor in isolation cannot generate usable energy by this process. Additional materials are needed to create an electric field which separates the electron and hole and direct the carriers through an external circuit. If the electron-hole pair is not extracted it will recombine either radiatively (by emitting light) or non-radiatively (by emitting heat), and produce no useable work. To separate the electron-hole pair, a p-n junction is most commonly used. A p-n junction is a physical junction between a p-type material (hole conductor) and a n-type material (electron conductor). A typical device architecture for a thin film solar cell is shown in Figure 1.2. The Fermi level is the energy level at which a state has a 50% chance of being occupied by an electron at a given temperature. A p-type material has a Fermi level located near the valence band due to a relative excess of holes. An n-type material has a Fermi level located close to the conduction band due to an excess of electrons. When these two materials are

put into contact electrons flow from the n-type material into the p-type material leaving behind positive fixed charge, and holes flow from the p-type material into the n-type material leaving behind negative fixed charge. This process occurs until the Fermi levels are equal, and results in the establishment of a fixed electric field. This electric field is what separates the electron and hole and directs them through an external circuit to perform work. However, we can only extract useable energy from a solar cell if the current that it produces is driven by a potential difference (a voltage).

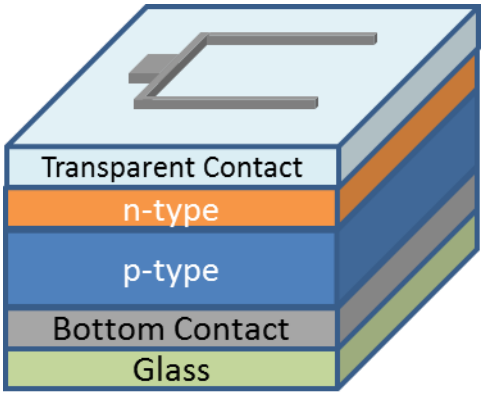

Figure 1.2 Schematic showing a common device architecture for a thin film solar cell. Sunlight enters the device through the transparent top contact.

1.1.3 *The Open-Circuit Voltage*

When light is absorbed by a semiconductor, it generates an electron-hole pair. Under constant illumination, the semiconductor quickly reaches a steady-state between the generation and recombination of these free carriers. The difference between the number of charge carriers under constant illumination and in equilibrium (dark) is referred to as the excess charge carrier concentration (Δn or Δp). The open-circuit voltage (Voc) is directly related to the quantity of excess charge carriers. The Voc is the difference between the chemical potential of the excess electrons in the conduction band and holes in the valence band. These chemical potentials are referred to as the quasi-Fermi levels, and the difference between the quasi-Fermi level for electrons in the conduction band and the quasi-Fermi level for holes in the valence band is called the quasi-Fermi level splitting (QFLS). In an ideal solar cell, the QFLS is exactly equal to the

open-circuit voltage (Voc). As shown in Equation 1.1, for a p-type material, the quasi-Fermi level for electrons ($E_{f,n}$) is dependent on the excess carrier concentration (Δn), which is dependent on the carrier lifetime (τ_{eff}), which is dependent on the relative rates of radiative (τ_{rad}) and non-radiative recombination (τ_{SRH}), which is dependent on the density of defects (N_D), the capture cross-section (σ_n) of the defect, and the electron thermal velocity (v_n). E_i is the intrinsic Fermi level, and n_i is the intrinsic carrier concentration. Therefore as the number of defects increases, the excess carrier concentration decreases, which reduces the chemical potential and thus reduces the open-circuit voltage.

$$E_{F,n} = E_i + kT\ Ln\left[\frac{\Delta n}{n_i}\right] = E_i + kT\ Ln\left[\frac{R\tau_{eff}}{n_i}\right] = E_i + kT\ Ln\left[\left(\frac{1}{\tau_{rad}} + \frac{1}{\tau_{SRH}}\right)/n_i\right]$$
$$= E_i + kT\ Ln\left[\left(\frac{1}{\tau_{rad}} + \sigma_n v_n N_D\right)/n_i\right]$$

Equation 1.1

Table 1.1 summarizes the performance of the champion devices of different photovoltaic technologies compared to their theoretical limits. Most inorganic photovoltaic technologies do a good job of collecting the photo-generated carriers, as demonstrated by a comparison of the current extracted at short circuit (Jsc) to the theoretical maximum under AM1.5G illumination (Jsc^{SQ}). However, with the exception of GaAs, most of these materials produce a smaller portion of the theoretical maximum voltage (Voc^{SQ}). In particular, we see that the world record CZTSSe device produces 81% of the maximum current (Jsc/Jsc^{SQ}), but only 58% of the maximum voltage (Voc/Voc^{SQ}). A low Voc primarily results from having too many defects, both intrinsic and extrinsic, but a low Voc can also result from improper band alignment between layers, band gap fluctuations, or electrostatic potential fluctuations. Determining the exact nature of the loss mechanism is critical for developing a solution to the problem. One technique that can help us to do that is absolute intensity photoluminescence (AIPL). AIPL allows us to determine the quasi-Fermi level splitting, the magnitude of electrostatic potential fluctuations, and the band gap. A discussion of this technique is included in Chapter 6.

These core concepts describe the basic function of a solar cell, a device which allows us to harness the energy of the sun. The electric field produced by putting two electronically different

materials in contact allows us to extract current; the excess carrier population sustained under illumination produces the potential (voltage); and the output power is the simple product of the current and voltage. However, both the electric field and the excess carrier population are diminished as a result of defects within the absorber layer. Thus developing ways to identify and eliminate these defects is a central theme of solar cell research, and is a topic that will be elaborated upon in the following chapters.

TABLE 1.1 COMPARISON OF PHOTOVOLTAIC TECHNOLOGIES TO THEIR THEORETICAL LIMITS.

Record	E_g (eV)	η (%)	$\frac{\eta}{\eta_{max}}$	J_{SC} (mA/cm^2)	$\frac{J_{SC}}{J_{SC,Max}}$	V_{OC} (V)	$\frac{V_{oc}}{V_{oc,Max}}$	FF (%)	$\frac{FF}{FF_{,Max}}$
GaAs	1.42	28.8	0.867	29.68	0.926	1.112	0.968	86.5	0.966
CdTe	1.45	21.5	0.655	30.25	0.981	0.876	0.738	79.4	0.885
x-Si	1.12	25.6	0.766	41.8	0.954	0.740	0.844	82.7	0.952
CIGSe	1.10	21.7	0.657	35.4	0.828	0.747	0.868	79.3	0.913
CZTSSe	1.13	12.6	0.376	34.5	0.812	0.460	0.579	69.8	0.800

Chapter 2.

A REVIEW OF KESTERITE MATERIALS AND DEVICES

2.1 INTRODUCTION

2.1.1 *Status of Global Energy Demand and Solar Energy Production*

Global energy consumption has increased dramatically over the past few decades due to continued population growth and increasing consumption per capita, particularly in countries with rapidly growing GDP. In 2011, approximately 535 EJ (1 EJ = 10^{18} J) of high value energy resources[4, 5] (BP report of 515.5 EJ and Exxon report of 555.3 EJ) were dissipated to ambient thermal energy – on average this is a rate of power dissipation of 16.6 TW or 2.4 kW/person. It is important to note though that this is the rate of consumption of *primary* energy (an energy resource such as coal that has not been subjected to any transformation). There is a significant efficiency loss when coal, natural gas, or petroleum products are combusted to do work (generate electricity, turn a drive shaft, etc.) but not when used for heating. As a result, the total work plus heating used by the world is much less than the reported total primary power dissipation rate. Based on statistics from the U.S. energy economy,[6] only 43% of the primary energy consumption goes to useful work and heating. Applying this fraction to global energy consumption yields an estimate of 7.3 TW of global need for work and heating. Since electricity can theoretically be converted to work or heat with 100% efficiency, 7.3 TW of electricity production could nearly satisfy world power demand (not including any efficiency losses required to generate high energy density liquid fuels that will likely always be needed for air-travel).

Meeting our energy needs with clean, carbon neutral, sustainable resources is important for human health and wellness, the long-term environmental health of our ecosystems, and climate stability. In addition, if high value energy is abundant and inexpensive it can contribute to increasing the standard of living, as quantified by the U.N.'s human development index.[7] Of the various clean carbon neutral energy resources, solar is particularly attractive because of its availability and abundance. The Sun provides approximately 86,000 TW of exergy (the maximum useful work possible, accounting for the 2nd Law of Thermodynamics) to the surface area of the earth [8]. About 25,000 TW strikes land (accounting for cloud cover). Thus, 0.03% of the incident sunlight energy hitting World land area would be sufficient to power the planet. Assuming an average efficiency of 15% in converting the free energy in the sunlight to electricity, this would require harvesting approximately 0.2% of sunlight incident on

global land area to meet current energy demands. In practice, one must account for the local demand curve, the local solar insolation, and the specific solar technology. It is also important to note that without significant energy storage mechanisms, other resources and technologies must be used to supply baseload capacity. This can be met with wind, hydro, and some nuclear or combined cycle natural gas generation.

Although PV is not currently suitable for baseload power generation, there is plenty of room for growth as an intermediate- or peak-load power supply. The last decade has seen rapid growth of solar PV and dramatic cost reductions. The median installed cost of PV installations >100kW in the US fell from an average of about $\$9/W_{DC}$ in 2002 to $\$4.2/W_{DC}$ in 2013.[9] In 2011 dollars, average global module prices decreased from $\$4.90/W_p$ in 1998 to $\$1.28/W_p$ in 2011,[10] however spot prices as low as $\$0.64/W_p$[11] can be found and installations yielding electricity at 15.2 ¢/kWh[12] exist for some commercial systems. Annual installations have increased by an average of 73% since 2005 with 38 GWp of capacity being installed worldwide in 2013 alone.[13] Current estimates place total installed capacity at 139 GWp.[13] Assuming a global average insolation (including cloud cover, nights, and seasons) of 168 W/m^2 (86,000 TW divided by 0.948 to convert solar exergy into energy and then divided by the $5.1x10^{14}$ m^2 surface area of the Earth), one can estimate that there are about 23.1 GW of electricity generating capacity globally from PV. This is equivalent to about 23 large nuclear or coal-fired power plants. In practice, the number will be higher by an amount accounting for the fact that PV installations are common in areas of higher insolation (Los Angeles averages 233 W/m^2 while Seattle averages 154 W/m^2) and lower by a factor accounting for less than ideal installations (shadowing by trees and non-optimized tilt angle and direction).

Thus far, crystalline silicon solar cells have dominated the market, accounting for 86% of module shipments in 2011,[14] but thin-film technologies that take advantage of lower materials and processing costs are increasing dramatically. Between 2009 and 2010, shipments of thin film modules grew by 72%.[15] One of the biggest growth areas for thin film is in building integrated PV (BIPV), which is expected to grow from $2 billion (USD) in 2011 to over $11 billion in 2016, driven by new products such as Dow Chemical's POWERHOUSE Solar Shingle.[16, 17]

2.1.2 *Thin Film Photovoltaics from Earth-Abundant Elements*

CdTe and Cu(In,Ga)Se_2 (CIGSe) are currently the leading thin film technologies with cell efficiencies of 19.0%[18] and 20.3%[19], respectively. However, due to concerns over the price, availability, and price volatility of In and Te there has been increasing interest in the development of alternative materials. A 2009 study by Wadia et al.[20] brought widespread attention to earth abundant materials for PV. By looking at the crustal abundance, annual production, and bandgap, they identified materials such as FeS_2, Cu_2S, amorphous silicon (a-Si) and Cu_2ZnSnS_4 (CZTS) as top candidates for low-cost PV. However, single junction a-Si efficiencies have remained stagnant for some time. They seem to have effectively reached their limit due to Stabler-Wronski instability[21, 22] and may not be able to compete with other more efficient technologies. Cu_2S has promise, but suffers from serious stability limitations when paired with known n-type materials to form a heterojunctions.[23, 24] FeS_2, the top material based on abundance, material extraction cost, and bandgap appears to be to have serious fundamental challenges due the formation of native defects that have mid-gap energy states that facilitate electron-hole recombination[25-27] and thus significantly limit its practical PV efficiency. In contrast to these other materials, CZTS, the selenide $Cu_2ZnSnSe_4$ (CZTSe), and the sulfoselendide $Cu_2ZnSn(S,Se)_4$ (CZTSSe), collectively referred to as kesterites (due to their structure), form stable junctions and have remarkably serendipitous defect chemistry due to the formation of neutral defect complexes which are relatively benign.[24] Kesterites may thus be the most promising candidates for efficient Earth abundant element PV**.** In addition, due to the larger band gap, the theoretical voltage from a CZTS solar cell is 41% higher than the theoretical voltage from a c-Si solar cell which will result in lower balance-of-systems costs.

The bandgaps of both CZTS and CZTSe are nearly ideal for solar energy conversion. Detailed balance calculations show that the theoretical maximum efficiencies are 32.4% and 31.0% for CZTS and CZTSe, respectively (Figure 2.1).[28] These calculations are similar to that of Shockley and Queisser,[29] but here we use the ASTM G-173 standard AM1.5 gobal solar spectrum instead of the blackbody approximation and assume that there is no radiative emission from the back surface (due to the presence of a perfectly reflective back contact). In practice, the bandgap may be tuned between these two values by varying the S/(S+Se) ratio to form $Cu_2ZnSn(S,Se)_4$ or perhaps by cation substitution.[30] Experimental progress is advancing rapidly and devices have recently achieved efficiencies of 12.6%.[1] Given the favorable defect chemistry and junction stability of $Cu_2ZnSn(S,Se)_4$ devices, the PV community should be bullish about device efficiencies exceeding 20% power conversion efficiency with these materials.

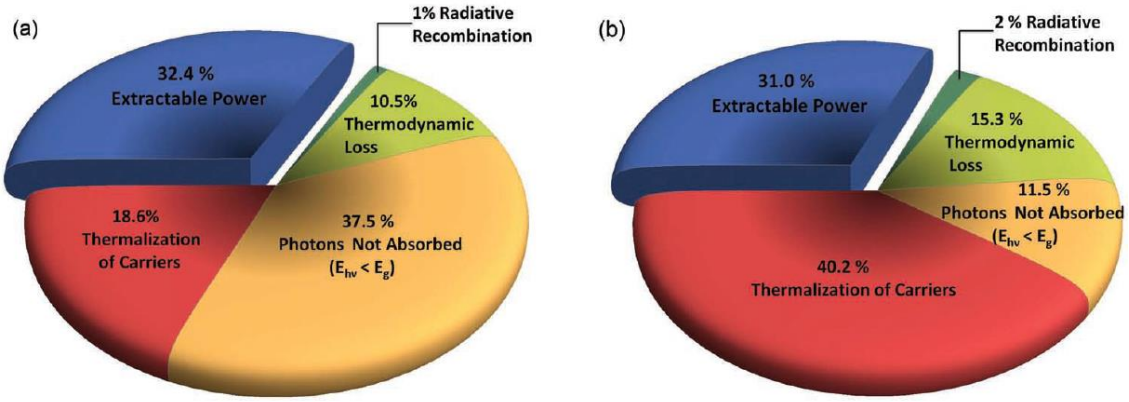

Figure 2.1 Where the energy goes. The pie charts show the results of detailed balance calculations for CZTS (a) and CZTSe (b). The blue shaded region shows the upper limits of efficiency for single junction cells that utilize these materials Reproduced from Ki and Hillhouse.[28]

2.1.3 *Elemental Abundance, Production Rates, Environmental Concerns*

The most commonly cited criticisms for the future potential of large-scale manufacturing of current thin film technologies such as CdTe and CIGSe are related to the elemental abundance and potential for price volatility of Te and In, and the toxicity and environmental concerns of Cd. As a result, there have been a number of analyses[20, 31-35] and even an analysis of those analyses.[36] The publications use a range of different assumptions and methodologies, but generally all agree that elemental abundance is more of an issue for CdTe than CIGSe. However, the three most recent reviews have all concluded that price, not abundance, is what will likely limit PV module production with these technologies.[20, 34, 36] While it is impossible to predict what the market will look like in the future, demand for indium (in the form of tin-doped indium oxide, ITO) in flat panel displays and touchscreens could raise indium prices to a point where the profit margins on solar cells like CIGSe could be significantly affected. This also should steer research efforts to avoiding indium in the transparent conducting layer of the solar cell (current CIGSe devices use aluminum doped zinc oxide, AZO, as opposed to ITO).

A key advantage of kesterite based solar cells is that they rely primarily on high production rate industrial metals that are mined for directly. As a result, the raw materials costs are lower, and concerns over future price volatility and availability are practically non-existent. In order to compare CZTS to current thin film technologies, we show the results of a simple analysis. With the exception of Te annual production rates, all mineral data comes from the United States Geological Survey (USGS) 2011 Mineral Commodity Summaries.[37-39] We used 2010 mineral production rates and a 5-year average (2007-2011) mineral price for all calculations. Because the USGS does not disclose US Te production,

annual production numbers for Te are taken from Ojebuoboh[40] and is therefore older (2008) than data from the USGS. As noted by Candelise *et al.*, a potential flaw of many prior sustainability assessments is that they all use data from the USGS mineral commodity summaries. This is primarily an issue when making projections based on reserves numbers, and therefore should not significantly impact our calculations. We calculated the raw material cost of different thin film technologies by material layer in the devices and by element, assuming a 50% materials utilization rate and assuming the layer thicknesses and device efficiencies listed in Table S1. The "raw" materials costs are calculated using a 5 year average (2007-2011). They do not include any additional processing costs such as refining to produce very high purity or the cost of making a sputtering target, but are used as representative figures since the actual material cost is highly dependent on deposition technology, precursors required, purity, and material utilization. The results shows that: (1) crustal abundance is not an issue for any of the elements in CZTS or CZTSe devices (Cu, Zn, Sn, S, Se, Mo, Cd) up to cumulative installed PV capacity of 1.4 TWp,(Se-limited for CZTSe) (2) production rates of the main absorber elements Cu, Zn, Sn, and S will not be a limiting factor for large-scale manufacturing up to annual PV production rates of 7.3 TWp/yr, (Sn-limited CZTS); and (3) Mo or Se could ultimately limit annual production of CZTS and CZTSe if the standard device architecture (AZO/i-ZnO/CdS/kesterite/Mo/glass) is used. For CZTSe solar cells, Se is the limiting element. Assuming 50% of annual Se production can be devoted to manufacturing of CZTSe solar cells with 50% materials utilization and no recycling, annual production of CZTSe is constrained to 23.9 GWp/year. If Se is avoided (i.e. pure sulfide CZTS is employed) then the next most constrained element is Mo in the back contact. Assuming 5% of annual Mo production is devoted to manufacturing CZTS and a 50% materials utilization rate, annual production of CZTS would only be constrained to 159 GWp/year. While, Mo and Se production might pose a small concern, the other metals used in a CZTS/CZTSe solar cells are massively more abundant. Using our assumptions, producing 1 TWp of CZTS in one year would require only a small fraction of the annual production rate (and known economic reserves) for each element, 0.187 wt% (0.00483 wt%) for Cu, 0.130 wt% (0.00626 wt%) for Zn, 10.88 wt% (0.546 wt%) for Sn, and 0.0451 wt% (5.11×10^{-6} wt%) for S. It should be noted that based on our analysis, the Mo back contact is by far the single most expensive layer in a CZTS device, accounting for over 80% of raw materials costs. In actual production, this could be even worse if materials yields during Mo sputtering are as low as noted in one report (12%).[41] For Se, the limiting factor is the relatively low recovery rate. Se is primarily collected from the anode sludge of electrolytic copper refining operations, so reserve estimates are based on identified copper deposits.[42, 43] Due to weak demand, as little as 12% of Se was recovered from Cu ores in the past.[40] In recent years, growing demand has increased recovery to as much as 50-60%, demonstrating that higher recovery rates

are possible if there is demand.[34, 37] Coal generally contains 80-90 times as much Se as average Cu deposits, and extraction is technically feasible. However, recovery of Se from coal is not anticipated in the foreseeable future and is therefore not included in reserves estimates.[42] A more detailed analysis of Se availability and recovery can be found elsewhere.[40]

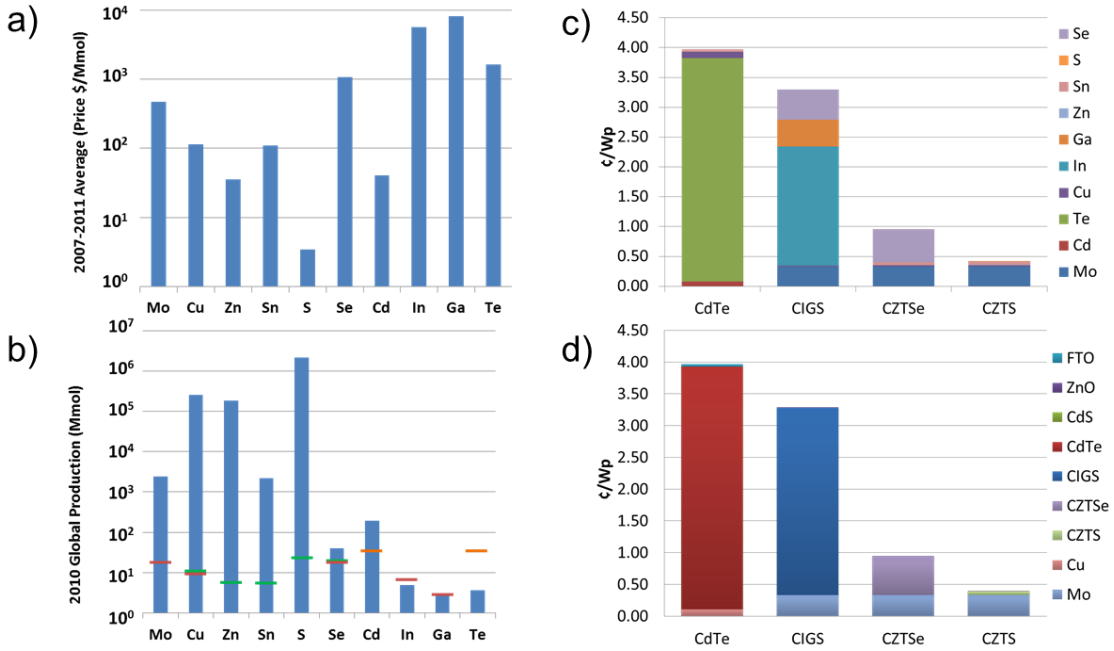

Figure 2.2 Element Cost & Production. (a) 2007-2011 average price per Mmol of each element. (b) Global production data in kmols from USGS. Note the logarithmic scales for both figures. Lines indicate minimum materials requirements for absorber layers at 50GWp annual production. Raw materials costs of different thin film technologies by absorber layer element (c) and thin film layer (d). Calculations based on 2007-2011 metals price data from USGS.

2.1.4 *Environmental Impact*

As previously mentioned, one of the commonly cited concerns with existing thin film technologies is the use of toxic elements. However, the use of an element that may be toxic in some forms or compounds does not necessarily represent a threat to public health and safety. It does mean that care needs to be taken to make sure that the form that it is used in does not degrade into more toxic forms in landfills, fires, or other expected events. In addition, special attention needs to be given to assess its full life cycle and potential effects on the environment and ecosystems. Even if these concerns are addressed, it can still present an obstacle for public acceptance. In this section we will briefly discuss the toxicity and environmental issues of metals used in kesterite solar cells.

With the exception of tin, all of the major metals used in a CZTS based solar cell are considered essential trace elements for plants and animals. Copper is normally bound to ceruloplasmin in blood, but when ingested in excess it can exist unbound. This free copper generates reactive oxygen species that damage proteins, lipids, and DNA causing copper toxicity.[44] Copper has been shown to have anti-microbial properties and is toxic to fish and other aquatic organisms. The toxicity of copper to freshwater aquatic organisms is dependent on a variety of ambient water chemistry parameters. For example, increases in hardness, pH, alkalinity, and natural organic matter result in increased lethality of copper to fish and other aquatic organisms.[45] Copper enrichment in soil can interrupt natural processes of earthworms and microorganisms, slowly or completely halting decomposition. The land surrounding current and former copper mines is often barren for this reason.[46, 47] Zinc is also an essential trace element that can be toxic if ingested in excess. Zinc interferes with iron and copper uptake, and thus excess zinc intake relative to copper or iron can lead to deficiencies. In high concentrations, zinc is toxic to plants, invertebrates, and vertebrate fish[48] as well as aquatic plants[49] and animals.[50, 51]

Tin has no known biological role in living organisms, and cases of tin poisoning resulting from tin metal and its oxides are "almost unknown."[52] For this reason tin has been used for cookware, utensils, and food preservation (tin cans). However, organotin compounds are industrially important chemicals that are extremely toxic. Compounds such as tributyltin (TBT) have been used as antifouling biocides for ship hulls since 1960. These chemicals are potent neurotoxins and act as endocrine disruptors, causing imposex (development of male features in females) in snails and bivalves.[53, 54] After the collapse of commercial shellfisheries in at least one area, these compounds were banned by the International Maritime Organization.[53, 55] Following the ban, cuprous oxide paints became the dominant class of antifouling paint. These have led to copper levels in marine environments that are toxic to some species.[54, 56]

Elemental sulfur and the majority of sulfate salts are not toxic; however, when burned in air sulfur produces sulfur dioxide, a major air pollutant that is toxic and leads to acid rain. Selenium has captured headlines in the US following reports of two-headed trout hatched from fish caught near an Idaho phosphate mine.[57] Though selenium is an essential trace element, excess intake can lead to selenosis. Symptoms in humans include hair loss and sloughing of finger nails, but it is most dangerous to aquatic egg-bearing animals such as birds, fish, and reptiles, where it can lead to serious deformities.[58] Environmentally, selenium can accumulate in plants if soil concentrations are high. This can occur

naturally in some areas, or through contamination of soils with selenium-rich fertilizers or other soil amendments.[59]

While no element or chemical is completely safe and benign in all forms and quantities, using relatively benign materials and developing appropriate methods to handle and dispose of wastes will become increasingly important as solar installations continue to grow. End of life considerations will also become increasingly important and has been the focus of at least one recent paper.[60] Previous work has shown that recycling of some PV components such as glass substrates from CIGSe devices[61] is possible but the biggest question is whether it could be economical. Further, when considering the potential for terawatt scale implementation, it is important to consider possible unintended consequences (ex. corn-based ethanol has caused unintended increases in food costs[62, 63]) through a rigorous consequential life-cycle analysis,[64, 65] doing this can ensure that "green" technologies really are green.

2.2 Absorber Layer Formation

Many approaches have been developed to fabricate Cu_2ZnSnS_4, $Cu_2ZnSnSe_4$, and $Cu_2ZnSn(S,Se)_4$ absorber layers. The majority of these techniques have been summarized by both Mitzi et al.[66] and Ramasamy et al.[67] and the reader is referred to those reviews for a comprehensive list. Physical vapor deposition techniques, such as thermal evaporation and sputtering, are by far the most well established means to deposit thin films. These techniques allow for good deposition control, repeatability, and are amenable to high purity processing. There are numerous reports of groups using PVD to deposit kesterites and fabricate devices.[68-84] However, the problem with PVD techniques is that they are slow and capital intensive for large-scale manufacturing. Solution-based processes are much more appealing because they can enable high-throughput roll-to-roll type processing which can be used to dramatically increase manufacturing output and reduce cost.

2.2.1 *Solution-Based Absorber Layer Formation*

Solution-based processes can be divided into two categories: true solutions and suspensions. True solutions are distinguished from suspensions (in particular nanocrystal inks, discussed below) in that the initial solution/mixture contains dissolved Cu, Zn, Sn, S/Se elemental or molecular compounds not pre-formed semiconductor particles. Depending on the precursors in the solution, there are two distinct

formulations: those that include chalcogens[28, 66, 85-87] and those that do not.[88-92] In both cases, thin films are formed by spin coating, spray coating, or knife coating multiple layers of the solutions. For precursors that contain chalcogens, kesterite phases may be formed upon annealing, with or without sulfur or selenium supply; for precursors that do not including chalcogens, the annealing is carried out in a sulfur or selenium environment in order to form the CZTS or CZTSe phase. An example of a true solution technique is the hydrazine-based process, which has been used to deposit the world record 12.6% efficient device. In this process, a coating solution is prepared by dissolving Cu_2S, S, SnSe, Se and a soluble Zn salt in hydrazine. Hydrazine has many advantages as a solvent. It contains no oxygen or carbon, and its strong reducing action has the ability to stabilize the formation of metal chalcogenide anions. It does not strongly coordinate and is volatile, which facilitates easy removal. In addition, it decomposes to N_2, NH_3, and H_2. All of these features contribute to its suitability as a solvent for depositing high purity semiconductors. However, safety and environmental concerns are a major drawback of this chemistry, as hydrazine is explosive, hepatotoxic,[93] and carcinogenic.[94, 95] Efforts have been pursued to decrease the toxicity by using a 50:50 mixture of water and hydrazine along with a proprietary additive, but it has not achieved the same conversion efficiencies.[96] A route that excludes hydrazine and any other toxic solvents is desirable. One such process is the "molecular precursor" process, in which metal salts such as $CuCl_2$, $ZnCl_2$, and $SnCl_2$ are dissolved in the non-toxic solvent DMSO by complexing with thiourea. Thiourea helps improve the solubility and stability of the metal cations, and also acts as the sulfur source. Using this process, devices with 11.8% efficiency have been demonstrated.[97]

2.2.2 *Solution-based Nanocrystal Inks*

The first solution-phase process to produce high efficiency kesterite solar cells was based on nanocrystal inks. A sulfoselenide thin film is made by knife-coating sulfide nanocrystals, then sintering them in a selenium environment to produce a polycrystalline absorber layer. This approach is different from true solution-based techniques in that the elements are in the correct (or close to the correct) stoichiometry, and the crystalline structure of the nanocrystals (NCs) is the same as the desired bulk phase. This reduces the need for solid-state diffusion of the metals and allows for the formation of a bulk film without passing through binary phases that may be kinetically stable or volatile. The use of NCs for solar cells was originally developed for CIGSe, and then quickly expanded to CZTSSe due to concerns over materials availability (as discussed in Section 2). The synthesis of CZTS nanocrystals was first reported in 2009 in three roughly concurrent reports by Guo[98], Riha[99], and Steinhagen[100], of which Guo presented a sintered CZTSSe device and Steinhagen presented an un-sintered CZTS NC device. Since

then, there have been many reports on the synthesis of CZTS NCs for solar cells.[30, 101-110] Selenide NCs have also been synthesized,[111, 112] but no reports exist regarding photovoltaic devices from those NCs. It is unclear at this time if sulfide NCs are superior or less effort has been directed towards making devices from selenide NCs. Synthesis techniques for CZTS NCs have included hot injection,[100, 102, 107] solvothermal,[104] microwave-assisted,[106, 113] and two-phase reaction[102] (inorganic salts dissolved in polymer solvent, and S and ligands in organic solvent). Typically, NCs are synthesized and sterically stabilized using long chain organic molecules. These molecules typically leave residual carbon in the film, but recent work has shown that after synthesis they can be removed and replaced with molecular metal chalcogenides (MCCs) such as $In_2Se_4^{2-}$ or $Sn_2S_6^{4-}$. MCCs electrostatically stabilize the NCs using native elements, rather than impurities. No devices have been reported using these ligands yet, but the results will likely be interesting.

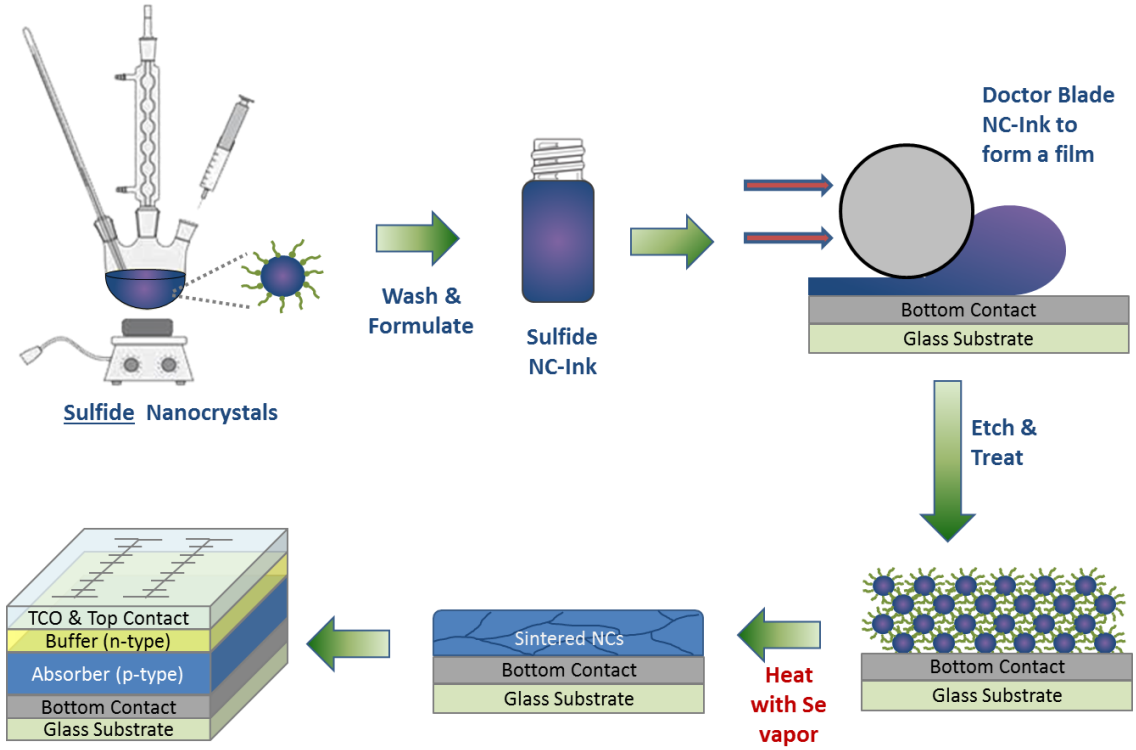

Figure 2.3 Schematic overview of nanocrystal ink-based solar cell fabrication process in which a nanocrystal-ink is spread and sintered to form a high photovoltaic quality absorber layer. This method can be applied to any nanocrystal-inks, but the best results have been achieved when sulfide nanocrystals are heated in a selenium atmosphere and converted to selenides during the sintering process.

Thus far, the most efficient devices have come from selenization of CZTS and CIGS NCs synthesized via the hot injection method. The overall device fabrication process is shown schematically in Figure

2.3 and with photographs in Figure 2.4. This process has been used to produce CIGSe, CZTSSe, and $Cu_2ZnSn_xGe_{1-x}S_y$ (CZTGS) solar cells with efficiencies of 12%[114], 9.0%[115], and 8.4%[108] respectively. A similar process has been used by Guo et al to produce a 8.5% CZTSSe device starting from a mixture of binary and ternary NCs.[116] The process involves: (1) the synthesis of sulfide nanocrystals in oleylamine via the hot injection method; (2) redispersion of the NCs in an organic solvent (to form an "ink"); (3) film formation via doctor blading; and (4) thermal annealing in a Se atmosphere to burn out organic ligands and convert the sulfide NCs to a polycrystalline selenide absorber layer. One of the limitations of the process is the use of the hot injection technique (though gradual heating has also been used), which is a batch process. However, Shavel et al have produced CZTS NCs in large quantities using a continuous flow reactor, demonstrating that NC based technologies are scaleable.[117] The use of NC inks for solar cell application has been around for less than a decade, yet rapid increases in understanding of formation mechanisms, device efficiencies, synthesis techniques, and avenues for scalability place this technology among the most exciting potentials for achieving large scale and economic PV utilization.

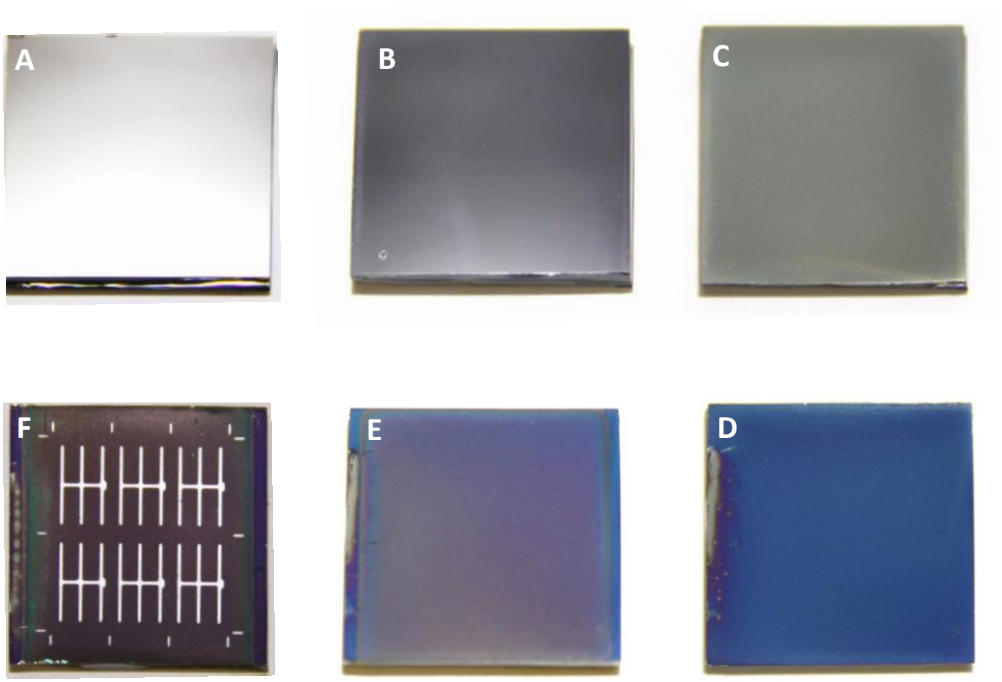

Figure 2.4 Photographs of CZTSSe photovoltaic devices at each stage of processing. From upper left to lower left: (a) Mo-coated SLG, (b) after doctor blading NCs, (c) after annealing in selenium, (d) after of chemical bath deposition of CdS, (e) after sputtering i-ZnO/Al:ZnO, and (f) after evaporation of Ni/Al contacts and scribing.

2.3 STRUCTURE AND PHYSICAL PROPERTIES

CZTS and CZTSe are tetrahedrally coordinated semiconductors that are structurally related to the cubic zinc blende structure that is common in III-V and II-VI compounds like GaAs and CdTe. Starting from the II-VI structure, the group II cation sites are replaced by an ordered sequence of group I and group III cations to yield the chalcopyrite structure (I-III-VI_2). From this structure, the group III sites are replaced by an ordered sequence of group II and group IV cations to yield the kesterite structure (I_2-II-IV-VI_4). The ordering of the cations forces the I_2-II-IV-VI_4 structures to be described by a tetragonal unit cell (nominally 1x1x2 times the lattice constants of the cubic zinc blende cell). Depending on the material a tetragonal distortion ($c/2a \neq 1$) may be present. Reports of the lattice constants of CZTS, CZTSe, and CZTSSe indicate that the tetragonal distortion is very small, but simulation and experiments have produced distortions that are greater than and less than 1. The largest values of c/2a are from crystals that were grown with an ICl_3 transport agent.[118] Currently, it is unclear whether experimental/computational error, purity, or disorder of the cation sublattice is responsible for the variation.

There are three possible structures for CZTS and CZTSe that result from distinct orderings of the cations: kesterite (space group $I\bar{4}$), stannite ($I\bar{4}2m$), and PMCA ($P\bar{4}2m$). The kesterite structure is the most stable phase as determined by *ab initio* calculations.[119-121] Recent x-ray[122] and neutron[123] diffraction experiments confirm kesterite as the structure for both CZTS and CZTSe, though significant Cu-Zn disorder has been noted. The energy difference between the kesterite and stannite structures is small (particularly for the selenide), much less than kT at room temperature, and a significant amount of cation site disorder likely exists in most materials.[120] All experiments and data suggest that there is no ordering of the anion sublattice in the sulfoselenide and that $Cu_2ZnSn(S_x,Se_{1-x})_4$ is a true solid solution. CZTS melts at 991 °C[124] and CZTSe melts at 805 °C.[125] The calculated enthalpies of formation of kesterite CZTS and CZTSe are -312.7 kJ/mol -361.9 kJ/mol, respectively, both of which are more negative than for the stannite and wurtz-stannite phases.[126] Experimental phase diagrams of the Cu_2S-ZnS-SnS_2[127] and Cu_2SnSe_3-ZnSe-$SnSe_2$[128] systems and density functional theory calculations show a small window of stability for CZTS and CZTSe.[129, 130] The stability region is particular narrow along the Zn axis, with ZnS or ZnSe easily precipitating out. Along the Sn axis, Cu_2SnS_3 and Cu_2SnSe_3 are the most stable tin-rich phases near the stability windows. Given the small composition window of cation ratios where pure CZTS and CZTSe exist, identification of binary and ternary impurities and achieving the desired cation ratios is of paramount importance.

2.3.1 *Identification of Binaries and Ternaries*

Powder X-ray diffraction (PXRD) is the standard primary technique used to identify phases. PXRD is widely used for confirming the presence of the kesterite phase, and it may be used to identify binaries such as CuS, Cu_2S, SnS, SnS_2, and ternaries such $Cu_2Sn_3S_7$, Cu_3SnS_4, and the associated selenides[131, 132] However, PXRD alone cannot exclude the presence of the stannite and PMCA structures and some common binary/ternary phases such as ZnS(e) and $Cu_2SnS(e)_3$ due to direct overlap of all four of the most intense x-ray diffraction peaks for each structure, the (112), (200)/(004), (220)/(024), and (312)/(116) of the kesterite structure.[131, 133]

Raman spectroscopy has been touted as a promising technique that may be used to identify secondary phases such as Cu_2SnS_3, Cu_4SnS_4, ZnS, and the associated selenides.[131-137] Khare *et al.* have calculated the lattice dynamics and Raman modes of CZTS and CZTSe using DFT and compared them to the experimental spectra.[134, 138] They isolated the contributions of each atom to the phonon density of states (DOS) of CZTS, CZTSe, and alloys. The atom-resolved phonon DOS and Raman spectra for pure CZTS and CZTSe are shown in Figure 2.5. Additionally, they have shown that deconvolution of experimental CZTS and CZTSe Raman spectra based on the calculated spectra can quantify the coexistence of the kesterite and stannite phase within polycrystalline thin film samples,[134] at least for pure sulfide and selenide materials. It is unlikely that this would be possible for sulfoselenides because of the peak shift with sulfur content. Due to their large band gap, the binary compounds ZnS or ZnSe can be difficult to detect using Raman spectroscopy. Previous work has shown that detection of ZnS phases is possible with UV (325 nm) but not visible (532 nm) laser excitation.[133] However, because of the strong absorption of the laser light near the top surface, the sampled area may not be representative of the entire film. Sputtering through the film and measuring the Raman at different depths can make a more complete measurement, but this requires destroying the film. A way to precisely identify secondary phases using non-destructive techniques would be preferable, and may eventually be important for inline process control and deposition monitoring. Developing non-destructive means to detect ZnS(e) phases is especially important because Zn binaries are the most prevalent secondary phase under Cu-poor/Zn-rich processing conditions, which thus far have yielded the most efficient devices (see sections 4.2 and 4.6).

While not as convenient or widely accessible as X-ray diffraction or Raman scattering, synchrotron based X-ray absorption techniques are useful for the identification of binaries in the kesterite system. X-ray absorption near edge structure (XANES) can be used to probe the average local structure around a

element. The XANES profile for CZTS cannot be reconstructed through a linear combination of secondary phases, which allows the method to be used to identify secondary phases. By looking at the sulfur K-edge absorption, it is possible to determine the volume fraction of CZTS and ZnS because both materials have the equivalent number of sulfur anions per volume and comparable lattice constants. Reports have claimed that it is possible to determine ZnS impurities to at least 3% by volume,[139] and the technique has already been used to unravel some properties of CZTS devices (see section 6.2).

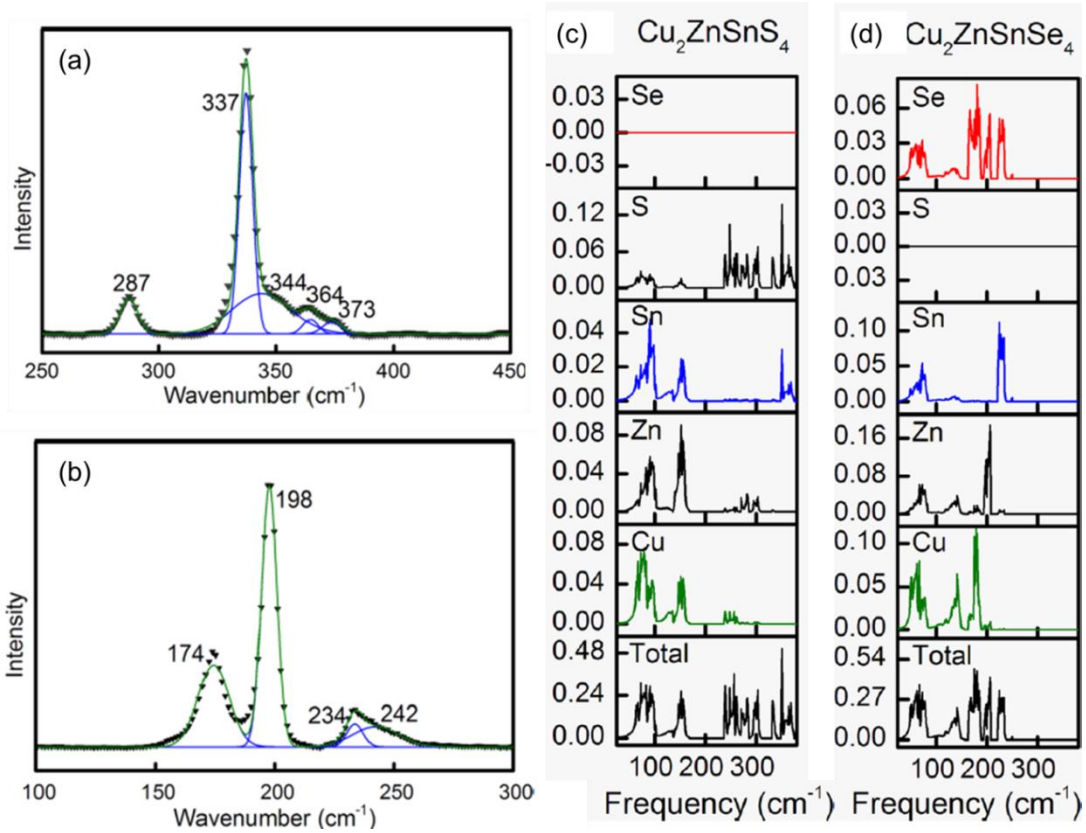

Figure 2.5 Raman spectra of CZTS (a) and CZTSe (b). Experimental data (filled triangles) are shown with peaks calculated assuming purely kesterite material. Atom-resolved phonon densities of states for CZTS (c) and CZTSe (d). Reproduced from Khare et al [134]

2.3.2 *Stoichiometry of the Kesterite Phase*

Small variations in the elemental ratios can have significant impact on the electronic and optoelectronic properties of chalcogenide semiconductors (see Chapter 6). It is now well established that Cu-poor/Zn-rich films produce the most efficient devices. The first study to investigate the effect of stoichiometry on CZTS device performance was by Katagiri et al.[140, 141] They found that the highest efficiencies (5-6% range) were clustered in a narrow band around cation ratios Cu/(Zn+Sn) = 0.8, Zn/Sn = 1.2, and

Cu/Sn=1.9.[140, 141] Since the initial studies by Katagiri et al., several additional studies have investigated the effect of composition on CZTS and expanded the work to include both CZTSe and CZTSSe,[142] including one by this author (see Chapter 6).

In agreement with the early work by Katagiri et al., these studies have found that the best kesterite devices (S or Se) are made under Cu-poor/Zn-rich conditions near Cu/(Zn+Sn) = 0.8 and Zn/Sn = 1.2. Absorbers grown with compositions so far from stoichiometric undoubtedly contain secondary phases due to the narrow range of phase stability for kesterite, but due to the difficulties identifying and quantifying secondary phases (refer to Chapter 2.3.1), it is not practical for most research labs to routinely measure the exact composition of the kesterite phase. Therefore, the reported cation ratios simply reflect the overall average composition of the film, not the composition of the kesterite phase.
Using combinatorial experiments, Collord et al.[142] have shown that the dominant factor influencing the optoelectronic properties of CZTSSe is the Cu-content. From stoichiometric, as the Cu-content is decreased both the band gap and the quasi-Fermi level splitting (QFLS) increase. By normalizing the QFLS to the maximum theoretical QFLS for the band gap ($QFLS^{SQ}$), they were able to show that the improvement in optoelectronic quality with decreasing Cu-content saturates near a bulk composition of Cu/(Zn+Sn) = 0.8 and Zn/Sn = 1.2. Additionally, they showed that despite large changes the other optoelectronic properties, the magnitude of sub-band gap absorptivity does not change significantly. This means that the defects responsible for causing electrostatic potential fluctuations are highly favorable and will be difficult to eliminate.

Band edge fluctuations may occur in kesterite devices as a result of both electrostatic potential fluctuations and band gap fluctuations. As discussed above, Collord et al. have shown that the bandgap of CZTSSe increases with decreasing Cu-content,[142] and a similar effect has been shown for CIGSe.[143] In addition, local variation in the S/Se ratio may also lead to variation in the bandgap. Minimizing spatial variations in elemental ratios is important because the resulting bandgap fluctuations reduce the open-circuit voltage. A variety of complementary methods are available for quantifying elemental ratios in CZTSSe (particularly the cations). The most often cited are electron dispersive X-ray spectrometry (EDS, EDX, or EDAX), secondary ion mass spectrometry (SIMS), and Auger electron spectrometry (AES). Quantification of the anions (the sulfur and selenium) by x-ray emission techniques is complicated by the low atomic number of sulfur as well as the overlap of the sulfur K emission line with the L line of molybdenum.[144, 145] However, the locations of the XRD peaks can be utilized for determining the S/(S+Se) ratio of the material assuming Vegard's rule applies for lattice parameter

shrinkage due to increasing sulfur content.[28, 95, 146, 147] Caution should be exercised when comparing composition measurements from techniques with differing degrees of surface sensitivity, because the surface may have quite different stoichiometry than the bulk.

2.3.3 *Tin Loss and Kesterite Equilibrium with Binary Phases*

Tin vacancies (V_{Sn}), copper on tin site defects (Cu_{Sn}), and defect complexes such as [Cu_{Zn}+Sn_{Zn}] create deep energy levels in both CZTS and CZTSe. The levels are beyond the electron demarcation energy and thus will facilitate non-radiative recombination (see section 5.3 below). As a result, they can be a serious detriment to device performance. A first principles study has found that the V_{Sn} defect has a relatively high formation energy in Cu-poor materials (1.77 eV for CZTS and 2.51 eV for CZTSe),[148, 149] and therefore, it should not readily form.[130] However, early on it was realized that the Sn content of films deposited using vacuum-based processes decreased with increasing substrate temperature. Using in situ XRD and XRF, Weber *et al*. found that the evaporation of SnS under vacuum was responsible for the changes in composition at high temperature.[150] Later, Redinger *et al.* showed that the evaporation of SnS leads to the decomposition of the CZTS absorber layer into ZnS and Cu_xS.[69] However, they showed that by maintaining a sufficiently high partial pressure of the volatile species the decomposition can be prevented. This was be achieved by providing additional SnS and was shown to lead to a dramatic improvement in device performance.

Both Redinger and Weber attributed the decomposition of CZTS to be a direct result of the high vapor pressure of SnS. However, Scragg et al[151] noted that the vapor pressure of sulfur at the same temperature is 6 orders of magnitude larger than SnS. To explain the observed Sn-loss from CZTS films, they experimentally tested two different kinetic models: a single step and a two-step decomposition reaction. They found that a single step, in which SnS is directly lost from CZTS, was insufficient to describe the observed reaction kinetics. However, the process is well described by a decomposition step followed by a reversible SnS desorption step.

$$Cu_2ZnSnS_4(s) \rightleftharpoons Cu_2S(s) + ZnS(s) + SnS(s) + \frac{1}{2}S_2(g)$$

$$SnS(s) \rightleftharpoons SnS(g)$$

Thus, the instability of CZTS at high temperatures is a direct result of Sn multi-valency and the fact that Sn(II) is only slightly less favored than Sn(IV). To ensure stability of CZTS at high temperatures, the authors calculate that the sulfur partial pressure must to be greater than 2.3 x 10^{-4} mbar and that the product of the partial pressures of SnS and S_2 ($p_{SnS}(p_{S2})^{1/2}$) has to be greater than 3.8 x 10^{-5} $mbar^{3/2}$. This

work has since been extended to produce a thermodynamic model for predicting phase stability of multinary semiconductors during thermal annealing. Using an equivalent binary model Scragg et al[152] calculated that material losses in CIGSe should be small, but a similar decomposition reaction should occur in the selenide (CZTSe) as well. Further, because the reduction of $SnSe_2$ by Mo has a large negative free energy, the formation of $MoSe_2$ is expected to be much more favorable in CZTSe than in CIGSe. This could explain the large $MoSe_2$ layers observed in devices.[153] It could also mean that Mo may not be a suitable back contact for CZTS(e). The authors also evaluated the compound $Cu_2ZnGeSe_4$ and predicted it should be significantly more stable than CZTSe. CZGSe has less favorable (more positive) free energy change with reduction from $GeSe_2$ to GeSe, so the extent of decomposition calculated to be only 0.1% of that for CZTSe. Ge-containing compounds are also predicted to form a more stable interface with Mo than CZTSe, though still significantly less stable than CIGSe. Experimental results appear to support the prediction that the Mo/CZTS interface is not stable during annealing. Significant quantities of the decomposition products Cu_2S, ZnS, and SnS were observed on delaminated films and cross sections that were annealed without excess sulfur.[154] This body of work has already proven to be very useful and will undoubtedly be important in further development and optimization of kesterite-based solar cells as discussed in Section 6.

2.4 Electronic and Optical Properties

I_2-II-IV-VI_4 kesterite structure CZTS and CZTSe are direct bandgap compound semiconductors that have a lot in common with I-III-VI_2 chalcopyrite structured CIS and CISe. Much can be learned about the electronic structure and defect chemistry of kesterites by comparison with their chalcopyrite parents. In addition to being structurally derived from the chalcopyrite (they are identical except the Group II and Group IV elements of the kesterite are ordered and reside on the Group III sites of the chalcopyrite), there are significant electronic similarities. All measurements of carrier type have shown CZTS and CZTSe to be p-type semiconductors, most likely doped by partially compensated native point defects (just as in CIS and CISe). Both CZTSSe and CIGSSe have advantages over other compound semiconductors, such as favorable native defect chemistry, but they also exhibit significant challenges like electrostatic potential fluctuations and absorber heterogeneity. Given the similarity of the two semiconductors, researchers often look to the more studied CIGSSe as a starting point for understanding the optoelectronic properties of CZTSSe.

2.4.1 *Electronic Structure*

The common Cu cation endows both the kesterite and chalcopyrite with similar electronic properties. Half of the bonds in each are Cu-chalcogen bonds that have high ionicity due to the weakly bound d-electrons of Cu.[155] This makes both the kesterite and chalcopyrite significantly more ionic than the III-V semiconductors like GaAs and II-VI semiconductors like ZnSe. *Ab initio* calculations show that the valence band maxima in both I-III-VI_2 and I_2-II-IV-VI_4 compounds are dominated by p-d orbital coupling between the group-I cation and the group-VI anion.[119, 121, 149, 156, 157] The group II, III, and IV atoms do not significantly contribute to the density of states near the valence band maximum (VBM). As a result, variation of these elements leads to only minor shifts the VBM, and any bandgap changes are due mainly to movement of the conduction band minimum (CBM). In I_2-II-IV-VI_4 kesterite structures like CZTS, the CBM is dominated by the anti-bonding state of the Group IV cation s- and the group VI anion s-orbitals. The group II cation states do not play a significant role in the density of states near either band extrema[119] (at least for the case of Zn in CZTS). In both chalcopyrite and kesterite compounds, decreases in the bandgap from substituting Se for S are the result of shifts to both the CBM and VBM. In I-III-VI_2 chalcopyrites, the CBM and VBM shift almost equally (VBM: +0.28 eV, CBM: -0.21 eV)[158]. In contrast, in I_2-II-IV-VI_4 kesterites the CBM down-shift is more prominent (VBM: +0.15 eV, CBM: -0.35 eV).[159] Compared to similar compounds, such as II-VI's, the shift in VBM resulting from anion substitution is small because strong Cu-S p-d hybridization pushes the VBM of the sulfide up relative to that of the selenide.

Both calculations and experiments generally agree that the bandgap of the pure sulfide CZTS and the pure selenide CZTSe are about 1.46 eV and 0.94 eV, respectively.[119, 121, 160] Electroreflectance measurements (one of the most accurate methods of bandgap determination) has been applied to single crystals to determine the bandgap as a function of S/(S+Se) in the sulfoselenide, $Cu_2ZnSn(S_x,Se_{1-x})_4$. The measurements[118] were combined with the other recently reported single crystal and thin film bandgap data[146, 161] and fit by least-squares to find the following expression for the bandgap of the entire spectrum of sulfoselenide compounds:[118] $E_g(x) = 1.46x + 0.94(1-x) – 0.08x(1-x)$, where the third term accounts for bowing (with a 0.08 eV bowing parameter). Note that the bowing parameter is small, but still it is an order of magnitude larger than that for $CuIn(S_x,Se_{1-x})_2$ (reported to be 0.005 eV).[162]

Values of the dielectric constant have been measured on CZTSSe using both spectroscopic ellipsometry[163] (from 10^{14} to 10^{15} Hz) and impedance spectroscopy[164] (from 10^2 to 10^6 Hz). However, because the "dielectric constant" is actually a frequency-dependent function the techniques are

complimentary but not comparable. Impedance measurements can be used to approximate the value at low frequency (static dielectric constant), while spectroscopic ellipsometry can be used to approximate the value at high-frequency (optical dielectric constant). *Ab initio* methods predict that the average (transverse and longitudinal) optical dielectric constants of CZTS and CZTSe are about 7.1 and 9.0.[165] These values compare favorably to those of CISe and CGSe at 8.0 and 7.8.[165] They also compare well to values determined experimentally on CZTS and CZTSe thin films at 7.1 and 9.2 (taken from the low energy limit of the dielectric spectra).[163] Similar measurements on CISe, CGSe, and CdTe have yielded values of 8.4 [166], 7.5 [166], and 7.3 [167], respectively.

Impedance measurements on CZTSSe thin films with varied sulfur/selenium content found values of the low-frequency dielectric constant of approximately 7 for the pure sulfide increasing to over 8 with increasing selenium content.[164] These values are significantly lower than the values obtained for CISe and CIGSe, which range from 9.8-13.6.[168] These values are estimated from the high-frequency plateau in the measured capacitance at temperatures where dielectric freeze-out of the acceptor states is observed (about 10^6 Hz). The admittance-derived values for the chalcopyrite materials are much higher than those reported for CZTSe and also much higher than the calculated optical dielectric constants for CISe and CIGSe. The reason for this discrepancy is unclear, though one possible explanation is that there is an unresolved capacitance step at frequencies between 10^8 and 10^{14} Hz in CIGSe. Such a high frequency step could result from dipoles due to defect-clusters.

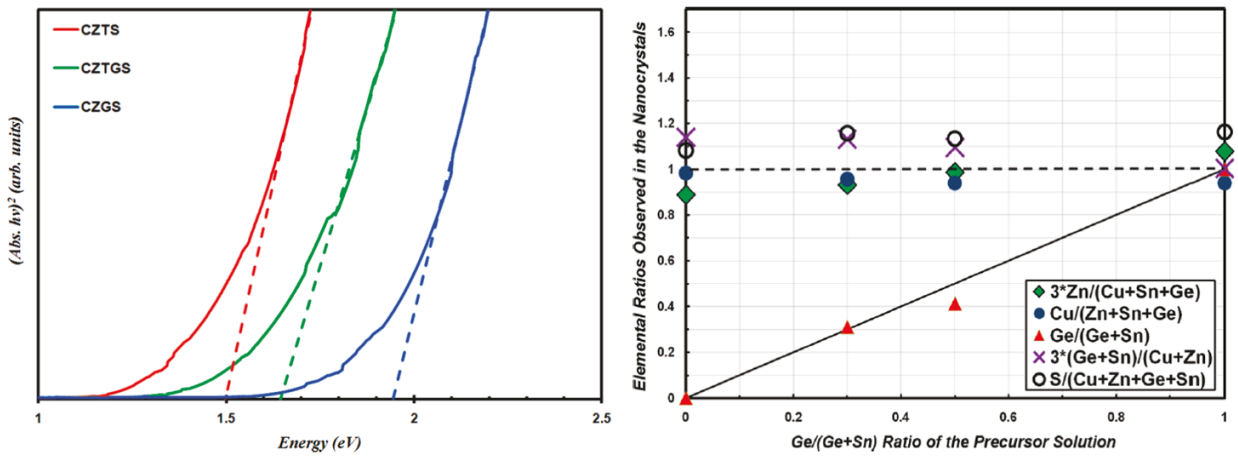

Figure 2.6. Germanium substitution for tin in CZTS nanocrystals. Left: Effect of Ge addition on absorption behavior. Right: Cation ratios in CZTGS nanocrystals as determined by EDS.

2.4.2 *Alloying and Cation Substitution*

Gallium substitution in $CuInSe_2$ (substituting Ga on the In site to form $Cu(In_{1-x},Ga_x)Se_2$ where x is around 0.3) yields better optoelectronic properties (lower concentration of the so called "N_2" defect observed in admittance spectroscopy) than either pure In or Ga variants, $CuInSe_2$ or $CuGaSe_2$.[169] Even within the same absorber layer, gradients of cation ratios may be used to create gradients in the band edges that direct minority carriers away from high recombination interfaces or increase the bandgap at the p-n junction to boost voltage. Both approaches are employed in the highest efficiency CIGSe devices that utilize a double graded Ga profile.[170]

The first attempt to develop a CZTSe-based chemistry with similar tunability of the bandgap via cation substitution was conducted by Ford *et al.*[30] While it is common to be able to adjust bandgap in compound semiconductors, it is more challenging to do so and retain good optoelectronic properties. Germanium alloying was selected based on a hypothesis that it could have similar effects to gallium alloying in CIGSe. Given that valence band maximum in both kesterites and chalcopyrites is dominated by the Cu-3d and chalcogen-4p it is unlikely that the valence band edge would shift substantially and more likely that the conduction band minimum would shift up. This hypothesis is supported by the *ab initio* calculations of Chen et al.[159] and Zhang et al.[171] Experimentally, Ford et al. has shown that by substituting Ge for Sn in CZTS (forming $Cu_2Zn(Sn_{1-y}Ge_y)S_4$) the bandgap may be continuously varied between about 1.45 eV (CZTS) and 1.94 eV (CZGS). Similarly, Collord et al. have shown that in the selenide system, the bandgap can be continuously varied from about 1.0 eV to 1.45 eV. Devices utilizing Ge-alloying have not yet reached efficiencies as high as pure-Sn devices, but have demonstrated very promising open-circuit voltages, and with further study may eventually help push the record efficiency even higher (see Chapter 7). Thus far germanium devices have been reported with efficiencies of 8.4% using nanocrystals;[172] 9.1% using hydrazine-based processing;[173] 10% using co-evaporation;[174] and 11.0% using molecular-inks (Chapter 7). These results demonstrate the viability of CZTGSSe materials and could open the door to using Ge to create conduction band edge gradients without degrading the optoelectronic quality.

Other cation substitutions have also been investigated. A broad range of quaternary I_2-II-IV-VI_4 and I-III-IV-VI_4 compounds have been analyzed theoretically by Chen et al[159, 175, 176] and experimentally by Matsushita et al[125, 177]. In addition, others have investigated partial substitution of Sn by Si[178], Ge [171, 173, 178-180], Pb[181], and Ti[182] as well as the substitution of Zn by Cd[136, 171] or Fe.[183, 184] Collord et al. have experimentally tested the incorporation of over 25 different extrinsic species (Chapter 8) as either

dopants or for alloying, including Si, Ge, Ni, Co, Fe, Cd, Ti, Hf, and Zr among others. Their results show that at relatively low concentrations the transition metals Co, Fe, and Ni are all highly detrimental to the optoelectronic quality of CZTSSe. This is likely because Fe, Co, and Ni have similar atomic radii and the proper oxidation state such that they may readily incorporate into the CZTSSe lattice on either Cu or Zn sites. Incorporating Ti, Zr, or Hf in the molecular ink had very little effect on the optoelectronic quality. This is likely because, as predicted by the theoretical work of Chen et al, the species do not form a stable quaternary compound. Further discussion is included in Chapter 8.

2.4.3 *Native Point Defects*

Thermodynamic modeling has indicated that V_{Cu} is the most readily formed native point defect in Cu-poor CIGSe. It is a very shallow acceptor (0.03 eV above the VBM) and is responsible for the p-type character of these films. In addition, the In_{Cu} antisite defect forms readily (which is a deep level electron tap), but the compensation of these two oppositely charged defects results in the formation of a neutral defect complex,[185] $[In_{Cu}^{+2} + 2V_{Cu}^{-1}]^0$, that is electrically benign. The free carrier density in good materials is on the order of 10^{16} cm^{-3} and is typically measured by various capacitance-voltage methods. Conventional capacitance-voltage profiling (and Mott-Schottky analyses) may yield an erroneous spatial distribution and an over estimation of the concentration of free carriers. However, drive-level capacitance profiling (DLCP) yields much more reliable data, free from the effects of interface defects.[186] Deeper level bulk defects and the energetic distributions of defects are typically studied by either admittance spectroscopy (AS), in which the capacitance as a function of frequency at varying temperatures is analyzed) or temperature-dependent DLCP, in which the capacitance is measured at various values of constant total bias (DC + AC) at different temperatures. The most commonly seen defect levels in CIGSe films are located at about 0.15 and 0.3 eV and have been dubbed the N1 and N2 defect, respectively.[187] The position of the N2 defect increases with the S/(S+Se) content in the film.[188] The density of N2 defects has been anti-correlated with device performance and is generally not observed using AS on devices over ~15% efficient.[189, 190] It has been suggested that chalcopyrites may suffer from the formation of intrinsic DX-like centers deep within the gap that eliminate free electrons.[191] These centers arise from a Ga_i and V_{Cu} Frenkel-like defect pair.

In the kesterite structure, first principles calculations predict that unlike chalcopyrite CIGSe where the dominant acceptor is V_{Cu}, the defect with the lowest formation energy in CZTS and CZTSe is the Cu_{Zn} antisite defect. The Cu_{Zn} defect is a deeper acceptor than V_{Cu} with values of 120 meV CZTS and 90

meV for CZTSe. Due to a negative formation energy, it is expected to form in large quantities.[130, 192] The depth of the Cu_{Zn} acceptor level must be kept in mind when performing temperature dependent measurements such as IVT or admittance, as carrier freeze will lead to increasing series resistance. For admittance measurements, Weiss et al have shown that the increased series resistance will lead to a capacitance step in the C-f profile which must be properly accounted for.[193] The shallow acceptor V_{Cu} is also present in CZTS and CZTSe and is believed to play an important role in defect compensation. Other native point defects such as V_{Sn}, Cu_{Sn}, Sn_{Cu}, and V_S or V_{Se} yield deep level states that will negatively impact the device performance, but are calculated to have higher formation energies.

As in CISe, defect complexes may also form in CZTS and CZTSe. Chen et al.[194] used first principles calculations to determine the formation energy and concentration of both individual defects and defect complexes at different points within the stable chemical potential region. The most favorable defect complexes include the fully compensated [V_{Cu}^{-} + Zn_{Cu}^{+}], [$2Zn_{Cu}^{+}$ + Zn_{Sn}^{-2}], [$2Cu_{Zn}^{-}$ + Sn_{Zn}^{+2}], and the partially compensated [Cu_{Zn}^{-} + Sn_{Zn}^{+2}]. The former two species have band edge positions close the those of CZTS/CZTSe, and therefore will not act as strong recombination sites. The latter two are expected to be produce strong recombination sites and electron trapping. In both the sulfide and the selenide, the partially compensated [Cu_{Zn}^{-} + Sn_{Zn}^{+2}] complex is calculated to produce a state about 0.8 eV above the VBM, while the fully compensated [$2Cu_{Zn}^{-}$ + Sn_{Zn}^{+2}] complex significantly narrows the bandgap. Both defects are present at higher concentrations in the selenide than the sulfide, but because the levels are shallower they are expected to be less detrimental. Experimental work appears to be mostly consistent with these calculations. Thus far the most efficient devices are those made Cu-poor, Zn-rich, chalcogen-rich. Such processing conditions favor the formation of V_{Cu} over Cu_{Zn} and the relatively benign charge-compensated defect clusters [V_{Cu}^{-} + Zn_{Cu}^{+}] and [$2Zn_{Cu}^{+}$ + Zn_{Sn}^{-2}], while suppressing the formation of detrimental defects such as Sn_{Zn}, Sn_{Cu}, Cu_{Sn}, V_S or V_{Se}, the partially compensated defect cluster [Cu_{Zn}^{-} + Sn_{Zn}^{+2}], and the fully charge compensated defect cluster [$2Cu_{Zn}^{-}$ + Sn_{Zn}^{+2}].[194-196]

Measurements on relatively efficient CZTS and CZTSe devices have found carrier concentrations around 10^{16} cm^{-3} and a dominant defect level near 120 meV, which can nominally be attributed to the Cu_{Zn} antisite defect,[164, 197-200] though several other defect levels have also been reported. Three reports have found a lower energy defect level: in CZTS near 40 meV[198, 201] and in CZTSSe at 70 meV,[197] which are higher than the expected V_{Cu} defect level (20 meV). Kask et al. also reported a defect at 167 meV in CZTS "monograins" but attributed it to an interface state because it varied between devices and its activation energy was dependent on the applied bias.[199] Gunawan et al. looked at the defect energy

level as a function of S:Se ratio and found a dominant acceptor level that increased with bandgap from 130 to 200 meV.[164] A similar study by Duan et al,[200] also using hydrazine processed absorber layers, found defect levels which increased with the S/(S+Se) ratio from 134-183 meV as the ratio was ranged from 0.35-1. Using DLCP, they also found that the trap density and carrier concentration increased with sulfur content while efficiency decreased. Additional characterization of devices with varying S:Se ratio has been performed by Miller et al. using transient photocapacitance.[202] They observed Urbach tails with increasing Urbach energy with increasing sulfur content from 13 meV for the pure selenide to 31 meV for the pure sulfide, suggesting that the degree of alloy disorder increases with band gap. In addition to the tail states, they also observed a deep level defect centered about 0.8 eV above the valence band maximum in all devices. This defect may very well result from the complex [Cu_{Zn}^{-} + Sn_{Zn}^{+2}] as predicted by Chen et al. Admittance spectroscopy measurements have also been applied to $Cu_2Zn(Sn_{1-y}Ge_y)(S_xSe_{1-x})$ alloys. Moore et al. reported defect levels that varied from 70 to 53 meV and from 106 to 170 meV as y increased from 0 to 0.5.[197]

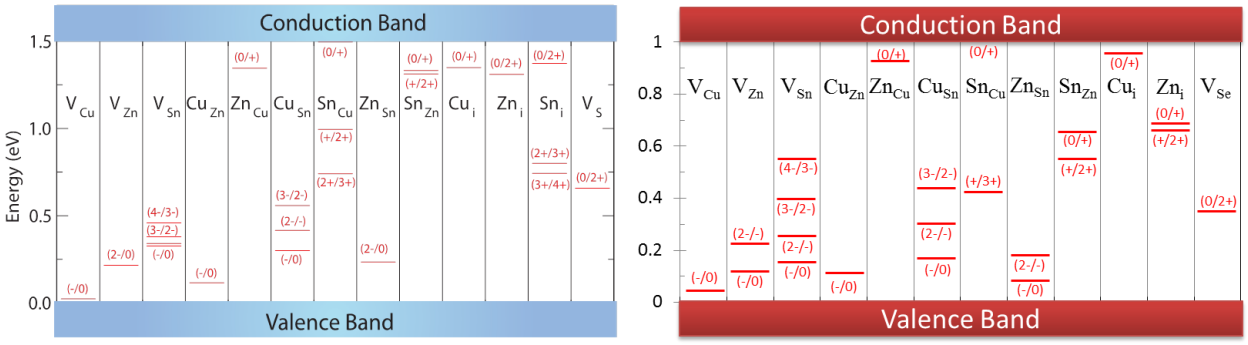

Figure 2.7 Native point defect energy levels from *ab initio* calculations for CZTS (left, reproduced from Walsh et al.[130]) and CZTSe (right, generated from reported data[149]).

Steady-state photoluminescence (PL) is a powerful tool to examine defects. The technique has traditionally been applied when narrow peaks are observed that can be traced to specific transitions such as band-band (BB), band-impurity (BI, also referred to as free-bound, FB, transitions by some authors), and donor-acceptor (DA) transitions as well as those involving excitions.[203] When CIGSe materials are made copper-rich (bad for PV), the low-temperature PL shows narrow peaks.[204-206] However, for copper-poor conditions, the PL is observed as a broad peak for both chalcopyrites as well as kesterites. There have been several studies investigating defect levels in kesterites using PL. Hönes et al. observed narrow DA transitions at 1.475 eV and 1.496 eV, an excitonic transition at 1.509 eV, and a broad peak at 1.33 eV in the 10K PL spectra of Cu-rich and Sn-poor CZTS single crystals.[207] The DA transitions

were associated with a donor state 5 ± 3 meV below the conduction band and an acceptor states 30 ± 5 meV and 10 ± 5 meV above the valence band, respectively. These values are surprisingly low since the lowest energy acceptor expected under the growth conditions is predicted to be a Cu_{Zn} defect at 110meV and the shallowest donor a Sn_{Zn} at 20meV. However, the observation of relatively narrow peaks at high energy is intriguing because other reports looking at stoichiometric single crystals only found the broad transition near 1.3 eV. For example, both Tanaka et al.[208] and Levcenko et al.[209] have examined stoichiometric near CZTS single crystals grown by iodine vapor transport. They both observed a broad peak (~200 meV FWHM at 300 K) centered about 1.29 eV that did not shift significantly with excitation power or temperature. The integrated intensity was found to increase with excitation power and the peak exhibited an asymmetric shift leading Levcenko et al. to attribute the peak to a free-bound (FB) transition with an activation energy of 140 meV. This value is consistent with those determined from capacitance-based measurements and near the expected value for the Cu_{Zn} anti-site defect. Other publications have reported DA pair transitions with energy near 50 meV on S-poor single crystals,[208] stoichiometric thin films,[198] and Cu-poor thin films.[207] These values agree with what is expected for a V_{Cu}. Surprisingly, despite a significant number of studies investigating the PL properties of kesterite crystals, no authors have yet observed deep defects using PL, and no authors have reported the quasi-Fermi level splitting (QFLS) from a single crystal sample. The value of the QFLS could be very enlightening, particularly if it deviated significantly from the values typically observed in device-quality thin films.

2.4.4 *Grain Boundaries*

One of the most important and fascinating properties of good polycrystalline semiconductors for photovoltaics (CIGSe and CdTe) is the relative benign electronic nature of their grain boundaries (the interface between two crystalline domains, or grains, within the film). In the classical picture, grain boundaries (GBs) are regions of discontinuity where charged defects and strained or dangling bonds exist. These features typically create energy levels within the bandgap that can capture photogenerated electrons or holes, impede transport, and facilitate recombination. In Si and GaAs GBs can be catastrophic to electronic properties and must be passivated or eliminated to make efficient devices. However, in CdTe, CIGSe, and CZTSe this is not the case. In fact, polycrystalline chalcopyrite and kesterite devices have outperformed single crystalline cells. Although, the exact nature of the grain boundaries in CIGSe is still a matter of debate, much can be learned about kesterite GBs by drawing on the vast body of literature that exists for chalcopyrites. Two reviews on grain boundaries in CIGSe[210,211] help set the stage for understanding CZTSe and CZTS. In the section below we will first briefly review

the models that have been developed to explain the observed behavior in chalcopyrites and then highlight the few existing studies on kesterites.

Grain Boundaries in Chalcopyrites. It is clear from experiments that GB boundaries are not highly detrimental to CIGSe performance, particularly for low Ga content and if the GBs are predominantly oriented through the thickness of the film. Two conceptual models have been proposed to understand this serendipitous property. One model[212] invokes a neutral grain boundary that is a barrier to holes and has little effect on the minority carrier electrons, while another model[213, 214] invokes a positively charged GB that both reflects holes and collects electrons. We will refer to these as the Neutral Hole Barrier (NHB) and Positive Electron Acceptor (PEA) grain boundary hypotheses. They are illustrated schematically in Figure 2.8 and briefly summarized below.

Neutral Hole Barrier (NHB) Model. Experimentally it has been shown that the majority of CIGSe GBs are (approximately) Σ3 twins.[215] Perfect twins are a special type of boundary that have strong congruence between the lattices of the intersecting grains. As a result the twin boundary has typically has low strain, few dangling bonds, and does not create states in the bandgap. For CISe, the most stable surface has been calculated to be the (112) polar surface.[216] Based on this, Persson and Zunger proposed the presence of a neutral hole barrier at the GBs which are assumed to be Cu-poor.[212, 217] Their argument is as follows: the valence band maximum (VBM) of CISe is comprised of Cu-3d and Se-4p orbitals, and the repulsion between these orbitals pushes the VBM to higher energies inside the grain. However, at a Cu-poor GB, the valence band can locally relax to lower energy. This is proposed to occur since Cu-vacancies have low formation energy both in the bulk and at (112) surfaces.[192, 216, 218] Using *ab initio* calcuations on a polar (112) surface, they showed that the Cu-vacancy reconstruction always depresses the VBM at the GB creating an effective hole barrier. Furthermore, the beneficial nature of Na was explained through the action of Na_{Cu} defects. Na lacks d-orbitals, so the valence band will be dominated by the chalcogen p-orbital and thus fall to a lower absolute level as with V_{Cu}. There have been multiple experimental reports that support the NHB model.[219-224] For example, Hetzer *et al.* performed a study on CIGSe samples grown at NREL and cleaved in ultrahigh vacuum. From AES they determined that the copper content at the GB was decreased relative to the grain interior by as much as a factor of 2. The work function, extracted from SET measurements, shows that the valence band at the GB is decreased by several hundred meV relative to the grain interior. CL measurements performed on adjoining grains and their common boundary showed very little difference, indicating that radiative recombination sites were not present despite the high concentration of defects. In addition, Hafemeister et al. grew bicrystals

of $CuGaSe_2$ with a single neutral Σ3 grain boundary or a charged Σ9 grain boundary. They modeled charge transport in both types of GBs and found that a small, narrow, neutral hole barrier was necessary to explain experimental data for both the Σ3 and Σ9 samples.[224] However, it must be noted that these bicrystals were grown under Cu-excess. Crystals grown under Cu-poor conditions could vary significantly since the barrier is associated with Cu-vacancies.

Postive Electron Acceptor (PEA) Model. On the basis of Kelvin Probe Force Microscopy (KPFM), Yan and colleagues proposed that the GBs in CISe and CIGSe have positively charged grain boundaries, and thus there is a built-in potential that acts to attract minority carrier electrons and repel holes.[213, 214] A key feature of this model is that it suggests that vertically oriented GB boundaries may serve as a conduit for electrons to the n-type material. This model has been examined experimentally and theoretically. Yan et al.[213] have pointed out that the structure of the (112) polar surface is different from the structure of the (112) polar GB. The *surface* terminates with either a cation or anion layer that is charge imbalanced and therefore energetically unstable which is why the *surface* forms Cu-vacancy rows. Yan points out that the atoms at the GB do not simply terminate. The cations are still bonded to Se atoms on the other side of the boundary and therefore do not experience the same driving force for reconstruction. Using high resolution z-contrast imaging and nanoprobe EDS they did not find any significant Cu deficiency or Cu-vacancy rowsin the (112) or any other boundary. More recently, Yan et al. examined dislocation cores in CISe films using DFT.[214] They found that CISe grain boundaries were likely to be electrically benign due to atomic relaxation of bonds near defects, which resulted in low density of states of mid-gap energy levels. Experimental support for this hypothesis has been provided by Moenig et al.[225] This dearth of deep trap states contributes to the neutral character of grain boundaries and would suggest a low rate of non-radiative recombination at grain boundaries. However, Yan et al. also conclude that Na inclusion is likely to occur at grain boundaries, and that Na atoms can occupy interstitial sites and act as shallow donors. This would lead to a local positive charge at the GBs. They confirm this through KPFM and show that CISe films grown on borosilicate glass have neutral grain boundaries while those grown on SLG have positively charged grain boundaries.[214]

As it stands there are at least two competing models (the NHB and PEA models) for the behavior of CISe and CIGSe grain boundaries, and both are supported by some first-principles explanations and experimental evidence. Unfortunately, neither model has yet been able to completely explain the many different results found experimentally. The shortcomings of these models could simply be due to the added complexities of extrinsic passivation and contamination below detectable limits, the different

processes by which the samples are prepared or it could signify that there are essential phenomena that are not being considered. Before proceeding to discuss kesterites, it is important to note that in addition to Na, other extrinsic passivation mechanisms have also been proposed to passivate chalcopyrite GBs. Early in the development of CISe it was realized that a post deposition air-annealing could be used to improve device performance. It has been hypothesized that the dominant defect at CIGSe GBs is the positively charged Se vacancy, which can be passivated by oxygen.[226] Oxygenation of the films results in three effects: passivation of Se-vacancies, elimination of charged defects at the CdS/CIGSe interface, and Cu-removal from grain boundaries.[227] The first effect is beneficial for devices, the latter two are not. However, the unintended coupling of Na-incorporation and CBD of CdS was shown to isolate only the beneficial effects of oxygenation;[227] Na acts to promote the oxygenation of V_{Se}, passivating GBs and minimizing Cu-loss during CBD, while CBD restores the CIGSe/CdS interface charge. The remainder of this section will examine experimental studies on kesterite grain boundaries, their relation to the above theoretical models, and the behavior observed in CIGSe.

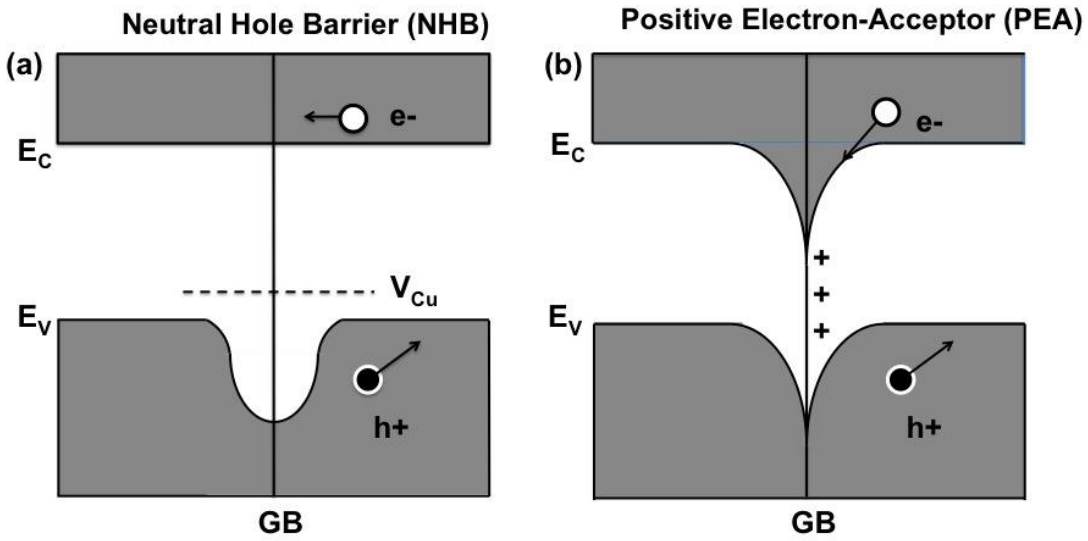

Figure 2.8 Schematics illustrating the proposed (a) Neutral Hole Barrier (NHB) and (b) Positive Electron Acceptor (PEA) grain boundary models.

Given the utility of KPFM in CIGSe GB studies, two groups have examined the grain boundaries of kesterite materials using KPFM. Li *et al.* examined CZTS (with a power conversion efficiency of 3.37%) and CZTSSe (with a PCE of 7.75%) thin films deposited on Mo/SLG through sputtering alongside high performance CIGSe films from NREL.[228] They found surface potentials for all three materials with average values of approximately 150, 200, and 120 mV for CIGSe, CZTS and CZTSSe,

respectively. The value they obtain for CIGSe is in the range commonly reported[210] and agrees with a previous report by Jiang *et al.* on a similarly prepared film.[229, 230] The surface potentials observed correspond to a downward bend in the energy band diagram, and thus the GBs should attract the minority carrier electrons and repel holes. Jeong *et al.* also reported higher surface potentials at CZTSe GBs using KPFM.[231] They examined films co-evaporated on Mo/SLG with 3 different compositions and found that the surface potential varied with composition. In the same study, Li *et al.* also used conductance-AFM to measure the passage of photocurrent in their films. They found increased current at the GBs and that the GBs may act as channels for current flow, see Figure 2.9 for the topography, surface potential, and local current images for CIGSe, CZTS, and CZTSe. These results more strongly support the PEA model and further more suggest that the qualitative nature of the GBs may be very similar in CIGSe, CZTS, and CZTSe. The electronic similarity is further supported by Oo *et al.*[75] who used electron backscatter selected-area diffraction (EBSD) to determine that the majority of CZTS grain boundaries are Σ3 twins, which is the same structure found in chalcopyrites.

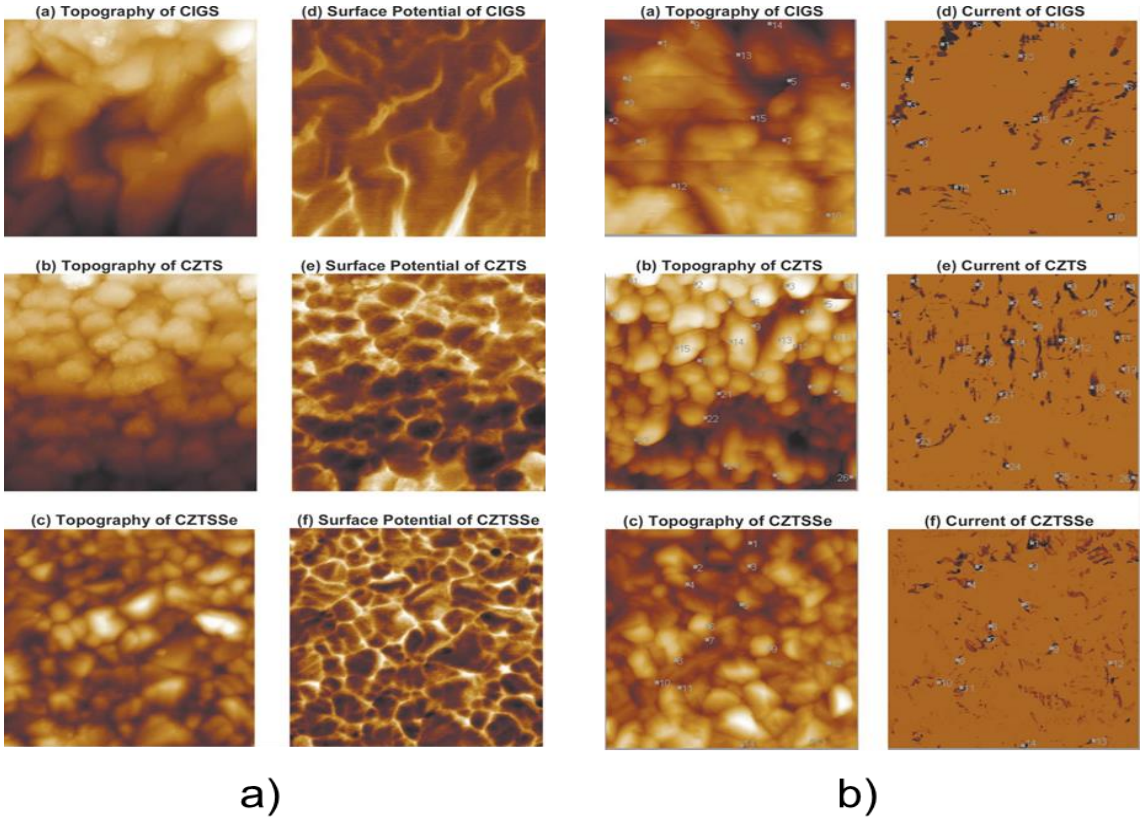

Figure 2.9 Topography (AFM), surface potential (KPFM), and electrical current maps of CIGSe, CZTS, and CZTSSe. The brighter areas in the surface potential maps indicate decreased work function, and can be attributed to positively charged grain boundaries. Reproduced from Li *et al.*[232]

Cathodoluminsecence has also been used to examine CZTS and CZTSe and compare them directly to CIGSe. Romero *et al*.[233, 234] extended their previous CIGSe work[235] to CZTS and CZTSe and observed a similar, though reduced, redshift at the grain boundaries of these kesterite materials. The CZTSe samples were synthesized using the same method that created the 9.15% efficient devices reported by Repins *et al*.,[236] but the CZTS was significantly less efficient at only 2.3%. As can be seen in Figure 2.10 the red-shift in CZTS is only a few meV and the emission spectrum is largely dominated by variation within the grain interior. In contrast, the magnitude of the redshift at the CZTSe GBs are near the same magnitude as those of the CIGSe (10-15 meV) though the CIGSe film has more grain boundaries with the red-shift. The difference between the CZTS and CZTSe results should not be too surprising (or given too much weight) given the stark contrast in device efficiencies. However, it is interesting to see that CZTSe again exhibits similar GB phenomena as CIGSe. The NHB model was invoked to explain the red-shift. However, it is not clear that the red-shift excludes the PEA model. Here, we propose that the red-shift could come from tunneling transitions from the CBM in the GB to the VBM adjacent to the GB but inside the grain interior. The same could be true if these are donor-acceptor transitions as well.

Some additional support for Cu-poor surfaces was recently reported by Bär *et al.*[237] They employed a combination of XPS and x-ray AES (XAES) to investigate the formation of surface oxides in CZTS absorber layers. They found that exposure of the absorber layer to ambient air leads primarily to the oxidation of surface Sn species. Zn and S oxides were present to a lesser extent, but Cu-oxides were notably missing. By comparing surface-sensitive XPS to bulk-sensitive EDS, they deduced that the surface exhibits a significant enhancement of Zn and Sn species and a relative absence of Cu. They proposed that the surface is composed of a Cu-free, Zn-Sn species, such as $ZnSnS_3$ or ZnS and SnS_2. This behavior is analogous to the V_{Cu} surface reconstruction proposed by Persson and Zunger for CIGSe. However, the authors here did not invoke the NHB or PEA model. In contrast to similar studies performed on chalcopyrites, the authors did not observe Na-related peaks on the CZTS surface.

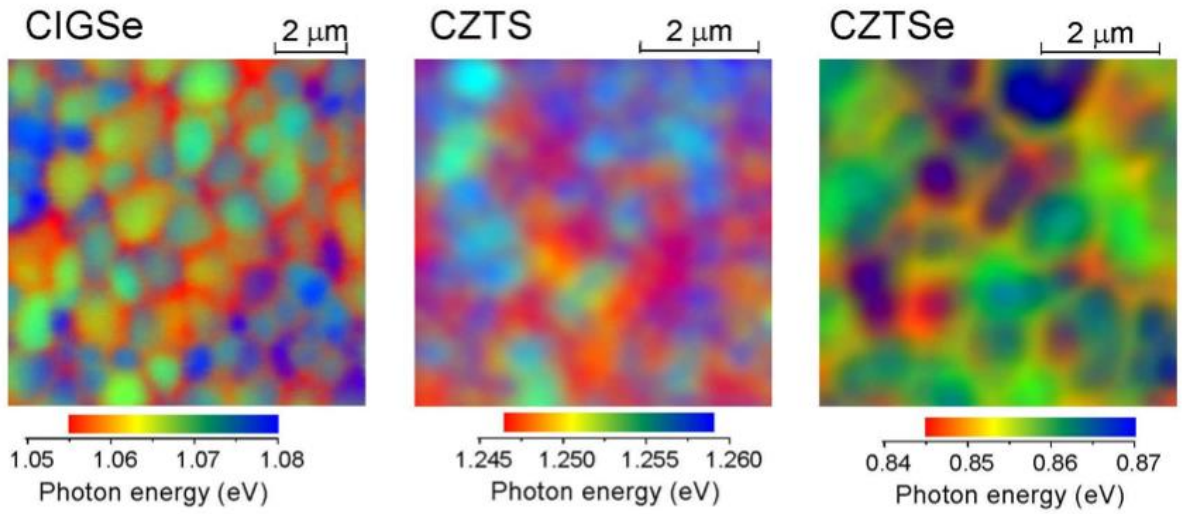

Figure 2.10 Cathodoluminescence images of CIGSe (left), CZTS (middle), and CZTSe (right) showing the energy shift of the CL emission peak. Note the distinct red-shift at grain boundaries in CIGSe. Reproduced with permission from Romero *et al*.[233]

CZTSe GBs have also been examined with *ab initio* calculations. Li *et al.* have examined the structure and electronic properties of both CISe and CZTSe grain boundaries. By varying the positions of the constituent atoms they constructed four different GBs for CZTSe and two different GBs for CISe (Se- or cation-terminated). Upon relaxation of the CISe structure it was found that there was only one defect that formed states within the bulk band gap, a Se-Se anti-bonding state. The rest of the states were within the bulk bands, a result that qualitatively agrees with that of Yan *et al*[214] despite differences in the calculation methods. However, for CZTSe, they found a relatively high density of defect states within the gap, and concluded that passivation techniques will need to be developed to improve the efficiency of CZTSe devices. One such passivation technique, is the growth under zinc-rich conditions which leads to precipitation of ZnS(e) at the grain boundaries. Mendis *et al* have used a cathodoluminescence-based technique to look at the surface recombination velocities of CZTS grain boundary hetero-interfaces with different secondary phases.[238] Grain boundaries with $Cu_xSn_yS_z$ and ZnS precipitates showed reduced recombination velocities relative to the bulk, while grain boundaries with SnS showed much higher recombination velocities. For polycrystalline samples, the effects of Sn-rich grain boundaries can be mitigated by using a post-selenization/deposition air anneal.[239, 240] The air anneal converts the $SnS(e)_x$ at surfaces and grain boundaries into SnO_x which is believed to help passivate the grain boundaries and has been correlated with improved device performance. [239]

In summary, KPFM, CL, temperature dependent conductivity measurements all show that the GBs in CZTSe have very similar properties to the GBs in CIGSe while the one density functional theory study of CZTSe suggests that there are some additional energy states in the bandgap, as compared to CISe. Some of these reports suggest a PEA model is appropriate for the kesterites while others are more suggestive of a NHB model. While we note that the samples were prepared in very different manners, it is possible that the NHB and PEA models provide limiting cases of, what in reality, may be a mixture of both phenomena.

2.5 PHOTOVOLTAIC DEVICE FABRICATION AND PERFORMANCE

Thre is a large and growing number of publications related to kesterite materials, and devices with efficiency greater than 6% have been achieved using a number of techniques, including hydrazine-inks [85, 241, 242], nanocrystal-inks,[30, 116, 180, 243] electrodeposition,[244] sputtering,[74, 232, 245] co-evaporation,[77, 153, 236, 246] molecular inks,[247] and monograin powders.[248] However, unlike many other PV technologies the most efficient devices to date have been made via solution processing. The reason for this remains to be elucidated but it is likely a result of tin volatility. The performance parameters of several of these devices (and other top performing PV technologies) are reported in Table 1 where they are compared to their theoretical maximums. Below we review design principles for thin film photovoltaics and discuss the state-of-the-art with CZTS and CZTSe.

TABLE 2.1 COMPARISON OF SELECTED PV TECHNOLOGIES TO THEIR THEORETICAL MAXIMUMS.

Record	E_g (eV)	η (%)	$\frac{\eta}{\eta_{max}}$	J_{SC} (mA/cm^2)	$\frac{J_{SC}}{J_{SC,Max}}$	V_{OC} (V)	$\frac{V_{oc}}{V_{oc,Max}}$	FF (%)	$\frac{FF}{FF_{,Max}}$
GaAs	1.42	28.8	0.867	29.68	0.926	1.112	0.968	86.5	0.966
CdTe	1.45	21.5	0.655	30.25	0.981	0.876	0.738	79.4	0.885
x-Si	1.12	25.6	0.766	41.8	0.954	0.740	0.844	82.7	0.952
CIGSe	1.10	21.7	0.657	35.4	0.828	0.747	0.868	79.3	0.913
CZTSSe	1.13	12.6	0.376	34.5	0.812	0.460	0.579	69.8	0.800

2.5.1 *Device Structure and Design Rules*

There are several good texts for the device design and operation of solar cells.[249-252] A recent and welcome addition to this body of literature is a text from Scheer and Schock[187] that focuses on thin film chalcogenide photovoltaics, mainly CdTe and CIGSe, but much insight can be gained about CZTS and

CZTSe devices. Here we summarize some of the basic requirements for good solar cell performance and review the status of kesterite devices:

- ***Bandgap well matched to the solar spectrum*.** Detailed balance calculations show that efficiencies greater than 30% are possible with bandgaps between 0.91 and 1.65 eV. The entire spectrum from x=0 to 1 of $Cu_2ZnSn(S_x,Se_{1-x})_4$ satisfies this metric.
- ***Absorber layer thickness such that almost all photons greater than Eg are absorbed***. The absorption coefficients for both CZTS and CZTSe are greater than 10^4 cm^{-1},[121] respectively. For photons of energy 1.05 Eg, the absorption lengths are just less than 1 μm. The optimum thickness can also be affected by the effective interfacial recombination velocity at the back of the device and the reflectivity of the back contact.
- ***Good absorber optoelectronic quality.*** The majority carrier concentration and the minority carrier lifetime and mobility should be such that the depletion length plus the minority carrier diffusion length should be greater than the photon absorption length for near-bandgap-energy photons, $W_{dep} + L_{diff} > (1/\alpha)$. There appears to be good prospects for this, particularly with absorbers that are rich in selenium. However, there are some issue controlling the doping concentration in CZTS. See section 6.2 for details on lifetimes, mobility, doping, and grain structure.

All photovoltaic device reports for CZTS and CZTSe utilize the standard n-type window layer / n-type buffer layer / p-type absorber layer heterojunction architecture that is employed in the most common chalcogenide solar cells. The basic principle of the window/buffer/absorber structure is to pass as much light through the window and buffer layers into the absorber layer as possible and create a charge distribution such that the “built-in” electric field resides primarily in the p-type absorber layer. This creates a strong drift mechanism for carrier collection, but it also simultaneously moves the region of fastest recombination (where n≈p even under low injection) away from the heterojunction interface where the concentration of defects can be high. In addition to guidelines 1-3 that apply to all conventional single junction solar cells, the following additional requirements should be met by devices with the window/buffer/absorber architecture:

- ***Strong inversion region in the absorber near the pn heterojunction***. Achieving this insures that the electric field resides predominately in the absorber and that the region of n≈p is inside the absorber, away from the junction. Achieving strong inversion is most commonly achieved by asymmetric doping where the buffer layer is thin and depleted and the n-type doping in the window layer is at least 10 times larger than the p-type doping in the absorber layer. However,

interface charge and Fermi level pinning can interfere with this. With n-type window layer carrier concentrations typically greater than 10^{18} cm^{-3}, the carrier concentration in the absorber should be between 10^{15} and 10^{17} cm^{-3}. Even if strong inversion can be achieved with higher absorber carrier concentrations, carrier concentrations higher than 10^{17} cm^{-3} should be avoided since they lead to depletion layers that are too thin and enhanced recombination due to tunneling effects. Good efficiencies can in principle be achieved without strong inversion. However, they would require a very low defect material junction and high quality buffer layer material. As a result, the most success has been achieved by aiming for strong inversion to avoid both of these issues.

- ***Good band alignment to the absorber layer.*** The two key places for good band alignment are typically the conduction band alignment between the absorber and buffer layers and the Fermi level alignment between the absorber and the back contact (see Figure 2.11). Modeling results have shown that the conduction band offset should be positive but less than about +0.3 eV.[253] A "positive" offset means the buffer layer conduction band edge is higher than absorber layer conduction band edge. This situation is commonly referred to as a conduction band "spike" whereas the opposite case is referred to as a "cliff." These terms are in reference to how the conduction band discontinuity may appear to a photogenerated electron in the absorber layer traveling into the buffer layer. The small positive offset helps support strong inversion in the near junction region of the absorber, but it does not significantly impede electron flow into the buffer layer until it become larger than +0.3 eV. Negative offsets tend to reduce inversion in the absorber and displace the ideal electric field into the buffer layer. See section 6.3 for details. At the back of the device, the barrier for hole flow due to misalignment of Fermi levels or compensation of dopants in the absorber should be small (0.3 eV),[187] if present at all. See section 6.4 for details about the back contact.

There are also several other design strategies that may be used to enhance efficiency in kesterite solar cells. One involves forming a bandgap gradient in the absorber near the junction by decreasing the valence band edge towards the junction.[254] This can help increase the open circuit voltage while preserving the photocurrent. The prospects for this approach are pretty good in the kesterite system. Alloying CZTSe with either sulfur or germanium can increase the conduction band minimum and direct minority carrier electrons towards the junction. This is particularly promising since good quality material can be formed up to band gaps of about 1.3 eV using when alloying with either sulfur or germanium (refer to Chapter 7). Another promising strategy involves forming a band gap gradient in the

absorber near the back contact by increasing the conduction band edge towards the back.[255] This creates a so-called back surface field (BSF) that can help reflect minority carriers (electrons) away from the back interface. Again, the prospects for this approach are very promising in the kesterite system by exchanging lighter group IV elements onto the Sn site. The first steps towards this were recently shown by forming good quality devices with germanium substituted absorbers, $Cu_2Zn(Sn_{1-y}Ge_y)Se_4$.[30, 180]

Beyond design guidelines, device stability is a major concern for all PV technologies. Devices need to maintain efficiency, losing no more than a percent or two (of their original power output) per year, for over 20 years. While CdTe and CIGSe devices do satisfy the minimum requirements, there are well known stability issues with back contact in CdTe solar cells[256] (copper diffusion) and the front contact in CIGSe devices[257] (stability to damp heat[258]). Recently, advances have been achieved in increasing the stability of the TCO in CIGSe by applying a final coating of SnO_2 over the entire device (top contacts included).[259]

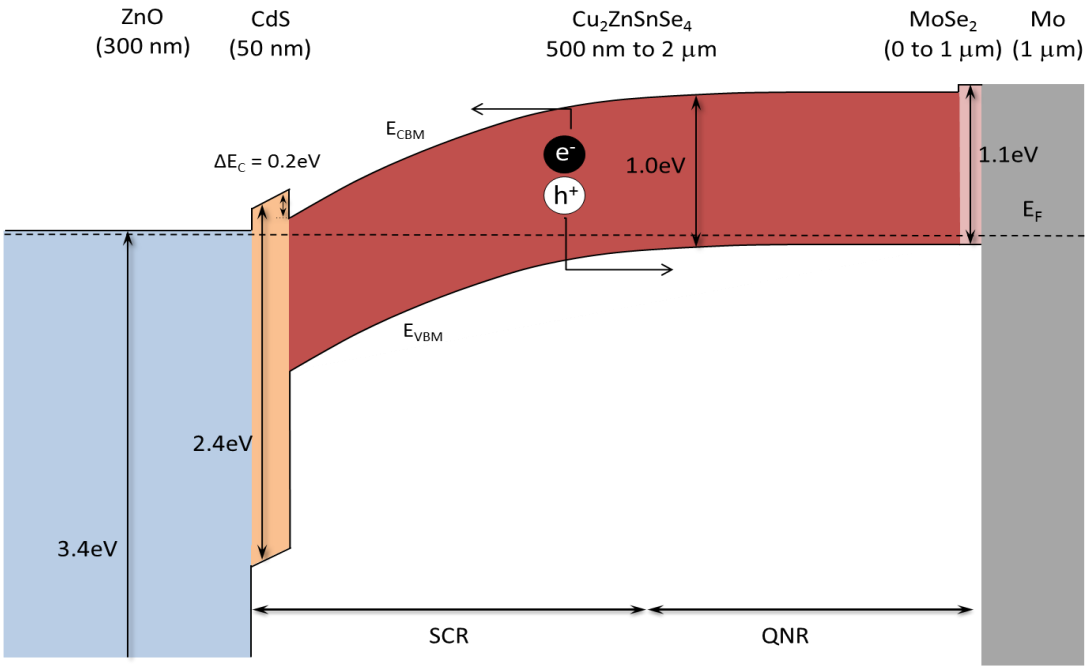

Figure 2.11 Device structure and band alignment for CZTSe solar cells. The schematic shows a small positive conduction band offset (spike) and an ohmic back contact.

2.5.2 *Absorber Quality*

The quality of the absorber layer is usually quantified in terms of the minority carrier lifetime, mobility, and carrier concentration. Typically reported values are from measurements that lack spatial resolution, and the values are average properties that result from numerous single-crystalline domains (with different size and perhaps with different defect concentrations and distributions), grain boundary properties, the tertiary grain structure, and any impurity phases that may have precipitated out.

Mobility, Lifetime, and Carrier Diffusion Length. The mobility and lifetime of the minority carrier combine to yield the minority carrier diffusion length, $(\mu\tau kT/q)^{1/2}$. This important parameter determines the carrier collection efficiency from the quasi neutral region of the solar and is typically on the order of 2 μm and 1 μm in good quality CdTe[187, 260] and CIGSe[187, 261] devices, respectively. Measuring the mobility of the minority carrier directly is difficult, but in many cases, an estimate based on the majority carrier mobility is used. A list of Hall-derived properties for the majority carrier holes, including carrier densities and Hall mobilities, for various synthesis methods was compiled by Mitzi et al., with the sulfides ranging from 6-12 $cm^2/V\cdot s$ and the selenide around 40 $cm^2/V\cdot s$.[66] More recently, Tanaka *et al*. investigated the effect of stoichiometry, the Cu/(Zn+Sn) ratio, on co-evaporated films and found that that mobility decreased slightly with increasing Cu content (from 11 $cm^2/V\cdot s$ to 0.3 cm^2/V-s for ratios of 0.7 to 1.3).[262] There has not been much work focused on minority carrier lifetimes thus far. There are only two reports of lifetimes in the literature, both used time-resolved photoluminescence (TRPL). One is from hydrazine processed sulfoselenide absorbers $Cu_2ZnSn(S_xSe_{1-x})_4$ A device with x=0.4 had a lifetime of 3.1 ns[241] while that with x=0.03 had a lifetime of 12 ns.[86] The other report is on devices with a sputtered selenide absorber layer in which the best devices had lifetimes up to 10ns.[263] The latter report also found that the measured lifetime decreases over time when the sample is exposed to ambient. A variety of surface treatments were investigated, but the only one found to have significant impact was KCN etching which had a beneficial effect. It is important to note that these lifetimes were for fully fabricated devices, not just the absorber layer. It has been shown previously that lifetimes can vary significantly depending on sample processing, with CIGSe absorbers coated with window and buffer layers exhibiting lifetimes an order of magnitude lower than that of the bare, un-degraded absorber.[264, 265] This has been attributed to the influence of charge separation due to the field created from the junction in a full device, and thus, the TRPL measured lifetime should be considered a property of the device, not the material alone. With these lifetime values, the minority carrier diffusion length would be

0.3 μm and 1.1 μm, respectively for the IBM $Cu_2ZnSn(S_x,Se_{1-x})_4$ devices with x=0.4 and x=0.03. Thus, particularly for CZTSe, it appears that lifetimes that would enable 20% efficient devices are possible.

Carrier Concentration. The carrier concentration in the absorber layer primarily affects the depletion width and carrier collection. Carrier concentrations that are too high can lead to depletion widths that are too thin and to tunneling enhanced recombination. Carrier concentrations that are too low lead to large regions of enhance recombination (where the n and p concentrations cross over) and can lead directly to Voc losses by increasing the energy between the VBM and the Fermi level at the back of the device (as is the case for CdTe). If the window and buffer layers are heavily doped, carrier concentration in CZTSe (ε=8.5) of 10^{15}, 10^{16}, 10^{17}, or 10^{18} cm^{-3}, lead to depletion widths of 914, 288, 88, 21 nm respectively. It is currently believed that the free carriers in CZTS and CZTSe arise from the native point defects (see section 5.3). Based on formation energies calculated via density functional theory, the dominant acceptor-like defect has been suggested to be the Cu_{Zn} antisite defect, which ionizes at 0.12 eV in CZTS and 0.09 eV in CZTSe. However, these acceptors are compensated by the donor-like Zn_{Cu} anitsite defects and the resulting carrier concentration is a result of stoichiometry and processing of the material.

There have been widely varying reports of carrier concentration for CZTS. Several reports using Hall measurements reported carrier concentrations for CZTS in the range of 10^{18}-10^{20} cm^{-3} [84, 266-268] while others report values closer to 10^{16} cm^{-3},[269, 270] a value in the range much more suitable for PV. For CZTSe there have been fewer reports of Hall measurements but the values reported have generally similar with values in the range of 10^{17}-10^{20}.[262, 271] A recent publication by Tanaka *et al.* tested carrier concentration in co-evaporated CZTSe films as a function of Cu/(Zn+Sn) ratios from 0.7-1.25[262]. Hall type measurements showed that the carrier concentrations increased with Cu-content from 10^{17}-10^{20} cm^3. For ratios above 0.9, Raman spectroscopy indicated that Cu_2Se phases were present, and carrier concentrations were always over 10^{20} cm^{-3}. Etching a film with a starting Cu/(Zn+Sn) ratio of 1.06 for 30 minutes in 10% KCN reduced the ratio to 0.98, eliminated the Cu_2Se peak, and reduced the carrier concentration to $2.5x10^{18}$ cm^{-3}. These values are in contrast to carrier concentrations measured using capacitance-based techniques, such as Mott-Schottky and DLCP which find values much lower. For example, Gunawan *et al,*[164] Repins *et al.,*[272] and Guo *et al.*[180] have all reported carrier concentration near 10^{16} cm^{-3} on efficient devices.

Effects of Grain Growth. In CIGSe it has been found that growth under Cu-rich conditions leads to better electronic properties and significantly larger grain sizes.[273-276] This is due to flux recrystallization via the low melting point binary compound Cu_xS or $Cu_{2x}Se$, which phase segregates to the surface of the grains leading to a liquid-solid type growth mechanism.[277] Although beneficial for grain growth, once the absorber layer has been formed, the highly conductive $Cu_xS/Cu_{2x}Se$ binaries are detrimental to device performance. Cu-poor materials form a good interface with CdS and exhibit much better defect properties due to the formation of the neutral defect complex ($2V_{Cu}^{-} + In_{Cu}^{2+}$) and restructuring at grain boundaries.[214, 234, 235] For these reasons, the highest efficiency absorber layers are those that experience a Cu-rich growth regime but are ultimately rendered Cu-poor. A common way to achieve this is using KCN etching after depositing the absorber layer. Indeed, reports have already shown that KCN can be beneficial for CZTS.[262, 278, 279] However, despite finding that CZTS absorbers grown Cu-rich had slightly larger grains it has not been shown to improve device efficiency.[280-282] A study of absorbers made via co-evaporation starting either Zn-rich or a Cu-rich and terminating at the same Cu-poor/Zn-rich composition have both been shown to achieve approximately the same grain size and device performance.[283] Interestingly, even when the film was very Cu-poor the presence of Cu_xSe_y phase was observed.

In order to grow homogenous large-grain absorbers, many groups have been annealing at 550-600°C [96, 283] which is at the upper limits of the soda-lime glass substrate. In-situ growth studies performed on both the sulfide and selenide grown from either metallic precursors or binary/ternary metal chalcogenides have shown that the formation of kesterite results from the solid state reaction of $Cu_2SnS(e)_3$ with ZnS(e) at a temperature near 550°C.[284-287] Similarly to CIGS, Na has also been shown to be beneficial for grain growth in kesterites, and can be incorporated by simply dipping the film in an aqeuous Na_2S solution.[75] Higher temperatures also lead to larger grains, but it also leads to the formation of a thicker $MoSe_2$ layer that can degrade performance. Shin et al.[153] have demonstrated that TiN can be used as a diffusion barrier to suppress excess $MoSe_2$ formation. With this barrier they were able to obtain larger grains via higher temperature annealing without forming excess $MoSe_2$ and demonstrated an 8.9% CZTSe device.

Effects of Binary Phase Formation. Using EBIC (electron beam induced current) and micro-IV measurements, Wätjen *et al.* have shown that, as expected, binary ZnSe phases act as insulating regions, increasing series resistance and reducing short-circuit current density.[288] In addition, using XANES, ZnS content has been directly correlated to losses in Voc, FF, and efficiency.[139, 289] A cell containing

25% ZnS (by volume) suffered a loss in efficiency of almost 50%. However, the mechanism of the degradation is not yet clear. Fairbrother *et al.* found that etching in HCl can be used to remove surface ZnS, leading to increased Jsc as a result of decreased series resistance as well as improved Voc, but the etch was much less effective for ZnSe.[279] HCl etching was also found to be ineffective at removing detrimental Cu-Sn based secondary phases from CZTSe absorbers, but the non-selective etchant Br_2 has been shown to be effective.[290]

While the studies above reflect a growing understanding of the effects of grain growth and formation of binaries, there have yet to be studies that directly connect the main metrics of absorber quality (mobility, lifetime, and carrier concentration) with processing conditions.

2.5.3 *Buffer Layer and Conduction Band Offset*

CdS has been the default buffer layer for CIGSe devices. It has yielded the most efficient devices[19] and has a modest positive conduction band offset of about 0.2 eV that varies with Ga-content.[291] However, for many years researchers have unsuccessfully tried to find an alternative to the CdS buffer layer (that is just as good) due to concerns about the toxicity of Cd and to reduce short-circuit current losses that result from poor collection of carriers generated in the CdS (2.4 eV). A number of different buffer layers have been tested,[292-294] but none produce as high of efficiencies as CdS, although in recent years, Zn(O,S) has gotten very close. The reason CdS works so well is two-fold. First, Metzger et al. have shown that the TRPL lifetimes of bare CIGSe absorber layers decrease by two orders of magnitude when samples are left in air for 1 day.[264] Samples were also found to degrade even when stored in dry boxes, or even vacuum chambers. This same degradation is not seen in materials after CdS chemical bath deposition, and thus CdS acts as a protective layer. This was recently also shown in steady-state PL measurements as well.[295] Another hypothesis for the benefits of CdS is the formation of a buried homojunction.[296-299] The hypothesis is that during CdS deposition Cu atoms are selectively etched from the CIGSe layer and substituted with Cd atoms forming a thin n-type $(Cd_yCu_{1-y})(In_xGa_{1-x})Se_2$ layer on the surface of the CIGSe absorber. While this has been expounded by some as a key feature of CIGSe PV (that it helps reduce the recombination at the interface), it has been pointed out by others that the same beneficial effects of an inverted region (n-type) in the p-type absorber near the junction can be obtained by strongly asymmetric doping (between the window/buffer and the absorber) without the presence of a buried homojunction.[253] For CZTS and CZTSe the energetics of Cd substitution during CBD has been calculated by Maeda et al.[300] They predict that both Cu and Zn will be leached from the film to form an aqueous ammonia complex allowing for Cd substitution. They report that the formation

energies for a Cd-substitional defect are all positive and large, but smaller than their corresponding values in CISe (i.e. Cd_{Cu} or Cd_{In}). In the presence of V_{Cu}, (i.e. once Cu or Zn has been leached) the formation energy of Cd_{Cu} is negative for both CZTS and CZTSe suggesting that the n-type defect Cd_{Cu} will result from the CBD process as it does in CISe.

For the kesterites, if CdS can be replaced with a higher bandgap buffer layer, such as Zn(O,S), it would not only increase the maximum photocurrent available, but CZTS could be the first non-silicon thin film technology to rely entirely on abundant and non-toxic elements. There have already been several reports of devices using alternative buffer layers.[140, 301-303] Solar Frontier has achieved conversion efficiencies of 6.3% and 5.8% on 5x5 cm submodules using In and Zn based buffer layers.[304] Barkhouse *et al.* recently reported devices with ZnO, ZnS and In_2S_3 buffer layers.[303] The devices had conversion efficiencies of 2.46%, 0.00%, and 7.59%. The poor performance of the ZnS device was attributed to a highly unfavorable conduction band offset, which they measured using femtosecond laser pump/probe UPS. They report that (with ±0.1 eV uncertainty) the ZnO conduction band aligns with the CZTS conduction band to yield zero offset, ZnS has a large positive offset of 1.1 eV (a spike) that blocks the photocurrent, and In_2S_3 has a favorable small positive offset of 0.15 eV. While the high efficiencies for the In_2S_3/CZTS system are promising, it should be noted that the impetus behind the development of CZTS was to avoid In-containing materials (though the buffer layer will be less material-intensive than the absorber layer). However, just as with CIGSe, the highest efficiency CZTS devices are still those that use a CdS buffer layer.

Density functional theory calculations predict that the CdS/CZTSe interface will have the same type of band alignment as CIGSe with a ~0.26 eV offset.[305] However, the pure sulfide CZTS is expected to have a slight negative (cliff-like) offset of 0.09 eV. The transition from spike to cliff would occur at some intermediate alloy composition. Experimentally, there have been three reports so far. Ming Wei et al. found a positive 0.34 eV spike for CZTSe using XPS, a value which generally agrees with theoretical predictions.[306] On the other hand, the values determined by Haight et al. do not agree with theoretical predictions. They looked at S/(S+Se) ratios from 0 to 0.65 using femtosecond laser pump/probe UPS and found a positive 0.4-0.5 eV spike in all cases.[161] Seeking to reconcile the discrepancy between the temperature-dependent Voc measurements, which could suggest a cliff like offset,[246, 307] and the reported large positive conduction band offsets, Bär *et al* used direct and inverse photoemission techniques to independently determine the position of the VBM and CBM with and without a KCN etch.[278] In contrast to the previous report and in agreement with the temperature dependent Voc

measurements, they found an unfavorable negative (cliff-like) offset of 0.3 eV for CZTS. This same offset was seen regardless of KCN etching, but the etch did serve to increase the interfacial band gap and thus should increase the energetic barrier to recombination across the interface. This observation appears to be supported by recent work from Repins et al.[236] They reported that the best device performance is achieved when the co-evaporated film is capped with extra Zn then oxidized briefly following deposition. Thus there are at least two reports that indicate that a Cu-poor kesterite/CdS interface is beneficial for performance.

2.5.4 *Back Contact and Back Hole Barrier*

The standard device architecture for CIGSe, CIGS,[308] and current CZTS and CZTSe devices use sputtered molybdenum for the back contact, due to its relative stability against reacting with the chalcogen, good sheet resistance, and nice ohmic contact. The Mo does react to form some MoS_2 or $MoSe_2$ during annealing, selenization, or sulfidation (and are believed to be necessary for forming an ohmic contact). $MoSe_2$ is described by a hexagonal unit cell that contains two Se-Mo-Se layers offset from one another. The MoS_2 structure is the same. The MoX_2 compounds are indirect semiconductors with indirect (and direct) band gaps of 1.29 (1.78) eV for MoS_2 and 1.10 (1.42) eV for $MoSe_2$, respectively.[309] A small amount of $MoSe_2$ formation has been found to be beneficial and conducive for forming an ohmic contact in CIGSe.[310, 311] However, while excessive $MoSe_2$ or MoS_2 formation may lead to increases in the series resistance and poorer device performance, 8.9% efficient CZTSe device have been achieved with the presence of a 220 nm thick MoSe2 layer at the back.[153] These devices employed a TiN barrier at the back and yielded a series resistance of 1.8 Ω-cm^2. Identical processing conditions without the TiN barrier yielded a 1300 nm thick MoSe2 layer, a series resistance of 3.4 Ω-cm^2, and a device efficiency of 2.95%. Recent experimental and theoretical work by Scragg et al.[154] suggests that the formation of a thick $MoS(e)_2$ layer is the result of a highly favorable free energy change with the reaction between Mo and CZTS(e) during thermal annealing. The decomposition reaction shown below has an estimated free energy of reaction of -100 kJ for CZTSe and -150 kJ for CZTS, and thus results in the formation of secondary phases at the interface.

$$2Cu_2ZnSnS(e)_4 + Mo \rightleftharpoons 2Cu_2S(e) + 2ZnS(e) + 2SnS(e) + MoS(e)_2$$

This suggests that decomposition into binaries at the back may be minimized or reversed by supplying a significant over-pressure of the chalcogen. However, high chalcogen pressures also lead to the formation of a thicker $MoS(e)_2$ layer. Since secondary phases can be very detrimental to device performance, it seems that Mo may not be the best back contact material for kesterite devices.

There have been only a few reports of alternative back contact materials for CIGSe. Nguyen *et al*, investigated the use of Al, Cu, Mo, Au, and carbon as back contacts on superstrate CISe solar cells. All of the devices initially showed similar performance (3%), but the Cu and Al devices were found to degrade over time. Orgassa *et al.* reviewed the use of W, Mo, Cr, Ta, Nb, V, Ti, and Mn as back contacts for CIGSe. The metals V, Cr, Ti, and Mn were found to be unsuitable due to their reactivity with Se, while Mo and W resulted in the best devices. By introducing a Ga-gradient and thus passivating the back contact, significant improvements were made with Ta and Nb. Similar results are likely to hold for CZTSe based devices, but sulfide devices might have fewer design constraints due to the reduced reactivity of the sulfide. To date there have been no comprehensive studies of different back contact materials for CZTS. However, our economic analysis (see section 2.1) indicates that replacing Mo with a less expensive material would be a nice step in minimizing materials costs for CZTS and CZTSe.

One interesting feature that is unique to solution-processed materials, is the carbon rich layer that often appears between the absorber and back contact.[312-315] This layer is most often seen in paste coating where large quantities of organic binder and filler are used to tune the rheology of the coating solution. However, we have also seen a carbon-rich layer in nanocrystal-ink based devices (determined from unpublished composition profiles). It can be seen as an amorphous or unsintered layer in cross-sectional images. While initially it was expected that this layer was detrimental to device performance, the results of Haug et al.[313] suggest that this layer can reduce back contact recombination and can be beneficial for device performance. This result is in stark contrast to traditional semiconductor processing where extreme measures are taken to achieve ultra-high purity.

The presence of high series resistance and cross-over in JV curves has been noted in a number of kesterite solar cells. Initially, it was believed to be the result of a blocking back contact barrier that prevents hole transport across the CZTS/Mo interface.[66, 246] Back contact barriers have been previously reported in both CIGSe and CdTe devices.[316, 317] However, more recent work utilizing admittance spectroscopy and DLCP (drive-level capacitance profiling) has revised previous assertions that a back contact barrier is to blame for the dramatic increase in series resistance as temperature decreases. Because the dominant p-type dopant is the acceptor-like Cu_{Zn} antisite defect (~0.12 eV), carriers begin to freeze out at temperatures near 150K, causing the series resistance to rise by several orders of magnitude as temperature is further decreased.[164, 318] The most recent result by Repins et al.[272] notably does not suffer from crossover in the JV curve or high series resistance at room temperature. Thus as they indicate, both are most likely associated with processing variables, it is not a fundamental limitation of the material.

Chapter 3.

DEVELOPMENT OF A COMBINATORIAL SCREENING PROCESS

3.1 INTRODUCTION

Crystalline silicon solar cells are the most efficient commercially available single junction solar cell technology with current module manufacturing costs of ~$1.30/Wp. However, to reach the DOE SunShot Initiative target of $1/Wp installed cost, the manufacturing cost of the module will have to be below $0.50/Wp. Thin film PV devices are perhaps best poised to reach this manufacturing cost target with CdTe devices already at ~$0.60/Wp and $CuInGaSe_2$ (CIGSe) approaching $1/Wp. However, it is unlikely that the current absorber layer compositions, device structures, and manufacturing techniques will be able to reach this ambitious $0.50/Wp target, especially for multi-terawatt scale production. Price and price-volatility issues with In & Ga, crustal abundance issues with Te, and environmental issues with Cd have raised some concern that these could reach $0.50/Wp or should be the materials of choice for ultra-low cost PV.[33, 36, 60, 319-325] If non-toxic Earth abundant element thin film solar cells can be developed with 20% efficiency, they will be the long-term solution of choice for low-cost terawatt scale PV. The strongest initial candidates appear to be kesterite materials (Cu_2ZnSnS_4 (CZTS) and $Cu_2ZnSnSe_4$ (CZTSe)). However, relatively little is known about the chemical and electronic properties in these materials. In order to effectively chart a course for kesterite-based materials to reach 20%, it is useful to examine other technologies, evaluate what limits each, and develop strategies to circumvent or overcome similar challenges that may arise in the kesterite system.

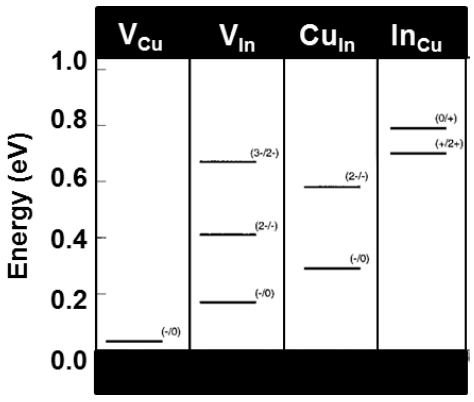

Table 3.1 Energetic position of native defects within the bandgap of CISe. Reproduced from Zhang et al.[188]

3.2 KEY DEVELOPMENTS IN CU(IN,GA)SE_2 THIN FILM PV

Like Cu(In,Ga)Se_2, CZTSSe is a multinary chalcogenide based off the zinc blende structure. It is derived from the I-III-VI_2 structure by replacing the rare group-III element indium with the earth-abundant zinc and tin. As a result, CIGSe and CZTSSe have many similar structural and electronic properties. Thus it is useful to examine what limits Cu(In,Ga)Se_2 technology and what has led to significant improvements in Cu(In,Ga)Se_2 solar cells. Historically, there have been 3 primary advances which have allowed CIGSe technology to achieve over 20% efficiency: (1) compositional tuning of intrinsic defects, (2) gallium incorporation, and (3) sodium doping.

In elemental semiconductors, such as Si and Ge, extrinsic species are the primary source of defects, and as a result, extreme measures are taken to make the material as pure as possible (99.9999999% for an electronics grade Si wafer). Following purification, an elemental semiconductor is doped with an element such as phosphorous or boron to produce a significant quantity of charge carriers. However, in multinary semiconductors, defects can also form when native elements are in the wrong crystallographic site or missing. Examples of this in CIGSe are an indium atom sitting on a copper site (In_{Cu}) and a copper vacancy (V_{Cu}). The In_{Cu} defect creates a midgap state that acts as a strong SRH recombination site, but the V_{Cu} acts as a shallow dopant, and is the primary source of the p-type conductivity of CIGSe. The formation of these defects is thermodynamically driven, but can be influenced by varying the relative abundance of the native elements. Theoretical calculations of the energetic position of various native defects in CISe are shown in Table 3.1[192] The first key advance in CIGSe was realizing that Cu-poor and In-rich conditions produced the higher quality materials than stoichiometric or other processing conditions. This results because Cu-poor and In-rich conditions discourage the formation of the worst defects, V_{In} and Cu_{In}, and instead favors the formation of V_{Cu} and In_{Cu}. Remarkably, two copper vacancies can pair with an indium-on-copper site defect to produce the neutral defect complex [$2V_{Cu}^{-}$ + In_{Cu}^{2+}], which passivates the In_{Cu} defect. Under Cu-poor and In-rich conditions this defect complex has a negative formation energy and thus readily forms.[185] This same defect complex is also believed to play a key role in passivating grain boundaries[214] and reducing interfacial recombination at the CdS interface.[326] Thus variation of the native species can have a profound impact on the optoelectronic properties of multinary semiconductors.

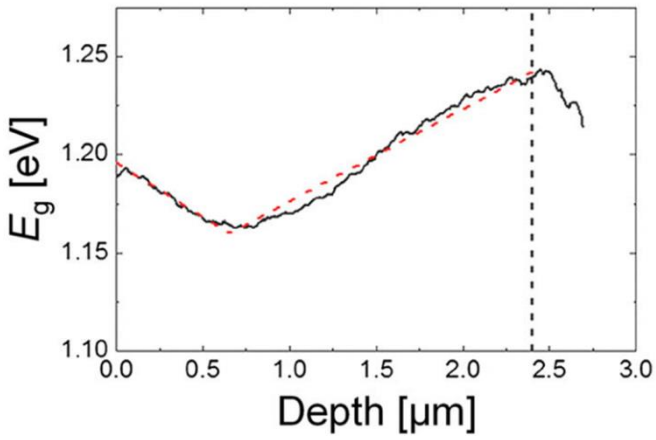

Figure 3.1 Bandgap profile through the depth of a CIGSe solar cell calculated from elemental composition data. The CdS junction is at 0μm. The image is re-produced from Ref 327.

The second key advance in CIGSe, was the incorporation of gallium to create a back surface field and passivate bulk defects.[169, 327] The small increase in bandgap associated with increasing Ga is not in itself that useful (the bandgap of $CuInSe_2$ yields a maximum theoretical efficiency of 31.7% compared to 33.6% for $Cu(In_{0.7},Ga_{0.3})Se_2$), it is mainly through its beneficial effect on minority carrier lifetime and the creation of a back surface electric field that directs n-type minority carriers away from the high recombination metal-semiconductor interface. This approach is not unique to CIGSe technology, both GaAs[328] and HIT silicon[329] solar cells use back-surface fields to reduce recombination at the contacts. For thin film devices where the entire back interface is a metal-semiconductor contact, significant surface recombination will occur, thus a back surface field is especially important for these devices. An example of the bandgap profile through the depth of an absorber which occurs from gallium grading is shown in.[330]

Sodium incorporation was another important discovery along the road to high efficiency CIGS. It was discovered unintentionally when sodalime glass was used as the substrate.[331-333] Current understanding of the role of sodium is based on several decades of experimental and modeling evidence,[334-340] which suggests that in small quantities sodium forms electrically inactive Na_{Cu} (and shallow level Na_{In}) defects, which compete with the formation of deep level In_{Cu} defects and thus increase the minority carrier lifetime. In larger quantities and in the presence of oxygen, sodium phases may precipitate at the grain boundaries. Several models have been proposed to explain the effect of sodium on grain boundaries including: the defect chemical model,[340] the positive electron acceptor model,[213, 214] and the neutral hole barrier model,[212, 217] all of which are discussed in detail in Chapter 1 section 5.4. These

models differ in mechanism, but all agree that Na passivates grain boundaries and reduces defect densities. Experimentally, it has been repeatedly shown that Na incorporation enhances film morphology, grain growth, conductivity, open-circuit voltage, and fill factor.[335, 341, 342] Practically all multinary chalcogenides have intrinsic defects that are centers for Shockley-Read-Hall recombination. However, as has been demonstrated with sodium doping in CIGS, extrinsic species may interact with the intrinsic defects to form complexes that are not electrically active.

3.3 KEY DEVELOPMENTS IN CDTE THIN FILM PV

Substantial progress has been made in recent years in improving the efficiency of CdTe devices. From 2001-2011 the highest reported device efficiency remained at 16.7%, but since then the efficiency has record has been broken at least 5 times, reaching the current record of 20.4% [343]. Unfortunately, the recent gains have been made by private industry, so little information is available about what has changed, but traditionally, there have been two main issues with CdTe: an inability to dope CdTe (and shift its equilibrium Fermi level to achieve maximum Voc) and a very short minority carrier lifetime of around 1-2 ns.

Theoretical calculations have shown that the most probable sources of hole dopants in CdTe films are: (1) Cd vacancies (V_{Cd}), (2) noble metal substitutions on Cd sites (usually Cu from the back contact, Cu_{Cd}), and (3) a defect complex formed by compensation of a double acceptor cadmium vacancy with a single donor Cl substitutional of Te $[Cl_{Te}^{+} V_{Cd}^{2-}]^{-}$.[344] The Cu substitutional is 0.22 eV above the valence band, and should theoretically only dope CdTe up to 2.4 x 10^{13} cm^{-3} (though larger doping concentrations have been measured); further, it tends to be compensated by a donor Cu interstitial. The main source of doping then must come from the other two sources whose energy levels are closer to the valence band and can theoretically dope up to 1.8 x 10^{17} cm^{-3}.[344] The main resistance to p-type doping of CdTe is not self-compensation, but the lack of dopants that have both high solubility in CdTe *and* form shallow acceptor levels.[345]

Short minority carrier lifetimes are generally attributed to defect recombination, mainly at grain boundaries and the back contact.[346-348] Similar to CZTS, no surface field exists in CdTe devices to reduce minority carrier recombination at the back contact, leading to a lower V_{OC} and efficiency.[346] Increased minority carrier lifetimes have been observed by chemically passivating films with O_2, $CdCl_2$ treatments, and controlled Cu diffusion from the back contact.[347] The exact nature of defects in CdTe and its grain boundaries are still debated;[347] however, it is observed that $CdCl_2$ treatments in the

presence of O_2 not only increase the majority carrier concentration (as discussed above), but also the CdTe grain size owing to a low-temperature eutectic in the CdTe-$CdCl_2$ system.[349] It's important to note that too much Cl can be detrimental to both carrier concentration and minority carrier lifetimes. Isoelectronic complexes of two Cl substitutionals at Te sites with a Cd vacancy [$2Cl_{Te}^{-}$ V_{Cd}^{2+}] will reduce carrier concentration, while electrically active intrinsic point defects caused by Cl will reduce minority carrier lifetime.[349] It has been observed experimentally that the addition of chloride is an absolute necessity for CdTe. However, it was not discovered from first principles calculations, but by experimentation. We could view this as the same lesson that arose from the sodium discovery in the CIGS system – there is a good chance of finding extrinsic species that can be added to the film to passivate intrinsic defects. However, in the case of CdTe it is extrinsic monovalent anions that are active in defect passivation.

3.4 Defect Chemistry of the Kesterite Absorber

CZTS and other similar I_2-II-IV-VI_4 quaternary semiconductors have attracted interest for a wide variety of applications. Their wide applicability stems from the incredible flexibility for tailoring the structural and chemical properties. However, with this added flexibility comes additional complexity. For example, early reports disagreed as to whether CZTS crystallized in the kesterite or stannite structure. It has since been shown that kesterite is the lowest energy structure, but that the energy difference between kesterite and stannite is only about 3 meV/atom.[120] As a result, both the kesterite and stannite phases may coexist in a single sample. Further proof of that complexity can be seen when looking at defect formation. Understanding the formation of defects and self-compensation is key to developing better quality absorber layers and higher efficiency devices. Theoretical work performed by Chen et al [120, 130, 156, 175, 196] has greatly facilitated the understanding of defects in CZTS. They have shown that unlike CIGS, where the dominant defect is V_{Cu}, the p-type conductivity observed in CZTS results from Cu_{Zn} which has a lower formation energy than V_{Cu} despite being a deeper acceptor.[350] The formation of Cu_{Zn} is preferred over V_{Cu} in CZTS because of the small difference between both the size and valence of Cu and Zn.[130] Figure 3.2 shows a summary of the different defects in CZTS and CZTSe and their energetic position within the bandgap.

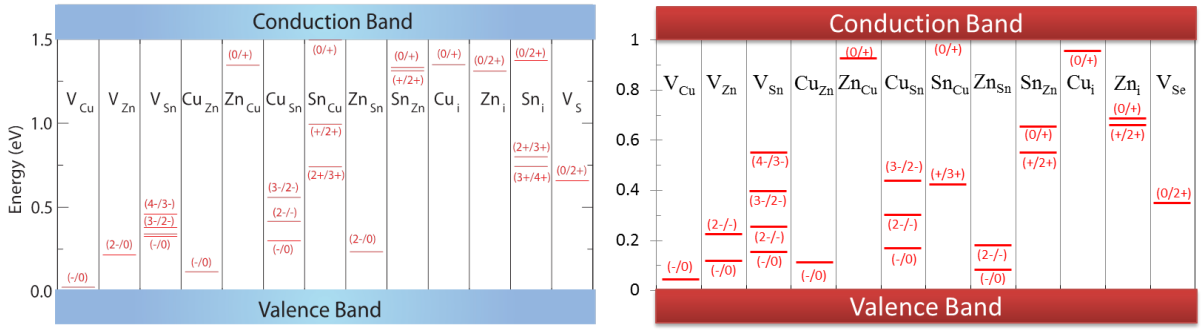

Figure 3.2 Defect energies in CZTS (left) and CZTSe (right) relative to the band edge positions [Reproduced from Chen et al. [130]]

One of the biggest benefits of using multinary semiconductors is the incredible potential for self-compensation through the formation of neutral defect complexes. Just as the formation of the neutral complex $[2V_{Cu}^{-} + In_{Cu}^{2+}]$ enables high efficiency $Cu(In,Ga)Se_2$ based devices by passivating the In_{Cu}^{2+} recombination center,[192] in CZTS the defect complex $[Cu_{Zn}^{-} + Zn_{Cu}^{+}]^0$ is expected to form easily.[196] Under Cu-poor Zn-rich conditions, this should bind the Cu_{Zn}^{-} defects and prevent the semiconductor from being degenerate. In addition, because of the presence of three different cations there are a large number of other defect complexes such as $[V_{Cu}^{-} + Zn_{Cu}^{+}]$, $[V_{Zn}^{2-} + Sn_{Zn}^{2+}]^0$ and $[Zn_{Sn}^{2-} + 2Zn_{Cu}^{+}]^0$ which have low formation energies and therefore are expected to form easily in non-stoichiometric samples.[130] The experimental observation that zinc-rich copper-poor CZTS absorbers produce the most efficient devices[351] clearly shows the importance of neutral defect complexes in passivating deep levels within the bandgap of CZTS. However, the realm of how extrinsic species will interact with this complex defect chemistry is completely unknown and the potential experimental space is incredibly large. Further, as we have learned from both Na in CIGSe and Cl in CdTe, extrinsic species can be beneficial, but only in certain concentrations. Too much is bad and too little will not have an effect. Thus, to rapidly and effectively screen this enormous experimental space we have developed a high-throughput screening method.

3.5 Development of a Combinatorial Spray Coater

From the development of both CIGSe and CdTe, we have learned several important lessons: (1) variation of native elements can have a profound impact on the optoelectronic properties, (2) band gap grading can greatly reduce interfacial losses, and (3) extrinsic species can passivate intrinsic defects. However, because of the complexity of the defect chemistry, particularly in a quaternary polycrystalline material, theoretical calculations are often unable to predict the exact energetic position of defects

within the gap, which elements will be beneficial or detrimental, whether a species will passivate grain boundaries, what quantities are beneficial, etc. Therefore, to rapidly and rationally advance the development of kesterite materials, we have designed and built a combinatorial deposition instrument. This instrument allows us to bring solution-phase combinatorial techniques to bear to discover regions of favorable defect chemistry, impurity compensation, doping, and low SRH recombination rates.

The combinatorial instrument is comprised of a Sonotek Exactacoat ultrasonic spray coating system with XYZ translation. The system is completely contained inside a controlled atmosphere glovebox which we have enlarged to accommodate the instrument and fitted with all the necessary electrical and pneumatic feedthroughs. The ultrasonic nozzle is mounted above a hot plate, and can be entirely computer controlled. From the manufacturer the system is designed to receive a liquid feed from a single syringe pump. However, to enable combinatorial experiments we have modified the system to accommodate 6 independently computer-controlled syringe pumps which are fed to a zero dead-volume rotary mixer. The pumps have been integrated into the system such that they can be directly triggered by the spray coater and thus synchronized with the nozzle. Further, the axial and radial dispersion of molecular species within the fluid delivery system has been modeled by Dr. Steven Gaik, allowing for the deposition of precisely controlled material gradients. For safety, we have incorporated an emergency interlock system which is tied to the glovebox oxygen sensor. Our calculations show that even under continuous spray conditions for several hours, we will not reach to lower explosive limits of any of the solvents used, but if the oxygen content unexpectedly increases all power to non-essential systems is shut off, and remains off until the oxygen content reaches safe levels.

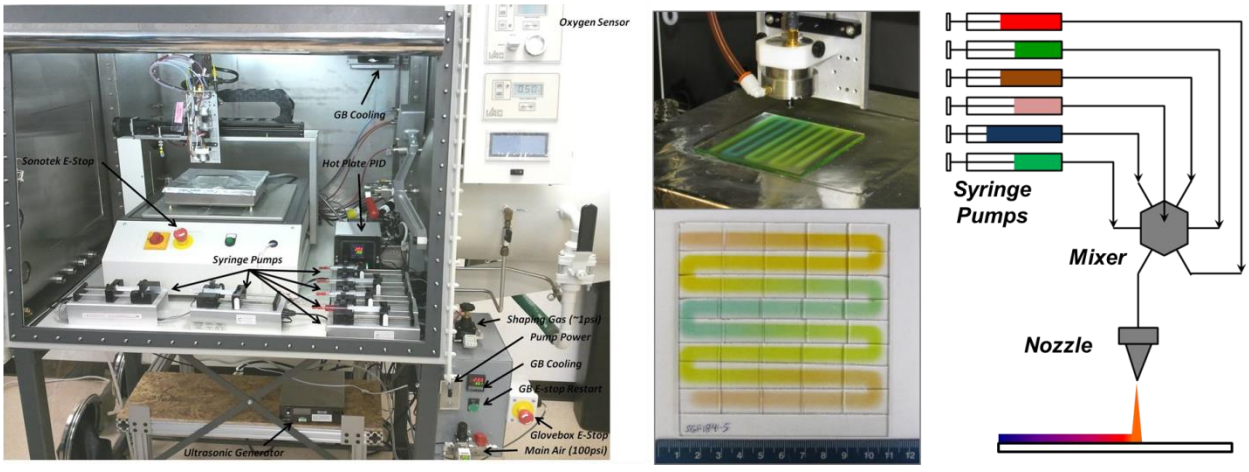

Figure 3.3 Picture showing the combinatorial spray coater housed in a customized glovebox (left) and diagrams illustrating the operation of the system (right).

The combinatorial spraying system can be operated in at least two modes to create either regions of uniform composition and thickness or continuous composition gradients. A typical spray line is about 5 mm wide, so in theory a 4"x 4" substrate can yield roughly 400 separate 5 mm x 5 mm devices. For a composition gradient, a wide variety of pump profiles are possible. In the simplest case, we use only two syringe pumps; one containing solution A and another containing species B. As the nozzle rasters over a substrate, the flow rate of solution B increases from 0 to 100% while the flow rate of solution A decreases from 100 to 0%. In doing this, we create a continuous gradient going from 100% solution A to 100% solution B. In such a film, the number of different "samples" or compositions probed is limited only by the spatial resolution of the characterization technique and the width of a spray line. Further, because this technique is general, it can be applied to any solution processable material. Although we have developed the system with the goal of advancing kesterite materials, it can easily be used to study other materials such as CIGSe, CdTe, or even the recently developed organo-metal halide perovskites.

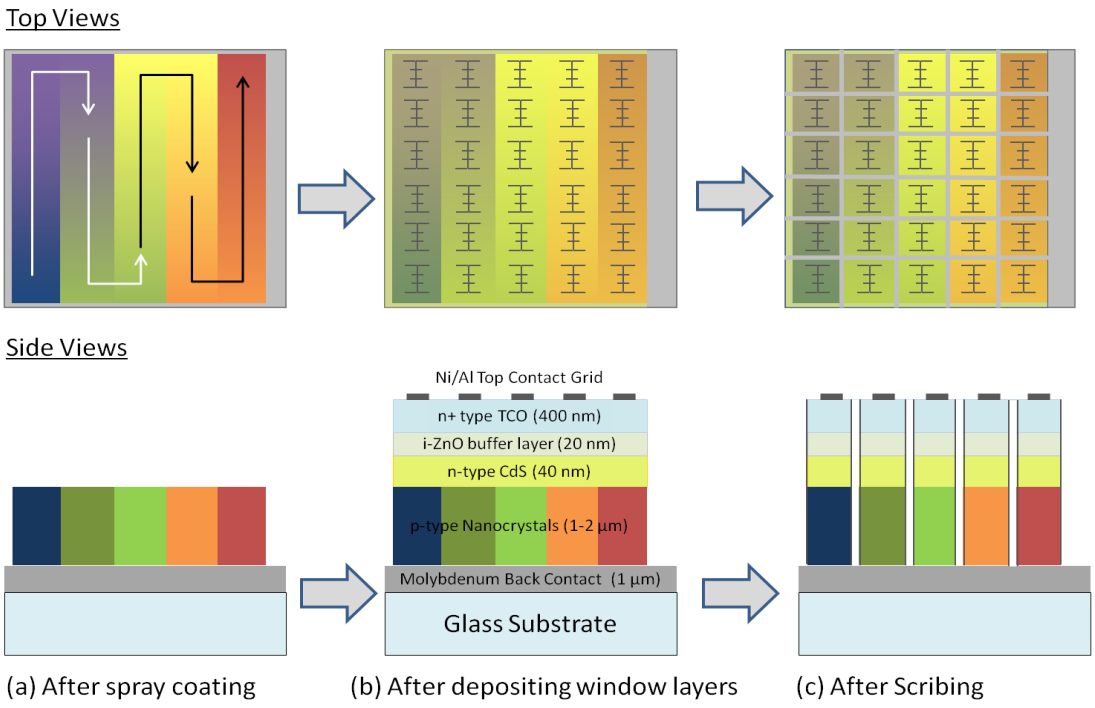

Figure 3.4 Schematic showing the use of the combinatorial spray-coating system to explore a large number of compositions for a nanocrystal-ink based thin film solar cell. The top row is a top-view while the bottom row is a side view.

3.6 Development of an Absolute Intensity Photoluminescence Technique

There are an incredibly large number of fundamental studies that can be conducted quickly using our high-throughput deposition tool. However, to gain the maximum utility from this system, we also need a characterization technique that is capable of rapidly screening the materials deposited by this system and analysis techniques that can process the resulting data. For this purpose we have developed an absolute-intensity photoluminescence (AIPL) mapping tool. Photoluminescence is a very powerful tool for evaluating material quality and using this technique we are able to measure spot sizes of 100 μm. Thus by combining optical characterization with a 5 mm width spray line, we can measure 20,000 different compositions on the same substrate. However, without automation, this would require making 20,000 measurements and processing 20,000 datasets. Thus, in the following I will briefly outline the tools I have developed for the automated analysis of combinatorial gradients.

The AIPL mapping instrument is a Horiba LabRam HR that has been calibrated using a NIST-certified blackbody source. By utilizing the known blackbody spectrum, we have determined the spectral response of all the optical components in the system. This allows us to convert the arbitrary intensity measured by the CCD into an absolute photon flux, which is a pre-requisite for extracting the quasi-Fermi level splitting and full spectral fitting of the photoluminescence spectra (discussed in Chapter 5.2).

Using the LabSpec software provided with the instrument, we are able to automate the collection of the AIPL data. To process the data, I have developed a Mathematica notebook. This notebook takes the experimental data, performs a background subtraction, spectrally corrects the data, and then extracts a number of parameters useful for quantifying materials properties. Because the maps require 12-24 hrs to collect, there can be numerous changes in the ambient lighting environment (e.g. sunrise/sunset or lab lights being turned on or off) and drift in the laser intensity. To minimize the impact of these issues, the code utilizes a periodic background subtraction. The mapping proceeds in rows moving horizontally across the substrate, at the end of each row, a background spectrum is collected. This background is subtracted from each of the data points in the row prior to extracting any parameters. The parameters extracted by the notebook include: the position of the peak maximum, the peak full-width-at-half-maximum, the individual half-widths-at-half-maximum, the peak asymmetry, the integrated intensity, and the quasi-Fermi level splitting. The quasi-Fermi level splitting may be determined either by a full spectral fitting of the AIPL data (in which much more data is also recovered, discussed in Chapter 5.2) or from a fit to the slope of the high energy tail. To ensure that the fit accurately represents the data, an

R-squared value is also included. Through optimization of this processing algorithm, I have been able to reduce the time to process ~2000 data points from 30+ minutes to only 1 minute (a full spectral fit still takes longer).

3.7 Summary and Conclusions

From the development of both CIGSe and CdTe, we have learned several important lessons: (1) variation of native elements can have a profound impact on the optoelectronic properties, (2) band gap grading can greatly reduce interfacial losses, and (3) extrinsic species can passivate intrinsic defects. However, because of the complexity of the defect chemistry, particularly in a quaternary polycrystalline material, theoretical calculations are often unable to predict the exact energetic position of defects within the gap, which elements will be beneficial or detrimental, whether a species will passivate grain boundaries, etc. Therefore, to rapidly and rationally advance the development of kesterite materials, I have designed and built equipment and developed procedures for the combinatorial screening of solution-processable materials. The equipment includes a customized ultrasonic spray coater which is capable of depositing films with continuous composition gradients, a calibrated absolute intensity photoluminescence instrument, and Mathematica notebooks that can rapidly process the data and extract quantitatively accurate metrics of material quality.

Chapter 4.

STOICHIOMETRY CONTROL AND FORMATION PATHWAY OF Cu_2ZnSnS_4 AND Cu_2ZnGeS_4 NANOCRYSTALS

4.1 INTRODUCTION

In recent years, kesterite structured $Cu_2ZnSn(S,Se)_4$ materials have attracted significant interest for thin film solar cells. Due to the high crustal abundance of the constituent elements, low cost, and rapidly improving efficiency, they have emerged as promising alternatives to $Cu(In,Ga)Se_2$ and CdTe. Kesterite materials have been deposited using a wide range of techniques, but many of the highest efficiency devices have been made using solution processing techniques. Solution-phase techniques can provide low-cost, high-throughput, and highly scalable routes to thin film solar cells. The current record efficiency of 12.6% was deposited using a hydrazine-based process,[1] but devices with efficiency as high as 9.85%[352] have been achieved by sintering sulfide nanocrystals in a selenium environment. Nanocrystal-ink based routes are appealing because the elements can be arranged with the proper structure and composition prior to film formation, and thus can reduce the need for solid-state diffusion and avoid the formation of volatile phases (such as SnS) or kinetically stable secondary phases (such as Cu_2SnS_3). However, the formation of CZTS nanocrystals with controlled composition and proper crystalline structure is a non-trivial task. Structural characterization of kesterite materials is known to be difficult,[353, 354] and the quaternary nature of the material makes studying nucleation and growth even more complex. The first published report using CZTS NCs for photovoltaic (PV) applications was reported by Guo et al. in 2009,[355] followed shortly thereafter by Steinhagen et al.[100] There have been many syntheses reported since then, but only a few publications have sought to elucidate the underlying formation mechanism.

One of the most heavily studied CZTS NC syntheses is the heat up reaction of metal precursors in a mixture of fatty amines and alkythiols.[356-362] Several publications have studied the formation pathway of this synthesis,[356-359] including one using surface enhanced Raman spectroscopy (SERS) to improve detection of secondary phases.[359] The authors have all proposed a formation mechanism wherein Cu_xS nucleates first, then both Zn and Sn interdiffuse, and eventually wurtzite CZTS is formed. A variety of parameters impacting this synthesis have been investigated, including the precursor concentration,[356]

precursor reactivity,[359] reaction temperature,[363] reaction time,[356] the coordinating solvent,[358] and the concentration of alkylthiol.[359, 361, 364] For photovoltaic applications where the NCs are sintered or selenized to form a kesterite thin film, it is unclear if the synthesis of wurtzite particles is acceptable. Despite a superior understanding of the synthesis, the best photovoltaic devices made from wurtzite NCs (4.3%)[362] are less than half as efficient as those made from a less-studied synthesis of kesterite NCs (9.0%).[115] The cause for this difference is unclear, and is complicated by the fact that very little is known about what NC properties (particle size, shape, phase, ligand, etc.) are important for producing efficient solar cells. One effect that is known to strongly affect photovoltaic device performance is the composition of the absorber layer.[365] Slight changes in the composition of the absorber layer can significantly alter the favorability of certain intrinsic defects and defect complexes, dramatically impacting device performance. Despite this, most published methods of controlling composition are heuristics based on changing the ratio of the starting precursors added to the reaction. These heuristics are rarely elaborated, can result in low reaction yields, fail to provide any insight into the reaction, and are not always effective. To address this shortcoming, we have investigated the effect of reaction time and precursor choice on the formation of CZTS NCs. We pay particular attention to the average composition of different NC size fractions obtained by size-selective precipitation. From this we determine the temporal evolution of ink composition and propose a formation pathway. This study provides a means to reproducibly produce nanocrystal inks with a specific composition using a synthetic pathway which has previously demonstrated an 8.4% efficient device.[366]

4.2 Materials and Methods

4.2.1 *Nanocrystal Synthesis*

All of the precursors were obtained from Sigma Aldrich in the highest purity available and were used without additional purification. To ensure maximum reproducibility, all reagents were stored and weighed out in a glovebox with O_2 and H_2O less than 10ppm. Nanocrystals (NCs) were synthesized by the hot injection method using oleylamine (technical grade, 70%) as the sole solvent and ligand. A standard synthesis consisted of 1.37 mmols copper(II) acetylacetonate (99.99%), 0.865 mmols zinc(II) acetylacetonate hydrate (99.995%), and 0.75 mmols tin(IV) bisacetylacetonate dichloride (98%). The precursors were added to a three-neck flask, 11 mL of oleylamine was added, then the flask was sealed with rubber septa and transferred out of the glovebox. The flask was quickly connected to a schlenk line where it was heated to 130°C under vacuum and held for 1 hour, cycling to atmospheric pressure with argon every 20 minutes and then returning to vacuum. After de-gassing, the solution was heated to

225°C and stabilized. Then 4mL of a 1 M sulfur in oleylamine solution was injected. The reaction timer was started immediately following the injection. After the set reaction time, the flask was removed from the heating mantle and allowed to cool naturally.

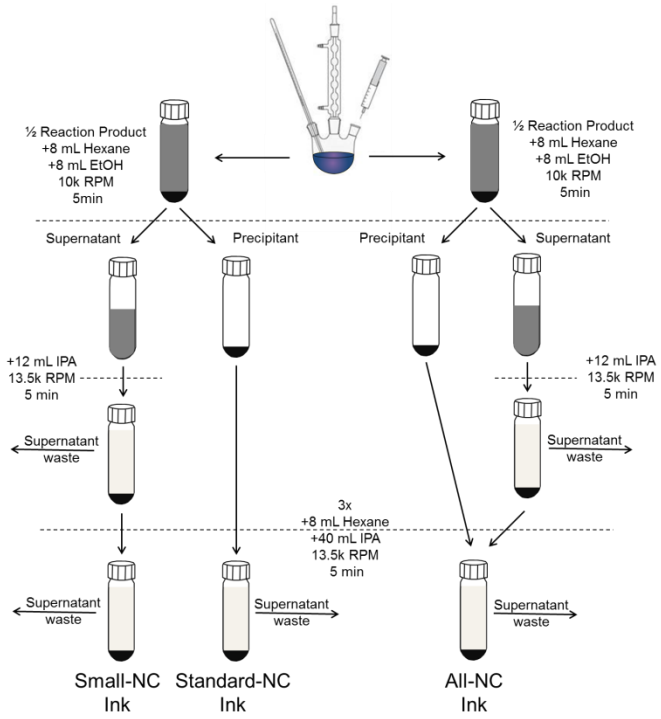

Figure 4.1 Schematic showing the precipitation process used to collect the Standard-NC, Small-NC, and All-NC fractions. Typically, for device making the Standard-NC fraction is used and the Small-NC fraction is discarded. The All-NC fraction is a combination of the Standard-NC and Small-NC fractions.

4.2.2 *Nanocrystal Precipitation*

Three different particle fractions were isolated from the nanocrystal reaction mixture using size selective precipitation. The process is shown schematically in Figure 4.1. The reaction mixture (15 mL) was agitated and split equally between two 30 mL centrifuge tubes. 8 mL of hexane (good solvent), then 8 mL of ethanol (poor solvent), were added to each tube. The solutions were mixed and then centrifuged at 10,000 RPM for 5 min. The supernatant was poured off of one of the solutions leaving behind the "Standard-NC" fraction. The Standard-NC fraction is typically used for device making, and contains the largest particles on average. The supernatant poured off the Standard-NC fraction was split between two 30 mL tubes. 6 mL of isopropanol (IPA, very poor solvent) was added to each tube, and then they were centrifuged at 13,500 RPM for 5 min to collect the "Small-NC" fraction. As the name implies, the Small-NC fraction contains the smallest particles. The "All-NC" fraction was collected following the same procedures, except the "Small-NC" fraction was not poured off of the "Standard-NC" fraction. Thus the All-NC fraction is a combination of the Standard-NC and Small-NC fractions. Once each size

fraction was isolated the particles were washed by repeatedly re-suspending the fraction in 4mL hexane then adding 20 mL isopropanol and centrifuging. Following the final precipitation, the nanocrystals were dried, weighed, and then re-suspended in hexanethiol at a concentration of 200 mg/mL to make the final NC inks.

4.2.3 *Composition and Structural Characterization*

For composition analysis, energy dispersive spectroscopy (EDS) was performed on films from each of the three particle fractions. Samples were prepared by doctorblading the NC-inks onto molybdenum coated soda lime glass (Mo/SLG) then drying on a hotplate at 300 °C for 1 min. This process was repeated twice for each film. EDS data were collected using a scanning electron microscope with an accelerating voltage of 20 keV. Data were averaged over a minimum of 8 distinct regions, each >500µm2. Raman scattering and x-ray diffraction (XRD) were performed on samples dropcast onto soda lime glass (without Mo) and allowed to dry overnight under gentle heating (~50 °C). The Raman spectra were collected using a Horiba LabRam HR with 532 nm laser excitation. Solution phase UV-Vis-NIR absorption spectra were collected from nanocrystals dispersed in hexane using a dual beam Perkin Elmer Lambda 1050 Spectrometer.

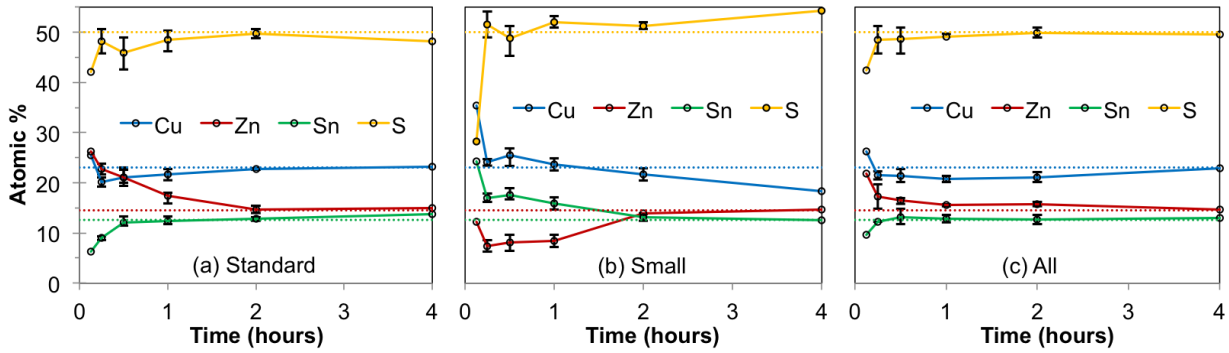

Figure 4.2 Change in the composition of the NC ink over the first 4 hours of reaction for the (a) Standard-NC, (b) Small-NC, and (c) All-NC fractions. The dashed lines indicate the starting values for the precursors (considering only the metal and chalcogen atoms). Data were averaged over multiple independent syntheses with error bars indicating the maximum range observed.

4.3 Results and Discussion

4.3.1 *Temporal Evolution of Ink Composition*

The change in composition as a function of reaction time is shown in Figure 4.2 for each size fraction. Figure 4.3 shows the same data using the cation ratios Cu/(Zn+Sn) and Zn/Sn. Here we emphasize that

we are measuring the average composition of the inks, not the composition of the individual particles. By comparing the cation ratios of the fractions it is clear that there are considerable composition differences between the biggest and smallest particles. In reactions less than 0.5 h, the Small-NC fraction is both Cu-rich and Sn-rich while the Standard-NC fraction is very Zn-rich. The heterogeneity between these size fractions means that the particle precipitation process will have a substantial impact on the average composition of the resulting ink. An aggressive precipitation process, such as that used for the All-NC fraction, may produce an ink that closely reflects the composition of the starting precursors, but it will be comprised of very disparate particles. The All-NC fraction accurately represents a weighted average of the Standard and Small fractions, and thus serves as a secondary validation of the measured compositions. Because the Standard-NC fraction is typically the major fraction (by mass), the All-NC fraction tends to follow the same trends as the Standard-NC fraction, but the composition is shifted to higher Cu/(Zn+Sn) and lower Zn/Sn by the addition of the Cu/Sn-rich particles in the Small-NC fraction. However, after about 2 h of reaction the mass of the Small-NC fraction becomes so small it no longer appreciably changes the average composition. This can be inferred from Figure 4 as the difference between the mass yield of the Standard-NC and All-NC fractions.

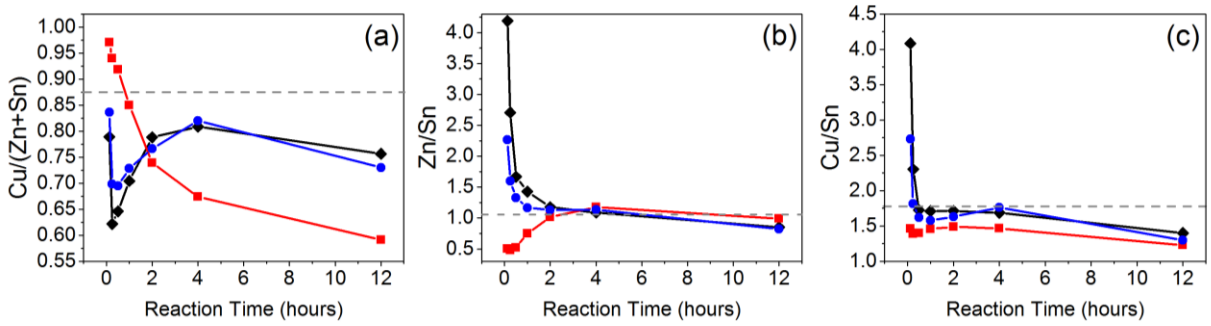

Figure 4.3 Change in the cation ratios as a function of time for the Standard-NC (black diamonds), All-NC (blue circles), and Small-NC (red squares) fractions. The dashed line indicates the starting value for the precursors. Composition was determined using EDS.

Using the combination of mass yield and the temporal changes in composition, we are able to discern two distinct stages in the evolution of the particles. The first stage is the nucleation and growth. It starts with the injection of sulfur and lasts for about 0.5 hr. After 0.5 h of reaction time, the mass yield (Figure 4.4) reaches a plateau near the theoretical maximum indicating that almost all the free precursor has been consumed. Changes in particle size and composition still occur beyond this time, but via the much slower Ostwald ripening mechanism. The transition can also be seen in the composition profiles (Figure

4.2ac) as a sharp decrease in the slopes of the individual composition lines in both the Standard-NC and All-NC fractions.

Figure 4.2 shows that during the first 0.5 h of reaction the Standard-NC fraction contains about equimolar quantities of Cu and Zn but very little Sn. Over time the concentration of Cu and Zn both decrease as Sn is incorporated, suggesting that the earliest particles may be both Cu_xS and ZnS (or a Cu-Zn-S compound). If pure Cu_xS formed first, as previous reports using the heat-up method found,[356-358] we would expect the Cu concentration to be significantly higher than that of Zn since the precursor concentration is about twice as high. We would also expect to see a region in the Standard-NC fraction where the Cu concentration decreases as the Zn concentration increases. We do not see either of these effects in our data, but it is possible that the kinetics of Zn addition are more rapid than our sampling time.

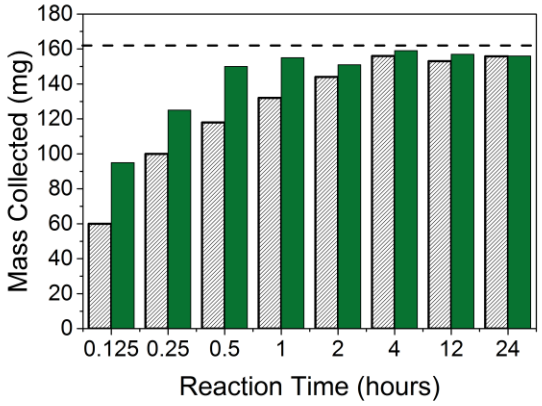

Figure 4.4 Mass collected from the Standard-NC (hashed grey) and All-NC (solid green) fractions. Theoretical yield is about 162 mg for each fraction. We calculate less than 10 mg of additional mass from the coordinating ligands.

The low Cu-content in the Standard-NC fraction following injection may be explained by looking at the temporal changes of the Small fraction. As shown in Figure 4.2, the small fraction is both Cu- and Sn-rich during the first 0.5 h., and the Cu:Sn ratio of the Small fraction remains approximately constant at 1.44±0.05. These observations suggest that Cu preferentially interacts with Sn in the reaction mixture, possibly forming a Cu-Sn-S compound or alloy particle. At the reaction temperature, Cu_3Sn and Cu_6Sn_5 are known to be stable alloys,[367] and ligands are known to have a stabilizing effect on metastable phases. Regardless, the interaction of Cu and Sn seems to reduce the amount of free Cu available for nucleation, and generates a secondary particle population. To reach the target composition, these

particles/complexes must be ripened into the larger (Zn-rich) particles. This behavior has not been reported in previous syntheses, but has a profound impact on the temporal evolution.

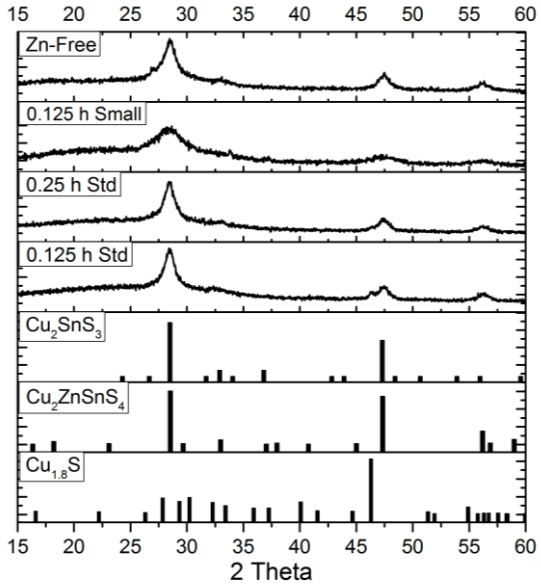

Figure 4.5 X-ray diffraction spectra from dropcast (unheated) nanocrystals. We only observe a peak associated with a secondary phase, Cu_xS, in the 0.125 h Standard-NC reaction spectra.

It is possible that using the hot-injection method increases the interaction of Cu with Sn. The species are allowed to freely interact in a hot solution of oleylamine for almost an hour prior to injection of sulfur. This may alter the formation pathway and explain why we observe so much Zn in the early particles. In the heat-up method, a strong coordinating ligand (such as an alkylthiol) is present even at low temperatures and can bind the metal precursors, preventing the interaction of Cu and Sn. As the temperature is ramped, Cu_xS forms first because it has the lowest formation energy. However, with the hot injection method, we can bypass the temperature at which the nucleation of only Cu_xS would occur and reach conditions where the nucleation of other species is favorable. Thus, even if the nucleation of Cu_xS is most favorable, some ZnS may also nucleate, particularly if the effective free Cu concentration is being reduced as a result of the interaction with Sn. In the XRD (Figure 4.5) and UV-Vis-NIR absorption data (Figure 4.11), we do find some evidence of a Cu_xS phase, however because of the well-known overlap of ZnS peaks with those of kesterite Cu_2ZnSnS_4 and Cu-Sn-S phases such as Cu_2SnS_3 we cannot distinguish these phases.[131, 368]

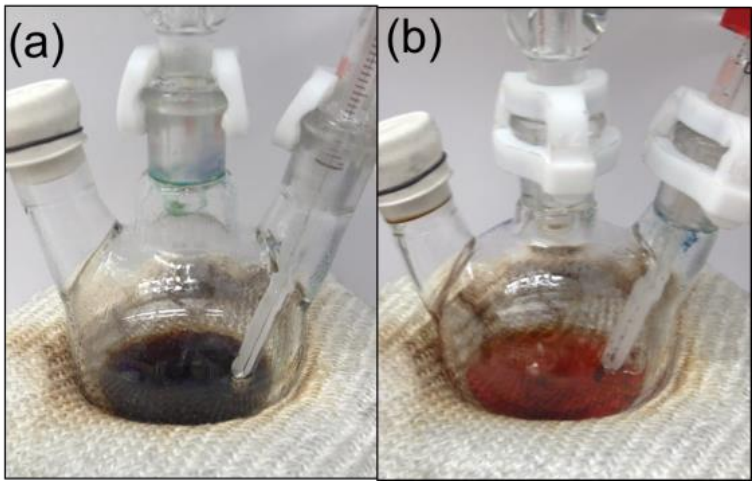

Figure 4.6 Photograph of two nearly identical syntheses at the same time during heat-up prior to sulfur injection. (a) Standard synthesis. (b) Standard reaction precursors with the exception of $ZnCl_2$ substituted for $Zn(acac)_2$•H2O. Note that the color changes with various precursor substitutions are summarized in Table 1.

TABLE 4.1 SUMMARY OF OBSERVED SOLUTION COLORS PRIOR TO INJECTION OF SULFUR WHEN USING SUBSTITUTING SELECT PRECURSORS.

Precursor Substitution(s)	Color Before Injection
None	Dark brown solution
Cu(I)Cl	Orange to yellow translucent
$Cu(II)Cl_2$ & $Sn(IV)Cl_4 \cdot 5H2O$	Orange to yellow translucent
$Sn(IV)(acac)_2Br_2$	Dark brown solution
$Zn(II)Cl_2$	Orange then dark brown
$Sn(IV)Cl_4$	Orange to yellow translucent
$Ge(IV)Cl_4$	Red translucent

4.3.2 *The Effect of Precursor*

The baseline synthesis employs $Cu(II)(acac)_2$, $Zn(II)(acac)_2$, and $Sn(IV)(acac)_2Cl_2$ dissolved in oleylamine. Initially, the solution is opaque light blue due to undissolved copper acetylacetonate, but upon heating, the precursor dissolves creating a deep translucent blue solution that slowly changes to dark brown. When heated in oleylamine independently, the precursor $Cu(II)(acac)_2$ transitions from blue to dark green while both $Zn(II)(acac)_2$, and $Sn(IV)(acac)_2Cl_2$ remain colorless. One conceivable explanation is that the dark brown color observed prior to injection is due to the formation of alloy

nanoparticles. Should such a species exist, we would expect that it would have a significant impact on nucleation and growth and could be the source of the small Cu/Sn-rich particles. We have unsuccesfully attempted to isolate these particles by heating the reaction mixture without injecting sulfur, but we were unable to isolate any stable species. Therefore, to further investigate this possibility, we have also synthesized nanocrystals by substituting the precursors Cu(I)Cl , $Cu(II)Cl_2$, $ZnCl_2$, $Sn(IV)Cl_4$, $Sn(acac)_2Br_2$, and $Ge(IV)Cl_4$ for the copper, zinc, and group IV precursors, respectively. Unlike the baseline synthesis, all syntheses employing alternative precursors produced translucent (but colored) solutions prior to the injection of sulfur, except $Sn(acac)_2Br_2$ and $ZnCl_2$. Substituting $ZnCl_2$ initially resulted in a transparent orange solution, as shown in Figure 4.6, but upon further heating it changed to brown. As summarized in Table 1, changing either the Cu or Sn precursor resulted in a translucent solution, but changing the Zn precursor did not, indicating that the color results from interaction of Cu and Sn.

The above observations show that the choice of reactant has an impact on the chemical state of the precursors prior to injection. However, the substitution of alternative precursors was found to have very little impact on the composition of the Standard-NC and Small-NC fractions, as summarized in Figure 4.7. We do observe some variation in composition between different precursors, but these effects are small when compared to the effect of reaction time, and are most likely the result of slight variation in reaction time (particularly cool down), temperature dynamics following injection, and small variations in the precipitation procedure. The rate of change in the Zn/Sn ratio is very rapid for short reaction times (0.20/min between 0.125 and 0.25 h), thus even small variations in reaction time can lead to cause significant difference in the cation ratios. Therefore, even though inks with a desired composition (but large heterogeneity) can be produced using shorter reaction times and an aggressive precipitation, longer reaction times are more desirable because they reduce the processing sensitivity.

Increasing the reaction temperature has a similar effect to reaction time. We find that reactions times of 0.5 h and 1.5 h at 250 °C produce inks with composition comparable to that of 2 h and 12 h of reaction at 225 °C, respectively. In the latter case, it may not take the full 12 hours to reach the final composition at 225 °C. However, the fact that all of the precursors show the same growth kinetics at 225 °C suggests that the composition evolution is not limited by the reactivity of the metal precursors but rather the slow dissolution of smaller particles. Similarly, the fact that solutions employing $GeCl_4$ show the same growth kinetics is surprising, but agrees with our observation that the Group IVA element (Sn or Ge) is not involved in nucleation.

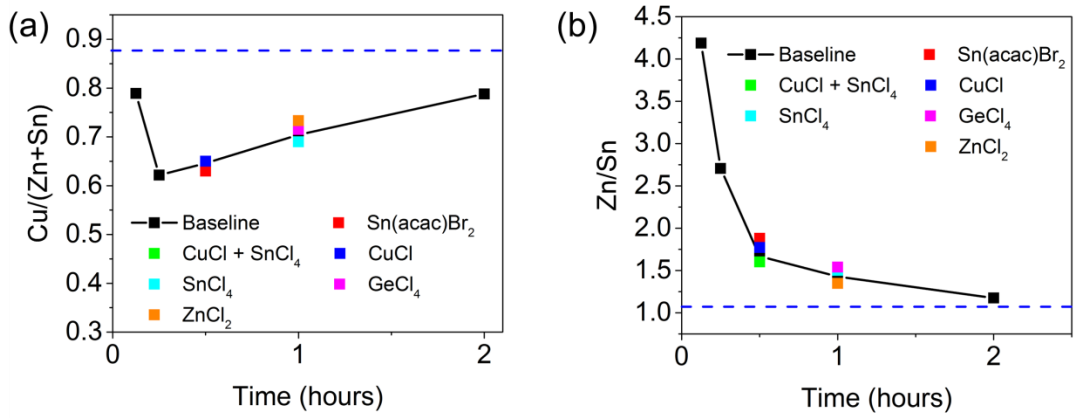

Figure 4.7 Cation ratios of the Standard-NC fraction obtained when substituting alternative precursors. The differences in composition most likely result from slight variation in reaction and precipitation procedure, not precursor reactivity.

4.3.3 *Particle Characterization*

Based on the composition data it is clear that there is significant heterogeneity among the different particle fractions, but the exact nature of the particles that comprise these size fractions is still unclear. To better understand these particles we have characterized the different size fractions using UV-Vis spectroscopy, TEM, and Raman spectroscopy.

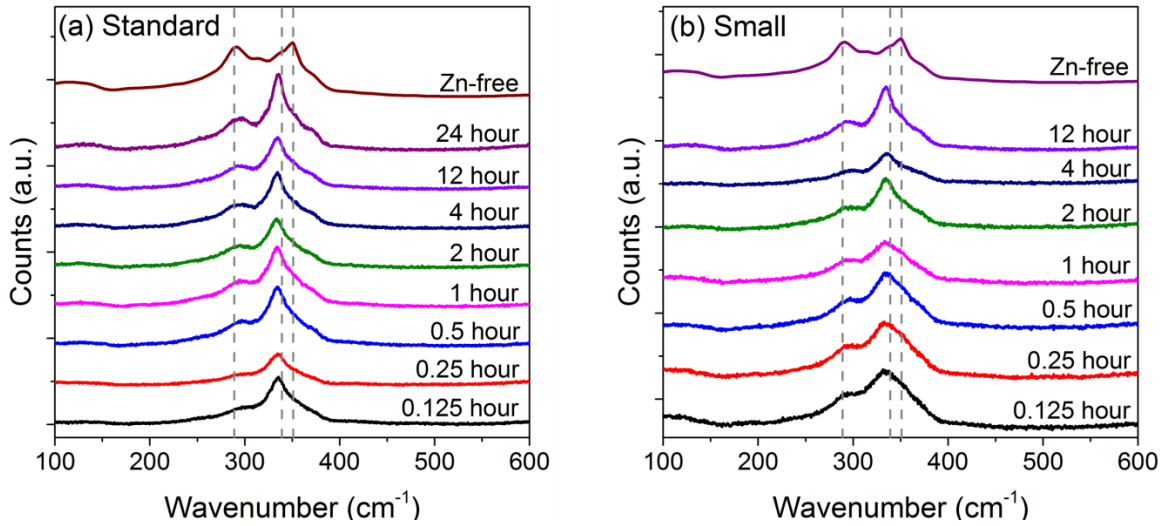

Figure 4.8 Raman spectra from the (a) Standard-NC and (b) Small-NC inks with different reaction times. All of the samples had peaks consistent with previously reported values for Cu_2ZnSnS_4 (289 and 339 cm^{-1}) Shown as a reference is the synthesis performed without Zn precursor ("Zn-free") which has peaks corresponding to monoclinic Cu_2SnS_3 (289 and 351 cm^{-1}).

The Raman spectra of the Standard-NC and Small-NC fractions are shown in Figure 4.8. The Standard-NC fraction has sharper peaks than the Small-NC fraction, but both are relatively broad, reflecting the nanocrystalline nature of the materials. We have not observed any ZnS modes even in samples with very large Zn excess. This may be explained by the fact that Raman scattering from ZnS is not easily detected without UV laser excitation.[133] The peaks observed for all of the Standard-NC and small-NC fraction generally correlate with those expected for kesterite CZTS at 289 and 339 cm^{-1}. [131, 134, 368] Interestingly, the Raman spectra does not change significantly despite large deviations from stoichiometric. This suggests that the signal may originate from either a kesterite Cu_2ZnSnS_4 phase that exists among undetected secondary phases, or a tetragonal $(ZnS)_x(Cu_2SnS_3)_{1-x}$ alloy. Due to the breadth of the peaks and the similarity of the spectra, we cannot rule out that the peaks result from tetragonal Cu_2SnS_3, which has peaks at 297 and 337 cm^{-1}.[131, 134, 368] To test this hypothesis, we performed an identical NC synthesis omitting only the Zn-precursor. The Raman spectrum from the "Zn-free" synthesis is shown at the top of Figure 4.8ab. The peaks correspond very well to those reported for monoclinic Cu_2SnS_3[369] at 289 and 351 cm^{-1}, an assignment which is consistent with the XRD (Figure 4.5) and UV-Vis-NIR absorption data (discussed below). Therefore, the primary Raman signal we observe in the Standard-NC fraction likely is not from tetragonal Cu_2SnS_3 since the formation of monoclinic Cu_2SnS_3 is favored under our reaction conditions. Minor features corresponding to those observed in the Zn-free synthesis are visible in almost all the spectra. Therefore, we conclude that some monoclinic Cu_2SnS_3 particles may be present but the dominant peak located near 339 cm^{-1} does not result from Cu_2SnS_3.

TEM images of the nanoparticles at different reaction times are shown in Figure 4.9. In general we see that the inks are quite polydisperse, but with time the mean particle size increases and the shapes become more homogeneous (histograms are provided in SI). Oleylamine and other fatty amines are known to have an "activating" effect on precursors,[370] and given the absence of any additional tightly binding ligands we should expect a large degree of polydispersity. Adding a strong ligand such as trioctylphosphine oxide (TOPO) could yield better control over particle size and shape, but may have unintended consequences. For applications where the NCs will be decomposed to form a bulk film, producing highly monodisperse particles is likely to be less important than having ligands that can be easily eliminated from the film during sintering.

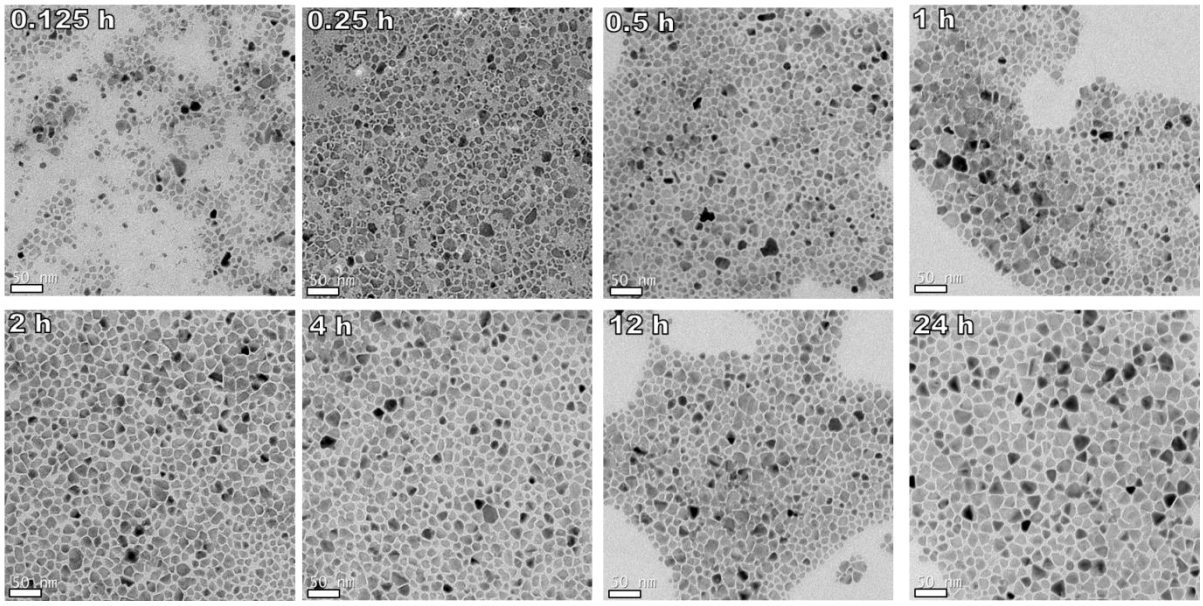

Figure 4.9 TEM Images from the Standard-NC fractions with different reaction times. The particles generally increase in size and become more regular with increasing reaction time. All images were taken at the same magnification. The scale bar is 50 nm. Refer to SI for size histograms.

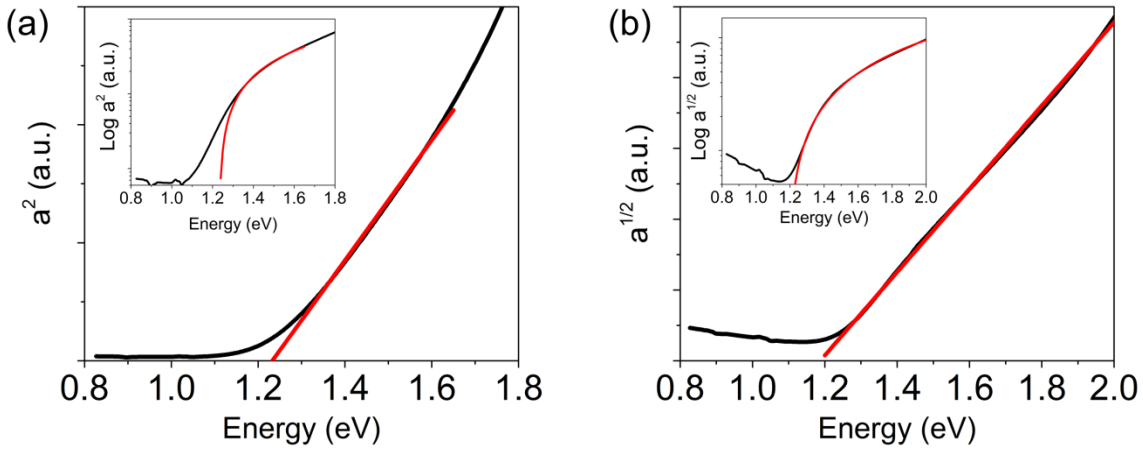

Figure 4.10 Absorption spectra from the 1 hour Standard-NC (a) and Small-NC (b) size fractions. Shown in the inset of each is the fit plotted on a logarithmic scale. The Standard-NC particles were best described by a direct transition while the Small-NC particles were best described by an indirect transition.

We have used a least squares fitting of the absorption onset to approximate the band gap of the different inks. The absorbance spectra from the Standard-NC fraction were best fit by linear extrapolation of α^2 versus energy (e.g. $\alpha \propto (h\nu\text{-}Eg)^{1/2}$), indicating a direct allowed transition.[371] The same type of transition did not produce accurate fits for the Small-NC fraction, but extrapolation of $\alpha^{1/2}$ versus energy did (e.g.

$\alpha \propto (h\nu - Eg)^2$). Such an exponent is characteristic of an indirect allowed transition,[371] and indicates that the particles in the Small-NC fraction are fundamentally different than those in the Standard-NC fraction.

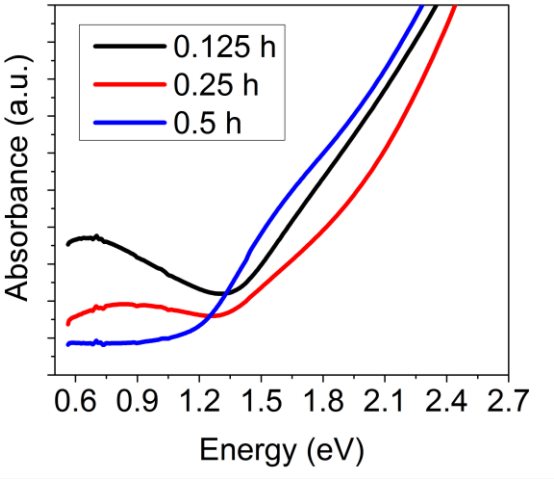

Figure 4.11 Absorption spectra from the Standard-NC size fraction with different reaction times. A low energy absorption feature is clearly evident and may result from Cu_xS localized surface plasmon resonances.

We observe a notable low energy absorption peak in the 0.125 h and 0.25 h Standard-NC spectra, as shown in Figure 4.11. We believe this peak results from localized surface plasmon resonances (LSPR) originating from Cu_xS particles. Such resonances were reported by Liao et al.[357] in a previous study on CZTS, and the phenomena has also been reported in syntheses of Cu_xS.[372-374] The band gaps we extract, summarized in Table 2, are consistent with the range of values reported for Cu_xS. This evidence, along with the XRD and composition data strongly suggests that Cu_xS is indeed present. The fact that we do not observe a band gap near 1.45 eV does not necessarily exclude the presence of kesterite CZTS in the ink, it simply indicates the presence of a smaller band gap material. The absorption onset could also result from tetragonal Cu_2SnS_3[375] or tetragonal $(ZnS)_x(Cu_2SnS_3)_{1-x}$ alloy particles.[376, 377] However, as discussed above, characterization of the Zn-free synthesis suggests that monoclinic, not tetragonal, Cu_2SnS_3 is favored under our synthesis conditions.

TABLE 4.2 BAND GAP OF THE NANOCRYSTAL DETERMINED USING A LEAST SQUARES FIT TO THE ABSORPTION ONSET.

Rxn Time	Eg Standard (eV)	Eg Small (eV)
0.125 h	1.29	1.19
0.25 h	1.31	1.18
0.5 h	1.30	1.23
1 h	1.23	1.19
2 h	1.14	1.19
4 h	1.11	1.26
12 h	1.13	1.30
24 h	1.20	--

4.3.4 *Synthesis of Inks with Precise Off-Stoichiometric Composition*

The ability to produce inks with precisely controlled composition is important because previous work has shown that composition has an enormous effect on device performance and that specific off-stoichiometric compositions are necessary for good device performance.[365, 378] In addition, the ability to produce inks of specific off-stoichiometric compositions can enable combinatorial screening and allow growth techniques that emulate the multi-stage co-evaporation method that has been effectively applied to grow record efficiency CIGSe (i.e. copper-rich grain growth followed by a copper-poor final stage).[379] We have shown above (Figure 4.2 and
Figure 4.3) that NC inks with longer reaction times more closely converge to the metal ratios of the added precursors. However, there is still an off-set, particularly with respect to copper. The Cu/(Zn+Sn) ratio of the NC ink with the Standard precipitation procedure is about 94% of the Cu/(Zn+Sn) ratio of the precursors added to the reaction flask after reacting for 4 hours at 225 °C. Applying this heuristic, we can see how specific off-stoichiometric compositions may be synthesized. As shown in Figure 4.12, the resulting inks have composition very close to the target. This demonstrates a means to rationally produce NC inks with specific off-stoichiometric compositions.

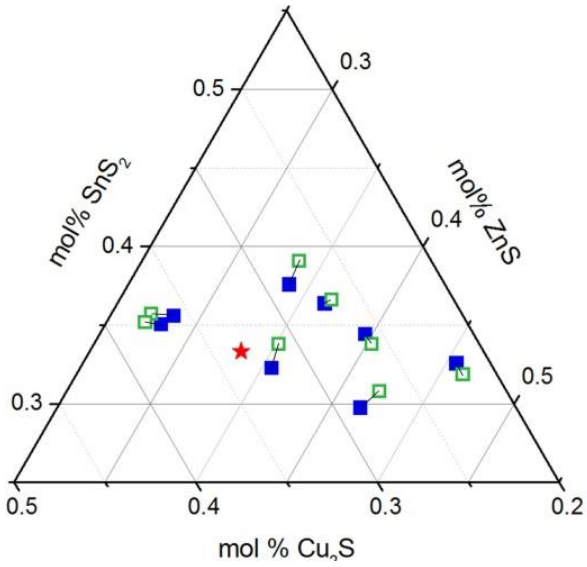

Figure 4.12 Ternary diagram demonstrating the ability to produce inks with precisely controlled off-stoichiometric compositions with a 4 hour reaction at 225 °C. Solid blue squares indicate the targeted composition (94% of the precursor Cu/(Zn+Sn) ratio) and hollow green squares indicate the actual ink composition. Lines connect the targeted and actual results. The red star indicates stoichiometric Cu_2ZnSnS_4.

4.3.5 *Combinatorial Screening of Compositional Effects*

By applying our new-found understanding of the synthesis we have been able to produce a continuous composition gradients via the combinatorial mixing of nanocrystal (NC) inks with different starting compositions. The cation ratios (Cu/(Zn+Sn), Zn/Sn) of the starting inks was determined using EDS to be (0.56, 1.48) and (1.28, 0.75). Inks were diluted with toluene to a concentration of 30mg/mL for combinatorial spray coating. Films were deposited using the custom built deposition system described in Chapter 2. The film is deposited onto Mo-coated soda-lime glass on a hot plate set to 250°C. Following deposition, the film is diced into approximately 1”x1” segments and then selenized in a tube furnace with excess selenium at 500°C for 20 min. The film is then coated with 50nm of CdS using chemical bath deposition immediately following annealing. After CdS deposition all time sensitive steps are assumed to be completed. The resulting films were characterized using a micro-PL instrument using a 785nm laser. PL data was collected over a 110 x 110µm spot size with a 1mm x 1.5mm mesh. Further detail about the PL instrument can be found in Chapter 2.

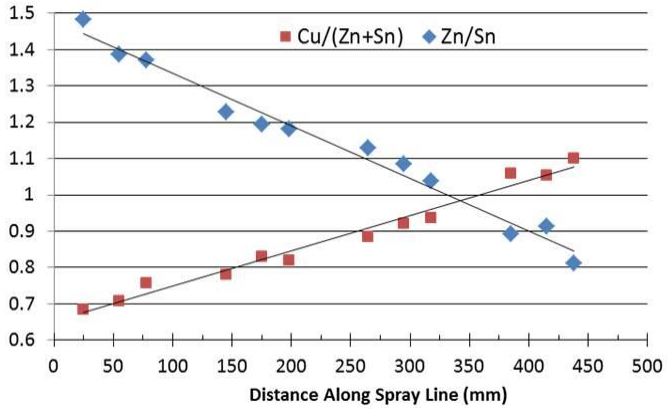

Figure 4.13 Cation ratios as a function of the distance along the spray line. Elemental analysis was performed using EDS. Lines are added as a guide to the eye.

Following deposition, the presence of a composition gradient in the selenized films was confirmed using energy dispersive spectroscopy (EDS) for 12 different points along the spray line and is shown in Figure 4.14a. Figure 4.14b shows a map of the PL intensity on the high energy tail of the PL peak for the compositionally graded film. Additionally, Figure 5 shows the average PL intensity at 1200nm of the 3 most intense points located laterally along a spray segment. From these two plots, the importance of absorber layer composition and the value of high-throughput experiments are clearly apparent. As expected, the PL intensity is highest in the approximate region (0.7, 1.4) – (0.9, 1.1) and dies off quickly beyond either extreme. This behavior is consistent with theoretical calculations, which predict that growth under Cu-poor/Zn-rich processing conditions favors the formation of the shallow V_{Cu} acceptor and the relatively benign defect complexes [Zn_{Cu} + V_{Cu}] and [$2Zn_{Cu}$ + Zn_{Sn}] while suppressing the formation of the relatively deeper Cu_{Zn} acceptor and detrimental defect complexes such as [$2Cu_{Zn}$ + Sn_{Zn}] [194]. Most importantly though, this data shows that we are able to clearly resolve trends in the optoelectronic properties using by depositing material gradients and characterizing them using photoluminescence.

4.4 CONCLUSIONS

In summary, we have determined the temporal evolution of Cu_2ZnSnS_4 nanocrystal ink composition. From detailed characterization of different particle size fractions over time, we find that at least two distinct particle populations form following injection of sulfur: large Cu and Zn containing particles and small Cu- and Sn-rich particles. XRD and absorption data indicating the presence of Cu_xS allow us to conclude that the formation pathway involves either the nucleation of Cu_xS followed by very rapid Zn

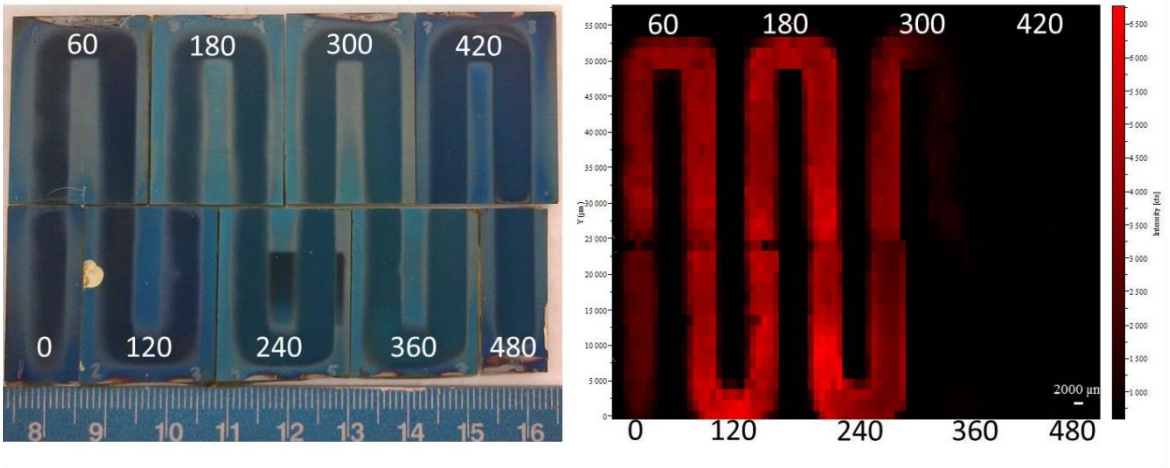

Figure 4.14 Photograph of the spray coated film with a continuous composition gradient,following chemical bath deposition (Left). Photoluminescence intensity map at 1200nm collected from the same film (right). The number at the top and bottom indicate the distance along the spray line in mm for reference to other figures.

addition or the simultaneous nucleation of both Cu_xS and ZnS. An unspecified interaction of Cu with Sn creates a secondary small particle fraction that has near constant composition for all reaction times. At short reaction times, the heterogeneity between these two particle fractions is very pronounced and as a result, the precise details of how the particles are precipitated can have an enormous impact on the composition of the resulting ink. Over time, ripening occurs and the population of small particles decreases resulting in an ink with larger particles, higher NC yield, and an average composition closer to that of the starting precursor ratios. Thus, a key finding of this study is that longer reaction times lead to a more reproducible reaction product. We have used this to demonstrate the ability to synthesize inks with specific off-stoichiometric compositions of Cu_2ZnSnS_4 and deposit continuous composition gradients. We have also investigated the impact of different metal precursors, and shown that the choice of precursor has relatively little impact on the dynamics of composition evolution even when substituting germanium for tin. These results are useful for the reproducibly fabricating solar cells from NC inks where precise control of composition is critical for managing intrinsic defects and for developing new NC based absorber growth methods that utilize Cu-rich or perhaps Sn-rich growth conditions.

Chapter 5.

THE EFFECT OF NANOCRYSTAL REACTION TIME ON SOLUTION-DEPOSITED $Cu_2ZnSn(S,Se)_4$ SOLAR CELLS

5.1 INTRODUCTION

The use of colloidal nanocrystals (NCs) as a precursor to a continuous thin film is a relatively new concept and little is known about what is required to make a high quality material. The sintering process in these PV materials has not been thoroughly studied, and strong criteria do not exist for predicting how ligands, particle size, and processing steps impact the resulting films and devices. Early attempts to make bulk materials from nanocrystals suggested that the carbonaceous ligands prevented effective sintering[380-382], but more recent work has shown large grained structures.[115, 383] Reports have even suggested that the carbonaceous layer often observed between the absorber and back contact[312-315] may benefit devices by reducing back contact recombination.[313] To better understand how the properties of the nanocrystal ink impacts the bulk film, we have made photovoltaic devices with CZTS nanocrystal synthesized for different lengths of time. The resulting inks vary in average particle size, compositional heterogeneity, and average composition.

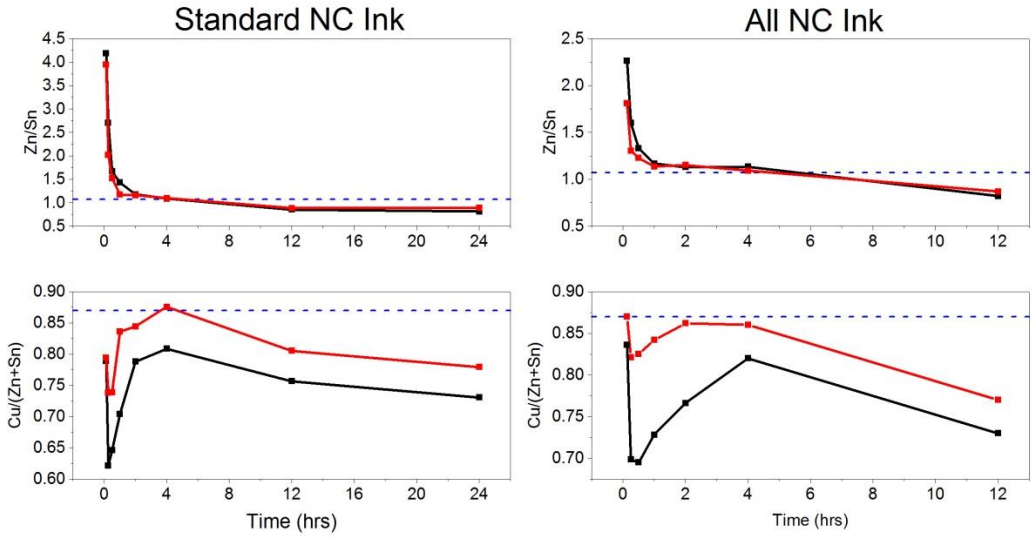

Figure 5.1 The change in film composition as a function of time for the (1) "Standard" and (2) "All" particle fractions. Black lines indicate the composition of the doctorbladed film, red lines indicate the composition after selenization. The dashed blue line indicates the ratio of precursors added for NC synthesis.

5.2 MATERIALS AND METHODS

5.2.1 *Nanocrystal Synthesis*

CZTSSe solar cells were made from nanocrystals characterized in detail in a previous publication.[384] The nanocrystals are synthesized by injecting a 1M sulfur in oleylamine solution into a flask containing copper(II) acetylacetonate (Sigma 99.999%), zinc(II) acetylacetonate hydrate (Sigma 99.999%), and tin(IV) bis(acetylacetonate) dichloride (Sigma 98%) in oleylamine (Sigma, technical grade) at 225 °C. After injection the reaction is allowed to proceed for a set duration. After that time, the reaction mixture is allowed to cool naturally. The reaction mixture is then split equally between two centrifuge tubes. From one tube, we precipitate nearly all of the particles (the "All" fraction); from the other we only collect particles above a certain size threshold (the "Standard" fraction). The Standard procedure is the same as was used to produce a 7.2% efficient device [243]. The nanocrystals are washed multiple times to remove excess oleylamine then dispersed in hexanethiol to form a dense ink.

5.2.2 *Device Fabrication*

Device fabrication closely follows a previously published method.[243] Thin films are made by doctorblading the NC inks onto molybdenum coated soda-lime glass and then drying on a hot plate at 300 °C in air. A film about 1.5μm thick is made by repeating this process twice. The films are then annealed in a graphite box with excess selenium at 500 °C for 20 minutes to form a polycrystalline CZTSSe film. Complete devices are made following standard procedures, including chemical bath deposition of CdS, RF sputtering of i-ZnO then ITO, and thermal evaporation of a Ni/Al top contact. The samples are scribed into devices with a typical area of about 0.45 cm^2.

5.2.3 *Characterization*

The composition of the films was measured before and after selenization using energy dispersive spectroscopy (EDS) on a FEI Sirion scanning electron microscope at 20 keV. Completed solar cells are tested under simulated AM1.5G illumination produced using a 300W Xe arc lamp with appropriate filters. The integrated light intensity is validated using a calibrated mono-crystalline Si reference cell. Current-voltage parameters are extracted using the method of Zhang et al.[385] The external quantum efficiency (EQE) is measured using a lock-in amplifier with monochromatic light, chopped at 153 Hz and the resulting spectrum is integrated over the AM1.5G spectrum and compared to the measured short circuit current. Drive-level capacitance profiling (DLCP) is performed at room temperature using a Solartron SI 1260. The DC peak voltage was varied from -0.5 to +0.5V with the AC signal ranging from

10-300 meV over the frequency range 0.1-46.4 kHz. For determining the defect density, the device was assumed to be a planar one-sided junction and the dielectric constant was assumed to be 8.6.[121] Absolute intensity photoluminescence (AIPL) spectra are collected on a modified Horiba Labram steady-state PL instrument calibrated using a NIST-calibrated blackbody source. The AIPL spectra are collected over a 110x110 μm area using 785 nm laser excitation at approximately 10 suns. A minimum of 6 PL measurements are taken on each sample and the fitted parameters are averaged. The crystallographic structure of the films was analyzed by powder x-ray diffraction (PXRD) using a Bruker D8 Focus with a Cu K-alpha radiation source. The XRD instrumental broadening was measured using a single crystal silicon wafer which had a FWHM of 0.115 2θ, less than half of the narrowest FWHM observed in any of the CZTSSe films.

TABLE 1. SUMMARY OF CATION RATIOS FOR THE SELENIZED FILMS

	Standard		All	
Reaction Time	Cu/(Zn+Sn)	Zn/Sn	Cu/(Zn+Sn)	Zn/Sn
0.125 hrs	0.79	3.94	0.87	1.81
0.25 hrs	0.74	2.02	0.82	1.31
0.50 hrs	0.74	1.52	0.83	1.23
1 hrs	0.84	1.17	0.84	1.14
2 hrs	0.84	1.16	0.86	1.15
4 hrs	0.88	1.10	0.86	1.09
12 hrs	0.81	0.88	0.77	0.87
24 hrs	0.78	0.89	--	--

5.3 RESULTS AND DISCUSSION

5.3.1 *Temporal Changes to Composition*

With increasing reaction time we see significant changes in the average composition of both the Standard and All NC inks. As detailed in a previous publication,[384] and shown in Figure 5.1, the short reaction time inks are very Sn-poor, but over time the composition of the ink approaches that of the starting precursors. Analysis of the particle size fractions shows that the reaction product contains at least two distinct particle populations: large Zn-rich particles and small Zn-poor particles. The small particles are not collected in the Standard fraction, but are included in the All ink. The addition of these small particles causes the All fraction to have higher Cu/(Zn+Sn) ratios and lower Zn/Sn ratios than the Standard fraction. After the first 0.5 h of reaction, the small particles dissolve to enrich the larger particles with Cu and Sn, thus the composition of the All fraction precedes that of the Standard fraction. For example, the Cu/(Zn+Sn) and Zn/Sn ratios for the Standard fraction reacted for 1 hour are 0.83 and

1.18; values close to that of the All fraction after only 30 min of reaction at 0.83 and 1.22. After about 4 h of reaction nearly all of the particles are collected in the Standard fraction, so the two compositions converge. Comparing the film compositions before and after selenization, we observe that both the Standard and All fraction shift to higher Cu/(Zn+Sn) ratio as a result of both Zn and Sn loss. When the film is very Zn-rich, the shift primarily results from Zn loss, as indicated by a reduction in the Zn/Sn ratio. However, we also see evidence of Sn loss, particularly for the longer reaction time samples, as has been documented previously.[69, 150-152, 154] The elemental losses are significantly lower for the longer reaction times, when the average composition is much closer to stoichiometric. Because ZnS(e) has a very low vapor pressure, the loss of Zn suggests that there is likely unbound (metallic) zinc present during annealing. Conveniently, for reaction times of 2-4 hours, the elemental losses that occur during selenization shift the composition ratios very close to the composition targeted by the NC synthesis (dashed line). A summary of the cation ratios is provided in Table 1.

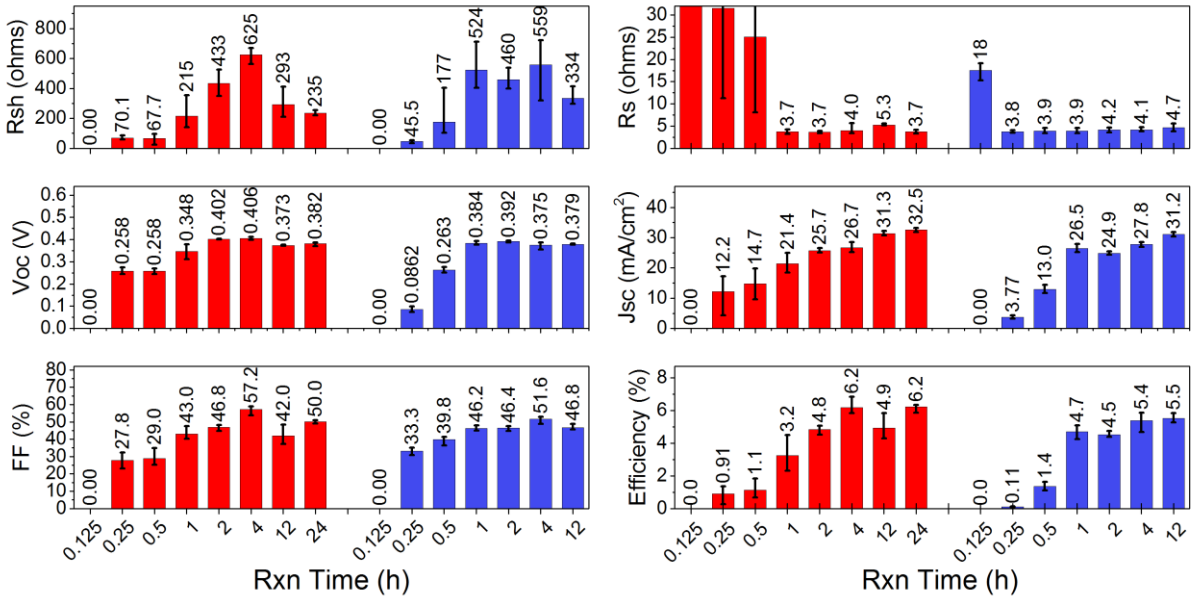

Figure 5.2 Parameters extracted from the current voltage characteristic of the Standard NC devices (red) and All NC devices (blue) with different reaction times. Error bars indicate the minimum and maximum values observed from 12 devices.

5.3.2 *Current-Voltage Characteristics*

CZTSSe solar cells were made from both the Standard and the All NC inks to evaluate how the synthesis and particle collection procedure impact the resulting devices. Parameters extracted from the I-V characteristic are summarized in Figure 5.2, and SEM cross sections of the Standard devices are shown in Figure 5.3. With increasing reaction time, we see improvements in Jsc, fill factor, Voc, and power conversion efficiency (PCE) for synthesis times up to 4 h for both the Standard and All devices.

Jsc continues to increase after the 4 h mark, offsetting the losses to fill factor and Voc observed for the 12 and 24 h reaction times to yield devices with comparable efficiency. The changes in composition with time complicate the data interpretation, but by comparing samples with similar cation ratios, we are able to make clear conclusions about the effect of reaction time and the impact of different particle fractions. For example, the 1-4 h Standard and the 0.5-4 h All devices have similar cation ratios, yet the Standard ink, which on average has larger particles and is more homogeneous, tends to make slightly more efficient devices. The difference primarily results from enhanced Voc and fill factor. This contrasts with previous work, which reported that the small Zn-poor particles (such as those included in the All fraction but not the Standard fraction) had a beneficial effect on devices.[366] However, in that report, the addition of the small particles caused a significant change in the cation ratio of the similarly synthesized particles (the "R1" particles), but not the particles synthesized using an alternative method (the "R2" particles). The R1 particles are comparable to our 0.5 h particles, while the R2 particles were synthesized using a higher temperature reaction for a longer amount of time, and thus may be most comparable to our 4 h particles. Comparing the Standard and All devices from these reactions, we see that the additional of the small particles benefits the 0.5 h but not the 4 h. For the 0.5 h reaction, the changes in composition are large, so it is difficult to precisely identify what impact the small particles have. We also note, that the efficiency of the 0.5 h All sample is much worse than expected given the composition. This may be a result of poor film quality or processing error.

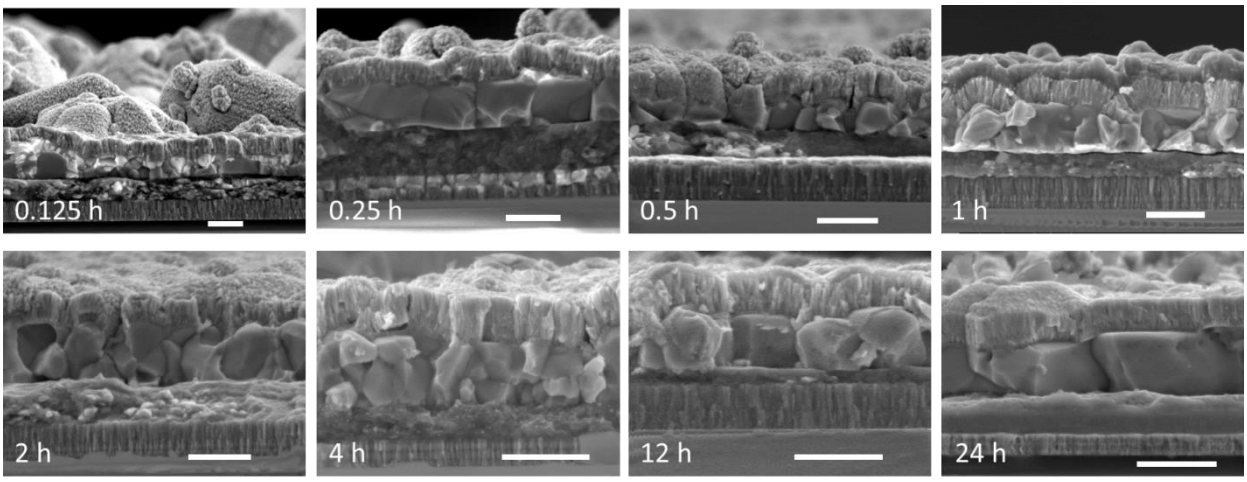

Figure 5.3 SEM cross-sectional images of the Standard devices with different NC reaction times. The samples are all approximately 1.2 μm thick and show varying degrees of grain growth. The scale bar is 1μm in each image.

Among the samples with similar compositions, the clearest trend is an improvement in efficiency with reaction time. Between 1-4 h the composition of the Standard devices changes only slightly, yet the average efficiency increases by 3.0%. The effect is less pronounced in the All devices, but between 0.5-4 h the efficiency does improve. Further, the performance of the longest reaction time devices suggests that the synthesis plays an important role in device performance. Reaction times up to 4 h produce films with a Cu-poor/Zn-rich composition. These conditions favor the formation of relatively benign defects and defect clusters such as [V_{Cu}+Zn_{Cu}] while suppressing the formation of more detrimental defects such as [$2Cu_{Zn}$+Sn_{Zn}] and Sn_{Zn}.[24, 194, 195] For this reason, the most commonly reported optimum cation ratios Cu/(Zn+Sn) and Zn/Sn are 0.8 and 1.2, respectively.[386] However, the 12 and 24 h devices are Sn-rich, with Zn/Sn ratios near 0.9. We would anticipate that under Sn-rich conditions, the defect chemistry should be much more unfavorable, yet these devices perform as well or better than devices that have compositions closer to the optimum. In Zn-rich films, we expect the precipitation of ZnSe, which is relatively benign, but the Sn-rich devices will likely have SnSe or $SnSe_2$, which are detrimental to devices.[238, 387] Some brightly colored precipitates are evident near the bottom of the film in the SEM cross-sections (Figure 5.3), which are likely ZnSe. We do not see any obvious signs of Sn-based secondary phases.

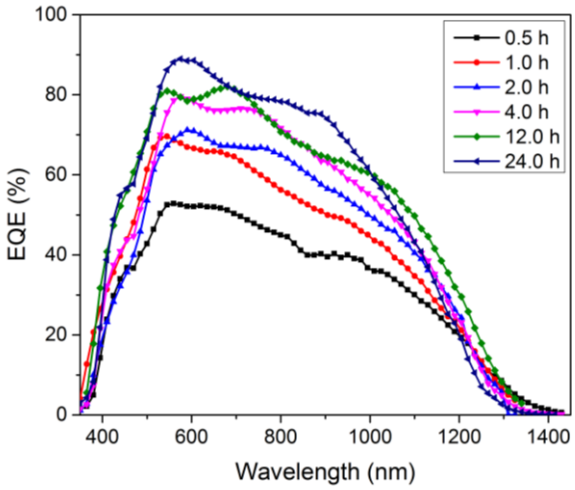

Figure 5.4 External quantum efficiency of the Standard nanocrystal devices. We see improved carrier collection at almost all wavelengths with increasing reaction time.

5.3.3 *External Quantum Efficiency and Drive-Level Capacitance Profiling*

The EQE of the highest efficiency Standard devices are shown in Figure 5.4. With increasing reaction time, the current collection improves across all wavelengths, suggesting a decrease in the defect concentration both in the quasi-neutral region and in the space charge region. The higher EQE between

400-500 nm for the 12 and 24 h devices could result from either a reduction in interfacial defects or a thinner CdS layer. Devices were characterized using drive-level capacitance profiling (DLCP) to quantify the changes in the defect density with reaction time. The DLCP derived defect densities are shown in Figure 5.5. Consistent with the I-V data and the EQE, we find that the defect density decreases with increasing reaction time. However, the overall defect concentration is still quite high even for the best devices.[1] Again, some of the trend can be ascribed to changes in composition, but the 0.5-4 h All and 1-4 h Standard devices have similar compositions and yet we still see substantial reductions in the defect density with reaction time. The defect densities of the 4-24 h devices at 1 kHz are all approximately the same, but at 100 Hz, we see a significant reduction in the defect density of the 24 h device. At lower frequencies, deeper defects are able to respond, thus the DLCP data indicates that the Sn-rich 24 h device has a lower density of deep defects than the Zn-rich 4 h device. Again, this data conflicts with what is expected based on first principles calculations,[387] but is consistent with the device performance and the photoluminescence data (discussed below).

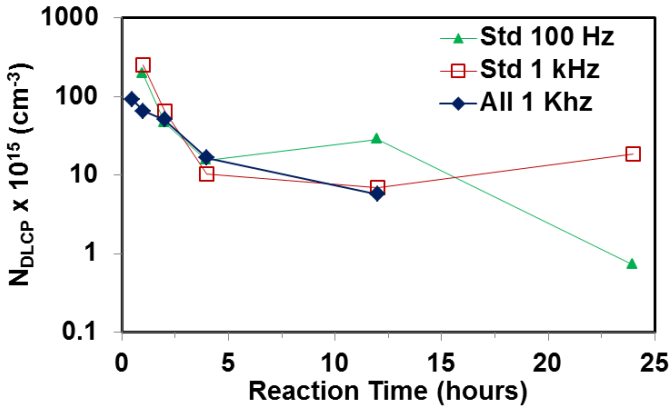

Figure 5.5 Change in the defect concentration as a function of reaction time for both Standard and All devices. Values were determined using drive-level capacitance profiling

5.3.4 *Absolute Intensity Photoluminescence*

The performance of the long reaction time devices becomes even more intriguing when we look at the steady state absolute-intensity photoluminescence (AIPL). AIPL is a powerful technique for evaluating the overall quality of a material without the complications of device making. The high-energy tail of the PL peak contains information about the quasi-Fermi level splitting (QFLS) which is the largest open-circuit voltage a sample can produce at a given illumination. The low-energy tail of the peak contains information about local electrostatic potential fluctuations. Electrostatic potential fluctuations (EPFs) result from charged defects or defect clusters. EPFs cause sub-bandgap absorption tail and thus emission of light. In the PL spectrum EPFs manifests a redshifting of the PL peak maximum and a broadening of

the peak full-width-at-half-maximum (FWHM). A good material should have a large quasi-Fermi level splitting (Δμ), a narrow FWHM, and the peak maximum close to or above bandgap. The PL spectra and the extracted parameters are shown in Figure 6 and 7 for the different reaction time devices. As with the device parameters, we see improvement in the PL characteristics with reaction time. The 4 and 24 h Standard were the highest efficiency devices, and we can see that they have the highest energy peak positions. However, despite having similar efficiencies, the 24 h sample has a much narrower FWHM, indicating reduced potential fluctuations, and a larger quasi-Fermi level splitting. This is consistent with the DLCP data, and indicates that the 24 h sample has fewer SRH-active defects.

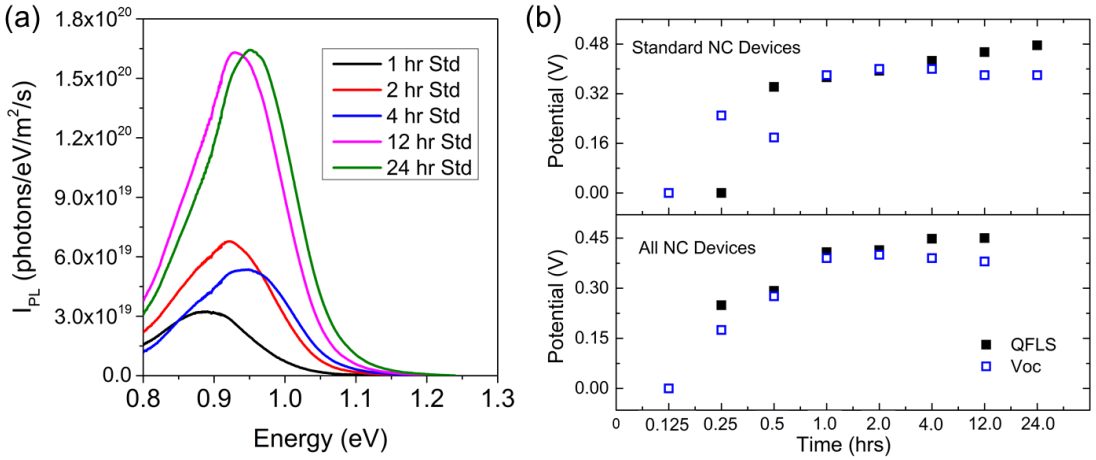

Figure 5.6 Typical absolute intensity photoluminescence spectra from the Standard devices (a) and comparison of the extracted quasi-Fermi level splitting to the measured Voc (b).

As shown in Figure 5.6, we find a good correlation between Δμ and Voc. The largest deviations occur at short and long reaction times. The short reaction times, such as the 0.5 h Standard, have Voc's lower than the Δμ, likely due to poor film quality and the large quantities of ZnSe that undoubtedly exist in such a Zn-rich film. ZnSe has not been found to produce non-radiative recombination sites but it will interfere with current flow,[288] and has been correlated with reduced Voc in CZTS.[139, 289] Interestingly, the 12 and 24 h reaction devices have the largest quasi-Fermi level splitting (Δμ), but we do not see this manifest as a higher Voc in the devices. Despite superior material quality, the Sn-rich devices may be degraded by a Sn-rich interface. In chalcopyrites, much work has been devoted to figuring out why Cu-poor materials perform better despite the fact that Cu-rich materials have better optical and electronic properties.[388, 389] A leading explanation is that Cu-poor absorbers form a more favorable interface with CdS.[10] A similar mechanism could be at play here, but further investigation is needed. Few studies have focused on Cu-poor/Sn-rich kesterites, and to the best of our knowledge this is the first report of large quasi-Fermi level splitting in devices with Zn/Sn < 1.

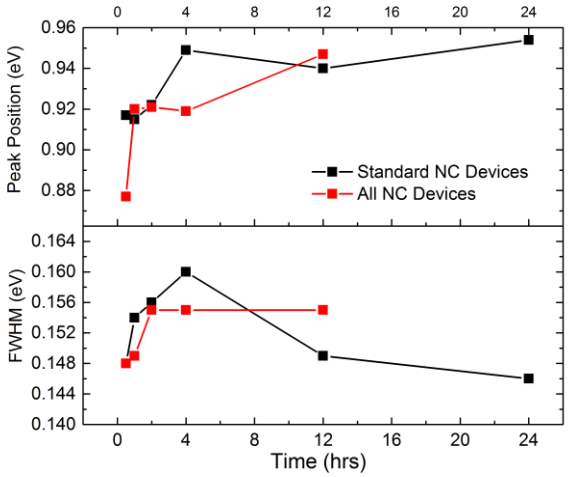

Figure 5.7 Photoluminescence peak position and peak full-width-at-half-max (FWHM) for the Standard and All devices.

5.3.5 *X-ray Diffraction and Crystalline Domain Size*

Thus far all data has indicated that longer reaction times lead to lower defect densities, larger quasi-Fermi level splitting, and thus better devices, but the question remains: why? The answer is found by examining the XRD data, shown in Figure 5.8. The most intense XRD peaks are all consistent with kesterite CZTSSe, but we are unable to distinguish secondary phases, such as a Zn(S,Se) due to the overlap of the most intense peaks with those of CZTS(e), an issue which is well documented in literature.[131, 133] However, we do observe a number of minor peaks that are solely associated with the kesterite phase, and their relative intensities agree well with that of the diffraction standard (PDF #01-070-8930). By analyzing the relative intensity of the CZTSe peaks we can conclude that any secondary phases that may be present do not have a strong contribution to the diffraction pattern. Evidence of a Cu_xSe phase is observed in the 0.125 h Standard, 0.25 h Standard, and 0.125 h All films, despite these films being very Zn-rich. Applying Vegards law, we calculate that the sulfur content is relatively consistent between samples at approximately 17%. Assuming an even distribution of the sulfur within the film, this should correspond to an optical band gap of 1.02eV.[195] Comparing this value with the position of the PL data(Figure 5.7), we see that the peak maximum is well below bandgap, as we would expect with significant potential fluctuations.

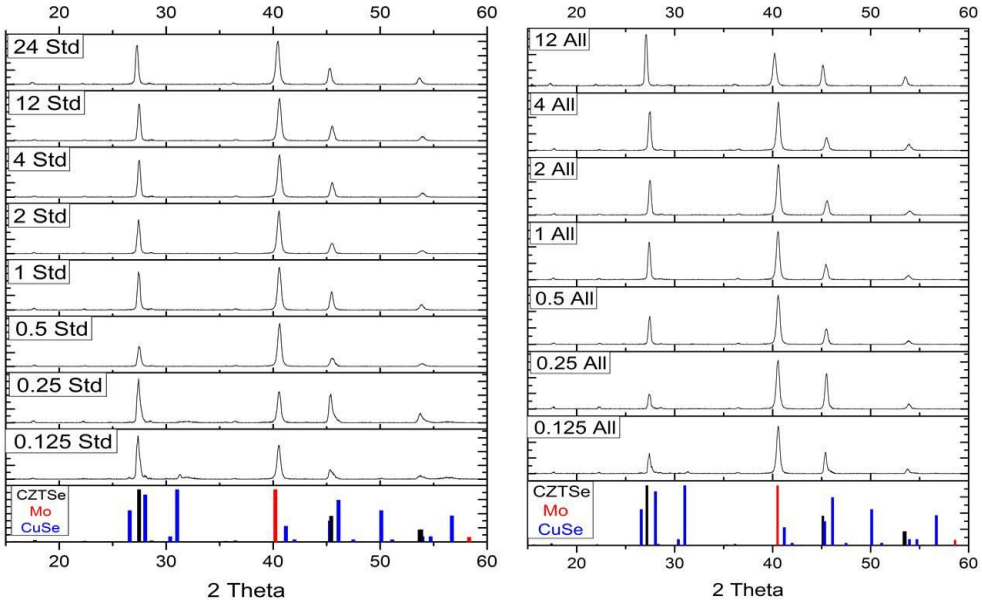

Figure 5.8 XRD from selenized Standard (left) and All (right) inks. Peaks corresponding to secondary phases are only observed in the 0.125 Std and All samples.

The most interesting result comes from looking at the changes in the FWHM of the primary CZTS diffraction peak. As shown in Figure 5.9, the crystalline domain size of the selenized film, determined using Scherrer's equation, increases with reaction time, and is consistently 2-2.5 times as large as the diameter of the starting sulfide NCs (assuming the particles are spherical). From exchange of sulfur with selenium, we would expect a volume change of about 15%, so some interparticle sintering must occur, but the extent is approximately similar in all of the films. The SEM cross-sections show that there (Figure 5.3) there is some improvement in the apparent grain size and morphology with reaction time. The grains of the longest reaction times are larger and less faceted than those with shorter reaction times, but in all of the samples a significant un-sintered layer is present.

Interestingly, the crystalline domain size calculated from Scherrer's equations correlates very well with device efficiency, as shown in Figure 5.10. Samples with larger crystalline domain sizes have higher efficiency, suggesting that the grain boundaries act as a significant source of non-radiative recombination. This also explains why samples with longer reaction times exhibit comparable device performance, even when they have less favorable compositions. Longer NC reaction times lead to larger NCs; larger NCs lead to larger crystalline domains in the selenized film; and larger crystalline domains lead to fewer grain boundaries which are a source of detrimental defects. This conclusion would be consistent with previous theoretical calculations indicating that the grain boundaries of kesterites are not

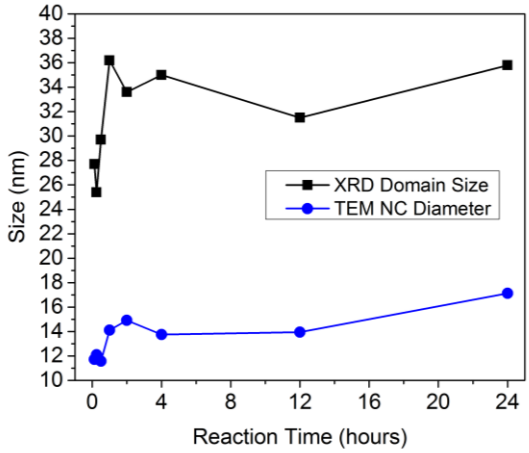

Figure 5.9 Plot of the crystalline domain size determined using Scherrer's equation showing the correlation with the size of the starting sulfide nanocrystals. We find that the size of the starting nanocrystal is proportional to the crystalline domain size in the film, indicating that limited interparticle sintering is occurring.

as passive as those of chalcopyrites.[390, 391] This suggests that a route to improving the efficiency of NC-derived solar cells is to simply synthesize larger NCs. However, we must emphasize that this is not the only interpretation of the XRD data. The narrowing of the FWHM could also result from a reduction in crystallographic defects or strain. Additionally, because of the possible co-existence of secondary phases with overlapping XRD peaks, the narrowing of the peak FWHM could simply indicate a reduction in the presence of weakly crystalline secondary phases. From looking at the minor diffraction peaks, we know that the contribution of secondary phases is minor, but they may still contribute to the breadth of the peak. Elimination of these phases would likely also have a beneficial effect on the devices, and may also explain the increase in efficiency with narrowing FWHM.

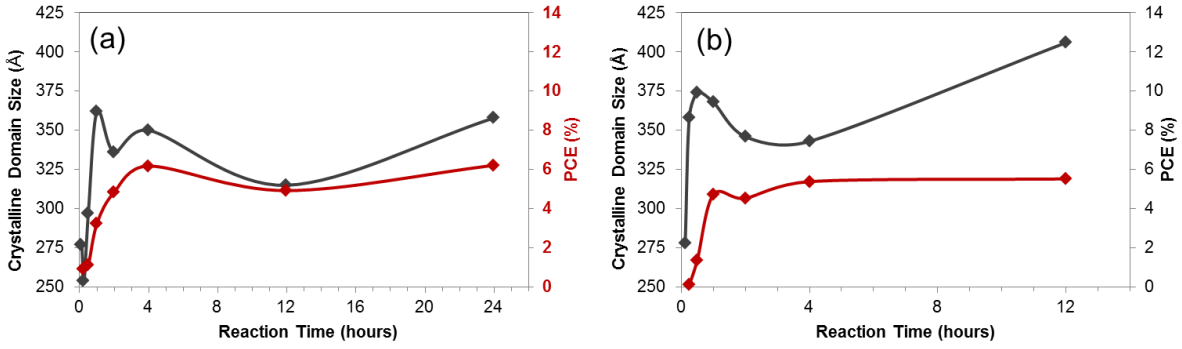

Figure 5.10 Plot of the crystalline domain size determined using Scherrer's equation showing the correlation with power conversion efficiency (PCE) for the Standard (left) and All (right) devices. The correlation is consistent with theoretical predictions that the native grain boundaries are not passive.

5.4 CONCLUSIONS

We have investigated how Cu_2ZnSnS_4 nanocrystal inks with different particle size, size distribution, average composition, and compositional heterogeneity impact the properties of the selenized absorber layer. We find that longer NC synthesis produce larger NCs, and larger NCs lead to larger crystalline domain sizes after sintering, a lower concentration of deep defects, and more efficient solar cells. The strong correlation between crystalline domain size and the defect concentration (and resulting device efficiency) suggests that grain boundaries are a significant source of non-radiative recombination. Thus to make high efficiency devices, grain boundary passivation techniques or NC synthesis and sintering methods that allow better grain growth will need to be developed. In contrast to previous reports, we find that the inclusion of small Sn-rich particles, leading to increased ink heterogeneity, has a slightly negative impact on device performance, but not on grain growth. Finally, we note for the first time large quasi-Fermi level splitting in devices with Zn/Sn < 1.

Chapter 6.

COMBINATORIAL EXPLORATION OF THE EFFECTS OF INTRINSIC DEFECTS IN $Cu_2ZnSn(S,Se)_4$

6.1 INTRODUCTION

Chapters 3 and 4 have highlighted a few of the many challenges associated with using nanocrystals (NCs) as precursors to bulk films. By studying the NC synthesis reaction we have been able to produce nanocrystals inks with controlled compositions and deposit a composition gradient using the ultrasonic spray coater. However, as we have shown in Chapter 4, even if NC inks have nominally similar composition, the efficiency of the resulting devices can vary significantly depending on how the inks were synthesized. This makes it difficult to decouple the effects of NC synthesis from the intrinsic defect properties. In addition, the use of nanocrystals for combinatorial experiments is undesirable for a number of other reasons: (1) the synthesis and washing/precipitation procedure is time consuming. (2) Different precursor ratios lead to different particle size distributions, and particle size may be very important for device performance (refer to Ch. 4). (3) Different particle size distributions lead to rheological differences between the inks, and as a result the spray coating parameters must be optimized for each ink. (4) Producing a homogenous film from particles of different compositions requires solid state diffusion which may or may not sufficiently occur during selenization. (5) The ligands are necessary to produce a stable ink, but they leave behind carbonaceous impurities that are very hard to eliminate. (6) It is difficult to incorporate dopants. Many salts such as NaCl are not soluble in non-polar solvents such as hexane or toluene and adding any other species to the synthesis could be very problematic. However, during this same time period our group made considerable progress in making devices using the "molecular precursor" route. In contrast to the nanocrystal route, the molecular precursor inks can be made quickly, provide easy control of composition, have consistent rheological properties, mix at the molecular level, contain primarily volatile chloride impurities, and can easily be doped. Thus moving forward, I have exclusively used the molecular precursor route for combinatorial experiments.

Drawing on years of research into $Cu(In,Ga)Se_2$, the performance of kesterite devices has improved rapidly even though the materials themselves are still poorly understood. To further improve the efficiency, we must understand both the native defect chemistry, and how extrinsic species encountered during processing impact the resulting materials properties. Currently, the biggest problem facing

kesterite-based photovoltaics is their low open circuit voltage (relative to the detailed balance limit for their bandgap). This is clearly apparent even in the current world record 12.6% efficient CZTSSe device.[1] A detailed balance using the AM1.5GT spectrum at 25 °C reveals that although the current world record device captures 81% of the theoretical maximum photocurrent, but only produces 58% of the maximum open circuit voltage. A low Voc can result from a number of problems including: (1) the presence of a high concentration of Shockley-Read-Hall (SRH) active defects (or a smaller concentration with high capture cross-section), (2) the presence of a high density of states in the gap that pin the Fermi level, (3) spatial compositional disorder that results in bandgap variations, (4) charged point defects that result in electrostatic potential fluctuations (EPFs), or (5) improper band alignment between device layers. Phenomena (1) through (4) may all be considered to reduce the optoelectronic quality of the material. However, (5) is quite different and is highly dependent on the choice of the other layers of the device and on the processing steps required to deposit them. Absolute intensity photoluminescence (AIPL) [392] provides a means to separate material quality from device fabrication and can quantify the presence of EPFs.

There have been several PL studies on kesterite materials, but the majority of these investigations have been on single crystals of the sulfide grown at high temperature.[199, 207, 208, 393-395] Far fewer studies have been carried out on device relevant thin film materials[3, 396-399] or the higher efficiency selenides and mixed sulfoselenides.[3, 147, 400] There have been PL studies looking at different S/Se ratios, but none which have systematically investigated the role of different cation ratios for the selenide, and only one with a large sample size for the sulfide.[399] A key part of growing high quality compound semiconductors is managing intrinsic defects. For example, with CIGSe it is well known that the best devices are those grown Cu-poor, with Cu/(In+Ga) ~ 0.8.[401] Such processing conditions favor the formation of the shallow acceptor V_{Cu} and the donor like defect In_{Cu}, which is passivated by the formation of the neutral defect complex $[2V_{Cu} + In_{Cu}]$. For kesterites, empirical optimization has shown that the most efficient devices are those made Cu-poor and Zn-rich.[281] The composition is often reported in terms of the cation ratios Cu/(Zn+Sn) and Zn/Sn with the majority of high efficiency devices reporting ratios in the range 0.7-0.9 and 1.0-1.3, respectively.[243, 318, 378, 402] The size of this range is surprising considering the narrow range of phase stability[403] and because slight changes in composition can dramatically alter the favorability of defects and defect complexes.[194]

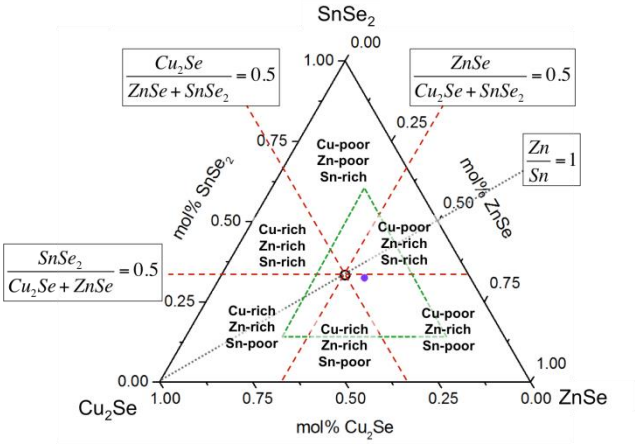

Figure 6.1 Ternary diagram showing the different Cu-poor composition regions. The green triangle indicates the region examined in greater detail here and shown in the figures. Stoichiometric is indicated by the black circle and is centered. The composition Cu/(Zn+Sn) = 0.8 and Zn/Sn = 1.2 is indicated by the purple dot.

Theoretical calculations predict that the sulfide and the selenide should have similar defect chemistry,[194, 195, 387] but experimental validation is still needed. Furthermore, with the exception of one recent study on CZTS,[399] previous studies have been performed using traditional approaches (making uniform composition devices with different compositions). This approach is time consuming and experiments typically are composed of a relatively small number of samples. The inherent variability in sample processing and device fabrication can make it difficult to elucidate systematic trends, local maxima, minima, or narrow regions of interest. Here, we present the results of high-throughput experiments where we mix CZTS molecular precursor solutions to produce continuous composition gradients of CZTSSe. The gradients are analyzed using a customized confocal steady-state AIPL mapping instrument. In all, we have measured over 30,000 distinct AIPL spectra (6,000 unique compositions), allowing us to isolate the effect of each individual cation, clearly identify trends with composition, and locate the regions of composition with the best optoelectronic properties.

Although commonly used for parameterizing the composition space, the two atomic ratios Cu/(Zn+Sn) and Zn/Sn do not have a strong physiochemical basis and are problematic since they hides the fact that even for Zn/Sn<1, the material may still be Zn-rich. This is seen schematically in Figure 6.1 where three distinct Cu-poor regions (all with $Cu_2Se/(ZnSe+SnSe_2) < 0.5$) are shown: (1) Zn-poor and Sn-rich where $ZnSe/(Cu_2Se+SnSe_2) < 0.5$, Zn-rich and Sn-poor where $SnSe_2/(Cu_2Se+ZnSe) < 0.5$, and a Zn-rich and Sn-rich region where both $SnSe_2/(Cu_2Se+ZnSe) > 0.5$ and $ZnSe/(Cu_2Se+SnSe_2) > 0.5$. Thinking about the composition space in these terms is useful and may be more easily connected with expectations about predominant defects. However, we note that there are many ways of classifying composition,

particularly in a quaternary material that undoubtedly has significant cation disorder and co-existing binary phases. We have chosen to plot the measured data on ternary diagrams in terms of the mole fraction of the most thermodynamically favored binaries (Cu_2Se, ZnSe, and $SnSe_2$), but one may also consider either site-weighted ratios, which are the same as the atomic ratios like Sn/(Cu+Zn), or charge-weighted ratios like 4Sn/(Cu+2Zn). This leads to slight changes in the composition boundaries (e.g. the transition from Cu-poor/Zn-rich/Sn-rich to Cu-poor/Zn-poor/Zn-rich), but we find that it does not change the interpretation of our data.

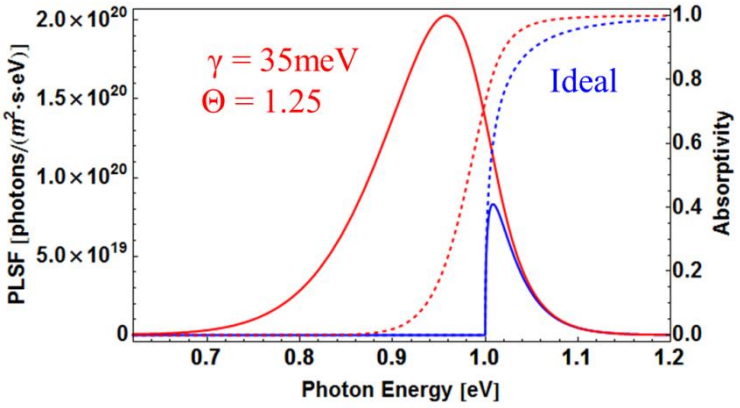

Figure 6.2 Theoretical AIPL with the same bandgap (Eg=1.0 eV), same local lattice temperature (T = 300K), and the same quasi-Fermi level splitting ($\Delta\mu$ = 0.6 eV) but using two different models for absorption coefficient. The dashed blue line is the absorptivity for an ideal direct gap semiconductor (absorption coefficient equal to zero below bandgap and with square-root dependence above gap), and the dashed red line corresponds to equation 4 with θ=1.25 and γ=35 meV. The solid lines are the calculated AIPL from equation 2.

6.2 THEORY

Shockley and Queisser [404] established the connection between the radiative emission of a solar cell and its efficiency. They showed that the larger the magnitude of the radiative photoemission (in the absence of sub-bandgap states), the better the material for photovoltaics. Non-radiative recombination of photoexcited electrons and holes is deleterious. Assuming that the material is in quasi-thermal equilibrium, there is a connection between the absorption coefficient and the photoemission. This is an extension of Einstein's work but was first articulated for volumetric-based internal spontaneous emission from band-band transitions at an "effective temperature" by van Roosbroeck and Shockley.[405] Lasher and Stern[406] noted that this could be written in terms of an actual lattice temperature and a quasi-

Fermi level splitting. Würfel modified this to account for external emission from the surface into the 2π sterad above the surface.[407] This is important since it alleviates the need to worry about photon recycling. Now, accounting for occupation of the bands,[408] an expression may be written in terms of the density-of-states based absorption coefficient, local lattice temperature, and occupation probabilities for each band:

$$I_{PL}(E) = \frac{2\pi}{h^3c^2}\frac{E^2\left(1-exp(-\alpha_{0K}(E)(f_V-f_C)d)\right)}{exp\left(\frac{E-\Delta\mu}{kT}\right)-1} \quad (1)$$

In cases where the material is not degenerately doped, this equation simplifies to an expression that is dependent on the density-of-states based absorption coefficient, local lattice temperature, and a single quasi-Fermi level splitting:[409]

$$I_{PL}(E) = \frac{2\pi}{h^3c^2}\frac{E^2\alpha_{0K}(E)d}{exp\left(\frac{E-\Delta\mu}{kT}\right)-1}\left(1-\frac{2}{exp\left(\frac{E-\Delta\mu}{2kT}\right)+1}\right) \quad (2)$$

For cases where the energy difference between the equilibrium Fermi level the band edge is greater than 5 kT, this expression is accurate within a few percent. Further, when the emission is at energies ~ 3kT greater than (E –Δμ), the above expression simplifies to the Lasher-Stern-Würfel (LSW) equation with good accuracy:

$$I_{PL}(E) = \frac{2\pi}{h^3c^2}\frac{E^2\alpha_{0K}(E)d}{exp\left(\frac{E-\Delta\mu}{kT}\right)-1} \quad (3)$$

The missing element necessary to use the LSW equation to fit AIPL data is the functional form of the absorptivity. Further, in all but the highest quality semiconductors, the PL peak position occurs below bandgap. Thus, in order to use (1), (2), or (3), we require a model of sub-bandgap absorption. Recently, a generalized model of absorption that incorporates sub-bandgap absorption (while remaining agnostic about the origin of the sub-bandgap states) was reported.[409] Drawing inspiration from Kane's semi-classical model for the density of states in the presences of disorder, the model convolutes an ideal density of states absorption coefficient with an exponential decay at energies below bandgap. With proper normalization, the absorption coefficient is given by:

$$\alpha(E) = \frac{\alpha_0}{\gamma 2\Gamma[1+1/\theta]}\int_{-\infty}^{\infty}\left(exp\left(-\left|\frac{u}{\gamma}\right|^{\theta}\right)\sqrt{(E-E_g)-u}\right)du \quad (4)$$

Here, γ and θ characterize the sub-bandgap absorption. The denominator in (1-3) drives the PL to increase exponentially with decreasing energy. It is the convolution with the exponential decay in the absorptivity below bandgap that produces a PL peak. As an illustration of the effect of non-zero sub-bandgap absorption coefficient, we show the calculated PL using (2) with the same quasi-Fermi level splitting but with two different absorption coefficients, one ideal and one based on (4) with sub-bandgap

absorption (Figure 6.2). The PL peak for the ideal case of no sub-bandgap absorption is highly asymmetric, located about 10 meV above bandgap, and has a sharp low energy cut off of emission at the band gap where the absorption and thus emission is zero. However, in real materials, disorder creates sub-bandgap absorption. For cases where the correlation length of the disorder is small (e.g. amorphous materials or thermal disorder in crystalline materials), the sub-bandgap absorption is characterized by an Urbach model (corresponding to $\theta=1$ in (4)). However, charged point defects can create more sub-bandgap absorption. These charged point defects (or defect clusters) create locally varying electric fields. This is referred to as electrostatic potential fluctuations (EPFs). The semi-classical model of this type of disorder (Thomas-Fermi) is captured by (4) with $\theta=2$. For situations with tunneling, a screened Thomas-Fermi model results in $\theta=1.25$. For all of these cases, the PL peak is shifted to energies below bandgap and the FWHM increases. Thus for a given material system with constant bandgap, the better quality material is the one which has a higher energy peak position and narrower full-width-at-half-maximum (FWHM). Note that the increased PL peak intensity observed for the case of sub-bandgap absorption in Figure 6.2 results from the fact that the QFLS has been artificially kept constant. In real materials, we would expect the sub-bandgap absorption from disorder to reduce the QFLS. So long as the assumption of quasi-thermal equilibrium is valid and the PL arises from band-band or free-bound transitions, (4) can be combined with (1), (2), or (3) and used to fit an experimental AIPL spectrum to determine Eg, T, $\Delta\mu$, θ, and γ. These data can then be used to understand the inherent optoelectronic quality of the material without making a photovoltaic device.

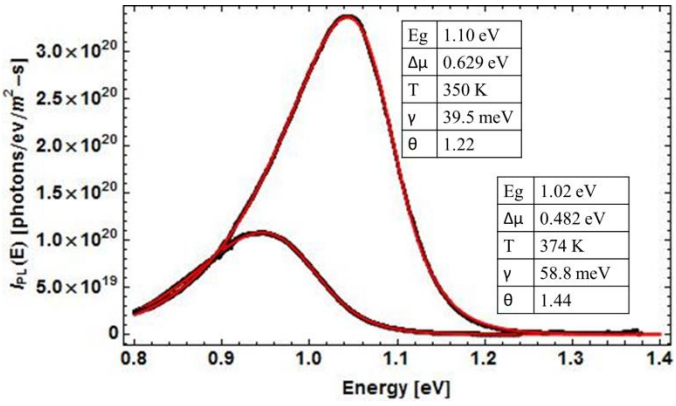

Figure 6.3 Two examples of full spectrum photoluminescence peak fitting showing excellent agreement between the experimental data and the peak fits.

6.3 EXPERIMENTAL

Molecular precursor inks are formed by dissolving copper, zinc, and tin precursors with thiourea in DMSO similar to previous reports [28]. Here, we use all anhydrous chloride precursors for the metals. Specifically, we use copper(II) chloride (99.999%), zinc(II) chloride (99.999%) and tin(II) chloride (99.99%). A gradient is deposited using a custom built ultrasonic spray coater where the liquid feed to the nozzle is set by an array of computer controlled syringe-pumps. Following deposition, the films are selenized at 540 °C in a graphite box with elemental selenium pellets [410]. Once the films have cooled they are immediately coated with 50 nm of CdS using chemical bath deposition. The CdS layer is included in standard processing because previous work on chalcopyrites [264, 295] and kesterites [263] has found it acts as a protective layer preventing degradation. However, previous work has also shown that the CdS alone does not create an n++-p junction, and thus does not create significant electric field in the absorber [264]. EDS was used to determine the composition profile along the length of each spray line by measuring at least 2 distinct sections on each line segment and averaging collections from multiple regions (>500μm^2) within those areas. The composition at intermediate points was calculated using a linear interpolation between measured points. The EDS does not provide a highly accurate measure of the S/Se ratio due to the overlap of Mo and S lines, the presence of a protective CdS layer, and formation of $MoSe_2$. AIPL maps were collected using a modified Horiba LabRam confocal steady-state photoluminescence instrument that was calibrated with a NIST-calibrated blackbody source for each optical set-up. Each AIPL spectrum is collected over a 110x110 μm area using 785 nm laser excitation at approximately 10 suns intensity (accounting for concentration through the objective lens). The peak position and full-width at half-maximum (FWHM) are extracted directly from the measured AIPL spectra. The spectra are then fit to (2) using (4) to extract the quasi-Fermi level splitting, bandgap, and the sub-bandgap absorption. Further details about the AIPL instrument, the measurement technique, the generalized theory of absorption with sub-bandgap features, and its connection to AIPL have been reported elsewhere.

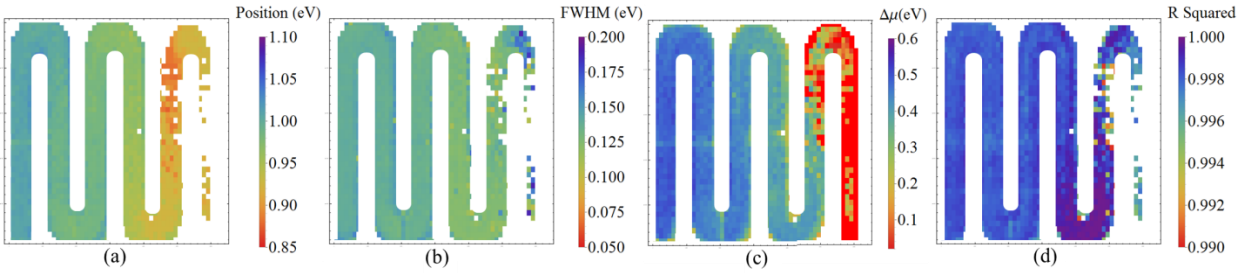

Figure 6.4 Maps of the data extracted from photoluminescence spectra. Each point on the map represents an AIPL spectrum. The (a) peak position and (b) peak full-width at half maximum (FWHM), and the (c) quasi-Fermi level splitting (QFLS). The R-squared value from full spectral fit is shown in part (d).

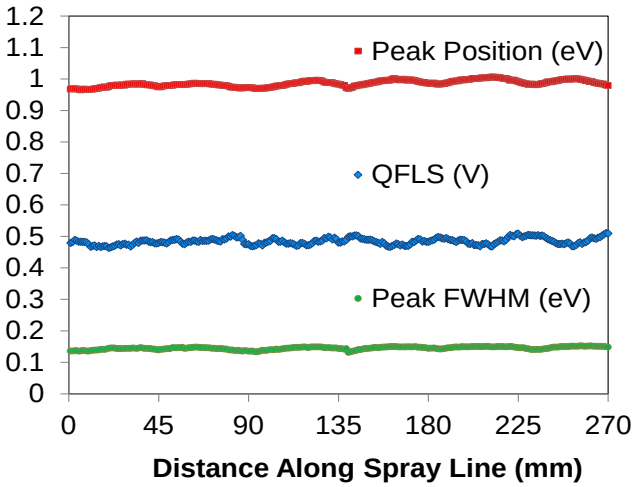

Figure 6.5 Extracted PL parameters from a spray line with constant composition. This data sets the baseline for the maximum expected variability of our processing procedure.

6.4 Results and Discussion

6.4.1 *Fitting the AIPL Spectra and Establishing Error*

To set a baseline of variability for our standard processing, we have deposited a spray line from a single ink with a constant composition. A plot of this data is included shown in Figure 6.5. The extracted PL parameters for this gradient show that there is indeed some variability along the spray line, but that the variation is small relative to the trends we see with composition variation. In the peak position, full-width-at-half-maximum, quasi-Fermi level splitting, and bandgap we see a maximum range (standard deviation) of 41 meV (10 meV), 21 meV (4 meV), 49 meV (11 meV), and 55 meV (18 meV),

respectively. Thus we should be able to reliably determine even small changes in material properties resulting from variation in the cation ratios. An example of the full spectrum fitting is shown in Figure 6.3 for two different PL peaks. Here we see that the algorithm produces an excellent fit of the experimental data. In addition, an example of a gradient showing clear changes in the PL parameters is shown in Figure 6.4.

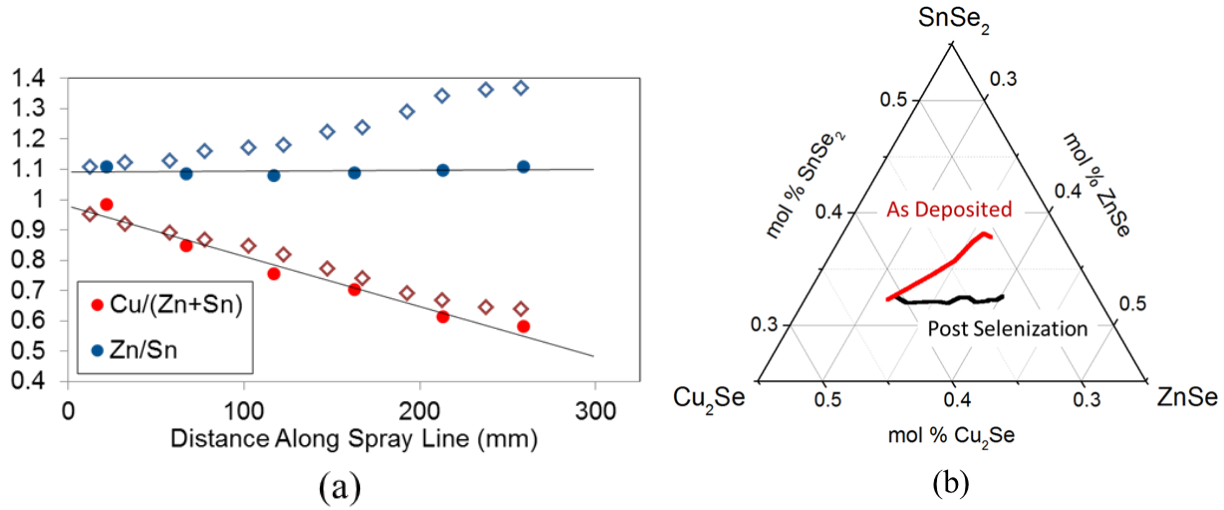

Figure 6.6 (a) Composition of a spray line before (solid points) and after selenization (hollow points) (b) Ternary diagram showing Sn-loss following selenization. Note that in both cases as the Cu-content decreases, the Sn-loss increases

6.4.2 *Tin Loss During Selenization*

To determine the final composition of the film, we have measured the composition of the spray lines following selenization using EDS. However, we emphasize that the measured composition is that of the film, and it is not necessarily that of an individual crystalline domain. The film may be *grown under Cu-poor conditions,* but the composition of any domain in the polycrystalline film is not necessarily the same since we cannot exclude the presence of secondary phases. For example, we should expect significant quantities of Zn(S,Se)e may form when Zn/Sn > 1, given the narrow range of phase stability for kesterite [24, 403]. In addition, as has been previously documented in literature [150-152], the films exhibit a notable degree of Sn-loss during the annealing (selenization) process. Figure 6.6ab show the measured composition of two different spray lines before and after selenization. In Figure 6.6a, the data is shown in terms of the cation ratios Cu/(Zn+Sn) and Zn/Sn; in Figure 6.6b, the change is shown on a ternary diagram. We demonstrate here, for the first time, a strong Cu-dependence on the Sn loss. As the Cu-content or Cu/(Zn+Sn) ratio decreases the Sn-loss during annealing increases, suggesting that the Cu

plays an important role in binding the Sn and preventing evaporation. To produce gradients with a flat Zn/Sn profile after selenization, the composition of the starting inks must be adjusted to compensate for this loss. For very Cu-poor samples, this may mean that the as-deposited film is actually Sn-rich, even though the selenized film is Zn-rich.

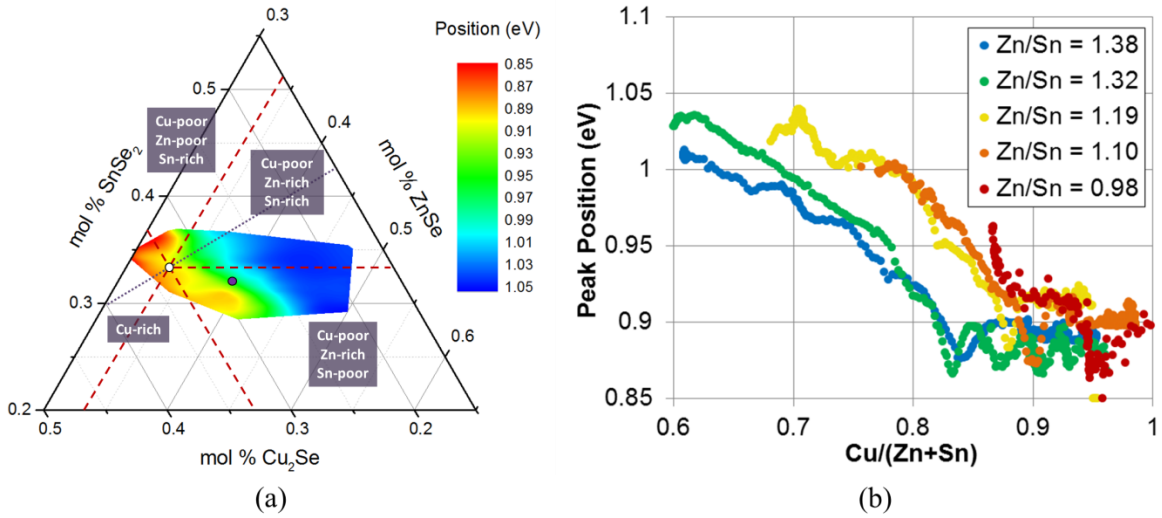

Figure 6.7 Plot of the PL peak position (a) as a function of composition (b) for select Zn/Sn ratios with varied Cu/(Zn+Sn).

6.4.3 *PL Peak Position and FWHM as a Function of Composition*

To clearly show how each individual cation impacts the optoelectronic properties, we have plotted the extracted PL parameters on ternary diagrams. To aid in the interpretation of this data, we have included labels for the regions shown in Figure 6.1 as well as a dot indicating stoichiometric $Cu_2ZnSnSe_4$ (white) and the commonly cited optimum composition Cu/(Zn+Sn) = 0.8 and Zn/Sn = 1.2 (purple).

As expected, we see significant changes in the PL parameters with composition. For example, Figure 6.7 shows a plot of the peak position as a function of composition. In this plot, we see that the most Cu-poor samples have the highest energy peak positions, while samples closer to stoichiometric have peaks located at lower energy. The change in peak position most closely follows changes in Cu-content, while changes in either Zn or Sn content have a minimal impact. The red-shifting of the peak with increasing Cu-content could be the result of increasing magnitude of EPFs. However, if that were the case, we would expect the peak to also simultaneously broaden. Looking at the peak full-width-at-half-maximum (FWHM), shown in Figure 6.8, we see that this is not the case. For most compositions, the FWHM is

approximately 150-160meV, with two notable exceptions: a narrow region near Cu/(Zn+Sn) = 0.8 and Zn/Sn = 1.2 (26-30 mol% Cu_2Se) where the peak narrows by approximately 10-20meV, and the regions with the highest Cu-content. In the latter case, we find that the peaks broaden significantly just prior to complete quenching of the PL signal. In this case, the broadening is accompanied by a red-shifting of the peak as shown in Figure 6.7. This is consistent with what we would expect for an increase in the magnitude of the EPFs, and indicates a significant increase in the defect density at nearly stoichiometric quantities of copper. These trends can be clearly seen in Figure 6.7b and Figure 6.8b, where the Position and FWHM are plotted as a function of the Cu/(Zn+Sn) ratio for 5 different Zn/Sn ratios.

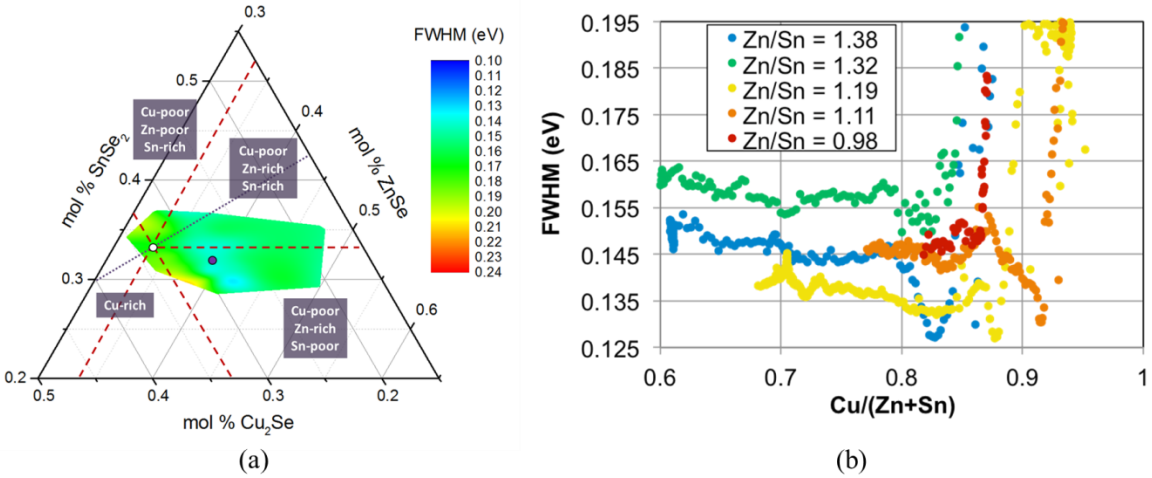

Figure 6.8 Plot of the PL peak FWHM (a) as a function of composition (b) for select Zn/Sn ratios with varied Cu/(Zn+Sn).

6.4.4 *Bandgap and Sub-Bandgap Absorption from Fitting AIPL*

Using our full spectrum fitting algorithm, we can also determine the energy of the optical transition from the PL data. Assuming that the PL signal originates from band-band recombination, which is favored at room temperature, the transition energy is the same as the bandgap. However, if there are large defect populations the transition energy may reflect a band-acceptor or donor-band (free-to-bound) transition. For the purpose of discussion here, we will simply refer to the energy of the optical transition as the bandgap. The bandgap is shown as a function of composition in Figure 6.10. Here we see that the trends in the bandgap very closely follow the trends in the peak position. Decreasing the Cu-content leads to an increase in the bandgap, while changes in the Zn or Sn content have little effect. At compositions near stoichiometric, the measured bandgap is approximately 0.95eV, in agreement with theoretical predications for the selenide [195] and electro-reflectance measurements [118], but as the Cu-content is decreased, the bandgap increases, reaching values as high as 1.10eV. Because the material is a

sulfoselenide, it is possible that the changes in the bandgap result from variation in the S/Se ratio, but we do not observe any systematic trends in the S/Se ratio that could account for this behavior. However, we note that EDS does not provide a very accurate measure due to the presence of both $MoSe_2$ and a protective CdS layer. A ternary diagram showing the S/(S+Se) ratio is provided in Figure 6.9 for reference.

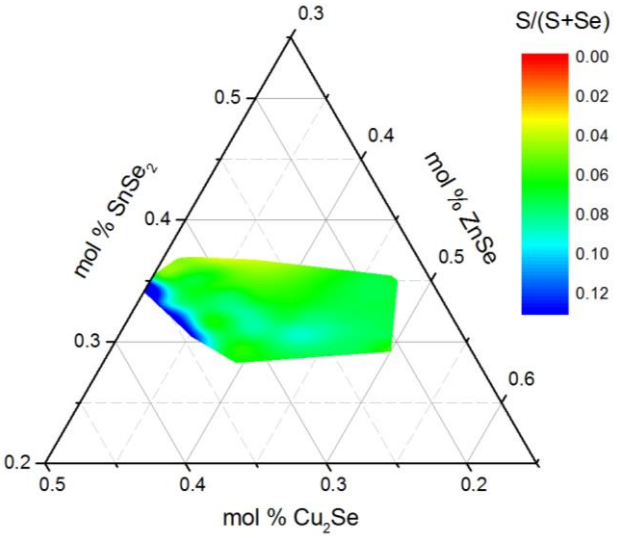

Figure 6.9 S/(S+Se) ratio determined from EDS for the different composition points. The S/Se ratio remains approximately constant over the majority of compositions measured. The increased Se content at high Cu-content likely results from the formation of Cu_xSe.

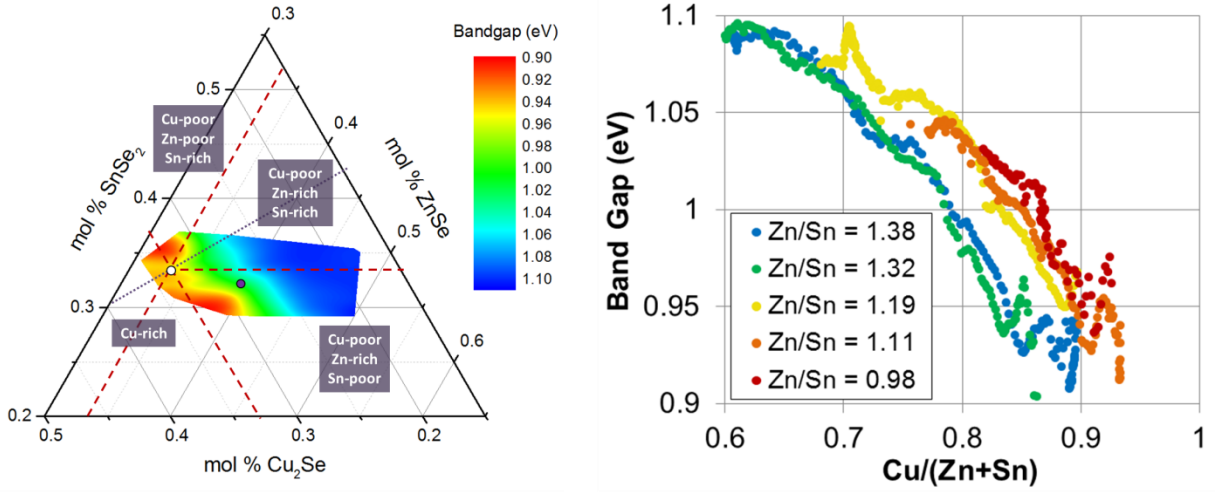

Figure 6.10 Plot of the bandgap, as determined from full spectrum PL fitting, (a) as a function of composition on a ternary diagram and (b) as a function of the Cu/(Zn+Sn) ratio at constant Zn/Sn ratio.

To test the accuracy of the fitted bandgap, we spin coated 4 samples with varying Cu-content on quartz substrates and characterized them using UV-Vis-NIR absorption in an integrating sphere. Figure 6.11 compares the band gap determined by linear extrapolation of the absorption onset (absorbance squared verus energy) to that determined by fitting the PL spectra. In general, we see excellent agreement between the two values, though we note that the bandgap as determined by PL measurement is systematically larger (5-20 meV) than that from the absorption measurements. This small offset may be due to a Burstein-Moss shift [411, 412] that exists because since we have not accounted for the occupation probability in the PL model (by use of (2) or (3) above). However, just as we saw in the composition gradients, the bandgap increases with decreasing Cu-content. These changes are consistent with previous work using spectroscopic ellipsometry on CISe [143] which found that the bandgap increases with decreasing Cu-content. Because the VBM in CISe results from the repulsive interaction of Cu-3d and Se-4p states, Cu-vacancies cause the VBM to decrease [192]. The VBM of kesterites also results from Cu-3d chalcogen-4p repulsion [159], thus we should expect that Cu-vacancies will have the same effect in both CZTS and CZTSe. Further, Cu-poor/Zn-rich conditions favor the formation of the defect complex [V_{Cu} + Zn_{Cu}] which is predicted to have band edges above those of CZTSe [387]. Thus, these data show that the changes in the peak position with composition primarily result from changes in bandgap not from changes in the magnitude of EPFs. In addition, the fact the bandgap determined from PL is slightly higher than the bandgap determined by optical absorption supports the fact that the PL arises from a band-band transition as opposed to free-bound transition or a quasi-donor-acceptor pair.

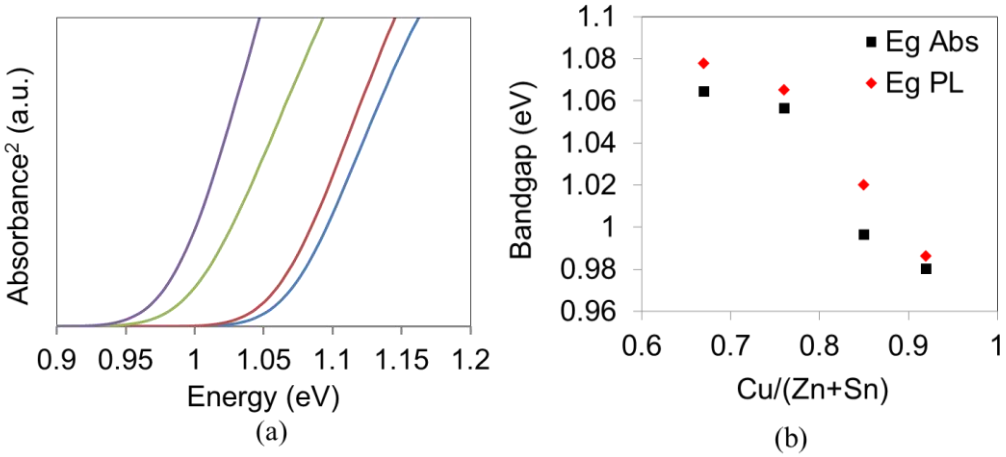

Figure 6.11 (a) Absorbance onset of CZTSSe samples on quartz substrates and (b) comparison of the PL derived bandgap to the bandgap determined by extrapolating the linear onset of absorption in (a).

To characterize how the EPFs vary with composition, we have calculated the average sub-bandgap absorption, as shown in Figure 6.12. Because the energy broadening parameter (γ) and the exponent (θ)

are strongly inter-dependent, it is most useful to look at changes in the magnitude of potential fluctuations by comparing their average sub-bandgap absorptivity, defined by (5).

$$\bar{a}_{SB} = \frac{1}{E_g}\int_0^{E_g} a(E)dE \qquad (5)$$

Consistent with the previous data, we find that the average sub-bandgap absorptivity does not change significantly with composition Starting from a very Cu-poor composition, both γ and θ increase slightly with increasing Cu-content leading to nearly constant magnitude of sub-bandgap absorptivity of approximately 0.04 to 0.05. The value increases at compositions with near stoichiometric amounts of Cu, consistent with an increase in the magnitude of EPFs, and decreases slightly at very Cu-poor compositions. Typical values of γ and θ are 40meV and 1.25-1.30, respectively. The value of θ is closest to that predicted by the screened Thomas-Fermi model. This may indicate thatelectron tunneling through potential barriers is an important factor. However, other electronic or optoelectronic phenomena such as photon-assisted tunneling from valence band to conduction band (an internal Franz-Keldysh effect) may be present as well. There is no clear one-to-one mapping between the value of θ and a specific model. However, most of the models that include tunneling yield values of θ close to those observed here. Thus, this may also point to the presence of tunnelling-enhanced recombination between charged defects. This would explain the relatively high diode quality factors observed in current-voltage measurements. Further work is being conducted to precisely understand interpretation of these parameters.

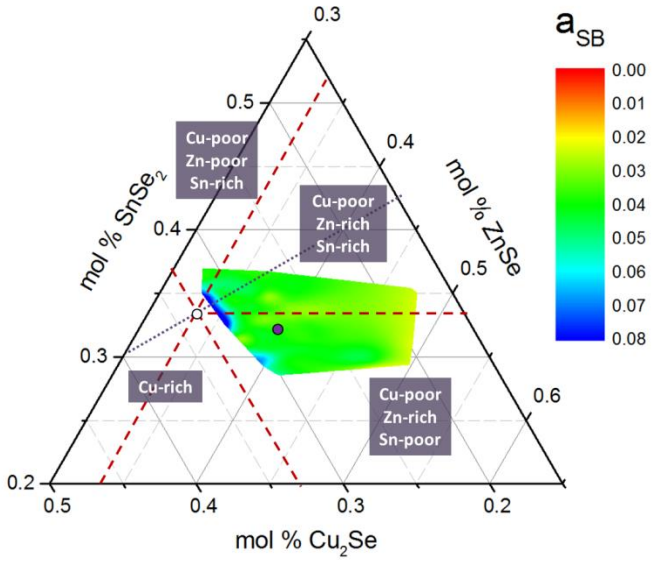

Figure 6.12 Plot of the average sub-bandgap absorptivity as a function of composition.

6.4.5 *Quasi-Fermi Level Splitting and Optoelectronic Quality from AIPL*

Figure 6.13 shows the quasi-Fermi level splitting (QFLS) as a function of composition. On the ternary diagram, we see that the changes in QFLS most closely follow changes in the Cu-content, while changes in either ZnSe or $SnSe_2$ content have only a minor impact. As the Cu-content is increased from very Cu-poor, it remains approximately constant up until about 29 mol% Cu_2Se, after which it begins slowly decaying. At approximately 31 mol% Cu_2Se the QFLS completely decays. This can clearly be seen in Figure 6.13b, where the QFLS is plotted as a function of the Cu/(Zn+Sn) ratio for 5 different Zn/Sn ratios. From this data, we can also see that as the Zn/Sn ratio increases, the onset of QFLS decay is shifted to lower Cu/(Zn+Sn) ratio. Comparing this data to the same data plotted on the ternary diagram, we see that this is merely an artifact of using the cation ratios Cu/(Zn+Sn) and Zn/Sn, not a result of the overall Zn-content. The region where the QFLS begins rapidly decaying corresponds with the red-shifting of the peak, an increase in the FWHM, and an increase in the sub-bandgap absorption indicating that this decay results from an increase the concentration of charged point defects, and thus EPFs. Beyond this region, the photoluminescence is too weak to be detected, and thus no PL parameters can be extracted. Interestingly, in Cu-gradients, just prior to the degradation, we consistently observe a narrowing of the FWHM and a dip in the peak position, bandgap, and QFLS. This behavior can clearly be seen in Figure 6.7b, Figure 6.8b, 8b, and Figure 6.13b. It is unclear what the source of this behavior is, but it may be indicative of the onset of Cu_xSe formation. During annealing Cu_xSe can aid in grain growth, however, if significant quantities remain after annealing, it will strongly degrade the optoelectronic properties.

Despite the strong dependence on Cu-content, the QFLS does not change significantly between growth under Sn-rich and Sn-poor conditions so long as the absorber is Cu-poor and Zn-rich. However, the QFLS is very small under Cu-poor/Zn-poor/Sn-rich conditions, indicating that the absorber can tolerate excess Sn only when there is also excess Zn. This may be due to the formation of uncompensated Sn_{Zn} anti-site defects, which can be passivated through forming the defect complex $[Zn_{Sn}+Sn_{Zn}]$ when excess Zn is present or from a sharp rise in the population of $[2Cu_{Zn}+Sn_{Zn}]$ which is expected under Zn-poor conditions [387]. We have attempted to deposit films with higher Sn content to probe how the optoelectronic properties change under Cu-poor/Sn-rich conditions in the transition from Zn-rich to Zn-poor conditions, however, due to significant Sn-loss, this was not possible.

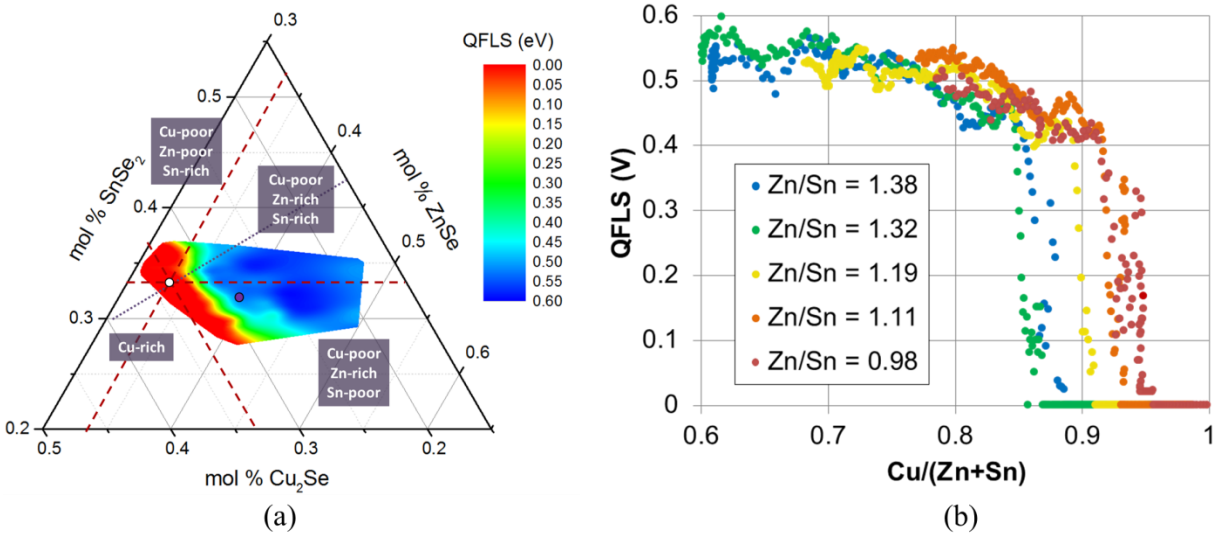

Figure 6.13 Plot of the QFLS (a) as a function of composition on a ternary diagram and (b) as a function of the Cu/(Zn+Sn) ratio at constant Zn/Sn ratio.

Because of the changes in the bandgap, comparing the QFLS of samples with different composition does not give an accurate representation of optoelectronic quality. To test how the materials with different composition compare, we have used the extracted bandgap to normalize the QFLS to the maximum theoretical QFLS determined using a detailed balance at 10 suns illumination ($QFLS/QFLS_{max}$). As shown in Figure 6.14, the materials that achieve the highest QFLS relative to the detailed balance limit are those with less than 29 mol% Cu_2Se. As the Cu-content is increased from this value, we find a significant decrease in the performance, further demonstrating that Cu-related defects play a critical role in determining material quality. However, based on this data alone, we cannot unambiguously determine the cause of the increase in QFLS with decreasing Cu-content. If the changes in bandgap result from a decrease in the valence band maximum (VBM), then the quasi-Fermi level for holes may also shift downward if the acceptor levels move with the band edge, increasing the QFLS. Because the overall optoelectronic quality ($QFLS/QFLS^{SQ}$) increases faster than the bandgap increases, there would also have be an increase in the quasi-Fermi level for electrons in the CB, indicating a reduction in electron trapping defects. Alternatively, if the acceptor levels do not move downward with the band edge (and since we expect a large concentration of acceptor-like defects), the quasi-Fermi level for holes could be pinned. As the VBM decreases, the acceptor would become deeper (closer to midgap from the VBM). This behavior would be consistent with work on disordered CZTS which found that as the Cu/Sn ratio was decreased, the energetic position of the dominant acceptor increases [413]. If this were the case, then all of the gains in QFLS would have to result from an increase the quasi-Fermi level for electrons, and thus a decrease in electron trapping defects. Determining the exact source of the gains is

important for further improving materials properties, but further study is necessary to elucidate the exact origin.

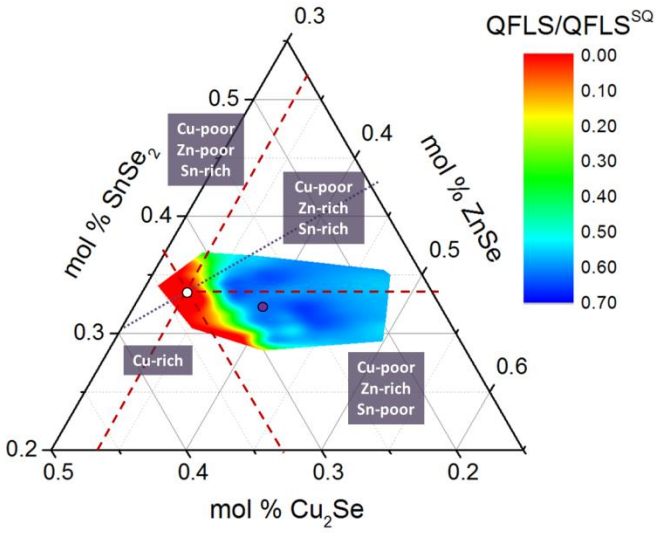

Figure 6.14 Plot of QFLS relative to the maximum possible QFLS as determined by a detailed balance calculation using the bandgap shown in Figure 6.10 and the measured illumination intensity. This parameter is means of comparing the optoelectronic quality of materials with different bandgaps.

Comparing our data to the predicted defect populations, we see good agreement between the decay of the optoelectronic quality (QFLS/QFLS,max shown Figure 6.14.) and the predicted onset of $[2Cu_{Zn}+Sn_{Zn}]$, which is expected to form in significant quantities (10^{16}) even under slightly Cu-poor/Zn-rich/Sn-poor conditions [387]. However, the degradation in the optoelectronic quality is stronger than we would expect based on the predicted energy level of this defect within the bandgap. This could be explained if the $[2Cu_{Zn}+Sn_{Zn}]$ defect has a particularly large capture cross section or alternatively by the formation of defects such as Cu_{Sn}, $[Cu_{Sn}+Sn_{Cu}]$, or $[Cu_{Sn}+Sn_{Cu}]^{+}$ which create states deeper within the gap, but are not predicted to be as favorable. The fact that we do not see significant degradation under very Cu-poor, Zn-rich, or Sn-poor conditions confirms that ZnSe and the defect complexes $[V_{Cu} + Zn_{Cu}]$ and $[Zn_{Sn} + 2Zn_{Cu}]$ are not particularly detrimental. However, for actual photovoltaic devices, extremely Cu-poor and Zn-rich conditions may lead to charge carrier transport issues (reduced mobility) due to co-existing ZnSe [288].

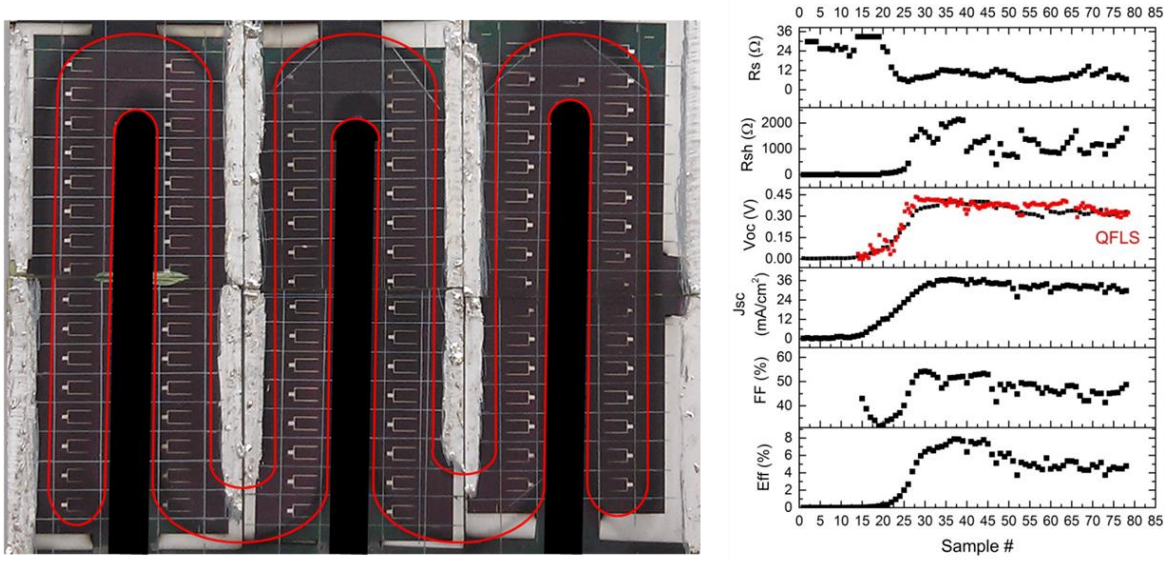

Figure 6.15 Device parameters from a composition gradient that was processed into solar cells. Note the very close agreement between the QFLS determined by fitting the AIPL to equation 2, using equation 4, and the measured Voc from devices.

6.4.6 *Photovoltaic Devices from a Composition Gradient and Comparison to AIPL*

To further validate the accuracy of the full spectrum PL fitting algorithm, and to ensure that the extracted QFLS accurately represents the open-circuit voltage, we have processed some of the spray lines into complete devices using the architecture SLG/Mo/CZTSSe/CdS/i-ZnO/ITO. The devices were measured under simulated AM1.5G illumination. A sample Cu-gradient is shown in Figure 6.15, where we show that the extracted QFLS qualitatively and quantitatively reproduces the measured trends in Voc. This demonstrates that our instrument has been properly calibrated and that we can clearly and precisely resolve trends in the open-circuit voltage using PL. Similar to what we observe in the photoluminescence data, as the film becomes Cu-poor, the material quality improves dramatically. The highest efficiency device from the spray line measures at 7.5% power conversion efficiency, the highest value reported for a spray-coated device, and comparable to previous reports of 8.3% efficient from spin coating [247].

6.5 CONCLUSIONS

We have systematically investigated native defect chemistry of CZTSSe by depositing continuous composition gradients and characterizing the films with absolute intensity photoluminescence. Consistent with previous reports, we find the highest optoelectronic quality material is obtained under Cu-poor and Zn-rich growth conditions. We show that this is true regardless of whether the film is Sn-rich or Sn-poor relative to stoichiometric. As the composition is changed, we see the most significant changes with variation in the Cu-content. From stoichiometric, as the Cu-content is decreased, the peak shifts to higher energy, narrows, and the QFLS increases. Initially these changes lead to an overall improvement in the optoelectronic quality of the material as indicated by the QFLS relative to the detailed balance limit ($QFLS/QFLS^{SQ}$), but beyond 29 mol% Cu_2Se, the gains in QFLS are entirely offset by the change in bandgap that occur with decreasing Cu-content. We attribute the changes in bandgap to reduced Cu-3d Se-3p repulsion resulting from to the large quantities of copper vacancies that are expected to form under Cu-poor conditions, similar to what has been observed in CISe. Based on this, we propose two possible mechanisms by which the QFLS increase, both of which require that the quasi-Fermi level for electrons moves closer to the conduction band, indicating that very Cu-poor conditions may lead to a reduction of defects in the gap in between midgap and the CBM. Comparing the changes in PL parameters to theoretical calculations of defect populations we find that the decay of optoelectronic quality with increasing Cu-content is consistent with the predicted onset of [$2Cu_{Zn}$ + Sn_{Zn}]. However, the decay is stronger than expected based on the predicted defect energy, and may indicate a particularly large capture cross section. The magnitude of sub-bandgap absorption was found to be approximately constant at all compositions suggesting that the defects that lead to electrostatic potential fluctuations may result from intrinsic disorder within the absorber (Cu_{Zn} and Zn_{Cu} antisite defects) and may not be eliminated through manipulation of the composition alone. However, by altering the thermal profile and cooling rate, it may be possible to affect these populations. Through optimization of the cation ratios, we have observed QFLS as large as 69% of the theoretical limit. This bodes well for the ability to incrementally increase the Voc. However, to reach commercially viable efficiencies, we will need to find ways to further reduce defect densities. For established thin film technologies CIGSe and CdTe, this has been done by finding extrinsic dopants which can passivate intrinsic defects, thus we propose a similar strategy here.

Chapter 7.
COMBINATORIAL EXPLORATION OF GERMANIUM ALLOYED KESTERITES

7.1 INTRODUCTION

The current world record CZTSSe device and most of the highest efficiency devices have been those containing primarily selenium (with less than 20% S/(S+Se). The best reported pure sulfide device is only 9.1% efficient,[414] while the world record device is 12.6% efficient.[1] This may be due to superior defect chemistry of the selenium containing compounds.[194, 195] However, higher selenium content materials have smaller band gaps, [161, 195] which is less desirable from a balance-of-systems perspective.

One method for increasing the band gap of kesterite materials is to alloy with germanium, forming $Cu_2Zn(Sn_xGe_{1-x})Se_4$. By doing this the band gap can be continuously varied from about 1.0 to 1.5 eV,[30, 178] the optimum range for photovoltaic devices. Analogous to gallium alloying on the indium site in CuInSe2,[415] germanium alloying on the tin site in $Cu_2ZnSn(S,Se)_4$ may also provide a means to reduce the defect density and create a back-surface field.[30] However, the Ge-containing kesterites, have been much less studied than their tin-containing relatives. This may be partly due to a perception that germanium is a less viable material for earth-abundant PV. Germanium is not a primary metal like tin, but rather a by-product of zinc production.[37] However, both Ge and Sn have similar abundance in the earth's crust. U.S. Geological Survey notes that "the amount of germanium potentially recoverable from coal fly ash is essentially unlimited", but demand for germanium has been too weak to prompt large-scale production from coal ash.[37]

Here we present a composition-spread study looking at the effects of Ge-alloying on the properties of sulfoselenide kesterites. Using spray-coated composition gradients, we show that there are significant losses in the optoelectronic properties at Ge-concentrations higher than about 50% Ge. We use absolute intensity photoluminescence (AIPL)[416] to show that the degradation at high Ge-content results from both unfavorable band alignment and a deep defect near 0.8 eV. However, we also show that the deep defect can be passivated after ageing in ambient conditions, leading to improvements in the Voc as large as 227 mV (an 84% increase). After ageing, devices from spray-coated layers reach efficiencies as high as 11.0%, which is the highest reported value for any Ge-containing kesterite.

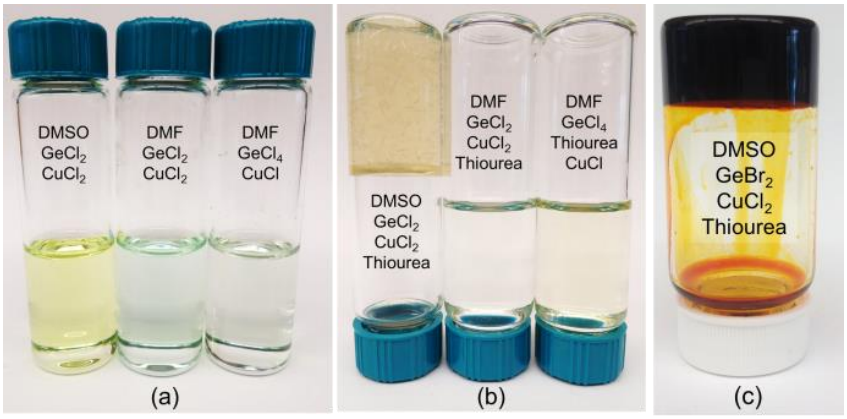

Figure 7.1 (a) Photograph of molecular inks containing dissolved copper and germanium species in either DMF or DMSO. (b) The same inks shown inverted 12 hours after the addition of thiourea. The DMSO ink has formed a rigid gel. (c) Photograph of an ink made using $GeBr_2$. The vial is shown inverted to show that the ink has gelled.

7.2 Germanium Ink Formulation

Several previous publications have demonstrated means to produce thin films of CZTGSSe, but these approaches have been primarily limited to nanocrystal[30, 110, 417, 418] or hydrazine[173] based techniques. Here we present a means to deposit films of CZTGSSe using a simple, non-toxic molecular ink. These inks allow for easy compositional tuning, have near 100% materials utilization, and can be easily scaled. We have previously reported formulating CZTS molecular inks by dissolving $Cu(II)(OAc)_2{\cdot}H_2O$, $ZnCl_2$, $SnCl_2{\cdot}2H_2O$, and thiourea in dimethyl sulfoxide.[28] The formulation of these inks relies on the redox reaction 2Cu(II) + Sn(II) → 2Cu(I) + Sn(IV) to generate species with the proper oxidation state.[419] However, attempts to replicate this chemistry using $GeBr_2$, GeI_2, or $GeCl_2$:dioxane instead of $SnCl_2{\cdot}2H_2O$ have proven unsuccessful. Although the germanium halides all have reasonable solubility in DMSO, the completed inks are not stable. Over time, they turn dark red-brown, gel, and form needle-like precipitates, an example of this is shown in Figure 1b and 1c. Similar behavior is also observed when the proper oxidation state precursors (no redox reaction required) $Ge(IV)Cl_4$ and Cu(I)Cl are used.

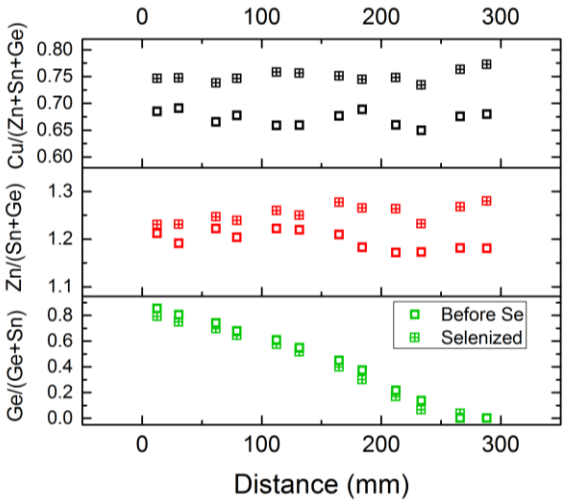

Figure 7.2 The composition of the gradient before and after selenization. Values were determined using EDS.

However, by substituting dimethyl formamide (DMF) for DMSO, a stable solution can be made using either $GeCl_2$:dioxane or $GeBr_2$. GeI_2 forms a translucent yellow solution, but precipitates are clearly present. It is also possible to form a stable solution using the proper oxidation state precursors $Ge(IV)Cl_4$ and CuCl in DMF, as shown in Figure 1b. Using precursors with the proper oxidation state is appealing in that it eliminates the need for the redox reaction to occur between Cu(II) and Sn(II). The redox reaction takes time to complete; may proceed to varying degrees depending on the concentration, time, temperature, etc.; and cannot proceed to completion when formulating off-stoichiometric inks (e.g. when $Cu/Sn \neq 2$). The use of $Ge(IV)Cl_4$ instead of $Ge:Cl_2$:dioxane also avoids the addition of dioxane (which is necessary to stabilize the $GeCl_2$), but because it is a fuming liquid precursor additional safety measures are required to handle it. These considerations may ultimately be important for process design, but the current experiments suggest that high quality material may be grown from DMF-based inks using either Cu(II) plus Sn(II) or Cu(I) plus Sn(IV) precursors (see Figure S2). Examples solutions after adding the copper precursor and after ageing the completed solution for 1 week are shown in Figure 1. In the present study, we used the proper oxidation state precursors Cu(I)Cl, $Zn(II)Cl_2$, $Sn(IV)Cl_4$, and $Ge(IV)Cl_4$ in DMF.

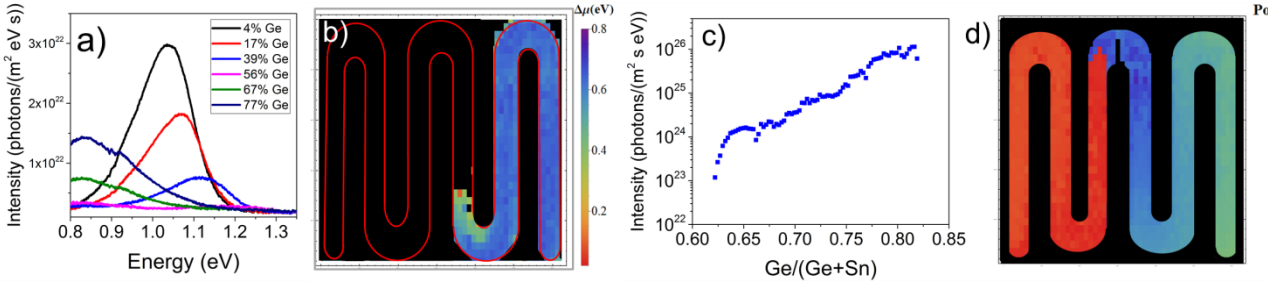

Figure 7.3 a) Change in the photoluminescence peak as a function of Ge/(Ge+Sn); b) Map of the PL peak position showing the onset of the low energy peak. The Sn-concentration increases from left to right along the length of the gradient; c) Increase in the absolute intensity of the peak near 0.8 eV as a function of Ge/(Ge+Sn) ratio.

7.3 Composition and Structure of Lateral Germanium Gradients

As a first step to understanding how Ge-alloying impacts the Sn-based kesterites, we deposited a gradient where Ge/(Ge+Sn) was continuously varied from 0 to 90%. Following deposition, the gradient was annealed in a Se atmosphere in a graphite enclosure to form the mixed sulfoselenide CZTGSSe. Issues with Sn volatility during high temperature annealing are well established for kesterite materials.[150, 151] Consistent with theoretical predictions,[152] we find that more Ge is lost than Sn. This is seen by a decrease in the Ge/(Ge+Sn) ratio and an increase in the Zn/(Sn+Ge) ratio after annealing. As shown in Figure 1, after selenization the Ge/(Ge+Sn) ratio decreases, while the Cu/(Zn+Sn+Ge) and the Zn/(Sn+Ge) ratios increase. Longer (or multiple) selenization steps lead to even more Ge loss, as shown in Figure S3. As a result of these losses, the maximum Ge/(Ge+Sn) value observed in the final film following a single selenization is only about 80%. This causes the band gap to vary between about 1.0 to 1.4 eV, [178] plus a nearly constant offset resulting from residual sulfur.

XRD data collected on the completed devices (SLG/Mo/CZTGSSe/CdS/ZnO/ ITO) confirms that the Ge is indeed being alloyed into the absorber and forming a $Cu_2Zn(Sn_xGe_{1-x})(S_ySe_{1-y})_4$ phase. As shown in Figure S4, there is a clear peak shift with increasing Ge-content, and we see the splitting of the (312) and (116) peaks into distinct peaks, as expected. The spectra are slightly shifted to higher angle due to residual sulfur, but all of the peaks can be indexed to the expected phases (including CdS, ZnO, ITO). No evidence of secondary phases was detected. However, they cannot be ruled out.

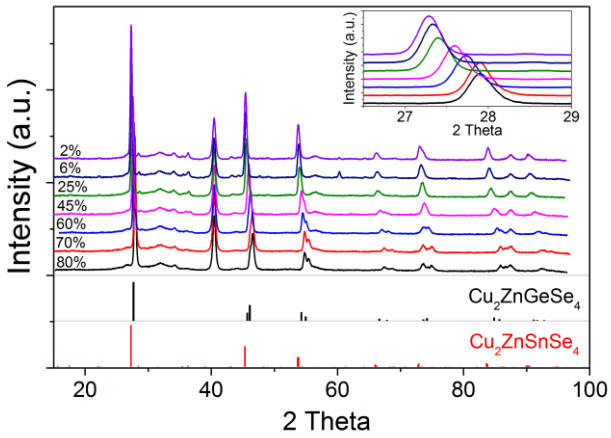

Figure 7.4. X-ray diffraction data from devices with varying quantities of germanium. The data correspond to a mixed $Cu_2Zn(Sn,Ge)(S,Se)_4$ phase. No secondary phases were observed.

7.4 Optoelectronic Quality of Absorber Layers from AIPL

Absolute intensity photoluminescence (AIPL) analysis of the gradients reveals significant changes in the radiative recombination pathway with Ge content. Representative spectra from different composition regions on the gradient are shown in Figure 3a. The pure-Sn samples have a peak centered at about 1.04 eV. As the Ge concentration is increased, the band gap increases, and thus the peak shifts to higher energy while decreasing in intensity. However, near 39% Ge a low energy PL peak begins to emerge near 0.8 eV. As the Ge concentration increases further the high energy peak decreases until it is below the detection limit, but the broad low energy peak near 0.8 eV increases in intensity. The increase in the absolute intensity of the 0.8 eV peak is shown in Figure 3c. With longer selenization times, the low-energy peak can be mostly eliminated, and a higher energy peak emerges.

By using 3 consecutive selenizations, we are also able to resolve the AIPL over a broader range of Ge/(Ge+Sn), and investigate changes in the optoelectronic properties at various stages of device processing. Figure 4 shows the change in the QFLS between the long selenization and after deposition of CdS/i-ZnO/ITO, noted as ΔQFLS. This data suggests that the formation of the p-n junction degrades the optoelectronic quality of the CZTGSSe layer, and that the degradation worsens with increasing bandgap or Ge/(Ge+Sn) ratio. This may be due to unfavorable band alignment (discussed below), but other explanations are possible. For example, the surface may become depleted of Ge and Sn due to the longer processing time, allowing Cd to more readily incorporate at the surface, or making the surface more prone to oxidative degradation. Alternatively the formation of the junction will change the position of the Fermi level near the front of the device, and thus change the occupation of defects.

Further work is necessary, but the results could explain why larger band gap kesterites and chalcopyrites have failed to achieve as high of efficiencies.

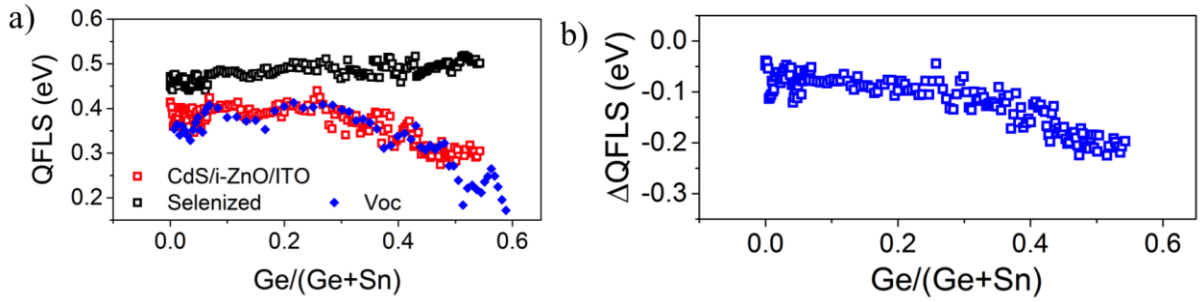

Figure 7.5 (a) QFLS measured after 3 consecutive selenizations and after deposition of CdS/i-ZnO/ITO. (b) Change in the quasi-Fermi level splitting measured after forming the junction. ΔQFLS = (QFLS after CdS/i-ZnO/ITO and before aging) - (QFLS after selenization). The increase in QFLS with aging is roughly constant across this range, and thus ΔQFLS has the same trend. Beyond Ge/(Ge+Sn) = 0.6 we are unable to extract the QFLS due to a secondary peak.

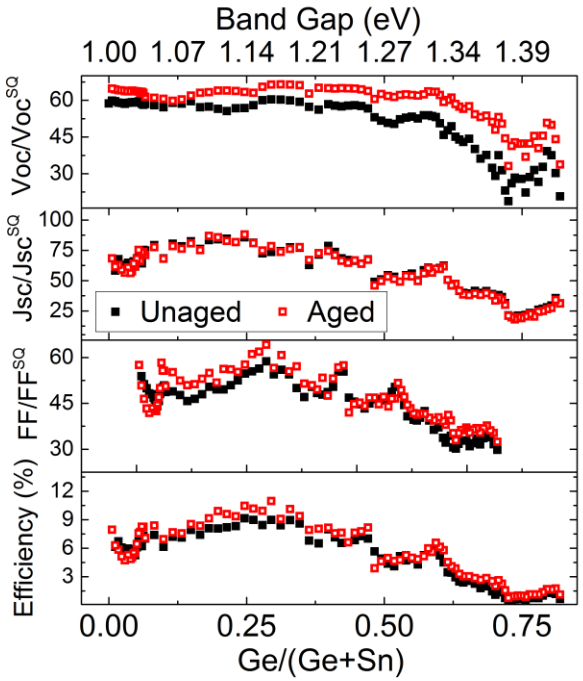

Figure 7.6 Current-voltage parameters before and after the sample was aged in the ambient lab environment. All values are normalized to the theoretical limit for the band gap. The bandgap was determined from the long-wavelength EQE decay (see Figure 6).

7.5 PHOTOVOLTAIC DEVICE PERFORMANCE

Gradients were processed into completed devices using standard techniques, including CBD of CdS, RF sputtering of i-ZnO/ITO, and then thermal evaporation of Ni/Al grids. A photograph of one of the gradients is shown in Figure S1. Current-voltage (J-V) and external quantum efficiency (EQE) were measured for each device. The current-voltage parameters are summarized in Figure 5. We find that the open-circuit voltage (Voc) of the devices increases with increasing Ge-content up until about 50% Ge (Figure S6). However, these gains are entirely offset by the increase in band gap. As shown in Figure 5, the Voc normalized to the theoretical limit for the band gap (Voc/Voc^{SQ}) remains approximately constant at 60% up until about 50% Ge. After 50% Ge, the Voc begins rapidly decreasing as does the overall device efficiency. The trend and peak in the efficiency that we observe near 25% Ge (Figure 5) results primarily from the trend in the carrier collection (Jsc). The short-circuit current normalized to the theoretical limit for the band gap (Jsc/Jsc^{SQ}), reaches a maximum near 25% Ge.

To determine where the gains in current collection come from, we measured the external quantum efficiency (EQE) along the length of the gradient. The spectra are shown in Figure 6a. From the EQE we can clearly see the shift in the absorption onset with increasing Ge content. The band gaps were obtained by extrapolating $(\ln(1\text{-EQE})^2$ versus energy for the long-wavelength EQE data (results in Figure 6b). Also shown in Figure 5b is the band gap calculated using the composition data, the theoretically predicted bowing parameter,[178] and a constant offset to account for residual sulfur. We find that there is good agreement between these two values, further indicating that the Ge is fully alloyed into the lattice.

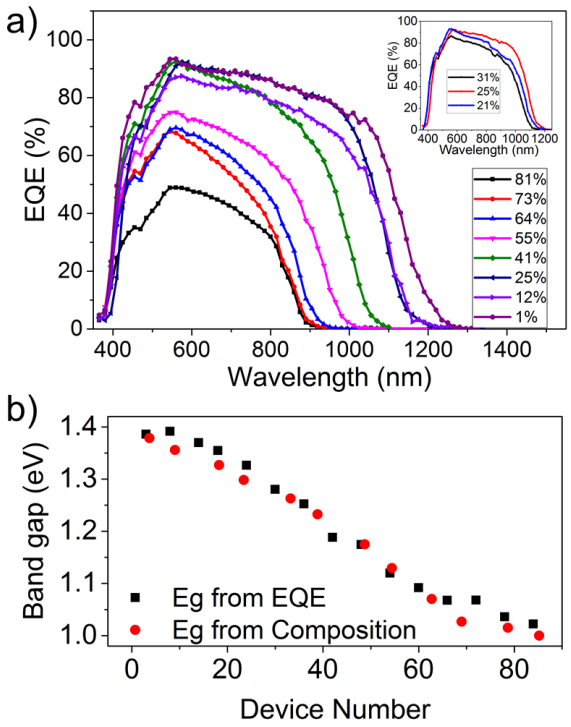

Figure 7.7 (a) External quantum efficiency of devices with varying Ge/(Ge+Sn). EQE of the devices with the highest efficiencies (inset). (b) Comparison of the bandgap determined from the EQE versus from bulk composition.

Comparing the EQE of devices with different Ge concentrations, we see that the decrease in Jsc/Jsc^{SQ} at Ge > 30% results from losses at all wavelengths. The EQE of the 81% Ge device reaches only a maximum of about 50%, while those with <35% Ge collect practically all the high energy photons (minus reflectivity losses). If we compare the EQE of the devices with the highest Jsc/Jsc^{SQ} (25% Ge), we find that they have superior collection efficiencies at longer wavelengths than the devices with either less or more Ge (Figure 6 inset).

7.6 Changes with Ageing

After allowing the completed devices to sit in an ambient lab environment for one month, we see dramatic changes in the materials properties. The AIPL at select compositions before and after ageing are shown in Figure 7. The low energy peak previously observed at higher Ge concentrations can no longer be detected. Even in the spectra without the 0.8 eV peak, we observe a significant blue-shifting of the peak, and an increase in the quasi-Fermi level splitting. The increase in the QFLS is commensurate with an increase in the open-circuit voltage as measured

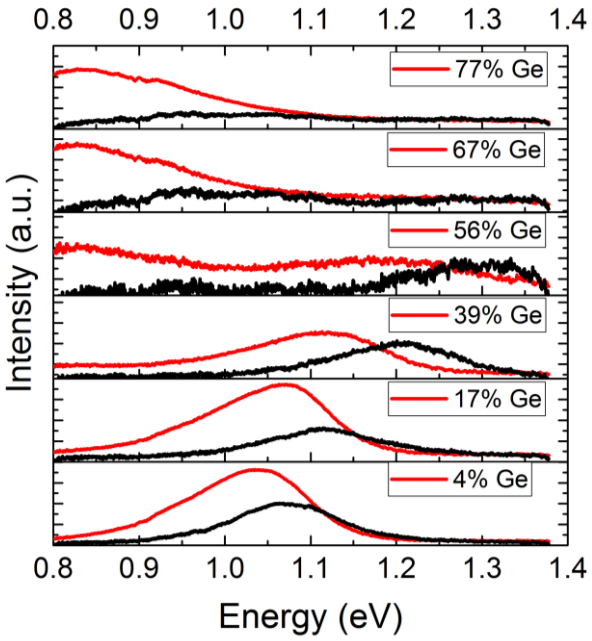

Figure 7.8 AIPL spectra before (red) and after (black) ageing in ambient for 1 month.

from the aged devices. As shown in Figure 5, the aged devices show large gains in the Voc, FF and consequently in the overall power conversion efficiency. The gains in Voc increase with Ge content, reaching values as large as 227 meV for a 70% Ge device (Figure S8). Despite the improvements, the highest efficiency devices are still located near 25% Ge, and the decay in efficiency still occurs near 1.3 eV. Figure 8 shows the J-V parameters of the champion spray-coated device before and after ageing. The aged device has the highest power conversion efficiency of any previously published Ge-containing kesterite (11.0%), and produces 63% of the maximum Voc (Voc^{SQ}), a value higher than that of even the record 12.6% CZTSSe device (58%). However, the device suffers from a high series resistance (1.34 ohm cm^2) leading to the relatively low fill factor. If the FF could be improved to 65%, a reasonable value for good kesterite devices, the device efficiency would increase to 12.8%, without an anti-reflective coating, the highest value for any kesterite device.

Note that if we calculate the Voc deficit using the relation Eg/q-Voc, as shown in Figure S8b, it appears that the champion device does not have the lowest Voc deficit. The lowest Voc deficit (calculated as Eg/q-Voc) has a minimum value of 0.548 for a nearly pure-Sn device (but still with a small amount of Ge). This value is substantially lower than that of the current world record device (Eg/q-Voc = 0.617),[1] high voltage double-emitter devices (Eg/q-Voc = 0.593),[420] and other recent high efficiency devices with a "low voltage deficit" (Eg/q-Voc = 0.57).[421] However, using Eg/q-Voc as a metric for material quality is misleading because a material with a 1.0 eV bandgap that produces 50% of it the theoretical maximum Voc (0.382 V) has a voltage deficit of 0.618 V, while a material with a 1.2 eV bandgap that

produces 50% of its theoretical maximum Voc (0.475 V) has a deficit of 0.725 V. The voltage deficit is larger for a larger band gap material, even though both materials achieve the same percentage of their theoretical limit. Thus the voltage deficit Eg/q-Voc is not a good metric for comparing samples with different band gaps. Comparing the open circuit voltage to the theoretical limit from a detailed balance provides a more accurate and universal comparison. The maximum theoretical Voc can be easily calculated over the range 0.8-2.5 eV using the linear relation $Voc^{SQ}(V) = 0.932* Eg(eV) – 0.166$.

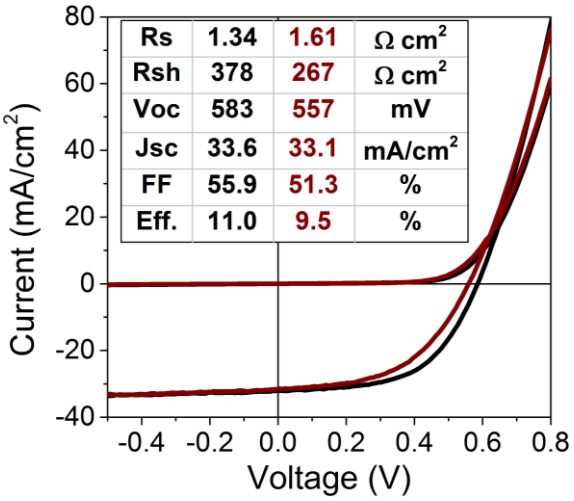

Figure 7.9 Current-voltage characteristics of the champion spray-coated Ge-alloyed device before and after ageing.

Based on the above data, there are at least two primary causes for the decrease in material quality when Ge/(Ge+Sn) is greater than 50%: (1) unfavorable band alignment or (2) an increasingly deep defect.

The AIPL data at different processing stages provides some of the strongest evidence for an unfavorable band alignment for the larger bandgap materials. Comparing the QFLS before and after deposition of CdS/i-ZnO/ITO (Fig. 4a) clearly shows that the QFLS in the completed device decreases with increasing band gap while the QFLS of the absorber layer alone increases with bandgap. Similarly, looking at the plot of the Voc/Voc^{SQ} vs band gap (Figure 5), we see that the highest Voc/Voc^{SQ} values occur when Eg < 1.30 eV. After about 1.30 eV the Voc quickly decays, even after ageing. These values are very similar to what has been observed with Ga-grading in CIGS.[169, 422] The band positions of CIGS and CZTSe are predicted to be very similar,[195] and as with Ga-alloying in CIGS, Ge-alloying in CZTSe is expected to primarily increase the CBM, while leaving the VBM almost unchanged.[195] Therefore, the conduction band minimum (CBM) in a material with a band gap of 1.3 eV would be about 0.3 eV higher than that of the pure selenide material. UPS measurements have shown that the band alignment

between CZTSe and CdS is a spike with an approximate conduction band offset (CBO) of about +0.3-0.4 eV.[161, 423] Therefore, as the Ge-content is increased, the CBO should transition from spike-like to cliff-like, near 1.3-1.4 eV. The decrease in the Voc/Voc^{SQ} starts in this range, and thus may be explained by an increasingly cliff-like band offset. Previous work has shown that a cliff-like offset reduces the maximum possible Voc from the device, and makes the device more sensitive to surface states at the absorber/buffer interface.[422] Initially, we suspected that the low energy peak observed at higher Ge concentrations could be the result of tunneling recombination from the CdS to the VBM (or acceptor states) in the CZTGSSe. To test this hypothesis, we mapped the photoluminescence at different stages of device processing, and found that the low energy peak is present even when no CdS is present. Thus the low energy PL peak must result from defect states entirely within the CZTGSSe or on the surface.

The other primary loss mechanism is the deep defect states which produce the PL peak near 0.8 eV. Previous work has reported a 0.8 eV defect CZTSSe, with depth that increases with sulfur content.[202, 424, 425] Sulfur and germanium are predicted to have a similar effect on the band structure. Both elements increase the band gap primarily by raising the CBM. Thus similar to what has been observed with sulfur, as the CBM increases due to Ge addition, the defect moves closer to mid gap and becomes a stronger recombination site. A schematic illustrating this hypothesis is shown schematically in Figure 9. Because of the proximity to the CBM, the defect likely is not beyond the demarcation level in CZTSe (the energy level where a CB electron, once captured, is equally likely to be emitted back into the conduction band or recombine with a hole from the VB) and thus is not as detrimental in CZTSe as it is in CZTS or CZTGSSe. Such a defect would explain the decay in the efficiency with increasing band gap, and would be consistent with the increasingly intense 0.8 eV PL peak (Figure 3c). Further, the reduction or elimination of this defect explains the enhanced device performance after ageing since the PL peak at 0.8 eV disappears with aging as well. At this time it is unclear how the defect is eliminated and further studies are necessary, but possible explanations include: (1) oxygenation, (2) migration of charged defects under the electric field formed by the junction, or (3) diffusion of defects or defect clusters. The fact this defect exists in the sulfide, selenide, and germanium containing kesterites suggests that the defect could be related to either Cu or Zn. Based on DFT calculations the most likely defect is a Cu_{Sn} or Cu_{Ge} defect.[24, 387] The Cu_{Sn} defect has a favorable formation energy near the front of the device (when the Fermi level is near the CBM), and is predicted to be increasingly favorable in larger band gap materials.[387] However, it is not clear how this defect would be eliminated with time. A chalcogen vacancy, such as V_{Se}, that is slowly oxygenated (forming O_{Se}) could also explain the behavior.

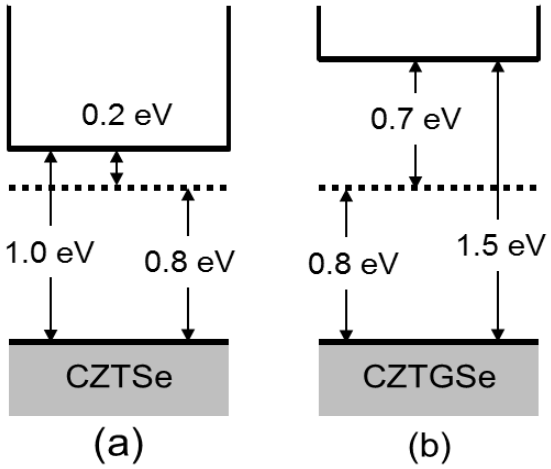

Figure 7.10 Schematic showing the increasing depth of a defect as the CBM is increased. Such a defect could explain the decay of the Voc with increasing Ge content.

7.7 CONCLUSIONS

We have used composition spread libraries to investigate the changes in material quality that occur with Ge-alloying of CZTSSe. The highest efficiency devices at Ge/(Ge+Sn) ratios near 0.25, corresponding to a band gap of about 1.2 eV, very similar to the optimum bandgap in CIGSe. This maximum results from improved Jsc and FF. We present data suggesting that the decay of the efficiency for band gaps larger than 1.3 eV results from both an unfavorable band alignment and from a deep defect located about 0.8 eV above the VBM that moves towards mid gap as the band gap increases. Such a defect has been previously reported for both CZTS and CZTSe, and we observe a broad PL peak centered about this energy for Ge/(Ge+Sn) > 50%. The low energy peak may be eliminated by using longer selenization times or ageing the sample in ambient for about 1 month. Thus far longer selenizations have not lead to improved device performance, but after ageing we see significant improvements in the devices. Following ageing we demonstrate an 11.0% efficient spray coated CZTGSSe that achieves 63% of the theoretical Voc, the best of any reported high efficiency kesterite device.

Chapter 8.
COMBINATORIAL EXPLORATION OF EXTRINSIC DOPANTS IN KESTERITES

8.1 INTRODUCTION

In the development of both Cu(In,Ga)Se_2 (CIGS) and CdTe thin film solar cells, one of the most effective strategies for improving device efficiency has been to find extrinsic species that can dope the absorber layer and passivate intrinsic defects. $CdCl_2$ treatments of CdTe absorber layers enhance grain size,[426] passivate grain boundaries and surfaces,[427, 428] and significantly improve the overall efficiency. For CIGS it has been shown repeatedly that sodium improves conductivity, open-circuit voltage, and fill factor.[335, 341, 342] Potassium (K) surface treatments have also been shown to benefit CIGS by aiding in the formation of a buried homojunction and allowing for a thinner CdS layer.[401, 429] Antimony (Sb) and Bismuth (Bi) have both been shown to aid in the crystallization of CIGS, leading to improved efficiency, particularly for devices processed at lower temperatures.[430-432]

Although these extrinsic species have been experimentally shown to benefit the absorbers, the exact mechanism is often still debated or unknown. For example, the benefits of sodium in CIGS were discovered when researchers substituted soda-lime glass for more traditional alkali-free substrates.[341] Soda-lime glass was used because it had a thermal expansion coefficient closer to that of CIGS, but it was quickly discovered that the anomalously high performance resulted from sodium diffusion into the absorber layer. Despite this realization, the exact role of Na in CIGS is still debated, and has been the subject of intense research over the last several decades. Several models have been proposed to explain the observed behavior including: the defect chemical model,[340] the positive electron acceptor model,[213, 214] and the neutral hole barrier model.[212, 217] These models differ in mechanism, but agree that Na helps passivate grain boundaries, improves conductivity, and reduces defect densities.

In recent years, concerns about the price and availability of the elements In and Te have spurred research into earth-abundant thin film materials. One of the leading candidates is

$Cu_2ZnSn(S,Se)_4$ (CZTSSe), a material which bears many resemblances to CIGS in its structural and electronic properties, but is comprised of abundant, low-cost primary metals (metals mined for directly). CZTSSe devices have reached 12.6% efficiency using hydrazine-based inks,[1] and several groups have demonstrated efficiencies over 11% using a non-toxic DMSO based ink.[97, 421] However, further efficiency improvements are needed to be competitive with current technologies. Comparing the performance of the world record CZTSSe device to the theoretical limits under AM1.5G illumination, it is clear that a low open-circuit voltage limits the power conversion efficiency. The world record CZTSSe device collects 81% of the maximum current (Jsc^{SQ}) but only produces 58% of the maximum voltage (Voc^{SQ}). Studies indicate that the low voltage results from a large quantity of intrinsic defects.[2, 3] These defects are relatively shallow and are mostly compensated, but still lead to significant electrostatic potential fluctuations and reduced carrier mobility.[2, 3, 398] In previous work, we used a high-throughput screening technique to precisely show how the optoelectonic properties (and thus intrinsic defects) change when the absorber is grown under a broad range of different stoichiometries.[365] We found that certain deep defects can be reduced or eliminated by growing the material under non-stoichiometric conditions, but a significant quantity of charged defects are still present even in materials with the best optoelectronic quality. Based on these results, and following the lessons learned from the development of CIGS and CdTe, we proposed investigating extrinsic species as a means to passivate intrinsic defects. We reported the results of ink-based doping of Na, Hf, and Cd in concentrations ranging from 0 to 10%, and showed that although none of the dopants had a strong impact on the optoelectronic properties, Na-doping improves FF and thus can lead to higher efficiencies.[365] Here we greatly expand upon this work, presenting the results from 25 different extrinsic elements, paying particular attention to the group-I (alkali) elements. The elements evaluated in this way are summarized in Figure 1. From our screening we find that that the kesterite absorber is quite tolerant of many extrinsic elements, even at relatively high concentrations (>1 at%). We identify several species that are highly detrimental and several which preliminary investigations suggest may be beneficial. These results have important implications for process design (e.g. avoiding Fe contamination), the use of metal foil substrates, and controllably doping CZTSSe.

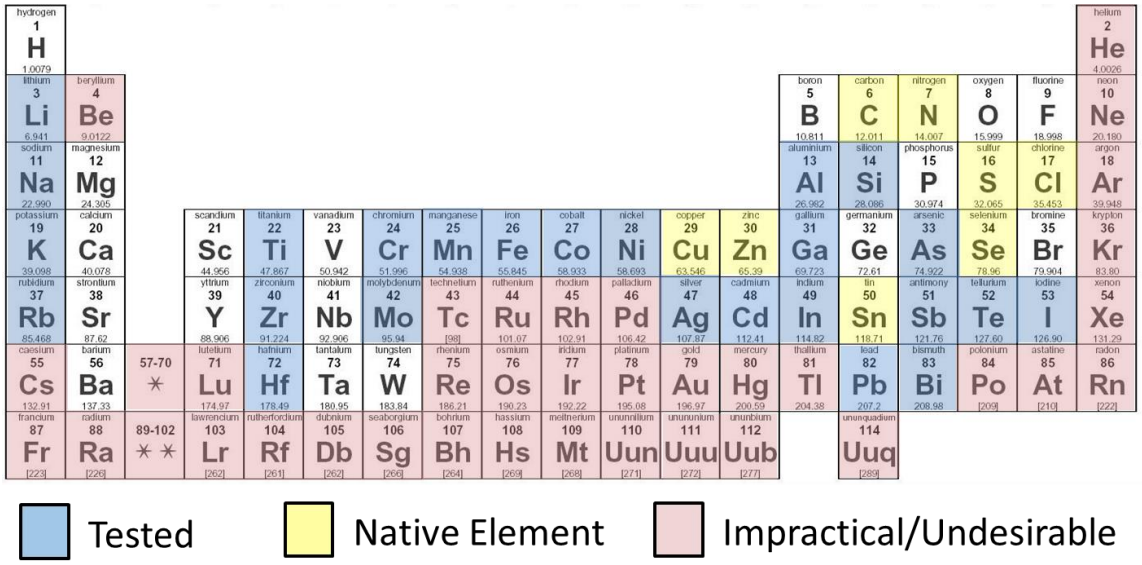

Figure 8.1 Summary of elements screened using our high-throughput testing process. The elements were added to the ink as metal chlorides in concentration ranging from 0 to as high as 10 mol%. Carbon, nitrogen, and chlorine originating from thiourea and metal precursors are likely present to some degree in all the samples.

8.2 EXPERIMENTAL

A single molecular precursor solution was prepared by mixing $CuCl_2$, $ZnCl_2$, $SnCl_2$, and thiourea in either dimethyl sulfoxide (DMSO) or dimethyl formamide (DMF) similar to previous reports.[28] The precursors were mixed targeting a composition of Cu/(Zn+Sn) = 0.75 and Zn/Sn = 1.05. The solution was then divided into multiple vials and an extrinsic dopant was added to each, and one was reserved with no dopant added ("Undoped"). The extrinsic dopants utilized, the precursor, and the concentration added are summarized in Table 1. A continuous gradient was formed via the combinatorial mixing of the doped inks with the Undoped solution to produce films with a dopant concentration that increases along the length of the line. Films were deposited using a custom-built deposition system based on a Sono-Tek ultrasonic spray coater fitted in a modified glovebox and fed with an array of independently controlled syringe pumps.[365] The films were sprayed onto both quartz substrates and Mo-coated soda-lime glass. Following deposition, the films were annealed in a tube furnace for 20 minutes at 550°C with excess selenium. Absolute intensity photoluminescence (AIPL) mapping was performed using a confocal instrument with a 785 nm laser excitation over a 110 x 110 μm spot size with a 1.2 mm

x 1.2 mm mesh. The data was then analyzed using a full spectrum peak fitting algorithm detailed in a previous publication.[416] For further characterization doped films were spray coated on Mo/SLG and processed into completed devices using standard techniques including CBD of CdS, RF sputtering of i-ZnO then ITO, and thermal evaporation of Ni/Al grids. Each spray coated substrate produces 84 devices with approximately 0.11cm^2 area. Devices were also made via spin coating, using a process similar to that previously published.[419] All devices were tested under simulated AM1.5G illumination.

TABLE 1. EXTRINSIC ELEMENTS USED IN THE SPRAY GRADIENTS, THEIR PURITY, AND THE CONCENTRATION IT WAS ADDED TO THE INK IN.

Extrinsic Species	**Precursor (purity)**	Conc.
Lithium	LiCl (99%+) / LiI (99.9%)	2%
Sodium	NaCl (99%) / NaI (99.5%)	2%
Aluminum	$AlCl_3$ (99.99%)	10%
Silicon	$SiCl_4$ (99.999%)	5%
Potassium	KCl (99%) / KI (99%+)	2%
Titanium	$TiCl_4$ (99.999%)	10%
Chromium	$CrCl_3$ (99.99%)	5%/1%
Manganese	$MnCl_2$ (99.99%)	5%
Iron	$FeCl_2$ (99.998%)	10%
Cobalt	$CoCl_2$ (99.999%)	5%
Nickel	$NiCl_2$ (99.99%)	5%
Gallium	$GaCl_3$ (99.999%)	10%
Arsenic	$AsCl_3$ (99.99%)	5%
Rubidium	RbCl (99%) / RbI (99.8%)	2%
Zirconium	$ZrCl_4$ (99.99%)	5%
Molybdenum	$MoCl_5$ (99.999%)	5%
Silver	AgCl (99.999%)	5%
Cadmium	$CdCl_2$ (99.999%)	10%
Indium	$InCl_3$ (99.999%)	10%
Antimony	$SbCl_3$ (99.95%)	10%
Tellurium	Te (99.999%)	2%
Iodine	I_2 (99.999%)	5%
Hafnium	$HfCl_4$ (99.999%)	10%
Lead	$PbCl_2$ (99.999%)	5%
Bismuth	$BiCl_3$ (99.999%)	10%

8.3 GROUP-I DOPANTS ON QUARTZ SUBSTRATES

Group-I elements are known to have a highly beneficial effect on $Cu(In,Ga)Se_2$, and due to the similarities between chalcopyrites and kesterites it is likely that they will have a similar effect on kesterites. However, because to the different defect chemistries of these two materials, the optimum concentration and the way in which the dopants interact with native point defects will be very different. For example, in chalcopyrites the primary effect of sodium is to occupy copper sites (Na_{Cu})[334] which helps prevent the In_{Cu} defect. However, it has also been shown that sodium will occupy In sites (Na_{In}) providing an additional shallow acceptor.[337] In kesterites, sodium is predicted to readily occupy either Cu or Zn sites.[433-435] Multiple experiments have found that sodium doping increases the hole concentration and mobility and reduces the activation energy for conduction.[436-438] The first two effects likely result from Na_{Cu} preventing the donor like Zn_{Cu}, while the latter may be from Na_{Zn} forming an additional shallow acceptor.[434] These effects lead to increased Voc, FF, and thus the overall efficiency.[365, 439-441] Similar results have been found for lithium doping of CZTSSe,[97] though the benefits appear to be greater because Li substitutions are even more favorable than Na substitions.[433] Here we use ink-based doping to investigate how the concentration of the Li, Na, K, and Rb impacts the optoelectronic properties of CZTSSe.

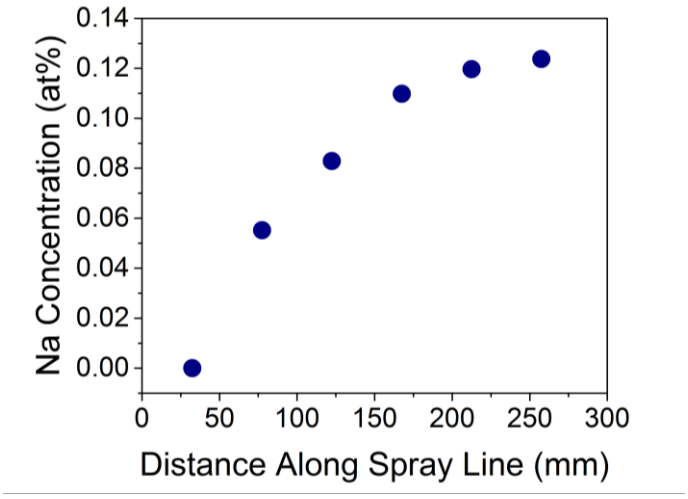

Figure 8.2 A typical concentration profile measured on a gradient following selenization. The concentration of sodium increases along the length of the spray line. The concentration was determined using ICP-MS and is calculated as Na/(Cu+Zn+Sn).

Continuous concentration gradients were deposited on high purity quartz substrates spanning 0.01 to 0.30 at%. A typical concentration profile following selenization is shown in Figure 2. The concentration is calculated as M/(Cu+Zn+Sn) where M = Li, Na, K, or Rb. Immediately following selenization the gradients were mapped using absolute intensity photoluminescence (AIPL) while held under vacuum (< 1 mTorr). Using AIPL we can accurately extract the quasi-Fermi level splitting (QFLS), the band gap (Eg), and the extent of sub-bandgap absorptivity (a_{SB}).[416]

An accurate measure of the band gap is important because one of the proposed mechanisms by which Na benefits CIGS (and CZTSSe) is by forming a fluxing agent that aids in the incorporation of Se.[442] In the present study a measure of the band gap is also important because we are selenizing a sulfide material and variation in the S/Se ratio can cause variation in the band gap. This can artificially inflate the QFLS without actually increasing material quality. The band gap determined from a full spectrum PL fit is shown in Figure 3 for each group-I element. Comparing to the baseline (gray solid line), we see that as the Li concentration increases, the band gap also increases. The opposite trend occurs with Rb; the bandgap decreases with increasing concentration. The change in band gap may result from enhanced (or reduced) Se-fluxing or from incorporation of the group-I element into the lattice. Given the extremely large ionic radii of Rb (152 pm) it is unlikely that it will be incorporated. However, Li (59 pm) has a similar radius to Cu, Zn, and Sn (60, 60, and 55 pm, respectively), and thus may easily be incorporated. For lithium, previous work suggests that it can readily incorporate into the lattice, occupying both Cu and Zn sites,[97] but no previous studies have investigated Rb.

Because we know that there is a change in the band gap, the only way to make a fair comparison of the QFLS between samples is to normalize to the theoretical limit (QFLS/$QFLS^{SQ}$). This is done in Figure 3 for the various group-I elements. Among the dopants, both Li and Rb stand out as having the largest effects. Despite the increase in band gap, Li doping still significantly improves the QFLS/$QFLS^{SQ}$, reaching a maximum near 0.30 at%. For Rb, the relatively smaller band gap means that when normalized to the limit, the QFLS/$QFLS^{SQ}$ is actually as large as that seen with Li. However, the concentration of Rb where we observe the greatest enhancement (0.03 at %) is much lower than that for Li. Neither Na nor K was found to result in any significant changes to the QFLS/$QFLS^{SQ}$ over the measured range.

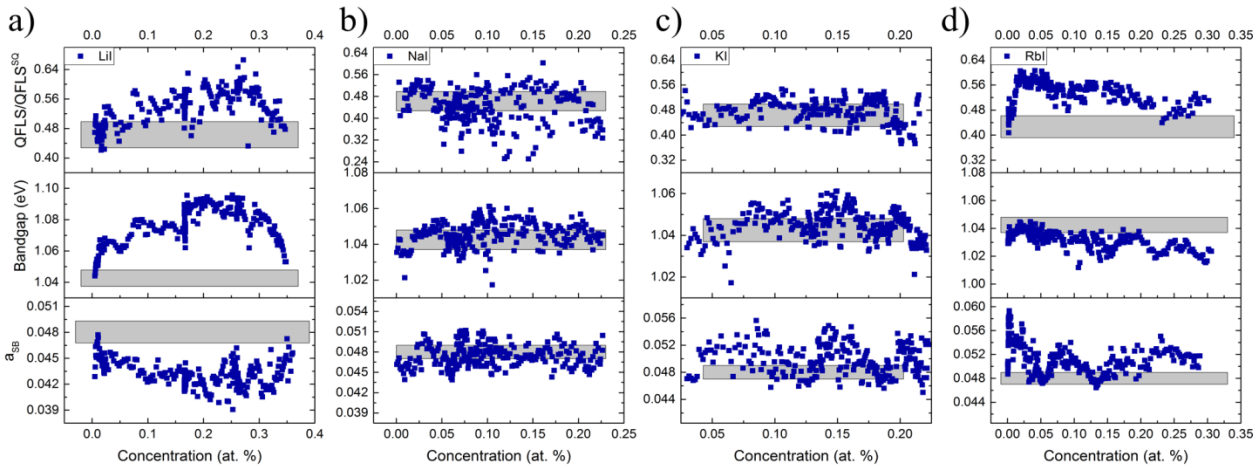

Figure 8.3 Summary of photoluminescence parameters as a function of the concentration of the group-I dopants (a) Li, (b) Na, (c) K, and (d) Rb. The parameters include the quasi-Fermi level splitting (QFLS) normalized to the theoretical limit based on the band gap ($QFLS^{SQ}$), the band gap, and the sub-band gap absorptivity (a_{SB}).

To better characterize what effect the group-I dopants have on the absorber we look at the sub-bandgap absorptivity. The sub-bandgap absorptivity is determined from the full spectrum PL fitting algorithm and is defined in Equation 8.1.

$$\bar{a}_{SB} = \frac{1}{E_g}\int_0^{E_g} a(E)dE \qquad (1)$$

Kesterites are a highly disordered material, and the large populations of charged defects lead to electrostatic potential fluctuations (EPFs). These fluctuations lead to sub-bandgap absorption and thus emission, and can lead to significant losses in the Voc. EPFs cause the PL peak to broaden and shift to energies below the bandgap. The more charged defects, the greater the magnitude of EPFs, and thus the larger the sub-bandgap absorptivity. Therefore, a_{SB} is a useful measure of material quality because it is directly related to the number of charged defects. The value of a_{SB} for each of the group-I gradients is shown in Figure 3. We find that the only elements that significantly alter a_{SB}, as compared to the baseline, are Li and Rb. If lithium does incorporate into the lattice, the reduction in a_{SB} may result from Li passivating charged copper vacancies or preventing Zn_{Cu}. This would make sense from a steric perspective, and would be consistent with the observation of increased band gap. The slight increase in a_{SB} for Rb containing samples may

result from increased formation of a defective kesterite layer, and is discussed in greater detail below.

8.4 Devices with Group-I Dopants on Soda Lime Glass

To determine whether the effects of the group-I dopants could be directly translated into improvements in device performance we spray coated films on Mo/SLG substrates and processed them into completed devices. The films were doped using group-I chlorides and the final concentration was measured using ICP-MS to be 0.21±0.05, 0.26±0.04, 0.25±0.06, and 0.05±0.01 at% for Li, Na, K, and Rb, respectively. Making devices allows us to resolve changes in other device parameters such as fill factor and current collection, however, because the films are deposited on SLG there will be an additional flux of sodium from the substrate. This is important to keep in mind when comparing the results to the samples on quartz substrates. We have also found that annealing the completed devices on a hotplate at low temperature (150 °C for 5 min) leads to significant improvements in the overall efficiency. A comparison of the current-voltage characteristics before and after annealing is shown in Figure S1. The only sample which did not benefit from annealing was the KCl sample, which had losses to both Voc and FF. All other samples had as good or better Voc and FF after annealing. The origin of the improvement is unclear, but it is possible that the anneal increases the carrier concentration in the ITO or helps to improve the interfaces. Consistent with our PL study, we find that all of the dopants, except KCl, lead to slight improvements in Voc (though not necessarily Voc/Voc^{SQ}). However, only Li lead to an overall improvement in device performance compared to the baseline ("None"). Aided by a shunt resistance that was 2-3x higher than any of other devices, the Li-doped samples had the best FF, as shown in Figure 4a. In contrast, the efficiency of both the Na and Rb devices was hampered by a low FF. The K devices suffered from poor shunt resistance. For Li, these results are consistent with what we have observed using traditional device making.[97] Overall we consistently find that Li doped samples out-perform both the un-doped samples as well as the other group-I dopants. Rb doping still appears promising, and is investigated further in the following section.

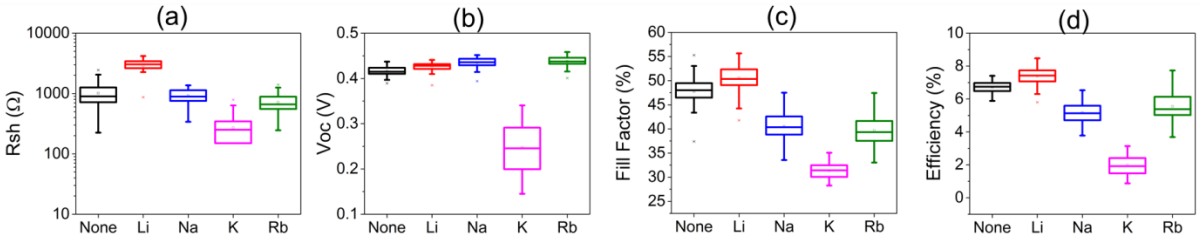

Figure 8.4 The shunt resistance (a), open-circuit voltage (b), fill factor (c) and efficiency (d) of spray coated devices with added group-I dopant. Statistics are based on measurement of 80 devices, each approximately 0.11cm^2.

8.5 AIPL ON NON-GROUP-I ELEMENTS

In addition to the group-I elements, we have also screened a wide variety of other extrinsic species as summarized in Figure 1. There are many different cation sites in the kesterite lattice and thus a large number of ways in which an extrinsic species may interact with it. The understanding of the defects in kesterites is still in its infancy; therefore, we have opted to test many different species of varying ionic radii and oxidation states. As a first step, concentration gradients were deposited and then mapped using absolute intensity photoluminescence (AIPL).[416] From the AIPL spectra we extract the quasi-Fermi level splitting, which we use as our primary performance metric. We used the QFLS as our primary metric because it is directly related to the quantity and type (depth, valence, etc) of defects. All thin film solar cells suffer from low Voc, and even the best kesterite devices produce only 58% of the theoretical Voc.[1] Therefore, our first step in screening extrinsic species was to look for elements that significantly improve the QFLS. The QFLS as a function of extrinsic dopant concentration for 25 different extrinsic species are shown in Figure 5.

Overall, we find that CZTSSe is quite tolerant of extrinsic species, even in the high concentrations we have tested here. Many of the species, such as $GaCl_3$, $ZrCl_4$, $HfCl_4$, $PbCl_2$, and I_2, have almost no detectable impact on the QFLS over the sampled concentration range. For Zr and Hf, this is consistent with first principles studies which have reported that the quaternary compounds containing these elements are not stable.[176] Therefore, the Zr and Hf added to the film forms binary or ternary phases that phase segregate leaving a (mostly) unadulterated CZTSSe phase. In actual devices, this may lead to complications, particularly if the secondary phases are electrically active. However, the most detrimental elements are the transition metals

located near copper on the periodic table. Iron, cobalt, and nickel all strongly degrade the QFLS, likely because they can readily incorporate into the lattice forming $Cu_2(X,Zn)Sn(S,Se)_4$ where X = Fe, Co, or Ni. They will likely also form donor-like defects by substitution on Cu-sites, as Zn commonly does in CZTS.[387] Other species, such as $AlCl_3$, $MnCl_2$, and the group-V elements $AsCl_3$, $SbCl_3$, and $BiCl_3$ have a slightly negative impact on the QFLS, suggesting they may be incorporated to some extent, but they are not nearly as detrimental as Fe, Co, or Ni.

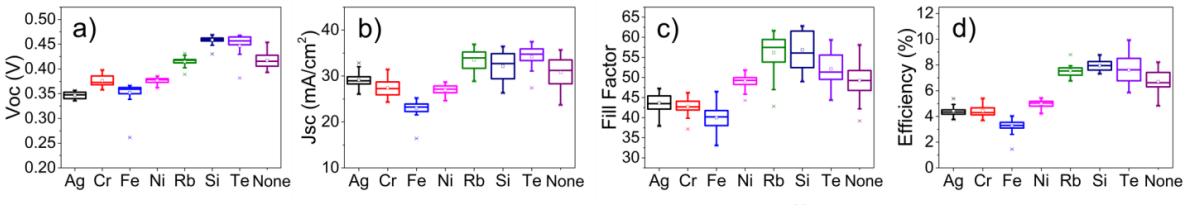

Figure 8.5 Current-voltage parameters from spin coated devices made with extrinsic dopants. The samples were measured under simulated AM1.5G illumination. 27 devices from 3 different substrates were measured for each dopant.

It is important to bear in mind the method by which the extrinsic species are being supplied. We have chosen metal chlorides because many of them can be complexed with thiourea then decomposed to form metal sulfides. Metal chlorides are readily available in high purity and generally have good solubility. This makes it very easy to test a broad range of species, but providing the extrinsic species in this way does have limitations. The exact form and method by which a species is provided can have an enormous difference. For example, both Sb and Bi were of particular interest because they have been shown to improve low-temperature crystallization of CIGS.[431, 432] In the published reports, Sb/Bi is supplied as a metal thin film. Because of the low melting point of both Sb and Bi, it is believed that they act as a fluxing agent to improve grain growth. However, because we supply the Sb/Bi as a metal chloride the behavior is different. The species are still available for incorporation into the lattice, but large grain growth is not observed. An example of this is shown in Figure S2. Bismuth selenide has precipitated as a secondary phase, but the grain growth in the surrounding area is poor. Therefore, our finding that $SbCl_3$ and $BiCl_3$ degrade CZTSSe should not be misinterpreted to mean that Sb and Bi cannot benefit CZTSSe, or that it that either species does not enhance the growth of CZTSSe. Our finding is that bulk doping with $SbCl_3$ or $BiCl_3$ does not benefit CZTSSe or enhance the grain growth.

8.6 Electrical Characterization of Devices with Select Extrinsic Dopants

Based on the results of the PL screening, we selected Ag, Cr, Fe, Ni, Si and Te for further investigation. Ag, Cr, and Si where chosen because they showed at least some sign of having a positive effect, while Ni and Fe were chosen to validate the negative effect that we have seen. We additionally chose to investigate Te doping. The addition of Te was accomplished through first synthesizing a tellurium tetrathiourea chloride complex following previous publications.[443] The dopants were added to the inks in quantities ranging from 1-5 at% as specified in Table S2.

Devices were made via spin coating following a procedure similar to that used in previous reports [419]. The resulting current-voltage parameters are summarized in Figure 6. Consistent with the PL results, we find that both Ni and Fe have a detrimental effect on the devices as compared to the undoped baseline ("None"). We also find that the Cr sample and the Ag sample perform poorly, primarily as a result of low fill factor and Voc. The Rb, Si, and Te samples all performed as well or better than the baseline and were further characterized.

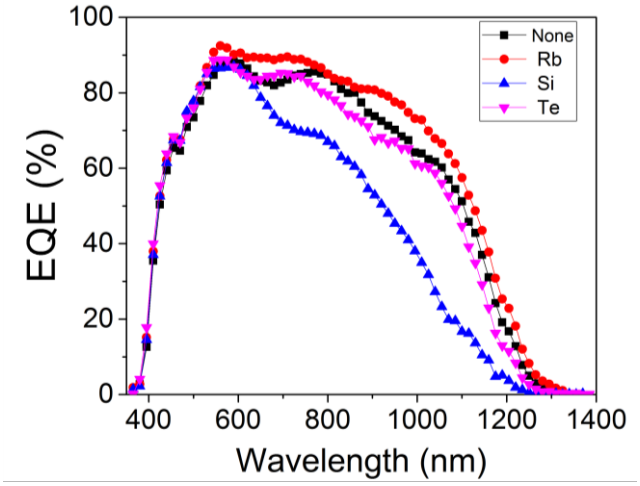

Figure 8.6 External quantum efficiency of the champion devices made with extrinsic dopants.

First principles studies indicate that both Si and Te should be able to substitute into the kesterite lattice and form a stable compound. Silicon is expected to substitute on the Sn site to form the larger bandgap material $Cu_2Zn(Sn,Si)Se_4$,[178] while Te will substitute on the chalcogen site to form a smaller band gap material $Cu_2ZnSn(Se,Te)_4$.[176] However, for the concentrations we have explored (5%), the effect on the band gaps should be minimal. Extrapolating the low energy tail

of the EQE (Figure 7), we approximate the bandgap of the Si, Te, Rb, and undoped devices to be 1.02, 1.00, 0.97, and 0.99 eV, respectively. Compared to the other devices, we see that the low Jsc of the Si device results from poor carrier collection at long wavelengths. This could result from a thin absorber, poor grain growth, high reflectivity, or a Si-related bulk defect.

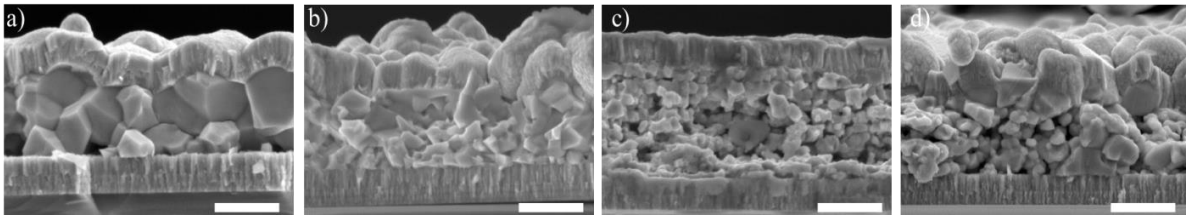

Figure 8.7 Cross sectional SEM images of the (a) undoped, (b) rubidium, (c) silicon, and (d) tellurium containing devices. The scale bars are 1 μm.

Cross sectional SEM images (Figure 8), show that the absorber layers are about 1.5 μm thick and have quite different morphologies. Interestingly, the undoped device (8a) shows the best grain morphology despite having the lowest efficiency. The grains of the Si and Te devices are both quite small and significant voids are clearly present, yet these devices had the highest efficiencies. Compared to the other devices, the Si-containing sample was very planar and appears very smooth and reflective. It is unclear what causes this difference, but the smoothness of the interface may contribute to the high FF.

The champion devices from each extrinsic dopant were further characterized using drive-level capacitance profiling (DLCP) at 200K and 300K. The DLCP derived defect densities are shown in Figure 9. At 300 K and 1 kHz, the Rb, Si, and Te devices all show similar profiles, but have a lower overall defect density than the undoped sample. Interestingly, the defect densities correspond with the device efficiencies. The Te device had the lowest defect density and the highest efficiency; the undoped sample had the highest defect density and the lowest efficiency. This suggests that the measured difference in the defect density results from a reduction in the quantity of deeper defects, not just variation in the carrier concentration.

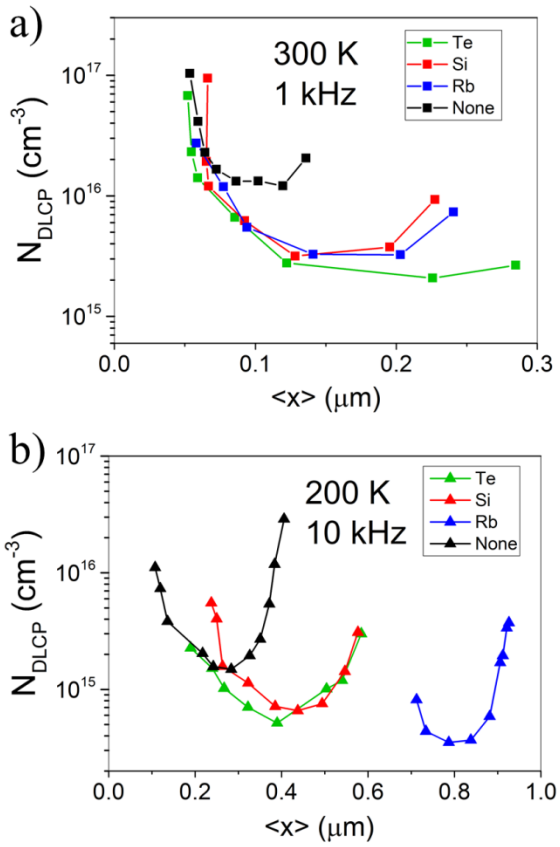

Figure 8.8 DLCP derived defect densities at 10 kHz for measurement temperatures of 300 K (a) and 200 K (b)

The profiles at 200 K at 10 kHz are shown in Figure 9b. Compared to the higher temperature and low frequency data, we see very significant differences between the samples. As expected, the defect density is lower for all of the samples because at higher frequencies and lower temperature deeper defects are unable to respond. The undoped sample still has the highest defect density, but the Rb sample now has the lowest and it is about an order of magnitude below that of the undoped sample. The first moment of the charge response (<x>) is also shifted to much larger values for the Rb sample. This indicates that the defect population in the Rb device is quite different than in the undoped, Si, or Te devices. There are several possible causes for the shift in <x>, including: (1) a reduction in defects near the front of the device and thus that the charge response is originating from a physically deeper location within the device, or (2) the charge response originates from shallower defects because of a reduction in deep defects. In either case, we see that a defect population that is present in the other devices is not present in the Rb sample. Assuming a thermal emission prefactor of v = 8.536 ($v = N_v v_n \sigma_n$ obtained from

prior admittance studies where we observed a defect at E_v + 150 meV) the defects being frozen out by the change in temperature and frequency would approximately lie in the range 90-220 meV. Prior studies using admittance[164, 197, 421, 444] and photoluminescence[400] have reported a defect within this energy range for CZTSe, and it is often assumed to result from a Cu_{Zn} anti-site defect based on values predicted from DFT calculations.[387] Previous work on CIGS has correlated changes in a defect state near 110 meV with varying Se activity during growth.[445] As the Se activity was reduced; the formation of the defective chalcopyrite layer was enhanced causing an increase in the capacitive response. If Rb acts as a Se fluxing agent, it could effectively increase the Se activity and reduce the degree of disorder/compensation in the kesterite layer, particularly near the top surface. This could explain why an element as large as Rb could still benefit CZTSSe, but it is inconsistent with our PL results on quartz substrates. We found that Rb lead to increased sub-band gap absorptivity, suggesting a greater extent of disorder/compensation. Therefore, the most likely effect of Rb is (1) reducing the quantity of defects near the front of the device. This may be possible via an ion exchange mechanism, similar to what has been proposed for K in CIGS.[446]

8.7 Conclusions

Using ink-based doping, we have deposited continuous composition gradients of 25 different extrinsic species, paying particular attention to the group I elements. The gradients were mapped using absolute intensity photoluminescence to evaluate the impact of these species on the quasi-Fermi level splitting, the extent of sub-bandgap absorptivity (potential fluctuations), and the band gap. Based on our initial photoluminescence screening, we identified several elements that had potentially beneficial effects. These species were further investigated by making devices and performing electrical characterization. We find that transition metals located near Cu on the periodic table have a strongly deleterious effect on the absorber layer, while a many other elements have little to no impact on the optical properties, likely due to exclusion from the crystalline lattice. The species Li, Rb, Si, and Te were all found to help improve the overall power conversion efficiency compared to an undoped baseline. Using temperature-dependent DLCP, we find that Rb has a significant effect on defect population. Similar to what has been proposed for K in CIGS, we hypothesize that Rb helps reduce defects near the CZTSSe/CdS interface.

Chapter 9. CONCLUSIONS AND FUTURE WORK

Kesterites are very promising materials for PV, and by building on over 40 years of research on chalcopyrites, the efficiency has been rapidly increased to the current world record of 12.6%. To help push the efficiency higher, and to improve the community's understanding of these materials, I developed a high-throughput screening process. At its core, this process includes an ultrasonic spray coater that can deposit continuous composition gradients, and a confocal absolute-intensity photoluminescence instrument. Together these instruments allow us to evaluate the optoelectronic quality and maximum possible open-circuit voltage of a material without the complications of device fabrication. Using this process, I have investigated off-stoichiometric growth as a means to limit intrinsic defects; doping with 25 different extrinsic species in varying concentration; and alloying germanium to tune the band structure. This work has resulted in 4 peer-reviewed publications, helped our lab reach 11.8% efficiency using a non-toxic solution-phase chemistry, and has greatly improved the communities understanding of kesterite materials and devices. However, as our understanding of kesterites has grown, a number of new challenges have surfaced, and it has become clear that there will be no easy path to reaching over 20% efficiency. This is not unexpected; semiconductor materials typically take decades of intense study before reaching commercialization. Therefore, in this section I will briefly outline what I believe to be some of the biggest challenges facing kesterite devices, and areas that I believe need future study.

9.1 CHALLENGE 1: REDUCING DISORDER

Perhaps one of the biggest issues facing kesterites is the high degree of disorder in the lattice. This occurs between both copper/zinc and copper/tin. For copper/zinc, the fundamental problem is the small difference in both atomic radii and valence, which makes a number of defects an defect complexes such as [V_{Cu}+Zn_{Cu}] and [Cu_{Zn}+Zn_{Cu}] highly favorable. Unpublished reports place this disorder to be on the scale of 10% of all Cu/Zn sites. This creates a large population of charged defects and leads to a number of problems, including both reduced carrier mobility and electrostatic potential fluctuations. In CIGS, an effective strategy for dealing with this issue is

sodium doping. Sodium can occupy copper vacancies, and limit the extent to which indium substitutes on copper sites. However, my own research has shown that neither group-I elements or large variations in the stoichiometry substantially reduce the potential fluctuations. This isn't a surprising result; lithium and sodium have similar atomic radii and valence to both copper and zinc, and thus are almost as likely to substitute on zinc sites as they are on copper sites. The only strategy that has thus far proven somewhat successful at reducing the Cu/Zn disorder, is long low-temperature anneals,[447, 448] but this has yet to lead to any substantial gains in efficiency, and is undesirable from a manufacturing perspective. Future work may instead focus on controlling the rate of heating/cooling during selenization to help address this issue.

In Chapter 8, I presented data from doping CZTSSe with extrinsic elements, but I believe that the most successful strategy for reducing defects and disorder would be to completely substitute a larger element for either Cu or Zn. Since there are only a few +1 cations and the majority of +2 cations have similar atomic radii to Cu and Zn, I believe the best candidates would be Ag for Cu or Cd for Zn. Cd is an undesirable choice with regards to toxicity and abundance. Additionally, first principles calculations predict that the energy difference between kesterite and stannite is small for $Cu_2CdSn(S,Se)_4$,[175] meaning that Cd substitution would likely create more problems than it solves. This leaves silver as the most promising candidate. Because of the relatively small quantity of material necessary for a thin film, silver is not as bad of an idea as it may sound. USGS Mineral Commodity summaries show that in 2014, the US consumed about 6,900 tons of silver at an average price of about $612/kg. This compares favorably to indium for example, which the US consumed 120 tons of at an average price of $710/kg.[42] However, no group has yet demonstrated a silver based kesterite with high power conversion efficiency, and even less is known about $Ag_2ZnSnSe_4$ than $Cu_2ZnSnSe_4$. Recent theoretical studies have suggested that Ag alloying/substitution may help reduce disorder, but pure Ag_2ZnSnS_4 may be an n-type material.[449] This could open up a variety of interesting research opportunities for using AZTS as a window/buffer layer. However, experimental validation is needed.

9.2 CHALLENGE 2: CONTROLLED SELENIZATION

In my 5 years of research on CZTSSe at UW, I have found that one of the most important and highly variable stages in our device processing is the selenization. Selenization is the process by which we convert our sulfide precursor material into a large-grained polycrystalline selenide material. The process is carried out in a 2" diameter tube furnace at temperatures of about 550°C. Substrates coated with a thin film of CZTS are put in a graphite box with a large excess of elemental selenium. The tube furnace is evacuated and back-filled with an inert gas and then heated to the desired temperature with the graphite box resting outside the hot zone. Once the temperature has stabilized, the graphite box is pushed into the hot zone, and the gas flow is set to maintain a slight overpressure inside the tube. After 20 minutes, the furnace is opened and a fan is used to provide convective cooling. Cooldown typically takes about 1 hour, but is not carefully controlled.

During selenization several different processes are occurring simultaneously. These include: (1) sodium diffusing from the soda-lime glass into the absorber layer; (2) sulfur is being exchanged for selenium; (3) the grains are sintering and growing; (4) volatile impurities are evaporating, and (5) the defects that ultimately will exist in the absorber layer are forming. Because of these many different processes, selenization suffers from poor reproducibility, and sight variation in processing parameters can lead to unexpected results. In addition, recent publications have suggested that selenium-related defects and the selenium activity during growth can have a profound effect on CIGS device efficiency.[445, 450, 451] One such set of experiments correlated reduced selenium activity with formation of a larger order-defect compound (ODC), and a larger defect signal in admittance data.[445] Therefore, there is ample reason to investigate and design processes by which we can better control the selenium activity during selenization.

One way that we can improve our control over the selenization process is to transition from an open to a closed system. In our current system (open), the selenium partial pressure varies with time. Convective currents transport the volatilized selenium out of the hot zone to unheated regions where it will condense. However, in a closed system we can set the selenium partial pressure by controlling both the temperature and selenium quantity added to the reactor. We can

also greatly reduce the quantity of selenium consumed during each run, because the residual selenium will be safely contained inside the reactor where it can be used during the next run. Selenium is the most toxic, most expensive, and rarest element used in CZTSSe devices (refer to Chapter 1), so reducing our consumption is desirable. A closed system would also allow us to limit the volatilization of SnSe or GeSe, which has previously been shown to be important for high efficiency devices.[150] I believe that this system will provide higher quality and more consistent selenizations if (1) residual solvent and processing impurities can be successfully eliminated prior to selenization and (2) selenium condensation on the films can be prevented or etched away.

9.3 Challenge 3: Developing a Model System: Single Crystal Studies

Kesterites are a very complicated material, and there is still a lot that we don't know. However, what I think would be most valuable is developing a model system where we can ask the question "Can this material reach our efficiency goal?" If we forget about the notion of making an economically viable material or process, and simply focus on making the absolute best kesterite that we can, regardless of the cost, how good of a material can we make? Can we reach over 80% of the theoretical Voc? Can we reach 80% of the theoretical efficiency? I don't think anybody yet knows the answer to these questions, but I think the only way that we can figure it out, is by studying single crystals; either epitaxial films or bulk single crystals. Several research groups have already grown single crystals of CZTSe and CZTS, there are no big obstacles to doing so. Several people have even studied single crystals using PL. However, I have yet to see anybody extract the quasi-Fermi level splitting from these samples. What is it? Is it large? Is it small? How does it compare to values from polycrystalline materials? Can we improve it?

Are the worst defects on the surface or in the bulk? Using techniques like two-photon photoluminescence we could easily answer these questions. By looking at single crystals we can start to understand how detrimental the grain boundaries are, and what defects exist at the grain boundaries, so that we can better passivate them in a polycrystalline system. I think that if we take the time to understand how to grow a good single crystal, then we can take that knowledge and find ways to make a good polycrystalline material (or if it is even possible). These are the questions that we must answer before we devote more time and money to kesterites.

BIBLIOGRAPHY

[1] Wang, W.; Winkler, M. T.; Gunawan, O.; Gokmen, T.; Todorov, T. K.; Zhu, Y.; Mitzi, D. B., Device Characteristics of CZTSSe Thin-Film Solar Cells with 12.6% Efficiency. *Advanced Energy Materials* **2013**.

[2] Gokmen, T.; Gunawan, O.; Mitzi, D. B., Semi-empirical device model for $Cu_2ZnSn(S,Se)_4$ solar cells. *Applied Physics Letters* **2014,** 105, (3).

[3] Gokmen, T.; Gunawan, O.; Todorov, T. K.; Mitzi, D. B., Band tailing and efficiency limitation in kesterite solar cells. *Applied Physics Letters* **2013,** 103, 103506.

[4] *The Outlook for Energy: A View to 2040*; Exxon Mobil: 2012.

[5] *BP Statistical Review of World Energy*; BP: 2011.

[6] Marburger, J. H. I.; Kvamme, E. F., The Energy Imperative. In Washington DC, 2006.

[7] Goldemberg, J.; Johansson, T. B. *United Nations Development Program World Energy Assessment*; 2004.

[8] Hermann, W. A., Quantifying global exergy resources. *Energy* **2006,** 31, (12), 1685-1702.

[9] Barbose, G.; Darghouth, N.; Wiser, R.; Seel, J. *Tracking the Sun IV: A historical summary of the installed cost of photovoltaics in the United States from 1998 to 2010*; Lawrence Berkeley National Laboratory: 2011.

[10] Feldman, D.; Barbose, G.; Margolis, R.; Wiser, R.; Darghouth, N.; Goodrich, A., Photovoltaic (PV) Pricing Trends: Historical, Recent, and Near-Term Projections. In Energy, U.S. Dept of Ed. 2012.

[11] Solar Buzz Retail Pricing Environment. http://www.solarbuzz.com/facts-and-figures/retail-price-environment/module-prices

[12] Solar Buzz-Solar Energy Industry Electricity Prices. http://www.solarbuzz.com/facts-and-figures/retail-price-environment/solar-electricity-prices

[13] Masson, G.; Latour, M.; Rekinger, M.; Theologitis, I.-T.; Papoutsi, M. *Global Market Outlook for Photovoltaics Until 2014-2018*; European Photovoltaics Industry Association: 2013.

[14] Schindler, R.; Warmuth, W., Fraunhofer Institute For Solar Energy Systems ISE Photovoltaics Report. 2012

[15] *2010 Solar technologies Market Report: January 2010*; NREL.

[16] Michaelson, R., BIPV Predicted to be Worth $11 Billion by 2016. *PV Magazine* 2011.

[17] *NanoMarkets Issues New Report on Building Integrated Photovoltaics (BIPV) Market*; NanoMarkets: http://www.nanomarkets.net/news/, 2011.

[18] Gloeckler, M.; Sankin, I.; Zhao, Z. In *CdTe Solar Cells at the Threshold to 20% Efficiency*, 39th IEEE Photovoltaic Specialists Conference, Tampa, FL, 2013.

[19] Jackson, P.; Hariskos, D.; Lotter, E.; Paetel, S.; Wuerz, R.; Menner, R.; Wischmann, W.; Powalla, M., New world record efficiency for $Cu(In,Ga)Se_2$ thin-film solar cells beyond 20%. *Progress in Photovoltaics: Research and Applications* **2011**.

[20] Wadia, C.; Alivisatos, A. P.; Kammen, D. M., Materials Availability Expands the Opportunity for Large-Scale Photovoltaics Deployment. *Environmental Science & Technology* **2009,** 43, (6), 2072-2077.

[21] Staebler, D. L.; Wronski, C. R., Optically induced conductivity changes in discharge-produced hydrogenated amorphous silicon. *Journal of Applied Physics* **1980,** 51, (6), 3262-3268.

[22] Stradins, P. In *Staebler-Wronski defects: Creation efficiency, stability, and effect on a-Si:H solar cell degradation*, 35th IEEE Photovoltaic Specialists Conference (PVSC), 2010; pp 000142-000145.

[23] Bryant, F. J.; Hariri, A. K.; Scott, C. G., Surface and interface processes influencing the stability of Cu_2S-CdS thin-film solar-cells. *Journal of Physics D-Applied Physics* **1983,** 16, (12), 2341-2348.

[24] Chen, S. Y.; Yang, J. H.; Gong, X. G.; Walsh, A.; Wei, S. H., Intrinsic point defects and complexes in the quaternary kesterite semiconductor Cu_2ZnSnS_4. *Physical Review B* **2010,** 81, (24), 245204-245214.

[25] Birkholz, M.; Fiechter, S.; Hartmann, A.; Tributsch, H., Sulfur deficiency in iron pyrite (FeS_2) and its consequences for band-structure models. *Physical Review B* **1991,** 43, (14), 11926-11936.

[26] Bronold, M.; Pettenkofer, C.; Jaegermann, W., Surface photovoltage measurements on pyrite (100) cleavage planes: Evidence for electronic bulk defects. *Journal of Applied Physics* **1994,** 76, (10), 5800-5808.

[27] Yu, L.; Lany, S.; Kykyneshi, R.; Jieratum, V.; Ravichandran, R.; Pelatt, B.; Altschul, E.; Platt, H. A. S.; Wager, J. F.; Keszler, D. A.; Zunger, A., Iron Chalcogenide Photovoltaic Absorbers. *Advanced Energy Materials* **2011,** 1, (5), 748-753.

[28] Ki, W.; Hillhouse, H. W., Earth-Abundant Element Photovoltaics Directly from Soluble Precursors with High Yield Using a Non-Toxic Solvent. *Advanced Energy Materials* **2011,** 1, (5), 732-735.

[29] Shockley, W.; Queisser, H. J., Detailed balance limit of efficiency of p-n junction solar cells. *Journal of Applied Physics* **1961,** 32, (3), 510.

[30] Ford, G. M.; Guo, Q.; Agrawal, R.; Hillhouse, H. W., Earth Abundant Element $Cu_2Zn(Sn_{1-x}Ge_x)S_4$ Nanocrystals for Tunable Band Gap Solar Cells: 6.8% Efficient Device Fabrication. *Chemistry of Materials* **2011,** 23, (10), 2626-2629.

[31] Andersson, B. A.; Azar, C.; Holmberg, J.; Karlsson, S., Material constraints for thin-film solar cells. *Energy* **1998,** 23, (5), 407-411.

[32] Andersson, B. A., Materials availability for large-scale thin-film photovoltaics. *Progress in Photovoltaics: Research and Applications* **2000,** 8, (1), 61-76.

[33] Feltrin, A.; Freundlich, A., Material considerations for terawatt level deployment of photovoltaics. *Renewable Energy* **2008,** 33, (2), 180-185.

[34] Fthenakis, V., Sustainability of photovoltaics: The case for thin-film solar cells. *Renewable & Sustainable Energy Reviews* **2009,** 13, (9), 2746-2750.

[35] Keshner, M.; Arya, R. *Study of Potential Cost Reductions Resulting from Super-Large-Scale Manufacturing of PV Modules*; 2004.

[36] Candelise, C.; Spiers, J. F.; Gross, R. J. K., Materials availability for thin film (TF) PV technologies development: A real concern? *Renewable and Sustainable Energy Reviews* **2011,** 15, (9), 4972-4981.

[37] Bleiwas, D. I. *Byproduct Mineral Commodities Used for the Production of Photovoltaic Cells: U.S. Geological Survey Circular 1365*; United States Geological Survey: 2010.

[38] Kelly, T. D.; Matos, G. R. Historical Statistics for Mineral and Materials Commodities in the United States.

[39] U.S. Geological Survey, Mineral Commodity Summaries 2011. In U.S. Geological Survey: 2011.

[40] Ojebuoboh, F., Selenium and tellurium in copper refinery slimes and their changing applications. *World of Metallurgy-Erzmetall* **2008,** 61, (1).

[41] Britt, J. S.; Huntington, R.; VanAlsburg, J.; Wiedeman, S.; Beck, M. E. In *Cost Improvement for Flexible CIGS-Based Product*, Conference Record of the 2006 IEEE 4th World Conference on Photovoltaic Energy Conversion, May 2006, pp 388-391.

[42] *Mineral Commodity Summaries 2011*; U.S. Geological Survey: 2011.

[43] Lossin, A., Copper. In *Ullmann's Encyclopedia of Industrial Chemistry*, Wiley-VCH Verlag GmbH & Co. KGaA: 2000.

[44] George J, B., Copper toxicity in the general population. *Clinical Neurophysiology* **2010,** 121, (4), 459-460.

[45] Di Toro, D. M.; Allen, H. E.; Bergman, H. L.; Meyer, J. S.; Paquin, P. R.; Santore, R. C., Biotic ligand model of the acute toxicity of metals. 1. Technical Basis. *Environmental Toxicology and Chemistry* **2001,** 20, (10), 2383-2396.

[46] Santo, C. E.; Lam, E. W.; Elowsky, C. G.; Quaranta, D.; Domaille, D. W.; Chang, C. J.; Grass, G., Bacterial Killing by Dry Metallic Copper Surfaces. *Applied and Environmental Microbiology* **2011,** 77, (3), 794-802.

[47] Li, K. F.; Ramakrishna, W., Effect of multiple metal resistant bacteria from contaminated lake sediments on metal accumulation and plant growth. *Journal of Hazardous Materials* **2011,** 189, (1-2), 531-539.

[48] Smolders, E. In *Environmental Issues of Zinc*, 3rd International Zinc Symposium, 2011; Hyderabad, India, 2011.

[49] Huebert, D. B.; Shay, J. M., Zinc toxicity and its interaction with cadmium in the submerged aquatic macrophyte Lemna Trisulca L. *Environmental Toxicology and Chemistry* **1992,** 11, (5), 715-720.

[50] Giesy, J. P.; Bowling, J. W.; Kania, H. J., Cadmium and zinc accumulation and elimination by freshwater crayfish. *Archives of Environmental Contamination and Toxicology* **1980,** 9, (6), 683-697.

[51] Widianarko, B.; Kuntoro, F. X.; Van Gestel, C. A.; Van Straalen, N. M., Toxicokinetics and toxicity of zinc under time-varying exposure in the guppy (Poecilia reticulata). *Environ Toxicol Chem* **2001,** 20, (4), 763-8.

[52] Graf, G. G., Tin, Tin Alloys, and Tin Compounds. In *Ullmann's Encyclopedia of Industrial Chemistry*, Wiley-VCH Verlag GmbH & Co. KGaA: 2000.

[53] Mergel, M. *Tributyltin*; 2011.

[54] Sanders, J. S. *Background of Copper Antifouling Paint Issues and Evaluation of the Department of Pesticide Regulation's Options*; California Department of Pesticide Regulation: 2005.

[55] *Anti-Fouling Systems*; International Maritime Organization: 2002.

[56] Carson, R. T.; Damon, M.; Johnson, L. T.; Gonzalez, J. A., Conceptual issues in designing a policy to phase out metal-based antifouling paints on recreational boats in San Diego Bay. *Journal of Environmental Management* **2009,** 90, (8), 2460-2468.

[57] Kaufman, L., Mutated trout raise new concerns near mine sites. *The New York Times* Feb 22, 2012.

[58] Hamilton, S. J., Review of selenium toxicity in the aquatic food chain. *Science of The Total Environment* **2004,** 326, (1–3), 1-31.

[59] Lo, M. T.; Sandi, E., Selenium: occurrence in foods and its toxicological significance--a review. *J Environ Pathol Toxicol* **1980,** 4, (1), 193-218.

[60] Anctil, A.; Fthenakis, V., Critical metals in strategic photovoltaic technologies: abundance versus recyclability. *Progress in Photovoltaics: Research and Applications* **2012**.

[61] Kushiya, K.; Ohshita, M.; Tanaka, M. In *Development of recycling and reuse technologies for large-area Cu(InGa)Se_2 based thin-film modules*, Proceedings of 3rd World Conference on Photovoltaic Energy Conversion, 2003; pp 1892-1895 Vol.2.

[62] Jason, H.; Nelson, E.; Tilman, D.; Polasky, S.; Tiffany, D., Environmental, Economic, and Energetic Costs and Benefits of Biodiesel and Ethanol Biofuels. *Proceedings of the National Academy of Sciences of the United States of America* **2006,** 103, (30), 11206-11210.

[63] Searchinger, T.; Heimlich, R.; Houghton, R. A.; Dong, F.; Elobeid, A.; Fabiosa, J.; Tokgoz, S.; Hayes, D.; Yu, T.-H., Use of U.S. Croplands for Biofuels Increases Greenhouse Gases Through Emissions from Land-Use Change. *Science* **2008,** 319, (5867), 1238-1240.

[64] Fava, J. A.; Smith, J. K., Integrating Financial and Environmental Information for Better Decision Making. *Journal of Industrial Ecology* **1998,** 2, (1), 9-11.

[65] Weidema, B., The Integration of Economic and Social Aspects in Life Cycle Impact Assessment. *The International Journal of Life Cycle Assessment* **2006,** 11, (0), 89-96.

[66] Mitzi, D. B.; Gunawan, O.; Todorov, T. K.; Wang, K.; Guha, S., The path towards a high-performance solution-processed kesterite solar cell. *Solar Energy Materials and Solar Cells* **2011,** 95, (6), 1421-1436.

[67] Ramasamy, K.; Malik, M. A.; O'Brien, P., Routes to copper zinc tin sulfide Cu_2ZnSnS_4 a potential material for solar cells. *Chemical Communications* **2012,** 48, (46), 5703-5714.

[68] Shin, S. W.; Pawar, S. M.; Park, C. Y.; Yun, J. H.; Moon, J. H.; Kim, J. H.; Lee, J. Y., Studies on Cu_2ZnSnS_4 (CZTS) absorber layer using different stacking orders in precursor thin films. *Solar Energy Materials and Solar Cells* **2011,** 95, (12), 3202-3206.

[69] Redinger, A.; Berg, D. M.; Dale, P. J.; Siebentritt, S., The Consequences of Kesterite Equilibria for Efficient Solar Cells. *Journal of the American Chemical Society* **2011,** 133, (10), 3320-3323.

[70] Katagiri, H.; Sasaguchi, N.; Hando, S.; Hoshino, S.; Ohashi, J.; Yokota, T., Preparation and evaluation of Cu_2ZnSnS_4 thin films by sulfurization of E-B evaporated precursors. *Solar Energy Materials and Solar Cells* **1997,** 49, (1-4), 407-414.

[71] Katagiri, H.; Ishigaki, N.; Ishida, T.; Saito, K., Characterization of Cu_2ZnSnS_4 thin films prepared by vapor phase sulfurization. *Japanese Journal of Applied Physics Part 1* **2001,** 40, (2A), 500-504.

[72] Kobayashi, T.; Jimbo, K.; Tsuchida, K.; Shinoda, S.; Oyanagi, T.; Katagiri, H., Investigation of Cu_2ZnSnS_4-based thin film solar cells using abundant materials. *Japanese Journal of Applied Physics Part 1* **2005,** 44, (1B), 783-787.

[73] Jimbo, K.; Kimura, R.; Kamimura, T.; Yamada, S.; Maw, W. S.; Araki, H.; Oishi, K.; Katagiri, H., Cu_2ZnSnS_4-type thin film solar cells using abundant materials. *Thin Solid Films* **2007,** 515, (15), 5997-5999.

[74] Katagiri, H.; Jimbo, K.; Yamada, S.; Kamimura, T.; Maw, W. S.; Fukano, T.; Ito, T.; Motohiro, T., Enhanced conversion efficiencies of Cu_2ZnSnS_4-based thin film solar cells by using preferential etching technique. *Applied Physics Express* **2008,** 1, (4).

[75] Oo, W. M. H.; Johnson, J. L.; Bhatia, A.; Lund, E. A.; Nowell, M. M.; Scarpulla, M. A., Grain Size and Texture of Cu_2ZnSnS_4 Thin Films Synthesized by Cosputtering Binary Sulfides and Annealing: Effects of Processing Conditions and Sodium. *Journal of Electronic Materials* **2011,** 40, (11), 2214-2221.

[76] Wang, K. J.; Shin, B.; Reuter, K. B.; Todorov, T.; Mitzi, D. B.; Guha, S., Structural and elemental characterization of high efficiency Cu_2ZnSnS_4 solar cells. *Applied Physics Letters* **2011,** 98, (5), 3.

[77] Shin, B.; Gunawan, O.; Zhu, Y.; Bojarczuk, N. A.; Chey, S. J.; Guha, S., Thin film solar cell with 8.4% power conversion efficiency using an earth-abundant Cu_2ZnSnS_4 absorber. *Progress in Photovoltaics: Research and Applications* **2011**.

[78] Schubert, B. A.; Marsen, B.; Cinque, S.; Unold, T.; Klenk, R.; Schorr, S.; Schock, H. W., Cu_2ZnSnS_4 thin film solar cells by fast coevaporation. *Progress in Photovoltaics* **2011,** 19, (1), 93-96.

[79] Sun, L.; He, J.; Kong, H.; Yue, F. Y.; Yang, P. X.; Chu, J. H., Structure, composition and optical properties of Cu_2ZnSnS_4 thin films deposited by Pulsed Laser Deposition method. *Solar Energy Materials and Solar Cells* **2011,** 95, (10), 2907-2913.

[80] Moriya, K.; Tanaka, K.; Uchiki, H., Fabrication of Cu_2ZnSnS_4 thin-film solar cell prepared by pulsed laser deposition. *Japanese Journal of Applied Physics Part 1-Regular Papers Brief Communications & Review Papers* **2007,** 46, (9A), 5780-5781.

[81] Moriya, K.; Tanaka, K.; Uchiki, H., Cu_2ZnSnS_4 thin films annealed in H_2S atmosphere for solar cell absorber prepared by pulsed laser deposition. *Japanese Journal of Applied Physics* **2008,** 47, (1), 602-604.

[82] Moholkar, A. V.; Shinde, S. S.; Babar, A. R.; Sim, K. U.; Lee, H. K.; Rajpure, K. Y.; Patil, P. S.; Bhosale, C. H.; Kim, J. H., Synthesis and characterization of Cu_2ZnSnS_4 thin films grown by PLD: Solar cells. *Journal of Alloys and Compounds* **2011,** 509, (27), 7439-7446.

[83] Moholkar, A. V.; Shinde, S. S.; Babar, A. R.; Sim, K. U.; Kwon, Y. B.; Rajpure, K. Y.; Patil, P. S.; Bhosale, C. H.; Kim, J. H., Development of CZTS thin films solar cells by pulsed laser deposition: Influence of pulse repetition rate. *Solar Energy* **2011,** 85, (7), 1354-1363.

[84] Ito, K.; Nakazawa, T., Electrical and Optical Properties of Stannite-Type Quaternary Semiconductor Thin Films. *Japanese Journal of Applied Physics Part 1* **1988,** 27, (11), 2094-2097.

[85] Todorov, T. K.; Reuter, K. B.; Mitzi, D. B., High-Efficiency Solar Cell with Earth-Abundant Liquid-Processed Absorber. *Advanced Materials* **2010,** 22, (20), E156.

[86] Bag, S.; Gunawan, O.; Gokmen, T.; Zhu, Y.; Todorov, T. K.; Mitzi, D. B., Low band gap liquid-processed CZTSe solar cell with 10.1% efficiency. *Energy & Environmental Science* **2012,** 5, (5), 7060-7065.

[87] Woo, K.; Kim, Y.; Moon, J., A non-toxic, solution-processed, earth abundant absorbing layer for thin-film solar cells. *Energy & Environmental Science* **2012,** 5, (1), 5340-5345.

[88] Moritake, N.; Fukui, Y.; Oonuki, M.; Tanaka, K.; Uchiki, H., Preparation of Cu_2ZnSnS_4 thin film solar cells under non-vacuum condition *Physica Status Solidi C* **2009,** 5, 1233-1236.

[89] Tanaka, K.; Fukui, Y.; Moritake, N.; Uchiki, H., Chemical composition dependence of morphological and optical properties of Cu_2ZnSnS_4 thin films deposited by sol-gel sulfurization and Cu_2ZnSnS_4 thin film solar cell efficiency. *Solar Energy Materials and Solar Cells* **2011,** 95, (3), 838-842.

[90] Tanaka, K.; Fukui, Y.; Moritake, N.; Uchiki, H., Chemical Composition Dependence of Morphological and Optical Properties of Cu_2ZnSnS_4 Thin Films Deposited by Sol-Gel Sulfurization and Cu_2ZnSnS_4 Thin Film Solar Cell Efficiency. *Solar Energy Materials and Solar Cells* **2011,** 95, (3), 838-842.

[91] Park, M. S.; Kim, D.-H.; Sung, S.-J.; Jo, H. J.; Kang, J.-K., Growth of $Cu_2ZnSnSe_4$ Thin Films by Spin-Coating and Selenization Process. In *2011 11th IEEE International Conference on Nanotechnology*, Portland Marriot, 2011; pp 222-226.

[92] Tanaka, K.; Moritake, N.; Uchiki, H., Preparation of Cu2ZnSnS4 thin films by sulfurizing sol-gel deposited precursors. *Solar Energy Materials and Solar Cells* **2007,** 91, (13), 1199-1201.

[93] Choudhary, G.; Hansen, H., Human health perspective on environmental exposure to hydrazines: A review. *Chemosphere* **1998,** 37, (5), 801-843.

[94] Roe, F. J. C.; Grant, G. A.; Millican, D. M., Carcingenicity of Hydrazine and 1,1-Dimethylhydrazine for Mouse Lung. *Nature* **1967,** 216, (5113), 375-&.

[95] He, J.; Sun, L.; Chen, S. Y.; Chen, Y.; Yang, P. X.; Chu, J. H., Composition dependence of structure and optical properties of Cu2ZnSn(S,Se)4 solid solutions: An experimental study. *Journal of Alloys and Compounds* **2012,** 511, (1), 129-132.

[96] Todorov, T.; Gunawan, O.; Chey, S. J.; de Monsabert, T. G.; Prabhakar, A.; Mitzi, D. B., Progress towards marketable earth-abundant chalcogenide solar cells. *Thin Solid Films* **2011,** 519, (21), 7378-7381.

[97] Xin, H.; Vorpahl, S. M.; Collord, A. D.; Braly, I. L.; Uhl, A. R.; Krueger, B. W.; Ginger, D. S.; Hillhouse, H. W., Lithium-doping inverts the nanoscale electric field at the grain boundaries in $Cu_2ZnSn(S,Se)_4$ and increases photovoltaic efficiency. *Physical Chemistry Chemical Physics* **2015,** 17, (37), 23859-23866.

[98] Guo, Q. J.; Hillhouse, H. W.; Agrawal, R., Synthesis of Cu_2ZnSnS_4 Nanocrystal Ink and Its Use for Solar Cells. *Journal of the American Chemical Society* **2009,** 131, (33), 11672-11673.

[99] Riha, S. C.; Parkinson, B. A.; Prieto, A. L., Solution-Based Synthesis and Characterization of Cu_2ZnSnS_4 Nanocrystals. *Journal of the American Chemical Society* **2009,** 131, (34), 12054.

[100] Steinhagen, C.; Panthani, M. G.; Akhavan, V.; Goodfellow, B.; Koo, B.; Korgel, B. A., Synthesis of Cu_2ZnSnS_4 Nanocrystals for Use in Low-Cost Photovoltaics. *Journal of the American Chemical Society* **2009,** 131, (35), 12554-+.

[101] Riha, S. C.; Parkinson, B. A.; Prieto, A. L., Compositionally Tunable $Cu_2ZnSn(S_{1-x}Se_x)_4$ Nanocrystals: Probing the Effect of Se-Inclusion in Mixed Chalcogenide Thin Films. *Journal of the American Chemical Society* **2011,** 133, (39), 15272-15275.

[102] Wang, X. Y.; Sun, Z. C.; Shao, C.; Boye, D. M.; Zhao, J. L., A facile and general approach to polynary semiconductor nanocrystals via a modified two-phase method. *Nanotechnology* **2011,** 22, (24).

[103] Zhou, Z.; Wang, Y.; Xu, D.; Zhang, Y., Fabrication of Cu_2ZnSnS_4 screen printed layers for solar cells. *Solar Energy Materials and Solar Cells* **2010,** 94, (12).

[104] Zhou, Y. L.; Zhou, W. H.; Du, Y. F.; Li, M.; Wu, S. X., Sphere-like kesterite Cu_2ZnSnS_4 nanoparticles synthesized by a facile solvothermal method. *Materials Letters* **2011,** 65, (11), 1535-1537.

[105] Khare, A.; Wills, A. W.; Ammerman, L. M.; Norris, D. J.; Aydil, E. S., Size control and quantum confinement in Cu_2ZnSnS_4 nanocrystals. *Chemical Communications* **2011,** 47, (42), 11721-11723.

[106] Shin, S. W.; Han, J. H.; Park, C. Y.; Moholkar, A. V.; Lee, J. Y.; Kim, J. H., Quaternary Cu_2ZnSnS_4 nanocrystals: Facile and low cost synthesis by microwave-assisted solution method. *Journal of Alloys and Compounds* **2012,** 516, 96-101.

[107] Lu, X. T.; Zhuang, Z. B.; Peng, Q.; Li, Y. D., Wurtzite Cu_2ZnSnS_4 nanocrystals: a novel quaternary semiconductor. *Chemical Communications* **2011,** 47, (11), 3141-3143.

[108] Guo, Q.; Ford, G. M.; Yang, W.C.; Hages, C.J.; Hillhouse, H.W.; Agrawal, R., Enhancing the Performance of CZTSSe Solar Cells with Ge Alloying. *Solar Energy Materials and Solar Cells*, **2012**, 105, 132-136.

[109] Tian, Q. W.; Xu, X. F.; Han, L. B.; Tang, M. H.; Zou, R. J.; Chen, Z. G.; Yu, M. H.; Yang, J. M.; Hu, J. Q., Hydrophilic Cu_2ZnSnS_4 nanocrystals for printing flexible, low-cost and environmentally friendly solar cells. *Crystengcomm* **2012,** 14, (11), 3847-3850.

[110] Collord, A. D.; Hillhouse, H. W., Composition Control and Formation Pathway of CZTS and CZTGS Nanocrystal Inks for Kesterite Solar Cells. *Chemistry of Materials* **2015,** 27, (5), 1855-1862.

[111] Shavel, A.; Arbiol, J.; Cabot, A., Synthesis of Quaternary Chalcogenide Nanocrystals: Stannite $Cu_2Zn_xSn_ySe_{1+x+2y}$. *Journal of the American Chemical Society* **2010,** 132, (13), 4514-4515.

[112] Wei, H.; Guo, W.; Sun, Y.; Yang, Z.; Zhang, Y., Hot-injection synthesis and characterization of quaternary $Cu_2ZnSnSe_4$ nanocrystals. *Materials Letters* **2010,** 64, (13), 1424-1426.

[113] Flynn, B.; Wang, W.; Chang, C.-h.; Herman, G. S., Microwave assisted synthesis of Cu_2ZnSnS_4 colloidal nanoparticle inks. *physica status solidi (a)* **2012**.

[114] Guo, Q.; Ford, G. M.; Agrawal, R.; Hillhouse, H. W., Ink formulation and low-temperature incorporation of sodium to yield 12% efficient $Cu(In,Ga)(S,Se)_2$ solar cells from sulfide nanocrystal inks. *Progress in Photovoltaics: Research and Applications* **2013,** 21, (1), 64-71.

[115] Miskin, C. K.; Yang, W.-C.; Hages, C. J.; Carter, N. J.; Joglekar, C. S.; Stach, E. A.; Agrawal, R., 9.0% efficient $Cu_2ZnSn(S,Se)_4$ solar cells from selenized nanoparticle inks. *Progress in Photovoltaics: Research and Applications* **2014**.

[116] Guo, Q.; Cao, Y.; Caspar, J. V.; Farneth, W. E.; Ionkin, A. S.; Johnson, L. K.; Lu, M.; Malajovich, I.; Radu, D.; Choudhury, K. R.; Rosenfeld, H. D.; Wu, W. In *A Simple Solution-based Route to High-Efficiency CZTSSe Thin-film Solar Cells* 38th IEEE Photovoltaics Specialist Conference, Austin, TX, 2012.

[117] Shavel, A.; Cadavid, D.; Ibanez, M.; Carrete, A.; Cabot, A., Continuous Production of Cu_2ZnSnS_4 Nanocrystals in a Flow Reactor. *Journal of the American Chemical Society* **2012,** 134, (3), 1438-1441.

[118] Levcenco, S.; Dumcenco, D.; Wang, Y. P.; Huang, Y. S.; Ho, C. H.; Arushanov, E.; Tezlevan, V.; Tiong, K. K., Influence of anionic substitution on the electrolyte electroreflectance study of band edge transitions in single crystal $Cu_2ZnSn(S_xSe_{1-x})_4$ solid solutions. *Optical Materials* **2012,** 34, (8), 1362-1365.

[119] Paier, J.; Asahi, R.; Nagoya, A.; Kresse, G., Cu_2ZnSnS_4 as a potential photovoltaic material: A hybrid Hartree-Fock density functional theory study. *Physical Review B* **2009,** 79, (11).

[120] Chen, S. Y.; Gong, X. G.; Walsh, A.; Wei, S. H., Crystal and electronic band structure of Cu_2ZnSnX_4 (X=S and Se) photovoltaic absorbers: First-principles insights. *Applied Physics Letters* **2009,** 94, (4).

[121] Persson, C., Electronic and optical properties of Cu_2ZnSnS_4 and $Cu_2ZnSnSe_4$. *Journal of Applied Physics* **2010,** 107, (5).

[122] Nozaki, H.; Fukano, T.; Ohta, S.; Seno, Y.; Katagiri, H.; Jimbo, K., Crystal structure determination of solar cell materials: Cu_2ZnSnS_4 thin films using X-ray anomalous dispersion. *Journal of Alloys and Compounds* **2012,** 524, (0), 22-25.

[123] Schorr, S., The crystal structure of kesterite type compounds: A neutron and X-ray diffraction study. *Solar Energy Materials and Solar Cells* **2011,** 95, (6), 1482-1488.

[124] H., M. G., Tin containing mineral systems. Part II: Phase relations and mineral assemblages in the Cu-Fe-Zn-Sn-S system. *Chem. Erde.* **1975,** 34, 1.

[125] Matsushita, H.; Maeda, T.; Katsui, A.; Takizawa, T., Thermal analysis and synthesis from the melts of Cu-based quaternary compounds Cu-III-IV-VI, and Cu_2-II-IV-VI_4 (II = Zn, Cd; III=Ga, In; IV=Ge, Sn ; VI=Se). *Journal of Crystal Growth* **2000,** 208, (1-4), 416-422.

[126] Maeda, T.; Nakamura, S.; Wada, T. In *Electronic structure and phase stability of In-free photovoltaic semiconductors, $Cu_2ZnSnSe_4$ and Cu_2ZnSnS_4 by first-principles calculation*, MRS Proceedings, 2009; pp 1165-M04-03.

[127] Olekseyuk, I. D.; Dudchak, I. V.; Piskach, L. V., Phase equilibria in the Cu_2S-ZnS-SnS_2 system. *Journal of Alloys and Compounds* **2004,** 368, (1-2), 135-143.

[128] Dudchak, I. V.; Piskach, L. V., Phase equilibria in the Cu_2SnSe_3–$SnSe_2$–ZnSe system. *Journal of Alloys and Compounds* **2003,** 351, (1–2), 145-150.

[129] Nagoya, A.; Asahi, R.; Wahl, R.; Kresse, G., Defect formation and phase stability of Cu_2ZnSnS_4 photovoltaic material. *Physical Review B* **2010,** 81, (11).

[130] Chen, S. Y.; Yang, J. H.; Gong, X. G.; Walsh, A.; Wei, S. H., Intrinsic point defects and complexes in the quaternary kesterite semiconductor Cu_2ZnSnS_4. *Physical Review B* **2010,** 81, (24).

[131] Cheng, A. J.; Manno, M.; Khare, A.; Leighton, C.; Campbell, S. A.; Aydil, E. S., Imaging and phase identification of Cu_2ZnSnS_4 thin films using confocal Raman spectroscopy. *Journal of Vacuum Science & Technology A* **2011,** 29, (5).

[132] Vora, N.; Blackburn, J.; Repins, I.; Beall, C.; To, B.; Pankow, J.; Teeter, G.; Young, M.; Noufi, R., Phase identification and control of thin films deposited by co-evaporation of elemental Cu, Zn, Sn, and Se. *Journal of Vacuum Science & Technology A: Vacuum, Surfaces, and Films* **2012,** 30, (5), 051201-7.

[133] Fontane, X.; Calvo-Barrio, L.; Izquierdo-Roca, V.; Saucedo, E.; Perez-Rodriguez, A.; Morante, J. R.; Berg, D. M.; Dale, P. J.; Siebentritt, S., In-depth resolved Raman scattering analysis for the identification of secondary phases: Characterization of Cu_2ZnSnS_4 layers for solar cell applications. *Applied Physics Letters* **2011,** 98, (18).

[134] Khare, A.; Himmetoglu, B.; Johnson, M.; Norris, D. J.; Cococcioni, M.; Aydil, E. S., Calculation of the lattice dynamics and Raman spectra of copper zinc tin chalcogenides and comparison to experiments. *Journal of Applied Physics* **2012,** 111.

[135] Redinger, A.; Hones, K.; Fontane, X.; Izquierdo-Roca, V.; Saucedo, E.; Valle, N.; Perez-Rodriguez, A.; Siebentritt, S., Detection of a ZnSe secondary phase in coevaporated $Cu_2ZnSnSe_4$ thin films. *Applied Physics Letters* **2011,** 98, (10), 101907-3.

[136] Altosaar, M.; Raudoja, J.; Timmo, K.; Danilson, M.; Grossberg, M.; Krustok, J.; Mellikov, E., $Cu_2Zn_{1-x}Cd_x$ $Sn(Se_{1-y}S_y)_4$ solid solutions as absorber materials for solar cells. *physica status solidi (a)* **2008,** 205, (1), 167-170.

[137] Marcano, G.; Rincon, C.; Lopez, S. A.; Perez, G. S.; Herrera-Perez, J. L.; Mendoza-Alvarez, J. G.; Rodriguez, P., Raman spectrum of monoclinic semiconductor Cu_2SnSe_3. *Solid State Communications* **2011,** 151, (1), 84-86.

[138] Khare, A.; Himmetoglu, B.; Cococcioni, M.; Aydil, E. S., First principles calculation of the electronic properties and lattice dynamics of $Cu_2ZnSn(S_{1-x}Se_x)_4$. *Journal of Applied Physics* **2012,** 111, (12).

[139] Just, J.; Luetzenkirchen-Hecht, D.; Frahm, R.; Schorr, S.; Unold, T., Determination of secondary phases in kesterite Cu_2ZnSnS_4 thin films by x-ray absorption near edge structure analysis. *Applied Physics Letters* **2011,** 99, (26).

[140] Katagiri, H.; Jimbo, K.; Tahara, M.; Araki, H.; Oishi, K. In *The Influence of Composition Ratio on CZTS-based Thin Film Solar Cells*, 2009 MRS Spring Meeting, pp 1165-M04-1.

[141] Katagiri, H.; Jimbo, K. In *Development of rare metal-free CZTS-based thin film solar cells*, 37th IEEE Photovoltaic Specialists Conference, Seattle, WA; 2011.

[142] Collord, A. D.; Xin, H.; Hillhouse, H. W., Combinatorial Exploration of the Effects of Intrinsic and Extrinsic Defects in $Cu_2ZnSn(S,Se)_4$. *IEEE Journal of Photovoltaics* **2015,** 5, (1), 288-298.

[143] Han, S. H.; Hermann, A. M.; Hasoon, F. S.; Al-Thani, H. A.; Levi, D. H., Effect of Cu deficiency on the optical properties and electronic structure of $CuInSe_2$ and $CuIn_{0.8}Ga_{0.2}Se_2$ determined by spectroscopic ellipsometry. *Applied Physics Letters* **2004,** 85, (4), 576-578.

[144] Egerton, R. F., *Electron energy-loss spectroscopy in the electron microscope*. Plenum Press: New York, 1996.

[145] Cizaire, L.; Vacher, B.; Le Mogne, T.; Martin, J. M.; Rapoport, L.; Margolin, A.; Tenne, R., Mechanisms of ultra-low friction by hollow inorganic fullerene-like MoS_2 nanoparticles. *Surface and Coatings Technology* **2002,** 160, (2–3), 282-287.

[146] He, J.; Sun, L.; Chen, S.; Chen, Y.; Yang, P.; Chu, J., Composition dependence of structure and optical properties of $Cu_2ZnSn(S,Se)_4$ solid solutions: An experimental study. *Journal of Alloys and Compounds* **2012,** 511, (1), 129-132.

[147] Grossberg, M.; Krustok, J.; Raudoja, J.; Timmo, K.; Altosaar, M.; Raadik, T., Photoluminescence and Raman study of $Cu_2ZnSn(Se_xS_{(1-x)})_4$ monograins for photovoltaic applications. *Thin Solid Films* **2011,** 519, (21), 7403-7406.

[148] Maeda, T.; Nakamura, S.; Wada, T., First-principles calculations of vacancy formation in In-free photovoltaic semiconductor $Cu_2ZnSnSe_4$. *Thin Solid Films* **2011,** 519, (21), 7513-7516.

[149] Walsh, A.; Chen, S.; Wei, S.-H.; Gong, X.-G., Kesterite Thin-Film Solar Cells: Advances in Materials Modelling of Cu_2ZnSnS_4. *Advanced Energy Materials* **2012**.

[150] Weber, A.; Mainz, R.; Schock, H. W., On the Sn loss from thin films of the material system Cu--Zn--Sn--S in high vacuum. *Journal of Applied Physics* **2010,** 107, (1), 013516-6.

[151] Scragg, J. J.; Ericson, T.; Kubart, T.; Edoff, M.; Platzer-Bjorkman, C., Chemical Insights into the Instability of Cu_2ZnSnS_4 Films during Annealing. *Chemistry of Materials* **2011,** 23, (20).

[152] Scragg, J. J.; Dale, P. J.; Colombara, D.; Peter, L. M., Thermodynamic Aspects of the Synthesis of Thin-Film Materials for Solar Cells. *ChemPhysChem* **2012,** 13, (12), 3035-3046.

[153] Shin, B.; Zhu, Y.; Bojarczuk, N. A.; Chey, S. J.; Guha, S., Control of an interfacial $MoSe_2$ layer in $Cu_2ZnSnSe_4$ thin film solar cells: 8.9% power conversion efficiency with a TiN diffusion barrier. *Applied Physics Letters* **2012,** 101, (5), 053903-4.

[154] Scragg, J. J.; Wätjen, J. T.; Edoff, M.; Ericson, T.; Kubart, T.; Platzer-Björkman, C., A Detrimental Reaction at the Molybdenum Back Contact in $Cu_2ZnSn(S,Se)_4$ Thin-Film Solar Cells. *Journal of the American Chemical Society* **2012**.

[155] Levine, B. F., D Electron Effects on Bond Susceptibilities and Ionicities. *Physical Review B* **1973,** 7, (6), 2591-2600.

[156] Chen, S. Y.; Gong, X. G.; Walsh, A.; Wei, S. H., Electronic structure and stability of quaternary chalcogenide semiconductors derived from cation cross-substitution of II-VI and I-III-VI_2 compounds. *Physical Review B* **2009,** 79, (16).

[157] Wei, S. H.; Zhang, S. B.; Zunger, A., Effects of Ga addition to $CuInSe_2$ on its electronic, structural, and defect properties. *Applied Physics Letters* **1998,** 72, (24), 3199-3201.

[158] Wei, S.-H.; Zunger, A., Band offsets and optical bowings of chalcopyrites and Zn-based II-VI alloys. *Journal of Applied Physics* **1995,** 78, (6), 3846-3856.

[159] Chen, S. Y.; Gong, X. G.; Walsh, A.; Wei, S. H., Electronic structure and stability of quaternary chalcogenide semiconductors derived from cation cross-substitution of II-VI and I-III-VI2 compounds. *Physical Review B* **2009,** 79, (16), 165211-165222.

[160] Siebentritt, S.; Schorr, S., Kesterites-a challenging material for solar cells. *Progress in Photovoltaics: Research and Applications* **2011**.

[161] Haight, R.; Barkhouse, A.; Gunawan, O.; Shin, B.; Copel, M.; Hopstaken, M.; Mitzi, D. B., Band alignment at the $Cu_2ZnSn(S_xSe_{1-x})_4$/CdS interface. *Applied Physics Letters* **2011,** 98, (25), 253502-3.

[162] Roa, L.; Rincon, C.; Gonzalez, J.; Quintero, M., Analysis of Direct Exciton Transitions in $CuGa(S_xSe_{1-x})_2$ Alloys. *Journal of Physics and Chemistry of Solids* **1990,** 51, (6).

[163] Choi, S. G.; Zhao, H. Y.; Persson, C.; Perkins, C. L.; Donohue, A. L.; To, B.; Norman, A. G.; Li, J.; Repins, I. L., Dielectric function spectra and critical-point energies of $Cu_2ZnSnSe_4$ from 0.5 to 9.0 eV. *Journal of Applied Physics* **2012,** 111, (3).

[164] Gunawan, O.; Gokmen, T.; Warren, C. W.; Cohen, J. D.; Todorov, T. K.; Barkhouse, D. A. R.; Bag, S.; Tang, J.; Shin, B.; Mitzi, D. B., Electronic properties of the $Cu_2ZnSn(Se,S)_4$ absorber layer in solar cells as revealed by admittance spectroscopy and related methods. *Applied Physics Letters* **2012,** 100, (25), 253905-4.

[165] Zhao, H.; Persson, C., Optical properties of $Cu(In,Ga)Se_2$ and $Cu_2ZnSn(S,Se)_4$. *Thin Solid Films* **2011,** 519, (21).

[166] Paulson, P. D.; Birkmire, R. W.; Shafarman, W. N., Optical characterization of $CuIn_{1-x}Ga_xSe_2$ alloy thin films by spectroscopic ellipsometry. *Journal of Applied Physics* **2003,** 94, (2), 879-888.

[167] Paulson, P. D.; Mathew, X., Spectroscopic ellipsometry investigation of optical and interface properties of CdTe films deposited on metal foils. *Solar Energy Materials and Solar Cells* **2004,** 82, (1–2), 279-290.

[168] Lee, J.; Cohen, J. D.; Shafarman, W. N., The determination of carrier mobilities in CIGS photovoltaic devices using high-frequency admittance measurements. *Thin Solid Films* **2005,** 480–481, (0), 336-340.

[169] Hanna, G.; Jasenek, A.; Rau, U.; Schock, H. W., Influence of the Ga-content on the bulk defect densities of $Cu(In,Ga)Se_2$. *Thin Solid Films* **2001,** 387, (1-2), 71-73.

[170] Schleussner, S.; Zimmermann, U.; Watjen, T.; Leifer, K.; Edoff, M., Effect of gallium grading in $Cu(In,Ga)Se_2$ solar-cell absorbers produced by multi-stage coevaporation. *Solar Energy Materials and Solar Cells* **2011,** 95, (2).

[171] Zhang, Y.; Sun, X.; Zhang, P.; Yuan, X.; Huang, F.; Zhang, W., Structural properties and quasiparticle band structures of Cu-based quaternary semiconductors for photovoltaic applications. *Journal of Applied Physics* **2012,** 111, (6).

[172] Guo, Q.; Ford, G. M.; Yang, W.-C.; Hages, C. J.; Hillhouse, H. W.; Agrawal, R., Enhancing the performance of CZTSSe solar cells with Ge alloying. *Solar Energy Materials and Solar Cells* **2012,** 105, (0), 132-136.

[173] Bag, S.; Gunawan, O.; Gokmen, T.; Zhu, Y.; Mitzi, D. B., Hydrazine-Processed Ge-Substituted CZTSe Solar Cells. *Chemistry of Materials* **2012**.

[174] Kim, S.; Kim, K. M.; Tampo, H.; Shibata, H.; Matsubara, K.; Niki, S., Ge-incorporated $Cu_2ZnSnSe_4$ thin-film solar cells with efficiency greater than 10%. *Solar Energy Materials and Solar Cells* **2016,** 144, 488-492.

[175] Chen, S. Y.; Walsh, A.; Luo, Y.; Yang, J. H.; Gong, X. G.; Wei, S. H., Wurtzite-derived polytypes of kesterite and stannite quaternary chalcogenide semiconductors. *Physical Review B* **2010,** 82, (19).

[176] Wang, C.; Chen, S.; Yang, J.-H.; Lang, L.; Xiang, H.-J.; Gong, X.-G.; Walsh, A.; Wei, S.-H., Design of I_2–II–IV–VI_4 Semiconductors through Element Substitution: The Thermodynamic Stability Limit and Chemical Trend. *Chemistry of Materials* **2014,** 26, (11), 3411-3417.

[177] Matsushita, H.; Ichikawa, T.; Katsui, A., Structural, thermodynamical and optical properties Of Cu_2-II-IV-VI_4 quaternary compounds. *Journal of Materials Science* **2005,** 40, (8), 2003-2005.

[178] Shu, Q.; Yang, J.-H.; Chen, S.; Huang, B.; Xiang, H.; Gong, X.-G.; Wei, S.-H., $Cu_2Zn(Sn,Ge)Se_4$ and $Cu_2Zn(Sn,Si)Se_4$ alloys as photovoltaic materials: Structural and electronic properties. *Physical Review B* **2013,** 87, (11), 115208.

[179] Guo, Q.; Ford, G. M.; Hillhouse, H. W.; Agrawal, R., Optimization of Cation Ratios to Increase the Efficiency of CZTSSe Solar Cells with Ge Alloying. **2012**.

[180] Guo, Q.; Ford, G. M.; Yang, W.-C.; Hages, C. J.; Hillhouse, H. W.; Agrawal, R., Enhancing the performance of CZTSSe solar cells with Ge alloying. *Solar Energy Materials and Solar Cells* **2012,** 105, 132-136.

[181] Lee, S. M.; Mohanty, B. C.; Jo, Y. H.; Yeon, D. H.; Cho, Y. S., Phase development, microstructure and optical properties of $Cu_2ZnSnSe_4$ thin films modified with Pb and Ti. *Surface & Coatings Technology* **2012**.

[182] Wang, X.; Li, J.; Zhao, Z.; Huang, S.; Xie, W., Crystal structure and electronic structure of quaternary semiconductors $Cu_2ZnTiSe_4$ and Cu_2ZnTiS_4 for solar cell absorber. *Journal of Applied Physics* **2012,** 112, (023701).

[183] Yan, C.; Huang, C.; Yang, J.; Liu, F.; Liu, J.; Lai, Y.; Li, J.; Liu, Y., Synthesis and characterizations of quaternary Cu2FeSnS4 nanocrystals. *Chemical Communications* **2012,** 48, (20), 2603-2605.

[184] Zhang, X.; Bao, N.; Ramasamy, K.; Wang, Y.-H. A.; Wang, Y.; Lin, B.; Gupta, A., Crystal phase-controlled synthesis of Cu_2FeSnS_4 nanocrystals with a band gap of around 1.5eV. *Chemical Communications* **2012**.

[185] Zhang, S. B.; Wei, S. H.; Zunger, A., Stabilization of ternary compounds via ordered arrays of defect pairs. *Physical Review Letters* **1997,** 78, (21).

[186] Heath, J. T.; Cohen, J. D.; Shafarman, W. N., Bulk and metastable defects in $CuIn_{1-x}GaxSe_2$ thin films using drive-level capacitance profiling. *Journal of Applied Physics* **2004,** 95, (3), 1000-1010.

[187] Scheer, R.; Schock, H. W., *Chalcogenide Photovoltaics: Physics, Technologies, and Thin Film Devices*. John Wiley & Sons: 2011.

[188] Turcu, M.; Kotschau, I. M.; Rau, U., Composition dependence of defect energies and band alignments in the $Cu(In_{1-x},Ga_x)(Se_{1-y},S_y)_2$ alloy system. *Journal of Applied Physics* **2002,** 91, (3), 1391-1399.

[189] Heath, J. T.; Cohen, J. D.; Shafarman, W. N.; Liao, D. X.; Rockett, A. A., Effect of Ga content on defect states in CuIn1-xGaxSe2 photovoltaic devices. *Applied Physics Letters* **2002,** 80, (24), 4540-4542.

[190] Eisenbarth, T.; Unold, T.; Caballero, R.; Kaufmann, C. A.; Abou-Ras, D.; Schock, H. W., Origin of defects in $CuIn_{1-x}Ga_xSe2$ solar cells with varied Ga content. *Thin Solid Films* **2009,** 517, (7), 2244-2247.

[191] Lany, S.; Zunger, A., Intrinsic DX centers in ternary chalcopyrite semiconductors. *Physical Review Letters* **2008,** 100, (1).

[192] Zhang, S. B.; Wei, S.-H.; Zunger, A.; Katayama-Yoshida, H., Defect physics of the $CuInSe_2$ chalcopyrite semiconductor. *Physical Review B* **1998,** 57, (16), 9642.

[193] Weiss, T. P.; Redinger, A.; Luckas, J.; Mousel, M.; Siebentritt, S., Admittance spectroscopy in kesterite solar cells: Defect signal or circuit response. *Applied Physics Letters* **2013,** 102, (20), 202105-4.

[194] Chen, S.; Wang, L.-W.; Walsh, A.; Gong, X. G.; Wei, S.-H., Abundance of $[Cu_{Zn} + Sn_{Zn}]$ and $[2Cu_{Zn} + Sn_{Zn}]$ defect clusters in kesterite solar cells. *Applied Physics Letters* **2012,** 101, (22), 223901-4.

[195] Chen, S.; Walsh, A.; Yang, J.-H.; Gong, X. G.; Sun, L.; Yang, P.-X.; Chu, J.-H.; Wei, S.-H., Compositional dependence of structural and electronic properties of $Cu_2ZnSn(S,Se)_4$ alloys for thin film solar cells. *Physical Review B* **2011,** 83, (12), 125201.

[196] Chen, S. Y.; Gong, X. G.; Walsh, A.; Wei, S. H., Defect physics of the kesterite thin-film solar cell absorber Cu_2ZnSnS_4. *Applied Physics Letters* **2010,** 96, (2).

[197] Moore, J.; Hages, C.; Lundstrom, M.; Agrawal, R., Influence of Ge Doping on Defect Distributions in $Cu_2Zn(Sn_xGe_{1-x})(S_ySe_{1-y})$ Fabricated by Nanocrystal Ink Deposition With Selenization. *38th IEEE PVSC*, Austin, TX, 2012.

[198] Fernandes, P. A.; Sartori, A. F.; Salome, P. M. P.; Malaquias, J.; da Cunha, A. F.; Graca, M. P. F.; Gonzalez, J. C., Admittance spectroscopy of Cu_2ZnSnS_4 based thin film solar cells. *Applied Physics Letters* **2012,** 100, (23), 233504-4.

[199] Kask, E.; Raadik, T.; Grossberg, M.; Josepson, R.; Krustok, J., Deep defects in Cu_2ZnSnS_4 monograin solar cells. *Energy Procedia* **2011,** 10, 261-265.

[200] Duan, H.-S.; Yang, W.; Bob, B.; Hsu, C.-J.; Lei, B.; Yang, Y., The Role of Sulfur in Solution-Processed $Cu_2ZnSn(S,Se)_4$ and its Effect on Defect Properties. *Advanced Functional Materials* **2012**.

[201] Leitão, J. P.; Santos, N. M.; Fernandes, P. A.; Salomé, P. M. P.; da Cunha, A. F.; González, J. C.; Ribeiro, G. M.; Matinaga, F. M., Photoluminescence and electrical study of fluctuating potentials in Cu_2ZnSnS_4-based thin films. *Physical Review B* **2011,** 84, (2), 024120.

[202] Miller, D. W.; Warren, C. W.; Gunawan, O.; Gokmen, T.; Mitzi, D. B.; Cohen, J. D., Electronically active defects in the $Cu_2ZnSn(Se,S)_4$ alloys as revealed by transient photocapacitance spectroscopy. *Applied Physics Letters* **2012,** 101, (14), 142106-4.

[203] Siebentritt, S., Shallow Defects in the Wide Gap Chalcopyrite $CuGaSe_2$. In *Wide-Gap Chalcopyrites*, Siebentritt, S.; Rau, U., Eds. Springer: Germany, 2006; Vol. 86, pp 113-156.

[204] Bauknecht, A.; Siebentritt, S.; Albert, J.; Lux-Steiner, M. C., Radiative recombination via intrinsic defects in CuxGaySe2. *Journal of Applied Physics* **2001,** 89, (8), 4391-4400.

[205] Siebentritt, S.; Rega, N.; Zajogin, A.; Lux-Steiner, M. C., Do we really need another PL study of CuInSe2? *physica status solidi (c)* **2004,** 1, (9), 2304-2310.

[206] Artaud-Gillet, M. C.; Duchemin, S.; Odedra, R.; Orsal, G.; Rega, N.; Rushworth, S.; Siebentritt, S., Evaluation of copper organometallic sources for $CuGaSe_2$ photovoltaic applications *Journal of Crystal Growth* **2003,** 252, (4).

[207] Hönes, K.; Zscherpel, E.; Scragg, J.; Siebentritt, S., Shallow defects in Cu_2ZnSnS_4. *Physica B: Condensed Matter* **2009,** 404, (23–24), 4949-4952.

[208] Tanaka, K.; Miyamoto, Y.; Uchiki, H.; Nakazawa, K.; Araki, H., Donor-acceptor pair recombination luminescence from Cu_2ZnSnS_4 bulk single crystals. *physica status solidi (a)* **2006,** 203, (11), 2891-2896.

[209] Levcenko, S.; Tezlevan, V. E.; Arushanov, E.; Schorr, S.; Unold, T., Free-to-bound recombination in near stoichiometric Cu_2ZnSnS_4 single crystals. *Physical Review B* **2012,** 86, (4), 045206.

[210] Rau, U.; Taretto, K.; Siebentritt, S., Grain boundaries in Cu(In, Ga)(Se, $S)_2$ thin-film solar cells. *Applied Physics a-Materials Science & Processing* **2009,** 96, (1), 221-234.

[211] Siebentritt, S.; Igalson, M.; Persson, C.; Lany, S., The electronic structure of chalcopyrites-bands, point defects and grain boundaries. *Progress in Photovoltaics* **2010,** 18, (6), 390-410.

[212] Persson, C.; Zunger, A., Compositionally induced valence-band offset at the grain boundary of polycrystalline chalcopyrites creates a hole barrier. *Applied Physics Letters* **2005,** 87, (21).

[213] Yan, Y.; Noufi, R.; Al-Jassim, M. M., Grain-Boundary Physics in Polycrystalline $CuInSe_2$ Revisited: Experiment and Theory. *Physical Review Letters* **2006,** 96, (20), 205501.

[214] Yan, Y.; Jiang, C. S.; Noufi, R.; Wei, S.-H.; Moutinho, H. R.; Al-Jassim, M. M., Electrically benign behavior of grain boundaries in polycrystalline $CuInSe_2$ films. *Physical Review Letters* **2007,** 99, (23).

[215] Abou-Ras, D.; Schorr, S.; Schock, H. W., Grain-size distributions and grain boundaries of chalcopyrite-type thin films. *Journal of Applied Crystallography* **2007,** 40, (5), 841-848.

[216] Jaffe, J. E.; Zunger, A., Defect-induced nonpolar-to-polar transition at the surface of chalcopyrite semiconductors. *Physical Review B* **2001,** 64, (24), 241304.

[217] Persson, C.; Zunger, A., Anomalous grain boundary physics in polycrystalline $CuInSe_2$: The existence of a hole barrier. *Physical Review Letters* **2003,** 91, (26), 4.

[218] Zhang, S. B.; Wei, S. H., Reconstruction and energetics of the polar (112) and ($1^{-}1^{-}2^{-}$) versus the nonpolar (220) surfaces of $CuInSe_2$. *Physical Review B* **2002,** 65, (8), 081402.

[219] Schmid, D.; Ruckh, M.; Grunwald, F.; Schock, H. W., Chalcopyrite/defect chalcopyrite heterojunctions on the basis of $CuInSe_2$. *Journal of Applied Physics* **1993,** 73, (6), 2902-2909.

[220] Hetzer, M. J.; Strzhemechny, Y. M.; Gao, M.; Goss, S.; Contreras, M. A.; Zunger, A.; Brillson, L. J., On microscopic compositional and electrostatic properties of grain boundaries in polycrystalline $CuIn_{1-x}Ga_xSe_2$. *Journal of Vacuum Science & Technology B* **2006,** 24, (4), 1739-1745.

[221] Lei, C.; Li, C. M.; Rockett, A.; Robertson, I. M., Grain boundary compositions in $Cu(InGa)Se_2$. *Journal of Applied Physics* **2007,** 101, (2).

[222] Hetzer, M. J.; Strzhemechny, Y. M.; Gao, M.; Contreras, M. A.; Zunger, A.; Brillson, L. J., Direct observation of copper depletion and potential changes at copper indium gallium diselenide grain boundaries. *Applied Physics Letters* **2005,** 86, (16).

[223] Couzinie-Devy, F.; Cadel, E.; Barreau, N.; Arzel, L.; Pareige, P., Atom probe study of Cu-poor to Cu-rich transition during $Cu(In,Ga)Se_2$ growth. *Applied Physics Letters* **2011,** 99, (23), 232108-3.

[224] Hafemeister, M.; Siebentritt, S.; Albert, J.; Lux-Steiner, M. C.; Sadewasser, S., Large Neutral Barrier at Grain Boundaries in Chalcopyrite Thin Films. *Physical Review Letters* **2010,** 104, (19).

[225] Monig, H.; Smith, Y.; Caballero, R.; Kaufmann, C. A.; Lauermann, I.; Lux-Steiner, M. C.; Sadewasser, S., Direct Evidence for a Reduced Density of Deep Level Defects at Grain Boundaries of $Cu(In, Ga)Se_2$ Thin Films. *Physical Review Letters* 105, (11), 4.

[226] Cahen, D.; Noufi, R., Defect chemical explanation for the effect of air anneal on $CdS/CuInSe_2$ solar cell performance. *Applied Physics Letters* **1989,** 54, (6), 558-560.

[227] Kronik, L.; Rau, U.; Guillemoles, J.-F.; Braunger, D.; Schock, H.-W.; Cahen, D., Interface redox engineering of $Cu(In,Ga)Se_2$–based solar cells: oxygen, sodium, and chemical bath effects. *Thin Solid Films* **2000,** 361–362, (0), 353-359.

[228] Li, J. B.; Chawla, V.; Clemens, B. M., Investigating the Role of Grain Boundaries in CZTS and CZTSSe Thin Film Solar Cells with Scanning Probe Microscopy. *Advanced Materials* **2012,** 24, (6), 720.

[229] Jiang, C. S.; Noufi, R.; Ramanathan, K.; AbuShama, J. A.; Moutinho, H. R.; Al-Jassim, M. M., Does the local built-in potential on grain boundaries of $Cu(In,Ga)Se_2$ thin films benefit photovoltaic performance of the device? *Applied Physics Letters* **2004,** 85, (13), 2625-2627.

[230] Jiang, C. S.; Noufi, R.; AbuShama, J. A.; Ramanathan, K.; Moutinho, H. R.; Pankow, J.; Al-Jassim, M. M., Local built-in potential on grain boundary of $Cu(In,Ga)Se_2$ thin films. *Applied Physics Letters* **2004,** 84, (18), 3477-3479.

[231] Jeong, A. R.; Jo, W.; Jung, S.; Gwak, J.; Yun, J. H., Enhanced exciton separation through negative energy band bending at grain boundaries of $Cu_2ZnSnSe_4$ thin-films. *Applied Physics Letters* **2011,** 99, (8).

[232] Li, J. B.; Chawla, V.; Clemens, B. M., Investigating the Role of Grain Boundaries in CZTS and CZTSSe Thin Film Solar Cells with Scanning Probe Microscopy. *Advanced Materials* **2012,** 24, (6), 720.

[233] Romero, M. J.; Repins, I.; Teeter, G.; Contreras, M. A.; Al-Jassim, M.; Noufi, R. In *A comparative study of the defect point physics and luminescence of the kesterites Cu_2ZnSnS_4 and $Cu_2ZnSnSe_4$ and Chalcopyrite $Cu(In,Ga)Se_2$*, 38th IEEE Photovoltaic Specialists Conference, Austin, Texas, 2012.

[234] Romero, M. J.; Du, H.; Teeter, G.; Yan, Y. F.; Al-Jassim, M. M., Comparative study of the luminescence and intrinsic point defects in the kesterite Cu_2ZnSnS_4 and chalcopyrite $Cu(In,Ga)Se_2$ thin films used in photovoltaic applications. *Physical Review B* **2011,** 84, (16), 5.

[235] Romero, M. J.; Ramanathan, K.; Contreras, M. A.; Al-Jassim, M. M.; Noufi, R.; Sheldon, P., Cathodoluminescence of $Cu(In,Ga)Se_2$ thin films used in high-efficiency solar cells. *Applied Physics Letters* **2003,** 83, (23), 4770-4772.

[236] Repins, I.; Beall, C.; Vora, N.; DeHart, C.; Kuciauskas, D.; Dippo, P.; To, B.; Mann, J.; Hsu, W.-C.; Goodrich, A.; Noufi, R., Co-evaporated $Cu_2ZnSnSe_4$ films and devices. *Solar Energy Materials and Solar Cells* **2012,** 101, (0), 154-159.

[237] Bar, M.; Schubert, B. A.; Marsen, B.; Krause, S.; Pookpanratana, S.; Unold, T.; Weinhardt, L.; Heske, C.; Schock, H. W., Native oxidation and Cu-poor surface structure of thin film Cu_2ZnSnS_4 solar cell absorbers. *Applied Physics Letters* **2011,** 99, (11), 112103-3.

[238] Mendis, B. G.; Goodman, M. C. J.; Major, J. D.; Taylor, A. A.; Durose, K.; Halliday, D. P., The role of secondary phase precipitation on grain boundary electrical activity in Cu_2ZnSnS_4 (CZTS) photovoltaic absorber layer material. *Journal of Applied Physics* **2012,** 112, (12), 124508-10.

[239] Sardashti, K.; Haight, R.; Gokmen, T.; Wang, W.; Chang, L.-Y.; Mitzi, D. B.; Kummel, A. C., Impact of Nanoscale Elemental Distribution in High-Performance Kesterite Solar Cells. *Advanced Energy Materials* **2015,** 5, (10).

[240] Haight, R.; Shao, X.; Wang, W.; Mitzi, D. B., Electronic and elemental properties of the $Cu_2ZnSn(S,Se)_4$ surface and grain boundaries. *Applied Physics Letters* **2014,** 104, (3).

[241] Barkhouse, D. A. R.; Gunawan, O.; Gokmen, T.; Todorov, T. K.; Mitzi, D. B., Device characteristics of a 10.1% hydrazine-processed $Cu_2ZnSn(Se,S)_4$ solar cell. *Progress in Photovoltaics: Research and Applications* **2012,** 20, (1), 6-11.

[242] Todorov, T. K.; Tang, J.; Bag, S.; Gunawan, O.; Gokmen, T.; Zhu, Y.; Mitzi, D. B., Beyond 11% Efficiency: Characteristics of State-of-the-Art $Cu_2ZnSn(S,Se)_4$ Solar Cells. *Advanced Energy Materials* **2012**, n/a-n/a.

[243] Guo, Q.; Ford, G. M.; Yang, W. C.; Walker, B. C.; Stach, E. A.; Hillhouse, H. W.; Agrawal, R., Fabrication of 7.2% Efficient CZTSSe Solar Cells Using CZTS Nanocrystals. *Journal of the American Chemical Society* **2010,** 132, (49), 17384-17386.

[244] Ahmed, S.; Reuter, K. B.; Gunawan, O.; Guo, L.; Romankiw, L. T.; Deligianni, H., A High Efficiency Electrodeposited Cu_2ZnSnS_4 Solar Cell. *Advanced Energy Materials* **2012,** 2, (2), 253-259.

[245] Sugimoto, H.; Hiroi, H.; Sakai, N.; Muraoka, S.; Katou, T. In *Over 8% Efficiency Cu2ZnSnS4 Submodules with Ultra-Thin Absorber*, 38th IEEE Photovoltaic Specialist Conference, Austin, TX, 2012.

[246] Wang, K.; Gunawan, O.; Todorov, T.; Shin, B.; Chey, S. J.; Bojarczuk, N. A.; Mitzi, D.; Guha, S., Thermally evaporated Cu_2ZnSnS_4 solar cells. *Applied Physics Letters* **2010,** 97, (14), 143508-3.

[247] Xin, H.; Katahara, J. K.; Braly, I. L.; Hillhouse, H. W., 8% Efficient $Cu_2ZnSn(S,Se)_4$ Solar Cells from Redox Equilibrated Simple Precursors in DMSO. *Advanced Energy Materials* **2014**.

[248] Kauk, M.; Muska, K.; Altosaar, M.; Raudoja, J.; Pilvet, M.; Varema, T.; Timmo, K.; Volobujeva, O., Effects of sulphur and tin disulphide vapour treatments of $Cu_2ZnSnS(Se)_4$ absorber materials for monograin solar cells. In Energy Procedia, 2011; Vol. 10, pp 197-202.

[249] Green, M. A., *Solar Cells: Operating Principles, Technology, and System Applications*. Prentice Hall: 1981.

[250] Nelson, J., The Physics of Solar Cells. In Imperial College Press: 2003.

[251] Fonash, S., *Solar Cell Device Physics*. Academic Press: 2010.

[252] Würfel, P., *Physics of Solar Cells: From Basic Principles to Advanced Concepts*. Wiley-VCH: 2009.

[253] Klenk, R., Characterisation and modelling of chalcopyrite solar cells. *Thin Solid Films* **2001,** 387, (1), 135-140.

[254] Dullweber, T.; anna, G. H.; Rau, U.; Schock, H. W., A new approach to high-efficiency solar cells by band gap grading in $Cu(In,Ga)Se_2$ chalcopyrite semiconductors. *Solar Energy Materials and Solar Cells* **2001,** 67, (1–4), 145-150.

[255] 255. Contreras, M.; Tuttle, J.; Du, D.; Qi, Y.; Swartzlander, A.; Tennant, A.; Noufi, R., Graded band-gap $Cu(In,Ga)Se_2$ thin-film solar cell absorber with enhanced open-circuit voltage. *Applied Physics Letters* **1993,** 63, (13), 1824-1826.

[256] Dobson, K. D.; Visoly-Fisher, I.; Hodes, G.; Cahen, D., Stability of CdTe/CdS thin-film solar cells. *Solar Energy Materials and Solar Cells* **2000,** 62, (3), 295-325.

[257] Deibel, C.; Dyakonov, V.; Parisi, J.; Palm, J.; Zweigart, S.; Karg, F., Influence of damp heat testing on the electrical characteristics of $Cu(In,Ga)(S,Se)_2$ solar cells. *Thin Solid Films* **2002,** 403–404, (0), 325-330.

[258] Wennerberg, J.; Kessler, J.; Stolt, L., $Cu(In,Ga)Se_2$-based thin-film photovoltaic modules optimized for long-term performance. *Solar Energy Materials and Solar Cells* **2003,** 75, (1–2), 47-55.

[259] Tosun, B. S.; Feist, R. K.; Gunawan, A.; Mkhoyan, K. A.; Campbell, S. A.; Aydil, E. S., Improving the damp-heat stability of copper indium gallium diselenide solar cells with a semicrystalline tin dioxide overlayer. *Solar Energy Materials and Solar Cells* **2012,** 101, 270-276.

[260] Wu, X.; Keane, J. C.; Dhere, R. G.; DeHart, C.; Albin, D. S.; Duda, A.; Gessert, T. A.; Asher, S.; Levi, D. H.; Sheldon, P. In *16.5% efficient CdS/CdTe polycrystalline thin-film solar cell*, 17th European Photovoltaic Solar Energy Conference, Munich, Germany, 2001.

[261] Repins, I. L.; Stanbery, B. J.; Young, D. L.; Li, S. S.; Metzger, W. K.; Perkins, C. L.; Shafarman, W. N.; Beck, M. E.; Chen, L.; Kapur, V. K.; Tarrant, D.; Gonzalez, M. D.; Jensen, D. G.; Anderson, T. J.; Wang, X.; Kerr, L. L.; Keyes, B.; Asher, S.; Delahoy, A.; Von Roedern, B., Comparison of device performance and measured transport parameters in widely-varying Cu(In,Ga)(Se,S) solar cells. *Progress in Photovoltaics: Research and Applications* **2006,** 14, (1), 25-43.

[262] Tanaka, T.; Sueishi, T.; Saito, K.; Guo, Q.; Nishio, M.; Yu, K. M.; Walukiewicz, W., Existence and removal of Cu_2Se second phase in coevaporated $Cu_2ZnSnSe_4$ thin films. *Journal of Applied Physics* **2012,** 111, (5).

[263] Buffiere, M.; Brammertz, G.; El Mel, A.-A.; Lenaers, N.; Ren, Y.; Zaghi, A.; Mols, Y.; Koeble, J.; Meuris, M.; Poortmans, J. In *Minority Carrier Lifetime Stability in Polycrystalline $Cu_2ZnSnSe_4$ Thin Films*, 39th IEEE Photovoltaic Specialist Conference, Tampa, FL, 2013.

[264] Metzger, W. K.; Repins, I. L.; Contreras, M. A., Long lifetimes in high-efficiency $Cu(In,Ga)Se_2$ solar cells. *Applied Physics Letters* **2008,** 93, (2).

[265] Repins, I. L.; Metzger, W. K.; Perkins, C. L.; Li, J. V.; Contreras, M. A., Correlation Between Measured Minority-Carrier Lifetime and $Cu(In, Ga)Se_2$ Device Performance. *Ieee Transactions on Electron Devices* **2010,** 57, (11), 2957-2963.

[266] Zhang, J.; Shao, L.; Fu, Y.; Xie, E., Cu_2ZnSnS_4 thin films prepared by sulfurization of ion beam sputtered precursor and their electrical and optical properties. *Rare Metals* **2006,** 25, (6, Supplement 1), 315-319.

[267] Tanaka, T.; Nagatomo, T.; Kawasaki, D.; Nishio, M.; Guo, Q. X.; Wakahara, A.; Yoshida, A.; Ogawa, H., Preparation of Cu_2ZnSnS_4 thin films by hybrid sputtering. *Journal of Physics and Chemistry of Solids* **2005,** 66, (11), 1978-1981.

[268] Zhou, Z. H.; Wang, Y. Y.; Xu, D.; Zhang, Y. F., Fabrication of Cu_2ZnSnS_4 screen printed layers for solar cells. *Solar Energy Materials and Solar Cells* **2010,** 94, (12), 2042-2045.

[269] Liu, F.; Li, Y.; Zhang, K.; Wang, B.; Yan, C.; Lai, Y.; Zhang, Z.; Li, J.; Liu, Y., In situ growth of Cu_2ZnSnS_4 thin films by reactive magnetron co-sputtering. *Solar Energy Materials and Solar Cells* **2010,** 94, (12), 2431-2434.

[270] Scragg, J. J.; Dale, P. J.; Peter, L. M., Synthesis and characterization of Cu_2ZnSnS_4 absorber layers by an electrodeposition-annealing route. *Thin Solid Films* **2009,** 517, (7), 2481-2484.

[271] Adhi Wibowo, R.; Soo Lee, E.; Munir, B.; Ho Kim, K., Pulsed laser deposition of quaternary $Cu_2ZnSnSe_4$ thin films. *physica status solidi (a)* **2007,** 204, (10), 3373-3379.

[272] Repins, I.; Beall, C.; Vora, N.; DeHart, C.; Kuciauskas, D.; Dippo, P.; To, B.; Mann, J.; Hsu, W.-C.; Goodrich, A.; Noufi, R., Co-evaporated $Cu_2ZnSnSe_4$ films and devices. *Solar Energy Materials and Solar Cells* **2012,** 101, (0), 154-159..

[273] Scheer, R.; Diesner, K.; Lewerenz, H. J., Experiments on the microstructure of evaporated $CuInS_2$ thin films. *Thin Solid Films* **1995,** 268, (1–2), 130-136.

[274] Gabor, A. M.; Tuttle, J. R.; Albin, D. S.; Contreras, M. A.; Noufi, R.; Hermann, A. M., High efficiency $CuIn_xGa_{1-x}Se_2$ solar cells made from $(In_xGa_{1-x})_2Se_3$ precursor films. *Applied Physics Letters* **1994,** 65, (2), 198-200.

[275] Mickelsen, R. A.; Chen, W. S.; Hsiao, Y. R.; Lowe, V. E., Polycrystalline thin-film $CuInSe_2$/CdZnS solar cells. *IEEE Transactions on Electron Devices*, **1984,** 31, (5), 542-546.

[276] Tuttle, J. R.; Contreras, M.; Bode, M. H.; Niles, D.; Albin, D. S.; Matson, R.; Gabor, A. M.; Tennant, A.; Duda, A.; Noufi, R., Structure, chemistry, and growth mechanisms of photovoltaic quality thin-film $Cu(In,Ga)Se_2$ grown from a mixed-phase precursor. *Journal of Applied Physics* **1995,** 77, (1), 153-161.

[277] Niki, S.; Fons, P. J.; Yamada, A.; Lacroix, Y.; Shibata, H.; Oyanagi, H.; Nishitani, M.; Negami, T.; Wada, T., Effects of the surface Cu_2Se phase on the growth and properties of $CuInSe_2$ films. *Applied Physics Letters* **1999,** 74, (11), 1630-1632.

[278] Bar, M.; Schubert, B. A.; Marsen, B.; Wilks, R. G.; Pookpanratana, S.; Blum, M.; Krause, S.; Unold, T.; Yang, W.; Weinhardt, L.; Heske, C.; Schock, H. W., Cliff-like conduction band offset and KCN-induced recombination barrier enhancement at the CdS/Cu_2ZnSnS_4 thin-film solar cell heterojunction. *Applied Physics Letters* **2011,** 99, (22).

[279] Fairbrother, A.; García-Hemme, E.; Izquierdo-Roca, V.; Fontané, X.; Pulgarín-Agudelo, F. A.; Vigil-Galán, O.; Pérez-Rodríguez, A.; Saucedo, E., Development of a Selective Chemical Etch To Improve the Conversion Efficiency of Zn-Rich Cu_2ZnSnS_4 Solar Cells. *Journal of the American Chemical Society* **2012,** 134, (19), 8018-8021.

[280] Repins, I.; Vora, N.; Beall, C.; Wei, S.-H.; Yan, Y.; Romero, M.; Teeter, G.; Du, H.; To, B.; Young, M.; Noufi, R., Kesterites and Chalcopyrites: A Comparison of Close Cousins. *Materials Research Society Spring Meeting*, San Francisco, California, 2011.

[281] Tanaka, T.; Yoshida, A.; Saiki, D.; Saito, K.; Guo, Q.; Nishio, M.; Yamaguchi, T., Influence of composition ratio on properties of Cu_2ZnSnS_4 thin films fabricated by co-evaporation. *Thin Solid Films* **2010,** 518, (21, Supplement), S29-S33.

[282] Schubert, B.-A.; Marsen, B.; Cinque, S.; Unold, T.; Klenk, R.; Schorr, S.; Schock, H.-W., Cu_2ZnSnS_4 thin film solar cells by fast coevaporation. *Progress in Photovoltaics: Research and Applications* **2011,** 19, (1), 93-96.

[283] Hsu, W.-C.; Repins, I.; Beall, C.; DeHart, C.; To, B.; Yang, W.; Yang, Y.; Noufi, R., Growth mechanisms of co-evaporated kesterite: a comparison of Cu-rich and Zn-rich composition paths. *Progress in Photovoltaics: Research and Applications* **2012**.

[284] Schorr, S.; Weber, A.; Honkimäki, V.; Schock, H.-W., In-situ investigation of the kesterite formation from binary and ternary sulphides. *Thin Solid Films* **2009,** 517, (7), 2461-2464.

[285] Schurr, R.; Holzing, A.; Jost, S.; Hock, R.; Voss, T.; Schulze, J.; Kirbs, A.; Ennaoui, A.; Lux-Steiner, M.; Weber, A.; Kotschau, I.; Schock, H. W., The crystallisation of Cu_2ZnSnS_4 thin film solar cell absorbers from co-electroplated Cu-Zn-Sn precursors. *Thin Solid Films* **2009,** 517, (7), 2465-2468.

[286] 286. Yoo, H.; Kim, J., Growth of Cu_2ZnSnS_4 thin films using sulfurization of stacked metallic films. *Thin Solid Films* **2010,** 518, (22), 6567-6572.

[287] Yoo, H.; Wibowo, R. A.; Hölzing, A.; Lechner, R.; Palm, J.; Jost, S.; Gowtham, M.; Sorin, F.; Louis, B.; Hock, R., Investigation of the solid state reactions by time-resolved X-ray diffraction while crystallizing kesterite $Cu_2ZnSnSe_4$ thin films. *Thin Solid Films* **2013,** 535, (0), 73-77.

[288] Wätjen, J. T.; Engman, J.; Edoff, M.; Platzer-Björkman, C., Direct evidence of current blocking by ZnSe in $Cu_2ZnSnSe_4$ solar cells. *Applied Physics Letters* **2012,** 100, (173510).

[289] Unold, T.; Kretzschmar, S.; Just, J.; Zander, O.; Schubert, B.; Marsen, B.; Schock, H. In *Correlation between composition and photovoltaic properties of Cu_2ZnSnS_4 thin film solar cells*, 37th IEEE Photovoltaic Specialists Conference (PVSC), 2011; pp 002820-002823.

[290] Mousel, M.; Redinger, A.; Djemour, R.; Arasimowicz, M.; Valle, N.; Dale, P.; Siebentritt, S., HCl and Br_2-MeOH etching of $Cu_2ZnSnSe_4$ polycrystalline absorbers. *Thin Solid Films* **2013,** 535, (0), 83-87.

[291] Kashiwabara, H.; Hayase, Y.; Takeshita, K.; Okuda, T.; Niki, S.; Matsubara, K.; Sakurai, K.; Yamada, A.; Ishizuka, S.; Terada, N. In *Study of Changes of Electronic and Structural Nature of CBD-CDS/CIGS Interface with Ga Concentration*, Conference Record of the 2006 IEEE 4th World Conference on Photovoltaic Energy Conversion, 2006; pp 495-498.

[292] Naghavi, N.; Renou, G.; Bockelee, V.; Donsanti, F.; Genevee, P.; Jubault, M.; Guillemoles, J. F.; Lincot, D., Chemical deposition methods for Cd-free buffer layers in CIGS solar cells: Role of window layers. *Thin Solid Films* **2011,** 519, (21), 7600-7605.

[293] Hariskos, D.; Spiering, S.; Powalla, M., Buffer layers in $Cu(In,Ga)Se_2$ solar cells and modules. *Thin Solid Films* **2005,** 480, 99-109.

[294] Siebentritt, S., Alternative buffers for chalcopyrite solar cells. *Solar Energy* **2004,** 77, (6), 767-775.

[295] Regesch, D.; Gutay, L.; Larsen, J. K.; Depredurand, V.; Tanaka, D.; Aida, Y.; Siebentritt, S., Degradation and passivation of $CuInSe_2$. *Applied Physics Letters* **2012,** 101, (11).

[296] Ramanathan, K.; Bhattacharya, R. N.; Granata, J.; Webb, J.; Niles, D.; Contreras, M. A.; Wiesner, H.; Hasoon, F. S.; Noufi, R. In *Advances in the CIS research at NREL*, Conference Record of the Twenty-Sixth IEEE Photovoltaic Specialists Conference, 1997; pp 319-322.

[297] Jiang, C.-S.; Hasoon, F. S.; Moutinho, H. R.; Al-Thani, H. A.; Romero, M. J.; Al-Jassim, M. M., Direct evidence of a buried homojunction in $Cu(In,Ga)Se_2$ solar cells. *Applied Physics Letters* **2003,** 82, (1), 127-129.

[298] Lei, B.; Hou, W. W.; Li, S.-H.; Yang, W.; Chung, C.-H.; Yang, Y., Cadmium ion soaking treatment for solution processed $CuInS_xSe_{2-x}$ solar cells and its effect on defect properties. *Solar Energy Materials and Solar Cells* **2011,** 95, (8), 2384-2389.

[299] Cojocaru-Miredin, O.; Choi, P.; Wuerz, R.; Raabe, D., Atomic-scale characterization of the $CdS/CuInSe_2$ interface in thin-film solar cells. *Applied Physics Letters* **2011,** 98, (10), 103504-3.

[300] Maeda, T.; Nakamura, S.; Wada, T., First-Principles Study on Cd Doping in Cu_2ZnSnS_4 and $Cu_2ZnSnSe_4$. *Japanese Journal of Applied Physics* **2012,** 51, (10).

[301] Jiang, F.; Shen, H.; Wang, W.; Zhang, L., Preparation and Properties of Cu_2ZnSnS_4 Absorber and Cu_2ZnSnS_4/Amorphous Silicon Thin-Film Solar Cell. *Applied Physics Express* **2011,** 4, (7).

[302] Htay, M. T.; Hashimoto, Y.; Momose, N.; Sasaki, K.; Ishiguchi, H.; Igarashi, S.; Sakurai, K.; Ito, K., A Cadmium-Free Cu_2ZnSnS_4/ZnO Hetrojunction Solar Cell Prepared by Practicable Processes. *Japanese Journal of Applied Physics* **2011,** 50, (3).

[303] Barkhouse, D. A. R.; Haight, R.; Sakai, N.; Hiroi, H.; Sugimoto, H.; Mitzi, D. B., Cd-free buffer layer materials on $Cu_2ZnSn(S_xSe_{1-x})_4$: Band alignments with ZnO, ZnS, and In_2S_3. *Applied Physics Letters* **2012,** 100, (193904).

[304] Hiroi, H.; Sakai, N.; Muraoka, S.; Katou, T.; Sugimoto, H. In *Development of High-Efficiency Cu_2ZnSnS_4 Submodule with Cd-Free Buffer Layer*, 38th IEEE PVSC, Austin, TX, 2012.

[305] Chen, S.; Walsh, A.; Yang, J.-H.; Gong, X. G.; Sun, L.; Yang, P.-X.; Chu, J.-H.; Wei, S.-H., Compositional dependence of structural and electronic properties of $Cu_2ZnSn(S,Se)_4$ alloys for thin film solar cells. *Physical Review B* **2011,** 83, (12), 125201.

[306] 306. Li, J.; Wei, M.; Du, Q.; Liu, W.; Jiang, G.; Zhu, C., The band alignment at $CdS/Cu_2ZnSnSe_4$ heterojunction interface. *Surface and Interface Analysis* **2012**.

[307] Gunawan, O.; Todorov, T. K.; Mitzi, D. B., Loss mechanisms in hydrazine-processed $Cu_2ZnSn(Se,S)_4$ solar cells. *Applied Physics Letters* **2010,** 97, (23), 3.

[308] Merdes, S.; Abou-Ras, D.; Mainz, R.; Klenk, R.; Lux-Steiner, M. C.; Meeder, A.; Schock, H. W.; Klaer, J., $CdS/Cu(In,Ga)S_2$ based solar cells with efficiencies reaching 12.9% prepared by a rapid thermal process. *Progress in Photovoltaics: Research and Applications* **2012**.

[309] Böker, T.; Severin, R.; Müller, A.; Janowitz, C.; Manzke, R.; Voß, D.; Krüger, P.; Mazur, A.; Pollmann, J., Band structure of MoS_2, $MoSe_2$, and α-$MoTe_2$: Angle-resolved photoelectron spectroscopy and ab initio calculations. *Physical Review B* **2001,** 64, (23), 235305.

[310] Wada, T.; Kohara, N.; Nishiwaki, S.; Negami, T., Characterization of the $Cu(In,Ga)Se_2$/Mo interface in CIGS solar cells. *Thin Solid Films* **2001,** 387, (1–2), 118-122.

[311] Kohara, N.; Nishiwaki, S.; Hashimoto, Y.; Negami, T.; Wada, T., Electrical properties of the $Cu(In,Ga)Se_2/MoSe_2$/Mo structure. *Solar Energy Materials and Solar Cells* **2001,** 67, (1-4), 209-215.

[312] Kaelin, M.; Rudmann, D.; Kurdesau, F.; Zogg, H.; Meyer, T.; Tiwari, A. N., Low-cost CIGS solar cells by paste coating and selenization. *Thin Solid Films* **2005,** 480–481, (0), 486-490.

[313] Haug, V.; Quintilla, A.; Klugius, I.; Ahlswede, E., Influence of an additional carbon layer at the back contact–absorber interface in $Cu(In,Ga)Se_2$ thin film solar cells. *Thin Solid Films* **2011,** 519, (21), 7464-7467.

[314] Lee, E.; Park, S. J.; Cho, J. W.; Gwak, J.; Oh, M.-K.; Min, B. K., Nearly carbon-free printable CIGS thin films for solar cell applications. *Solar Energy Materials and Solar Cells* **2011,** 95, (10), 2928-2932.

[315] Klugius, I.; Miller, R.; Quintilla, A.; Friedlmeier, T. M.; Blázquez-Sánchez, D.; Ahlswede, E.; Powalla, M., Growth mechanism of thermally processed Cu(In,Ga)S2 precursors for printed $Cu(In,Ga)(S,Se)_2$ solar cells. *physica status solidi (RRL) – Rapid Research Letters* **2012**.

[316] Eisenbarth, T.; Unold, T.; Caballero, R.; Kaufmann, C. A.; Schock, H.-W., Interpretation of admittance, capacitance-voltage, and current-voltage signatures in $Cu(In,Ga)Se_2$ thin film solar cells. *Journal of Applied Physics* **2010,** 107, (3), 034509-12.

[317] Niemegeers, A.; Burgelman, M., Effects of the Au/CdTe back contact on IV and CV characteristics of Au/CdTe/CdS/TCO solar cells. *Journal of Applied Physics* **1997,** 81, (6), 2881-2886.

[318] Repins, I. L.; Romero, M. J.; Teeter, G.; Li, J. V.; Wei, S.-H.; Kuciauskas, D.; Beal, C. L.; DeHart, C. M.; Mann, J. R.; Hsu, W.-C.; Goodrich, A. C.; Noufi, R. In *Kesterite Successes, Ongoing Work, and Challenges: A Perspective from Vacuum Deposition*, 38th IEEE PVSC, Austin, TX, 2012.

[319] Das, P.; Samantaray, S.; Rout, G. R., Studies on Cadmium Toxicity in Plants: A Review. *Enviorn. Pollut.* **1997,** 98, (1), 29-36.

[320] Phipps, G.; Mikolajczak, C.; Guckes, T., Indium and Gallium: Long-Term Supply. *Renewable Energy Focus* **2008,** 9, (4), 56, 58-59.

[321] Cohen, B. L., Anomalous Behavior of Tellurium Abundances. *Geochim. Cosmochim. Ac* **1984,** 48, (1), 203-205.

[322] Woodhouse, M.; Goodrich, A.; Margolis, R.; James, T. L.; Lokanc, M.; Eggert, R., Supply-Chain Dynamics of Tellurium, Indium, and Gallium Within the Context of PV Manufacturing Costs. *IEEE Journal of Photovoltaics*, **2013,** 3, (2), 833-837.

[323] Raugei, M.; Fthenakis, V., Cadmium flows and emissions from CdTe PV: future expectations. *Energy Policy* **2010,** 38, (9), 5223-5228.

[324] Fthenakis, V. M.; Wang, W., Extraction and separation of Cd and Te from cadmium telluride photovoltaic manufacturing scrap. *Progress in Photovoltaics: Research and Applications* **2006,** 14, (4), 363-371.

[325] Vasilis M, F., Life cycle impact analysis of cadmium in CdTe PV production. *Renewable and Sustainable Energy Reviews* **2004,** 8, (4), 303-334.

[326] Schmid, D.; Ruckh, M.; Grunwald, F.; Schock, H. W., Chalcopyrite/defect chalcopyrite heterojunctions on the basis of $CuInSe_2$. *Journal of Applied Physics* **1993,** 73, (6), 2902-2909.

[327] Dullweber, T.; Lundberg, O.; Malmström, J.; Bodegård, M.; Stolt, L.; Rau, U.; Schock, H. W.; Werner, J. H., Back surface band gap gradings in $Cu(In,Ga)Se_2$ solar cells. *Thin Solid Films* **2001,** 387, (1-2), 11-13.

[328] Demoulin, P. D.; Lundstrom, M. S.; Schwartz, R. J., Back-surface field design for n+p GaAs cells. *Solar Cells* **1987,** 20, (3), 229-236.

[329] Tsunomura, Y.; Yoshimine, Y.; Taguchi, M.; Baba, T.; Kinoshita, T.; Kanno, H.; Sakata, H.; Maruyama, E.; Tanaka, M., Twenty-two percent efficiency HIT solar cell. *Solar Energy Materials and Solar Cells* **2009,** 93, (6–7), 670-673.

[330] Witte, W.; Abou-Ras, D.; Albe, K.; Bauer, G. H.; Bertram, F.; Boit, C.; Brüggemann, R.; Christen, J.; Dietrich, J.; Eicke, A.; Hariskos, D.; Maiberg, M.; Mainz, R.; Meessen, M.; Müller, M.; Neumann, O.; Orgis, T.; Paetel, S.; Pohl, J.; Rodriguez-Alvarez, H.; Scheer, R.; Schock, H.-W.; Unold, T.; Weber, A.; Powalla, M., Gallium gradients in $Cu(In,Ga)Se_2$ thin-film solar cells. *Progress in Photovoltaics: Research and Applications* **2014**.

[331] Hedstrom, J.; Ohlsen, H.; Bodegard, M.; Kylner, A.; Stolt, L.; Hariskos, D.; Ruckh, M.; Schock, H. W.; Ieee, ZnO/CdS/$Cu(In,Ga)Se_2$ Thin-Film Solar Cells With Improved Performance. In *Conference Record of the Twenty Third IEEE Photovoltaic Specialists Conference, 1993*, pp 364-371.

[332] Basol, B. M.; Kapur, V. K.; Leidholm, C. R.; Minnick, A.; Halani, A.; Ieee, Studies on substrates and contacts for CIS films and devices. In *1994 IEEE First World Conference on Photovoltaic Energy Conversion/Conference Record of the 24th IEEE Photovoltaic Specialists Conference-1994, Vols I and II*, IEEE: New York, 1994; pp 148-151.

[333] Dawsonelli, D. F.; Moore, C. B.; Gay, R. R.; Jensen, C. L.; Ieee, Substrate influences on CIS device performance. In *1994 IEEE First World Conference on Photovoltaic Energy Conversion/Conference Record of the 24th IEEE Photovoltaic Specialists Conference-1994, Vols I and II*, IEEE: New York, 1994; pp 152-155.

[334] Wei, S. H.; Zhang, S. B.; Zunger, A., Effects of Na on the electrical and structural properties of $CuInSe_2$. *Journal of Applied Physics* **1999,** 85, (10), 7214-7218.

[335] Ruckh, M.; Schmid, D.; Kaiser, M.; Schaffler, R.; Walter, T.; Schock, H. W.; Ieee, Influence of substrates on the electrical properties of $Cu(In,Ga)Se_2$ thin films. *IEEE First World Conference on Photovoltaic Energy Conversion/Conference Record of the 24th IEEE Photovoltaic Specialists Conference-1994, Vols I and II*, IEEE: New York, 1994; pp 156-159.

[336] Contreras, M. A.; Egaas, B.; Dippo, P.; Webb, J.; Granata, J.; Ramanathan, K.; Asher, S.; Swartzlander, A.; Noufi, R.; Ieee, On the role of Na and modifications to $Cu(In,Ga)Se_2$ absorber materials using thin-MF (M=Na, K, Cs) precursor layers. *Conference Record of the 26th IEEE Photovoltaic Specialists Conference - 1997*, IEEE: New York, 1997; pp 359-362.

[337] Niles, D. W.; Ramanathan, K.; Hasoon, F.; Noufi, R.; Tielsch, B. J.; Fulghum, J. E., Na impurity chemistry in photovoltaic CIGS thin films: Investigation with x-ray photoelectron spectroscopy. *Journal of Vacuum Science & Technology a-Vacuum Surfaces and Films* **1997,** 15, (6), 3044-3049.

[338] Erslev, P. T.; Lee, J. W.; Shafarman, W. N.; Cohen, J. D., The influence of Na on metastable defect kinetics in CIGS materials. *Thin Solid Films* **2009,** 517, (7), 2277-2281.

[339] Schuler, S.; Siebentritt, S.; Nishiwaki, S.; Rega, N.; Beckmann, J.; Brehme, S.; Lux-Steiner, M. C., Self-compensation of intrinsic defects in the ternary semiconductor $CuGaSe_2$. *Physical Review B* **2004,** 69, (4), 9.

[340] Kronik, L.; Cahen, D.; Schock, H. W., Effects of sodium on polycrystalline $Cu(In,Ga)Se_2$ and its solar cell performance. *Advanced Materials* **1998,** 10, (1), 31-+.

[341] Hedstrom, J.; Ohlsen, H.; Bodegard, M.; Kylner, A.; Stolt, L.; Hariskos, D.; Ruckh, M.; Schock, H. In *ZnO/CdS/Cu(In,Ga)Se_2 thin film solar cells with improved performance*, Conference Record of the 23rd IEEE Photovoltaic Specialists Conference, 1993, 10-14, pp 364-371.

[342] Nakada, T.; Iga, D.; Ohbo, H.; Kunioka, A., Effects of sodium on Cu(In, Ga)Se_2-Based thin films and solar cells. *Japanese Journal of Applied Physics Part 1-Regular Papers Short Notes & Review Papers* **1997,** 36, (2), 732-737.

[343] Green, M. A.; Emery, K.; Hishikawa, Y.; Warta, W.; Dunlop, E. D., Solar cell efficiency tables (version 43). *Progress in Photovoltaics* **2014,** 22, (1), 1-9.

[344] Chin, K. K.; Wei, S. H., Local charge neutgrality condition, Fermi level, and carrier compensation of CdTe polycrystalline thin film in CdS/CdTe solar cells. In *35th IEEE Photovoltaic Specialists Conference (PVSC)*, IEEE: 2010; pp 000878-000884.

[345] Wei, S. H.; Zhang, S. B., Chemical trends of defect formation and doping limit in II-VI semiconductors: The case of CdTe. *Physical Review B* **2002,** 66, (15), 10.

[346] Sites, J.; Pan, J., Strategies to increase CdTe solar-cell voltage. *Thin Solid Films* **2007,** 515, (15), 6099-6102.

[347] Wolden, C. A.; Kurtin, J.; Baxter, J. B.; Repins, I.; Shaheen, S. E.; Torvik, J. T.; Rockett, A. A.; Fthenakis, V. M.; Aydil, E. S., Photovoltaic manufacturing: Present status, future prospects, and research needs. *Journal of Vacuum Science & Technology A* **2011,** 29, (3), 16.

[348] Sites, J. R., Voltage Deficit in Thin-Film Polycrystalline Solar Cells. In *Solar Energy Technologies Program*, DOE/EERE: 2007.

[349] Hajimammadov, R.; Fathi, N.; Bayramov, A.; Khrypunov, G.; Klochko, N.; Li, T., Effect of "$CdCl_2$ Treatment" on Properties of CdTe-Based Solar Cells Prepared by Physical Vapor Deposition and Close-Spaced Sublimation Methods. *Japanese Journal of Applied Physics* **2011,** 50, (5), 2.

[350] Chen, S. Y.; Gong, X. G.; Walsh, A.; Wei, S. H., Defect Physics of The Kesterite Thin-Film Solar Cell Absorber Cu_2ZnSnS_4. *Applied Physics Letters* **2010,** 96, (2), 3.

[351] Katagiri, H., Cu_2ZnSnS_4 thin film solar cells. *Thin Solid Films* **2005,** 480, 426-432.

[352] Guo, Q.; Cao, Y.; Caspar, J. V.; Farneth, W. E.; Ionkin, A. S.; Johnson, L. K.; Lu, M.; Malajovich, I.; Radu, D.; Choudhury, K. R.; Rosenfeld, H. D.; Wu, W. In *A Simple Solution-based Route to High-Efficiency CZTSSe Thin-film Solar Cells* 38th IEEE Photovoltaics Specialist Conference, Austin, TX, 2012; pp 002993-002996.

[353] Cheng, A. J.; Manno, M.; Khare, A.; Leighton, C.; Campbell, S. A.; Aydil, E. S., Imaging and phase identification of Cu_2ZnSnS_4 thin films using confocal Raman spectroscopy. *Journal of Vacuum Science & Technology A* **2011,** 29, (5).

[354] Fernandes, P. A.; Salome, P. M. P.; da Cunha, A. F., Study of polycrystalline Cu_2ZnSnS_4 films by Raman scattering. *Journal of Alloys and Compounds* **2011,** 509, (28), 7600-7606.

[355] Guo, Q.; Hillhouse, H. W.; Agrawal, R., Synthesis of Cu_2ZnSnS_4 nanocrystal ink and its use for solar cells. *Journal of the American Chemical Society* **2009,** 131, (33), 11672-11673.

[356] Li, M.; Zhou, W.-H.; Guo, J.; Zhou, Y.-L.; Hou, Z.-L.; Jiao, J.; Zhou, Z.-J.; Du, Z.-L.; Wu, S.-X., Synthesis of Pure Metastable Wurtzite CZTS Nanocrystals by Facile One-Pot Method. *The Journal of Physical Chemistry C* **2012,** 116, (50), 26507-26516.

[357] Liao, H.-C.; Jao, M.-H.; Shyue, J.-J.; Chen, Y.-F.; Su, W.-F., Facile synthesis of wurtzite copper-zinc-tin sulfide nanocrystals from plasmonic djurleite nuclei. *Journal of Materials Chemistry A* **2013,** 1, (2), 337-341.

[358] Regulacio, M. D.; Ye, C.; Lim, S. H.; Bosman, M.; Ye, E.; Chen, S.; Xu, Q.-H.; Han, M.-Y., Colloidal Nanocrystals of Wurtzite-Type Cu_2ZnSnS_4: Facile Noninjection Synthesis and Formation Mechanism. *Chemistry – A European Journal* **2012,** 18, (11), 3127-3131.

[359] Tan, J. M. R.; Lee, Y. H.; Pedireddy, S.; Baikie, T.; Ling, X. Y.; Wong, L. H., Understanding the Synthetic Pathway of a Single-Phase Quarternary Semiconductor Using Surface-Enhanced Raman Scattering: A Case of Wurtzite Cu_2ZnSnS_4 Nanoparticles. *Journal of the American Chemical Society* **2014,** 136, (18), 6684-6692.

[360] Luo, Q.; Zeng, Y.; Chen, L.; Ma, C., Controllable Synthesis of Wurtzite Cu_2ZnSnS_4 Nanocrystals by Hot-Injection Approach and Growth Mechanism Studies. *Chemistry – An Asian Journal* **2014,** 9, (8), 2309-2316.

[361] Lu, X.; Zhuang, Z.; Peng, Q.; Li, Y., Wurtzite Cu2ZnSnS4 nanocrystals: a novel quaternary semiconductor. *Chemical Communications* **2011,** 47, (11), 3141-3143.

[362] Yang, W.-C.; Miskin, C. K.; Hages, C. J.; Hanley, E. C.; Handwerker, C.; Stach, E. A.; Agrawal, R., Kesterite $Cu_2ZnSn(S,Se)_4$ Absorbers Converted from Metastable, Wurtzite-Derived Cu_2ZnSnS_4 Nanoparticles. *Chemistry of Materials* **2014,** 26, (11), 3530-3534.

[363] Cattley, C. A.; Cheng, C.; Fairclough, S. M.; Droessler, L. M.; Young, N. P.; Warner, J. H.; Smith, J. M.; Assender, H. E.; Watt, A. A. R., Low temperature phase selective synthesis of Cu_2ZnSnS_4 quantum dots. *Chemical Communications* **2013,** 49, (36), 3745-3747.

[364] Singh, A.; Geaney, H.; Laffir, F.; Ryan, K. M., Colloidal Synthesis of Wurtzite Cu_2ZnSnS_4 Nanorods and Their Perpendicular Assembly. *Journal of the American Chemical Society* **2012,** 134, (6), 2910-2913.

[365] Collord, A. D.; Xin, H.; Hillhouse, H. W., Combinatorial Exploration of the Effects of Intrinsic and Extrinsic Defects in $Cu_2ZnSn(S,Se)_4$. *IEEE Journal of Photovoltaics*, **2014,** PP, (99), 1-11.

[366] Carter, N. J.; Yang, W.-C.; Miskin, C. K.; Hages, C. J.; Stach, E. A.; Agrawal, R., $Cu_2ZnSn(S,Se)_4$ solar cells from inks of heterogeneous Cu–Zn–Sn–S nanocrystals. *Solar Energy Materials and Solar Cells* **2014,** 123, (0), 189-196.

[367] Saunders, N.; Miodownik, A. P., The Cu-Sn (Copper-Tin) system. *Bulletin of Alloy Phase Diagrams* **1990,** 11, (3), 278-287.

[368] Fernandes, P. A.; Salome, P. M. P.; da Cunha, A. F., Study of polycrystalline Cu_2ZnSnS_4 films by Raman scattering. *Journal of Alloys and Compounds* **2011,** 509, (28), 7600-7606.

[369] Berg, D. M.; Djemour, R.; Guetay, L.; Siebentritt, S.; Dale, P. J.; Fontane, X.; Izquierdo-Roca, V.; Perez-Rodriguez, A., Raman analysis of monoclinic Cu2SnS3 thin films. *Applied Physics Letters* **2012,** 100, (19).

[370] Pradhan, N.; Reifsnyder, D.; Xie, R.; Aldana, J.; Peng, X., Surface Ligand Dynamics in Growth of Nanocrystals. *Journal of the American Chemical Society* **2007,** 129, (30), 9500-9509.

[371] Pankove, J. I., *Optical Processes in Semiconductors*. Dover: New York, 1971.

[372] Luther, J. M.; Jain, P. K.; Ewers, T.; Alivisatos, A. P., Localized surface plasmon resonances arising from free carriers in doped quantum dots. *Nature Materials* **2011,** 10, (5), 361-366.

[373] Kriegel, I.; Jiang, C. Y.; Rodriguez-Fernandez, J.; Schaller, R. D.; Talapin, D. V.; da Como, E.; Feldmann, J., Tuning the Excitonic and Plasmonic Properties of Copper Chalcogenide Nanocrystals. *Journal of the American Chemical Society* **2012,** 134, (3), 1583-1590.

[374] Xie, Y.; Riedinger, A.; Prato, M.; Casu, A.; Genovese, A.; Guardia, P.; Sottini, S.; Sangregorio, C.; Miszta, K.; Ghosh, S.; Pellegrino, T.; Manna, L., Copper Sulfide Nanocrystals with Tunable Composition by Reduction of Covellite Nanocrystals with Cu+ Ions. *Journal of the American Chemical Society* **2013,** 135, (46), 17630-17637.

[375] Fernandes, P. A.; Salome, P. M. P.; da Cunha, A. F., A study of ternary Cu_2SnS_3 and Cu_3SnS_4 thin films prepared by sulfurizing stacked metal precursors. *Journal of Physics D-Applied Physics* **2010,** 43, (21).

[376] Dai, P.; Shen, X.; Lin, Z.; Feng, Z.; Xu, H.; Zhan, J., Band-gap tunable $(Cu_2Sn)_{x/3}Zn_{1-x}S$ nanoparticles for solar cells. *Chemical Communications* **2010,** 46, (31), 5749-5751.

[377] Liu, Q.; Zhao, Z.; Lin, Y.; Guo, P.; Li, S.; Pan, D.; Ji, X., Alloyed $(ZnS)_x(Cu_2SnS_3)_{1-x}$ and $(CuInS_2)_x(Cu_2SnS_3)_{1-x}$ nanocrystals with arbitrary composition and broad tunable band gaps. *Chemical Communications* **2011,** 47, (3), 964-966.

[378] Katagiri, H.; Jimbo, K.; Tahara, M.; Araki, H.; Oishi, K. In *The Influence of Composition Ratio on CZTS-based Thin Film Solar Cells*, 2009 MRS Spring Meeting, 2009; pp 1165-M04-1.

[379] Tuttle, J. R.; Contreras, M. A.; Ramanathan, K. R.; Asher, S. E.; Bhattacharya, R.; Berens, T. A.; Keane, J.; Noufi, R., Materials and processing issues in thin-film Cu (In, Ga) Se2 -based solar cells. *AIP Conference Proceedings* **1997,** 394, (1), 83-106.

[380] Ridley, B. A.; Nivi, B.; Jacobson, J. M., All-Inorganic Field Effect Transistors Fabricated by Printing. *Science* **1999,** 286, (5440), 746-749.

[381] Law, M.; Luther, J. M.; Song, Q.; Hughes, B. K.; Perkins, C. L.; Nozik, A. J., Structural, optical, and electrical properties of PbSe nanocrystal solids treated thermally or with simple amines. *Journal of the American Chemical Society* **2008,** 130, 5974-5985.

[382] Talapin, D. V.; Murray, C. B., PbSe nanocrystal solids for n- and p-channel thin film field-effect transistors. *Science* **2005,** 310, (5745), 86-89.

[383] Guo, Q.; Ford, G. M.; Hillhouse, H. W.; Agrawal, R., Sulfide Nanocrystal Inks for Dense $Cu(In,Ga)(S,Se)_2$ Absorber Films and Their Photovoltaic Performance. *Nano Letters* **2009,** 9, (8), 3060-3065.

[384] Collord, A. D.; Hillhouse, H. W., Composition Control and Formation Pathway of CZTS and CZTGS Nanocrystal Inks for Kesterite Solar Cells. *Chemistry of Materials* **2015,** 27, (5), 1855-1862.

[385] Zhang, C.; Zhang, J.; Hao, Y.; Lin, Z.; Zhu, C., A simple and efficient solar cell parameter extraction method from a single current-voltage curve. *Journal of Applied Physics* **2011,** 110, (6).

[386] Todorov, T. K.; Tang, J.; Bag, S.; Gunawan, O.; Gokmen, T.; Zhu, Y.; Mitzi, D. B., Beyond 11% Efficiency: Characteristics of State-of-the-Art $Cu_2ZnSn(S,Se)_4$ Solar Cells. *Advanced Energy Materials* **2013,** Vol. 3, (Issue 1), 34-38.

[387] Chen, S.; Walsh, A.; Gong, X.-G.; Wei, S.-H., Classification of Lattice Defects in the Kesterite Cu_2ZnSnS_4 and $Cu_2ZnSnSe_4$ Earth-Abundant Solar Cell Absorbers. *Advanced Materials* **2013,** 25, (11), 1522-1539.

[388] Siebentritt, S.; Gütay, L.; Regesch, D.; Aida, Y.; Deprédurand, V., Why do we make $Cu(In,Ga)Se_2$ solar cells non-stoichiometric? *Solar Energy Materials and Solar Cells*, (0).

[389] Gutay, L.; Regesch, D.; Larsen, J. K.; Aida, Y.; Depredurand, V.; Siebentritt, S., Influence of copper excess on the absorber quality of $CuInSe_2$. *Applied Physics Letters* **2011,** 99, (15), 151912-3.

[390] Yin, W.-J.; Wu, Y.; Wei, S.-H.; Noufi, R.; Al-Jassim, M. M.; Yan, Y., Engineering Grain Boundaries in Cu2ZnSnSe4 for Better Cell Performance: A First-Principle Study. *Advanced Energy Materials* **2014,** 4, (1).

[391] Li, J.; Mitzi, D. B.; Shenoy, V. B., Structure and Electronic Properties of Grain Boundaries in Earth-Abundant Photovoltaic Absorber $Cu_2ZnSnSe_4$ *Acs Nano* **2011,** 5, (11), 8613-8619.

[392] Katahara, J. K.; Hillhouse, H. W., Quasi-Fermi Level Splitting and Sub-Bandgap Absorptivity from Semiconductor Photoluminescence. *Journal of Applied Physics* **2014,** 116, 173504.

[393] 393. Le Quang, P.; Okano, M.; Yamada, Y.; Nagaoka, A.; Yoshino, K.; Kanemitsu, Y., Photocarrier localization and recombination dynamics in Cu_2ZnSnS_4 single crystals. *Applied Physics Letters* **2013,** 103, (19).

[394] Levcenko, S.; Tezlevan, V. E.; Arushanov, E.; Schorr, S.; Unold, T., Free-to-bound recombination in near stoichiometric Cu_2ZnSnS_4 single crystals. *Physical Review B* **2012,** 86, (4), 045206.

[395] Halliday, D. P.; Claridge, R.; Goodman, M. C. J.; Mendis, B. G.; Durose, K.; Major, J. D., Luminescence of Cu_2ZnSnS_4 polycrystals described by the fluctuating potential model. *Journal of Applied Physics* **2013,** 113, (22).

[396] Miyamoto, Y.; Tanaka, K.; Oonuki, M.; Moritake, N.; Uchiki, H., Optical properties of Cu_2ZnSnS_4 thin films prepared by sol-gel and sulfurization method. *Japanese Journal of Applied Physics* **2008,** 47, (1), 596-597.

[397] Gershon, T.; Shin, B.; Bojarczuk, N.; Gokmen, T.; Lu, S.; Guha, S., Photoluminescence characterization of a high-efficiency Cu_2ZnSnS_4 device. *Journal of Applied Physics* **2013,** 114, (15).

[398] Gershon, T.; Shin, B.; Gokmen, T.; Lu, S.; Bojarczuk, N.; Guha, S., Relationship between Cu_2ZnSnS_4 quasi donor-acceptor pair density and solar cell efficiency. *Applied Physics Letters* **2013,** 103, (19).

[399] Du, H.; Yan, F.; Young, M.; To, B.; Jiang, C. S.; Dippo, P.; Kuciauskas, D.; Chi, Z. H.; Lund, E. A.; Hancock, C.; Hlaing, O.; Scarpulla, M. A.; Teeter, G., Investigation of combinatorial coevaporated thin film Cu_2ZnSnS_4. I. Temperature effect, crystalline phases, morphology, and photoluminescence. *Journal of Applied Physics* **2014,** 115, (17).

[400] Kask, E.; Grossberg, M.; Josepson, R.; Salu, P.; Timmo, K.; Krustok, J., Defect studies in $Cu_2ZnSnSe_4$ and $Cu_2ZnSn(Se_{0.75}S_{0.25})_4$ by admittance and photoluminescence spectroscopy. *Materials Science in Semiconductor Processing*.

[401] Chirila, A.; Reinhard, P.; Pianezzi, F.; Bloesch, P.; Uhl, A. R.; Fella, C.; Kranz, L.; Keller, D.; Gretener, C.; Hagendorfer, H.; Jaeger, D.; Erni, R.; Nishiwaki, S.; Buecheler, S.; Tiwari, A. N., Potassium-induced surface modification of $Cu(In,Ga)Se_2$ thin films for high-efficiency solar cells. *Nature Materials* **2013,** 12, (12), 1107-1111.

[402] Todorov, T. K.; Tang, J.; Bag, S.; Gunawan, O.; Gokmen, T.; Zhu, Y.; Mitzi, D. B., Beyond 11% Efficiency: Characteristics of State-of-the-Art Cu2ZnSn(S,Se)4 Solar Cells. *Advanced Energy Materials* **2012**.

[403] Walsh, A.; Chen, S.; Wei, S.-H.; Gong, X.-G., Kesterite thin-film solar cells: Advances in materials modelling of Cu_2ZnSnS_4. *Advanced Energy Materials* **2012,** 2, 400-409.

[404] Shockley, W.; Queisser, H. J., Detailed balance limit of efficiency of p-n junction solar cells. *Journal of Applied Physics* **1961,** 32, (3), 510-519.

[405] Van Roosbroeck, W.; Shockley, W., Photon-Radiative Recombination of Electrons and Holes in Germanium. *Physical Review* **1954,** 94, (6), 1558-1560.

[406] Lasher, G.; Stern, F., Spontaneous and Stimulated Recombination Radiation in Semiconductors. *Physical Review a-General Physics* **1964,** 133, (2A), A553-&.

[407] Wurfel, P., The Chemical Potential of Radiation. *Journal of Physics C-Solid State Physics* **1982,** 15, (18), 3967-3985.

[408] Bhattacharya, R.; Pal, B.; Bansal, B., On conversion of luminescence into absorption and the van Roosbroeck-Shockley relation. *Applied Physics Letters* **2012,** 100, (22).

[409] Katahara, J. K.; Hillhouse, H. W., Quasi-Fermi Level Splitting and Sub-Bandgap Absorptivity from Semiconductor Photoluminescence. *Journal of Applied Physics* **2014**.

[410] Bucherl, C. N.; Oleson, K. R.; Hillhouse, H. W., Thin film solar cells from sintered nanocrystals. *Current Opinion in Chemical Engineering* **2013,** 2, (2), 168-177.

[411] Burstein, E.; Davisson, J. W.; Bell, E. E.; Turner, W. J.; Lipson, H. G., Infrared Photoconductivity due to Neutral Impurities in Germanium. *Physical Review* **1954,** 93, (1), 65-68.

[412] Avery, D. G.; Goodwin, D. W.; Lawson, W. D.; Moss, T. S., Optical and Photo-Electrical Properties of Indium Antimonide. *Proceedings of the Physical Society of London Section B* **1954,** 67, (418), 761-767.

[413] Erslev, P. T.; Young, M. R.; Li, J. V.; Siah, S. C.; Chakraborty, R.; Du, H.; Lad, R. J.; Buonassisi, T.; Teeter, G., Tetrahedrally coordinated disordered Cu_2SnS_3– Cu_2ZnSnS_4–ZnS alloys with tunable optical and electronic properties. *Solar Energy Materials and Solar Cells*, (0).

[414] Fukano, T.; Tajima , S.; Ito, T., Enhancement of Conversion Efficiency of Cu_2ZnSnS_4 Thin Film Solar Cells by Improvement of Sulfurization Conditions. *Applied Physics Express* **2013,** 6, (6), 062301.

[415] Lundberg, O.; Edoff, M.; Stolt, L., The effect of Ga-grading in CIGS thin film solar cells. *Thin Solid Films* **2005,** 480, 520-525.

[416] Katahara, J. K.; Hillhouse, H. W., Quasi-Fermi Level Splitting and Sub-Bandgap Absorptivity from Semiconductor Photoluminescence. *Journal of Applied Physics* **2014,** 116, 173504.

[417] Kim, I.; Kim, K.; Oh, Y.; Woo, K.; Cao, G.; Jeong, S.; Moon, J., Bandgap-Graded $Cu_2Zn(Sn_{1-x}Ge_x)S_4$ Thin-Film Solar Cells Derived from Metal Chalcogenide Complex Ligand Capped Nanocrystals. *Chemistry of Materials* **2014,** 26, (13), 3957-3965.

[418] Chesman, A. S. R.; van Embden, J.; Della Gaspera, E.; Duffy, N. W.; Webster, N. A. S.; Jasieniak, J. J., Cu_2ZnGeS_4 Nanocrystals from Air-Stable Precursors for Sintered Thin Film Alloys. *Chemistry of Materials* **2014,** 26, (19), 5482-5491.

[419] Xin, H.; Katahara, J. K.; Braly, I. L.; Hillhouse, H. W., 8% Efficient $Cu_2ZnSn(S,Se)_4$ Solar Cells from Redox Equilibrated Simple Precursors in DMSO. *Advanced Energy Materials* **2014,** 4, (11).

[420] Kim, J.; Hiroi, H.; Todorov, T. K.; Gunawan, O.; Kuwahara, M.; Gokmen, T.; Nair, D.; Hopstaken, M.; Shin, B.; Lee, Y. S.; Wang, W.; Sugimoto, H.; Mitzi, D. B., High Efficiency $Cu_2ZnSn(S,Se)_4$ Solar Cells by Applying a Double In_2S_3/CdS Emitter. *Advanced Materials* **2014,** 26, (44), 7427-7431.

[421] Haass, S. G.; Diethelm, M.; Werner, M.; Bissig, B.; Romanyuk, Y. E.; Tiwari, A. N., 11.2% Efficient Solution Processed Kesterite Solar Cell with a Low Voltage Deficit. *Advanced Energy Materials* **2015**.

[422] Gloeckler, M.; Sites, J. R., Efficiency limitations for wide-band-gap chalcopyrite solar cells. *Thin Solid Films* **2005,** 480-481, 241-245.

[423] Li, J.; Wei, M.; Du, Q.; Liu, W.; Jiang, G.; Zhu, C., The band alignment at CdS/$Cu_2ZnSnSe_4$ heterojunction interface. *Surface and Interface Analysis* **2013,** 45, (2), 682-684.

[424] Halim, M. A.; Islam, M. M.; Xianjia, L.; Chong, X.; Sakurai, T.; Sakai, N.; Kato, T.; Sugimoto, H.; Tampo, H.; Shibata, H.; Niki, S.; Akimoto, K. In *Study of recombination process in Cu_2ZnSnS_4 thin film using two-wavelength excited photoluminescence*, 40th IEEE Photovoltaic Specialist Conference (PVSC), 2014; pp 2334-2337.

[425] Miller, D. W.; Warren, C. W.; Gunawan, O.; Gokmen, T.; Mitzi, D. B.; Cohen, J. D., Electronically active defects in the $Cu_2ZnSn(Se,S)_4$ alloys as revealed by transient photocapacitance spectroscopy. *Applied Physics Letters* **2012,** 101, (14).

[426] Moutinho, H. R.; Al-Jassim, M. M.; Levi, D. H.; Dippo, P. C.; Kazmerski, L. L., Effects of $CdCl_2$ treatment on the recrystallization and electro-optical properties of CdTe thin films. *Journal of Vacuum Science & Technology a-Vacuum Surfaces and Films* **1998,** 16, (3), 1251-1257.

[427] Harvey, S. P.; Teeter, G.; Moutinho, H.; Al-Jassim, M. M., Direct evidence of enhanced chlorine segregation at grain boundaries in polycrystalline CdTe thin films via three-dimensional TOF-SIMS imaging. *Progress in Photovoltaics* **2015,** 23, (7), 838-846.

[428] Ringel, S. A.; Smith, A. W.; Macdougal, M. H.; Rohatgi, A., The Effects of $CdCl_2$ on the Electronic Properties of Molecular Beam Epitaxially Grown CdTe/CdS Heterojunction Solar Cells. *Journal of Applied Physics* **1991,** 70, (2), 881-889.

[429] Pianezzi, F.; Reinhard, P.; Chirila, A.; Bissig, B.; Nishiwaki, S.; Buecheler, S.; Tiwari, A. N., Unveiling the effects of post-deposition treatment with different alkaline elements on the electronic properties of CIGS thin film solar cells. *Physical Chemistry Chemical Physics* **2014,** 16, (19), 8843-8851.

[430] Nakakoba, H.; Yatsushiro, Y.; Mise, T.; Kobayashi, T.; Nakada, T., Effects of Bi Incorporation on $Cu(In_{1-x},Ga_x)Se_2$ Thin Films and Solar Cells. *Japanese Journal of Applied Physics* **2012,** 51, (10).

[431] Nakada, T.; Honishi, Y.; Yatsushiro, Y.; Nakakoba, H. In *Impacts of Sb and Bi incorporations on CIGS thin films and solar cells*, 37th IEEE Photovoltaic Specialists Conference (PVSC), 2011; pp 003527-003531.

[432] Yuan, M.; Mitzi, D. B.; Gunawan, O.; Kellock, A. J.; Chey, S. J.; Deline, V. R., Antimony assisted low-temperature processing of $CuIn_{1-x}Ga_xSe_{2-y}S_y$ solar cells. *Thin Solid Films* **2010,** 519, (2), 852-856.

[433] Maeda, T.; Kawabata, A.; Wada, T., First-principles study on alkali-metal effect of Li, Na, and K in Cu_2ZnSnS_4 and $Cu_2ZnSnSe_4$. *physica status solidi (c)* **2015,** 12, (6), 631-637.

[434] Xiao, W.; Wang, J. N.; Zhao, X. S.; Wang, J. W.; Huang, G. J.; Cheng, L.; Jiang, L. J.; Wang, L. G., Intrinsic defects and Na doping in Cu_2ZnSnS_4: A density-functional theory study. *Solar Energy* **2015,** 116, 125-132.

[435] Zhao, Z.-Y.; Zhao, X., First-Principles Study on Doping Effects of Sodium in Kesterite Cu_2ZnSnS_4. *Inorganic Chemistry* **2014,** 53, (17), 9235-9241.

[436] Li, J. V.; Kuciauskas, D.; Young, M. R.; Repins, I. L., Effects of sodium incorporation in Co-evaporated $Cu_2ZnSnSe_4$ thin-film solar cells. *Applied Physics Letters* **2013,** 102, (16).

[437] Gershon, T.; Lee, Y. S.; Mankad, R.; Gunawan, O.; Gokmen, T.; Bishop, D.; McCandless, B.; Guha, S., The impact of sodium on the sub-bandgap states in CZTSe and CZTS. *Applied Physics Letters* **2015,** 106, (12).

[438] Nagaoka, A.; Miyake, H.; Taniyama, T.; Kakimoto, K.; Nose, Y.; Scarpulla, M. A.; Yoshino, K., Effects of sodium on electrical properties in Cu2ZnSnS4 single crystal. *Applied Physics Letters* **2014,** 104, (15).

[439] Gershon, T.; Shin, B.; Bojarczuk, N.; Hopstaken, M.; Mitzi, D. B.; Guha, S., The Role of Sodium as a Surfactant and Suppressor of Non-Radiative Recombination at Internal Surfaces in Cu_2ZnSnS_4. *Advanced Energy Materials* **2015,** 5, (2).

[440] Werner, M.; Sutter-Fella, C. M.; Romanyuk, Y. E.; Tiwari, A. N., 8.3% efficient $Cu_2ZnSn(S,Se)_4$ solar cells processed from sodium-containing solution precursors in a closed reactor. *Thin Solid Films* **2015,** 582, 308-312.

[441] Sutter-Fella, C. M.; Stückelberger, J. A.; Hagendorfer, H.; La Mattina, F.; Kranz, L.; Nishiwaki, S.; Uhl, A. R.; Romanyuk, Y. E.; Tiwari, A. N., Sodium Assisted Sintering of Chalcogenides and Its Application to Solution Processed $Cu_2ZnSn(S,Se)_4$ Thin Film Solar Cells. *Chemistry of Materials* **2014,** 26, (3), 1420-1425.

[442] Braunger, D.; Hariskos, D.; Bilger, G.; Rau, U.; Schock, H. W., Influence of sodium on the growth of polycrystalline $Cu(In,Ga)Se_2$ thin films. *Thin Solid Films* **2000,** 361, 161-166.

[443] Foss, O.; Hauge, S., Tetrathiourea-Tellurium(II) Salts. *Acta Chemica Scandinavica* **1961,** 15, (7), 1616-&.

[444] Duan, H. S.; Yang, W. B.; Bob, B.; Hsu, C. J.; Lei, B.; Yang, Y., The Role of Sulfur in Solution-Processed $Cu_2ZnSn(S,Se)_4$ and its Effect on Defect Properties. *Advanced Functional Materials* **2013,** 23, (11), 1466-1471.

[445] Cao, Q.; Gunawan, O.; Copel, M.; Reuter, K. B.; Chey, S. J.; Deline, V. R.; Mitzi, D. B., Defects in Cu(In,Ga)Se2 Chalcopyrite Semiconductors: A Comparative Study of Material Properties, Defect States, and Photovoltaic Performance. *Advanced Energy Materials* **2011,** 1, (5), 845-853.

[446] Chirila, A.; Buecheler, S.; Pianezzi, F.; Bloesch, P.; Gretener, C.; Uhl, A. R.; Fella, C.; Kranz, L.; Perrenoud, J.; Seyrling, S.; Verma, R.; Nishiwaki, S.; Romanyuk, Y. E.; Bilger, G.; Tiwari, A. N., Highly efficient $Cu(In,Ga)Se_2$ solar cells grown on flexible polymer films. *Nature Materials* **2011,** 10, (11), 857-861.

[447] Scragg, J. J. S.; Choubrac, L.; Lafond, A.; Ericson, T.; Platzer-Bjorkman, C., A low-temperature order-disorder transition in Cu_2ZnSnS_4 thin films. *Applied Physics Letters* **2014,** 104, (4).

[448] Gershon, T.; Bishop, D.; McCandless, B.; Wang, W.; Haight, R. In *Capturing the effect of long low-temperature anneals on the sub-bandgap defect structure of CZTSSe*, 2015; pp 955209-955209-6.

[449] Yuan, Z.-K.; Chen, S.; Xiang, H.; Gong, X.-G.; Walsh, A.; Park, J.-S.; Repins, I.; Wei, S.-H., Engineering Solar Cell Absorbers by Exploring the Band Alignment and Defect Disparity: The Case of Cu- and Ag-Based Kesterite Compounds. *Advanced Functional Materials* **2015**.

[450] Lany, S.; Zunger, A., Light- and bias-induced metastabilities in $Cu(In,Ga)Se_2$ based solar cells caused by the (V_{Se}-V_{Cu}) vacancy complex. *Journal of Applied Physics* **2006,** 100, (11).

[451] Oikkonen, L. E.; Ganchenkova, M. G.; Seitsonen, A. P.; Nieminen, R. M., Redirecting focus in $CuInSe_2$ research towards selenium-related defects. *Physical Review B* **2012,** 86, (16), 165115.

VITA

Andrew Collord was born in Albuquerque, New Mexico as the 3rd son of Jane Ripple and Ross Collord. He received his bachelor's degree in Chemical Engineering from the University of New Mexico, and subsequently commenced graduate study at the University of Washington.